YEAR-END TECHNICAL REPORT

September 29, 2021 to September 28, 2022

Environmental Remediation Science and Technology

Date submitted:

December 22, 2022

Principal Investigator:

Leonel E. Lagos, Ph.D., PMP®

Florida International University Collaborators:

Yelena Katsenovich, Ph.D.
Ravi Gudavalli, Ph.D.
John Dickson, Ph.D.
Pieter Hazenberg, Ph.D.
Angelique Lawrence, M.S., GISP
Yan Zhou, Ph.D.
Hamid Bazgirkhoob, Ph.D.
Vadym Drozd, Ph.D.
DOE Fellows

Submitted to:

U.S. Department of Energy
Office of Environmental Management
Under Cooperative Agreement # DE-EM0005213

FIU | Applied Research Center
Florida International University

Addendum:

This document represents one (1) of five (5) reports that comprise the Year End Reports for the period of September 29, 2021 to September 28, 2022 prepared by the Applied Research Center at Florida International University for the U.S. Department of Energy Office of Environmental Management (DOE-EM) under Cooperative Agreement No. DE-EM0005213.

The complete set of FIU's Year End Reports for this reporting period includes the following documents:

Project 1: Chemical Process Alternatives for Radioactive Waste
Document number: FIU-ARC-2021-800012997-04b-006

Project 2: Environmental Remediation Science and Technology
Document number: FIU-ARC-2021-800013918-04b-004

Project 3: Waste and D&D Engineering and Technology Development
Document number: FIU-ARC-2021-800013919-04b-005

Project 4: DOE-FIU Science & Technology Workforce Development Initiative
Document number: FIU-ARC-2021-800013920-04b-017

Project 5: Long-Term Stewardship of Environmental Remedies: Contaminated Soils and Water and STEM Workforce Development
Document number: FIU-ARC-2021-800013922-04b-004

Each document will be submitted to OSTI separately under the respective project title and document number as shown above. In addition, the documents are available at the DOE Research website for the Cooperative Agreement between the U.S. Department of Energy Office of Environmental Management and the Applied Research Center at Florida International University: https://doeresearch.fiu.edu

DISCLAIMER

TABLE OF CONTENTS

LIST OF FIGURES

LIST OF TABLES

PROJECT 2 EXECUTIVE SUMMARY

This project targets research to support environmental remediation and long-term monitoring of contaminated sediment, surface water and groundwater at Hanford Site, Savannah River Site, Oak Ridge Reservation and the Waste Isolation Pilot Plant (WIPP). The aim is to reduce the potential for contaminant mobility or toxicity in the surface and subsurface through the development and application of state-of-the-art environmental remediation technologies at DOE sites. In FIU Year 2, FIU ARC provided research and technical support on contaminant remediation efforts at the Hanford Site under Task 1, at SRS under Tasks 2 and 3, at the WIPP under Tasks 5 & 6, and at the ORR under Task 7. The research involved laboratory-scale studies which utilized novel analytical methods and microscopy techniques for characterization of various mineral samples. Tasks also included the implementation of hydrological models, which help to predict the behavior and fate of existing and potential contaminants in the surface and subsurface. Photogrammetry techniques were also applied for development of high-resolution digital elevation models (DEMs) to support hydrological model development.

DOE Fellows supporting this project include Angel Almaguer (Undergraduate, Chemistry), Aubrey Litzinger (undergraduate, Environmental Engineering), Caridad Estrada (Undergraduate, Environmental Engineering), Gisselle Gutierrez (graduate, M.S. Environmental Engineering), Hannah Aziz (undergraduate, Environmental Engineering), Juan Morales (graduate, Ph.D., Envirnomental Health Sciences), Mariah Doughman (graduate, Ph.D., Chemistry), Phuong Pham (graduate, Ph.D., Chemistry) and Stevens Charles (undergraduate, Civil Engineering).

The following ARC researchers are supporting this project and mentoring the DOE-EM Fellows: Yelena Katsenovich (Ph.D., Env. Engineering, Tasks 1.1, 1.2, 1.3 & 1.4, Project Manager), Ravi Gudavalli (Ph.D., Env. Engineering, Tasks 2.1 & 2.2, Research Scientist), John Dickson (Ph.D., Agricultural Chemistry and Soil Science/Environmental Soil Chemistry, Tasks 5 & 7, Sr. Research Scientist), Pieter Hazenberg (Ph.D., Hydrology and Quantitative Water Management, Tasks 3 & 6, Snr. Research Scientist), Angelique Lawrence (M.S., Environmental Science, Tasks 3 & 6, Research Specialist II), Vadym Drozd (Ph.D., Inorganic Chemistry, Task 1.4, Research Associate), Jose Rivera (B.S., Civil Engineering, Research Analyst), Leonel Lagos (Ph.D., PMP®, Mechanical Eng./Civil/Env. Engineering, PI).

Task 1: Remediation Research and Technical Support for the Hanford Site

DOE EM has a critical need to understand the biogeochemical processes influencing the behavior of contaminants [uranium (U), iodine (I), technetium (Tc), chromium (Cr) and nitrate (NO_3^-)] in Hanford Site's deep vadose zone that can impact groundwater quality. These contaminants were accidentally released during production of atomic weapons at the Hanford Site from 1944 through the late 1980s, which has left a legacy of radionuclide contamination in soil and groundwater that poses technically complex environmental cleanup challenges that are unique to EM. The radioactive waste at Hanford Site contains about 195 million curies of radioactivity and 220,000 metric tons of chemicals. Of the 177 tanks onsite, sixty-seven have leaked about 3,800 cubic meters (1 million gallons) of liquids into the underlying sediment (Gephart, 2003). Most of this residual waste is in or near the 200 Area. These releases have created plumes that threaten groundwater quality due to potential downward migration through the unsaturated vadose zone (VZ) sediment.

The fastest-moving contaminants in the subsurface are technetium-99, iodine-129, chromium, uranium and nitrate (Gephart, 2003).

The Task 1 component of this end of year report presents an overview of subtasks supporting the cleanup mission at the Hanford Site that can complement ongoing work at PNNL for a better understanding of the long-term behavior of contaminants in the subsurface.

Task 2. Remediation Research and Technical Support for Savannah River Site

Iodine-129 and uranium are the major risk drivers from radiological acid waste contaminants released at the Savannah River Site's F-Area. Radionuclides previously disposed of through unlined seepage basins as a constituent of acidic, aqueous waste are moving towards Fourmile Branch and Tims Branch wetlands with natural groundwater flow, where they may subsequently be interacting with natural organic materials present in the wetland or with humic materials injected for remediation purposes.

There is a need for the Savannah River Site (SRS) to gather results to supplement permit requirements associated with the Area Completion Project (ACP), including the Phase 2 strategy to evaluate the performance of Phase 1 including "…downgradient of the F-Area inactive process sewer line and at Fourmile Branch". Per permitting requirements delineated in the corrective action plan, ^{129}I concentrations must be below groundwater standards in Fourmile Branch by October 31, 2025, and in the F-Area plume in surface water at the seepline by October 31, 2030. Because the DOE has no approved technology for remediation of subsurface iodine, it is essential to understand its long-term fate in plumes at the Savannah River Site. In addition, DOE-EM requires additional study of the fate of co-mingled contaminant plumes due to their complexity (McCabe, D., *et al.*, 2017). The experiments delineated in this subtask will contribute to both our understanding of the interactions of ^{129}I with organic materials and study the factors controlling the attenuation of ^{129}I in wetlands, as well as the potential for remediation of U via injection of modified humic materials, providing essential data for fulfillment of the abovementioned permitting requirements and goals for DOE-EM.

SRS is also conducting synergistic research, funded by the Department of Energy's Environmental Management Office of Soil and Groundwater Remediation, as part of the Attenuation-Based Remedies for the Subsurface Applied Field Research Initiative (ABRS AFRI). This applied research is geared towards developing science-based approaches to clean and close sites contaminated with combinations of metals, radionuclides, and other contaminants of concern. A primary objective of this program is to develop approaches for attenuation-based remedies, in this case, to investigate and validate the use of humate for subsurface stabilization of metals in contaminated groundwater plumes. SRS successfully conducted a field campaign that demonstrated the viability of dissolving and then injecting low cost agricultural humate into the subsurface and proposed that it may be a viable attenuation-based remedy for uranium and potentially for I-129 as well. Humic acid, which carries many functional groups, plays an important role in ion exchange and as a metal complexing ligand with a high complexation capacity, being able to affect the mobility of radionuclides in natural systems.

The fate and transport of uranium and iodine in the subsurface are controlled by various environmental factors such as pH, temperature, ORP, etc. A better understanding of the environmental conditions that affect these processes is critical to a more realistic risk assessment. During FIU Performance Year 1, FIU conducted research to investigate the factors controlling the attenuation of iodine in wetlands and continued ongoing research to investigate the impact of humic acid on U mobility at the Savannah River Site. Different types of humic substances such as KW-15 and KW-30 were used in this research to study their effect on uranium removal.

The Task 2 component of this end of year report presents an overview on subtasks supporting the Area Completion Project to reduce the contamination of Iodine as well as Attenuation-Based Remedies for the Subsurface Applied Field Research Initiative.

Task 3: Contaminant Fate and Transport Modeling for the Savannah River Site

This task involves the development and application of integrated hydrology and contaminant transport models for studying the fate of priority pollutants with emphasis on interactions between solute and sediment transport in the stream systems at SRS. The aim is to examine the response of these streams to historical discharges and environmental management remediation actions and to provide a means of assessment, evaluation and post-closure long-term monitoring of water quality and environmental conditions following remedial activities. In general, hydrological models are the standard tools used for investigating surface/subsurface flow behavior. They provide uncertainty quantification, risk and decision support for water resource management, and evaluation of water quality, erosion, deposition, and transport. The models being developed will serve as long-term monitoring tools that provide simulation capabilities to economically assess the fate and transport of heavy metals and radionuclides of concern (e.g., uranium and I-129), that may have direct or indirect impact on the SRS environment. The outcome of such models can potentially determine spatial and temporal distribution of suspended particles or contaminants in the area when heavy rainfall or storms occur.

The Task 3 component of this end of year report presents an overview on subtasks that will assist DOE-EM in ensuring the achievement and maintenance of regulatory compliance goals for water quality in these SRS watersheds..

Task 5: Research and Technical Support for WIPP

FIU is conducting basic research in collaboration with researchers from Los Alamos National Laboratory’s Actinide Chemistry and Repository Science (ACRSP) and DOE Carlsbad Field Office (DOE-CBFO) to support scientific basis for long-term disposition of nuclear wastes in WIPP repository. Actinide solubility is the key factor driving the fate and transport of radionuclides in the subsurface environment, especially in the far field of a nuclear waste disposal site such as the Waste Isolation Pilot Plant (WIPP). Along with low-probability groundwater intrusion the presence of metal-chelating organic ligands, iron oxide minerals (magnetite), and intrinsic actinide colloids may provide a potential release pathway for migration of the actinides. In this research the impact of gluconate (cellulose degradation product) and iron oxide minerals (magnetite, corrosion product) on actinide transport behavior under anaerobic conditions and high ionic-strength brine environments representative of the WIPP repository were studied using batch sorption experiments. Thus, a better understanding of the fate and transport of actinide in a high ionic-strength brine environment enriched in metal chelating ligands is critical to addressing the low-probability scenario of potential brine inundation and contaminant release due to human intrusions.

The Task 5 component of this end of year report presents an overview on Subtasks supporting acquisition of updated sorption data for interaction of actinides with minerals and organic ligands within the WIPP environment to with the goal of improving previous risk assessment models that have been characterized by high uncertainty.

Task 6: Hydrology Modeling for Basin 6 of the Nash Draw near the WIPP

Task 6 was developed to support research and development activities at the WIPP by scientists and researchers who are concerned about the impact of climate on the long-term vulnerability of this karst region and thus the eventual integrity and performance of this deep geologic transuranic waste repository due to the influence of characteristic surface features, such as sinkholes, swallets, and karst valleys on groundwater recharge over time. The task involves the development of a high-resolution digital elevation model (DEM) of Basin 6 of the Nash Draw, just west of the WIPP, to more accurately delineate surface hydrological features, and use of this DEM for development of regional hydrological models using the DOE-developed Advanced Terrestrial Simulator (ATS). A high-resolution DEM will improve the ability of the coupled surface/subsurface flow models to simulate the hydrologic response to a range of storm events, compute the surface water balance and provide more accurate estimates of regional-scale infiltration rates/groundwater recharge. With improved estimates of the spatial and temporal patterns of recharge to force the groundwater model, predictions of halite dissolution and propagation of the shallow dissolution front will be made possible and the potential impact on repository performance quantified.

The Task 6 component of this end of year report presents an overview of subtasks supporting the understanding of the role of heavy precipitation events on groundwater recharge through surface depressions like sinkholes and how this can impact the long-term stability of the WIPP.

Task 7: Engineered Multi-Layer Amendment Technology for Hg Remediation on Oak Ridge Reservation

This task involves the development of a sorbent-based technology for cost-effective remediation of mercury on the Oak Ridge Reservation (ORR). Mercury persistent geochemistry, bioaccumulative effect and continuous cycling through the environment complicate efforts to develop effective technologies for mercury remediation in freshwater stream ecosystems, such as the East Fork Poplar Creek (EFPC) in Oak Ridge, Tennessee. As a case study, the EFPC ecosystem received large point-source discharges during the 1950s. Although upstream mercury discharges to EFPC have declined, mercury releases still persist from point sources within the industrial facility where mercury was used and from diffuse downstream sources, such as contaminated bank soils. Recent results suggest that releases from diffuse and historical downstream sources, such as bank soils and sediment, are the key drivers of mercury contamination in the stream ecosystem. Despite widespread use of amendments for in-situ sequestration of organic contaminants, large-scale application of mercury sorbents is uncommon due to decreasing effectiveness in the presence of dissolved organic matter (DOM), cost and fouling problems that can potentially leach constituents and particles into waterbodies. Thus, the need to develop a sustainable, cost-effective solutions for mercury cleanup in EFPC is the main goal of this research.

The Task 7 component of this end of year report presents an overview of subtasks supporting the DOE’s Office of Environmental Management (EM) in addressing its priority mission of improving water quality and ecological health of EFPC.

MAJOR TECHNICAL ACCOMPLISHMENTS

Task 1: Remediation Research and Technical Support for the Hanford Site

- FIU completed solid characterization studies conducted in support of Project 2 Subtask 1.2 for the set of sediment samples amended with 0.1% ZVI and SMI. Results obtained through XRD showed that the mineralogy of both the post-treated experimental (aerobic), and sacrificial control batch samples (anaerobic) was composed of quartz (SiO_2), albite, muscovite, carbonate minerals, and aluminum silicates (Mg–, Na–, Ca–, and K–bearing). These mineral phases were observed in all samples and are typical of the natural makeup of Hanford Ringold Formation sediment.
- FIU has completed sampling of artificial groundwater (GW) & perched water (PW) solutions treated with 1% sulfur-modified iron (SMI) and zero valent iron (ZVI) in anaerobic conditions (Phase 1) followed by aerobic conditions (Phase 2) for Subtask 1.2. These experiments investigated re-oxidation behavior of PW and GW contaminants, such as Tc(VII), in the presence of U(VI) and NO_3^-, that have been initially reduced by strong reductants such as 1% ZVI and 1% SMI in batch-scale experiments under anaerobic initial conditions (Phase 1) followed by aerobic conditions (Phase 2). Sediment samples that were evaluated in these experiments included Tc(VII) comingled with U(VI) and nitrate. The experiments described herein will be continued in aerobic conditions to investigate for re-oxidation of U and Tc.
- FIU has completed anion analysis by ion chromatography for nitrate, nitrite and sulfate for samples treated with ZVI and SMI reductants. The concentration of SO_4^{2-} was larger in SMI-amended samples compared to ZVI in both anaerobic and aerobic conditions.
- FIU has completed analysis of hexavalent uranium [U(VI)] batch sorption experiments conducted with Hanford formation sediment. Data from both concentration ranges (0.05-9 mg/L and 20-100 mg/L) were best fit to the Langmuir adsorption isotherm (R^2=0.99) and the pseudo-second order kinetic model. The intraparticle diffusion kinetic model was also investigated. Results illustrated a multistep adsorption mechanism for 0.05-60 mg/L of U. At higher concentrations (80-100 mg/L) a different trend of decreasing sorption was observed over time that will be further investigated.
- FIU completed batch sorption experiments with hexavalent chromium [Cr(VI)] in artificial groundwater (AGW) onto Hanford Formation sediment for Subtask 1.3. Experiments suggested that Cr(VI) sorption onto Hanford Formation sediment became weaker at higher initial concentrations of Cr(VI).
- FIU completed the competitive batch adsorption experiment with hexavalent uranium [U(VI)] and hexavalent chromium [Cr(VI)]; data was analyzed and presented in the April monthly report.
- FIU completed the high and low-concentration uranium batch adsorption experiments for Subtask 1.3. This study investigates the impact major groundwater components have on the adsorption of uranium (VI) [U(VI)] onto Hanford Formation sediment. At higher initial concentrations, there was an observed decrease in K_d. This is indicative of the exhaustion of available adsorption sites on the sediment for U(VI). The Langmuir model gave the best

fit indicating nearly complete monolayer adsorption for U(VI). The small amount of adsorption (Q_{max}= 0.04 mg/g) observed in U(VI) batch experiments can be assumed to be due to the dominant $Ca_2UO_2(CO_3)_3^0$(aq) and $CaUO_2(CO_3)_3^{2-}$ species found in geochemical speciation modeling. This indicates that U(VI) is mobile in the vadose zone at the Hanford Site.

- FIU completed the analysis of data from the competitive commingled batch adsorption experiment between U(VI) and Cr(VI) to Hanford Formation sediment, which were fit to pseudo-first, pseudo-second, and intraparticle diffusion models. Experimental results suggested that Cr(VI) and U(VI) best fit the pseudo-second order model.
- For Subtask 1.3, FIU completed data was analyzed and fitted to the intraparticle diffusion model. Uranium [U(VI)] exposed to chromium [Cr(VI)] followed a two-step adsorption process; initial bulk diffusion followed by intraparticle diffusion. The significance between the adsorbed values of U(VI) present alone compared to being comingled with Cr(VI) will be further investigated.
- FIU completed comparison of the uranium removal by sediment coated with KW-30 with data previously obtained with KW-15 and plain sediment. KW-30 sorption increased 5 times compared to KW-15, while the uranium removal increased 30 times for KW-30-coated sediment compared to KW-15-coated sediment. The overall uranium removal increased 300 times for KW-30 compared to plain SRS sediment.
- For Subtask 1.3, FIU completed an evaluation of the summer internship experimental results at PNNL. Solid-water distribution coefficients, K_ds, determined from sorption isotherms in batch experiments (0.05-0.53 mg/L) ranged from 0.63-1.66 L/Kg. These values were significantly larger than the K_d of 0.04 L/Kg determined from a Cr(VI) (0.2 mg/L) column experiment. A retardation factor of 1.25 was also determined. This illustrates the importance of comparing multiple experimental techniques to determine contaminant fate and mobility at the laboratory scale. Overall, these results indicate that Cr(VI) remains mobile under natural site conditions.
- FIU initiated experiments with a grout-contacted solution that has also contacted Hanford sediment (the same as the lysimeter test and IDF) to replicate the co-disposal test conditions. FIU set up a column to collect grout-contacted solution that also contacted sediment.
- FIU completed the SPFT experiments using Ca-amended solutions at variable temperatures for Subtask 1.4.
- FIU has completed ICP-MS and ICP-OES analyses of leachates, which were collected in the SPFT experiment conducted at 70^{o}C using pH 12 buffer solutions amended with 130 ppm Ca^{2+}. The dissolution rate of borosilicate glass at 70^{o}C is reduced by an order of magnitude in the presence of Ca ions compared to pH 12 buffer solution.
- For Subtask 1.4, FIU completed the PCT test and B and Re analyses for sediment/grout-contacted solution.
- FIU completed ICP-OES analysis of leachates collected in the static PCT test using grout/sediment-contacted solution to quantify the released rates of Si, Al, Ca and K. The results showed that glass dissolution was slightly depressed compared to pH 12-adjusted

buffer solution and Si-amended solutions, but were higher compared to grout-contacted and Ca-amended solutions.

- FIU submitted two manuscripts to the proceedings of the Waste Management 2022 Symposia (WM2022): *"Effect of Grout-Contacted Solution on the Glass Dissolution Behavior"* by Vadym Drozd, Yelena Katsenovich, R. Matthew Asmussen, Shambhu Kandel, Alicia Maratos, Ravi Gudavalli, and Leonel Lagos; and *"Sustainable Sorbent Technology for Mercury Remediation in a Freshwater Aquatic System"* authored by John Dickson, Caridad Estrada, Yelena Katsenovich, Leonel Lagos, Alexander Johs, and Eric Pierce.
- FIU submitted an abstract to WM2023 based on the results of Subtask 1.2, Re-oxidation Behavior of Technetium-99 and Uranium Immobilized by Strong Reductants, authored by Yelena Katsenovich, Angel Almaguer, Nikolla Qafoku, Jim Szecsody, Hilary Emerson, and Leonel Lagos.

Task 2. Remediation Research and Technical Support for Savannah River Site

- FIU has conducted iodide (I^-) batch adsorption experiments onto 1.0 g/L of organoclays, PM-199 and MRM. The pseudo-first-order kinetic model describes the best fit to the kinetic adsorption of iodide ions on the organoclays PM-199 and MRM. The kinetic data were also used to investigate the existence of different phases in the adsorption process. This data suggested that iodide sorption exhibits a three-stage time dependent behavior with an initial adsorption on the surface of the organoclays, followed by the diffusion at the surface and/or within the organoclays before reaching equilibrium.
- FIU used kinetic data to investigate the initial stage of the adsorption process using Boyd's diffusion model. The linearity of the Boyd model's plots provided useful information to distinguish between film diffusion and intraparticle-transport-controlled rate of adsorption. The data suggested that the film diffusion controlled the sorption rate of iodide on organoclays PM-199 and MRM.
- FIU completed pre- and post-experimental characterization of SRS wetland sediment for Subtask 2.1. The characterization of Savannah River Site's F-Area wetland topsoil was conducted using scanning electron microscopy coupled with energy dispersive X-ray spectroscopy (SEM-EDS), X-Ray diffraction (XRD), and Fourier transform infrared spectroscopy (FTIR). The SEM images showed presence of fine clay particles with a wide range of particle sizes. The EDS analysis indicated presence of silicon, aluminum, iron, carbon, and oxygen in the soil composition. XRD identified quartz as the major mineral and kaolinite made up ~7% of the characterized soils. The FTIR spectra of untreated soil show the characteristic bands of kaolinite, quartz, and humic substances.
- FIU completed sorption experiments with 100 ppb iodide (I^-) and iodate (IO_3^-) onto 25 g/L of dried F-Area's wetland soil using ion chromatography (IC) for Subtask 2.1. Data suggested that natural iodine leached out from the wetland soil. Sequential extraction of iodine from the SRS wetland soil was carried out with 100 g/L SRS wetland soils at pH 5.5. Data showed that approximately 80% of iodine is water-soluble, 15% of iodine is bound to organic matter, 3% is associated with metal oxides, and 1% of iodine is ion-exchangeable.

- FIU created a conceptual model of the attenuation and release of iodine-129 to give insight into the mechanisms controlling the processes. There are several factors that contributed to the attenuation/release of I-129 in the study area such as the changes in water level, soil/water temperature, microbial activity, redox potential, organic matter, and pH of the environment. The FIU team provided a review on environmental influences such as primary productivity and redox conditions on the attenuation/release of contaminants.
- FIU completed experiments investigating the effect of pH on sorption of iodate and iodide on wetland sediment collected at 5-6ft depth. The results showed no sorption in the pH ranging from 4 to 8. These observations are in good agreement with field sampling data.
- FIU has completed a draft manuscript on the effect of environmental factors on iodine sorption onto SRS wetland sediment under Subtask 2.1. The journal of Science of Total Environment is being considered for publication. This study focuses on the elucidation of the attenuation and release mechanisms of ^{129}I occurring at the wetlands and evaluates the use of organoclays as a potential remediation technology for ^{129}I.
- For the Subtask 2.1, FIU performed the sequential extraction of iodine from wetland soils at different depth intervals (1-3, 5-6, 7-8, 10-11, and 13-14 feet). Results indicated that 50-80% of iodine is water soluble, thus becomes mobile with an increase in surface and groundwater levels due to rainfall events.

Task 3: Contaminant Fate and Transport Modeling for the Savannah River Site

For Subtask 3.1:

- FIU has transformed the MIKE SHE/MIKE 11 hyudrology model of the Tims Branch watershed from an event-based to a continuous model which allows for model execution for any period of interest. Efforts included the generation of model forcing at sub-daily temporal resolution, extension of the vegetation profile and incorporation of ponded areas of significance into the river network.
- FIU completed extending the Tims Branch model to run longer-term simulations, the FIU modeling team tested the revised model for 4 different periods (1991-1993; 1985-1993; 2007-2014; and 1982-2020). Simulation results indicate that the former event-based MIKE model was calibrated using a simulation period too short to properly account for the impact of model spin-up, which is currently resulting in an overestimation of discharge that could ultimately lead to incorrect heavy metal transport simulations. As such, there was a need to recalibrate some of the hydrological model parameters to improve model performance.
- FIU began the recalibration of certain hydrological model parameters (evapotranspiration and lateral groundwater flow) and started identifying the dominant transport model parameters from historical observations in Tims Branch and literature review. FIU also evaluated the ability of the MIKE 11 model to account for natural flow velocity variations occurring around the various ponds in Tims Branch. Model parameter estimates were finalized for uranium transport simulations using a spatially variable and uniform approach.
- FIU identified the importance of deep subsurface drainage while recalibration of the MIKE SHE/MIKE 11 model to enable long-term hydrological simulations in Tims Branch, but

was unsuccessful in recalibrating the Tims Branch hydrological model. The process of increasing the grid resolution was therefore initiated to speed-up the calibration process.

- FIU created a Python code was created to automate the generation of a MIKE SHE/MIKE 11 model at 250-meter grid resolution that could perform long-term simulations, as opposed to the former version of the model which was developed for event-based scenarios. The Python code was then used to create a MIKE SHE/MIKE 11 model at 250-meter grid resolution for both Tims Branch watershed (Subtask 3.1) and Fourmile Branch watershed (Subtask 3.2).
- FIU finalized the uranium transport modeling approach within ECO Lab for Tims Branch was finalized and FIU was successful in calibrating the advection-dispersion parameter of the MIKE 11 ECO Lab module for Tims Branch for the year 1993. FIU has since completed the optimization/calibration of the Tims Branch sediment & contaminant transport model for uranium including optimization of the ECO Lab module and has performed the first series of simulations of uranium transport in Tims Branch for the Year 1993 using the event-based MIKE SHE/MIKE 11 model.
- DOE Fellow Juan Morales who has supported and provided major contributions to the Pro ect 2 Tims Branch hydrological and contaminant transport modeling work at Savannah River Site transitioned to a new position at SRNL as a MSIPP Postdoctoral Fellow.

For Subtask 3.2:

- FIU refined the scope for the FIU Year 2 period of performance after discussion with DOE-EM collaborators at SRNL and Lawrence Berkeley National Lab to better support the current research being conducted in the SRS F-Area under the ALTEMIS project and be more complimentary to the existing groundwater modeling efforts in the F-Area. The revised scope involves the development of a detailed conceptual model of the hydrological flow processes occurring within the seepline over time in response to precipitation and throughout the different seasons (i.e., lateral (shallow) surface flow vs groundwater seepage) through a detailed assessment of in situ observations. Based on this conceptual understanding, FIU’s aim was to build a hydrological model focusing on the flow of groundwater downslope through the funnel and gate system and entering the seepline – riparian zone – river network using the MIKE model.
- FIU performed a watershed delineation using GIS and ArcHydro tools to establish a study domain and delineate hydrological features that are important for analyzing the surface hydrology in the SRS F-Area in the region extending from the existing seepline to the Fourmile Branch stream.
- FIU completed the hydrological conceptualization of the groundwater seep line interface downslope of the F-Area as set up using MIKE 11 and reported this milestone for Subtask 3.2 as completed.

Task 5: Research and Technical Support for WIPP

- FIU has completed Milestone 2021-P2-M14 on batch sorption experiments in WIPP-relevant brines spiked with high actinide concentrations (Subtask 5.2).
- Batch study results showed similar sorption trends in the gluconate-free and gluconate-amended brines.

- Under the batch experimental conditions employed in this study amendment of WIPP-relevant brines with gluconate resulted in little to no impact on sorption of actinides onto magnetite solid phase(s). This contradictory observation is likely due to the insufficient concentration of gluconate (~1 mg/L) that was used in these studies. Therefore, a 1:1:2 molar ratio of magnetite, actinide and gluconate is strongly suggested for copious formation of tertiary gluconate complexes with the studied actinides. These ongoing batch experiments are expected to improve the safety underpinning for storage of nuclear wastes in the WIPP salt repository and provide updated sorption data critical for robust safety/risk assessment modeling.

Task 6: Hydrology Modeling for Basin 6 of the Nash Draw near the WIPP

For Subtask 6.1:

- An FIU team of two DOE Fellows (Eduardo Rojas and Gisselle Gutierrez-Zuniga) and an FIU ARC Research Specialist (Mackenson Telusma) traveled to Carlsbad, NM from Dec. 13-18, 2021, and completed the UAV-based survey of Basin 6 located just west of the WIPP in Carlsbad, NM, covering the last ~5 km2 in the northernmost part of the study area. The complete dataset is being processed as per the photogrammetry workflow established during the pilot study to create a high-resolution DEM for use in the Basin 6 ATS model.

- FIU incorporated 3 additional vegetation removal methods to the process workflow for creating a high-resolution bare ground DEM of the Basin 6 study area west of the WIPP using the imagery from the February 2020 trip to Carlsbad, NM. As such, 6 different procedures in total were assessed, all generating a different high-resolution DSM. Based on the outcome, FIU will select the optimal method for creation of a bare ground DEM for use in the Basin 6 ATS model. FIU also set up training samples on the point cloud of Basin 6 for shrubs, bare ground, and vegetation using Cloud Compare in order to run a supervised classification. A Python script was also developed to obtain the elevation values of the ground control point (GCP) locations collected in situ during the February 2020 field trip so they can be compared to the elevation values of the DEM created from the previously tested vegetation removal methods using elevation graphs, boxplots and histograms. Several Python packages were reviewed as well as previously developed scripts to assist in this process.
- FIU completed the development of a 1-meter digital elevation model (DEM) for Basin 6 and submitted a report to DOE collaborators. The DEM was used for training of DOE Fellow, Aubrey Litzinger, on the ATS model during her Summer 2022 internship at LANL. Towards the end of the internship, the DEM was used to initiate the development of a high-resolution integrated surface/subsurface hydrology model of the Basin 6 study area west of the WIPP that is planned for FIU Year 3.

For Subtask 6.2:

- FIU completed the preliminary development of an ATS model for Basin 6 using a 10-meter resolution DEM. A draft report was submitted to DOE-EM that describes the procedure employed and the tools used for mesh generation and visualization of the initial simulation results.

Task 7. Engineered Multi-Layer Amendment Technology for Hg Remediation on Oak Ridge Reservation

- DOE Fellow Caridad Estrada, who is supporting Project 2 - Task 7, won 1st place among undergraduate research presentations at the annual Maximizing Access to Research Careers - Undergraduate Student Training for Academic Research (FIU MARC-U*STAR) symposium held on December 1, 2021. The title of her oral presentation was "*Sustainable Sorbent Technology for Mercury Remediation in Freshwater Aquatic Systems*".
- A poster titled "*Sorbent-Based Technology for Mercury Remediation in a Freshwater Aquatic System*" was presented at the American Geophysical Union conference held on December 13 -17, 2021 in New Orleans, Louisiana.
- FIU completed batch sorption isotherm experiments investigating mercury sorption onto eight sorbent media, powder activated carbon (PAC), Mackinawite +PAC, Si-thiol, Biochar, Filtrasorb 300, RemBind, Sorbster, and Organoclay PM199 in DOM-free artificial creek water.
- FIU evaluated two sorbents for the sorption of Hg-DOM: (1) *fsPAC* (Redox Solutions), which is an equal blend of mackinawite (Ferroblack) and finely ground lignite carbon. The Ferroblack is predominantly comprised of soluble S^{2-} and insoluble FeS.; and (2) *eSorb*, sourced from Sorbster, Inc. is a blend of an activated alumina, iron oxide and sulfur. The research results suggested that the rate of Hg-DOM adsorption was moderately rapid, approaching equilibrium at a 180-min time interval. Calculated kinetic model parameters demonstrated that the adsorption of Hg-DOM onto *fsPAC and eSorb* is primarily controlled by film diffusion.
- Under Task 7, FIU evaluated two new sorbent media: (1) *eBind* (RemBind Pty Ltd), which is a powdered blend of aluminum oxyhydroxide, activated carbon, clays and other proprietary additives. (2) *F300* (Calgon Carbon Corporation), which is a granular steam-activated carbon sorbent produced from bituminous coal via reagglomeration process. The kinetic data for mercury sorption as Hg-DOM onto *eBind and F300* sorbents showed that the rate of Hg-DOM adsorption was moderately rapid, approaching equilibrium at 60-1440-min time interval.
- Under Task 7, FIU completed the batch sorption studies (kinetic/isotherm) for a suite of sorbent media in DOM-amended creek simulants, thus completing Milestone 2021-P2-M5.

TASK 1: REMEDIATION RESEARCH AND TECHNICAL SUPPORT FOR THE HANFORD SITE

Subtask 1.2: Re-oxidation of Redox Sensitive Contaminants Immobilized by Strong Reductants

Subtask 1.2: Introduction

Technetium-99 (^{99}Tc) management is a high-priority activity for the EM complex due to its high aqueous solubility, toxicity and environmental mobility. Approximately 700 Ci of ^{99}Tc have been released to the Hanford subsurface and its remediation is challenging due to the variability of waste chemistries and heterogeneity of the deep vadose zone. A perched water zone located beneath 200-DV-1 Operable Unit at Hanford contains ^{99}Tc as pertechnetate ($Tc^{VII}O_4^-$) that can potentially migrate to the underlying aquifer. Reducing conditions without or with sulfides may temporarily immobilize ^{99}Tc as one or more Tc^{IV} precipitates. Previous research has shown that ^{99}Tc, as pertechnetate that has been reduced to $Tc^{IV}O_2$ or TcS_x precipitates, reoxidizes and will eventually remobilize back to the aqueous phase (Lukens, Bucher et al. 2005). Previous research has also shown that reduced Tc precipitates that have been coated with other low solubility precipitates can be effective for preventing Tc remobilization, so may be useful for remediation (Pearce, Serne et al. 2018). In addition, Tc can be incorporated into low solubility precipitates such as iron oxides (Boglaienko, Soltis et al. 2020) or tin oxides (Luksic, Riley et al. 2015), which may have application for ex-situ treatment. For this reason, there is a need for additional research under the specific conditions of subsurface remediation for the Hanford Site as other Tc species may form.

Recent bench scale evaluations provided insights on the pertechnetate reduction process using strong reductants in the sediment mixture (Lawter, Garcia et al. 2018); however, this process was not evaluated for the re-mobilization of ^{99}Tc under aerobic conditions. The study conducted at FIU between 2019 – 2021, investigated the re-oxidation behavior of ^{99}Tc to mimic field conditions, where the groundwater and perched water zone were slowly re-oxidized to naturally occurring conditions. Laboratory experiments evaluated re-oxidation behavior of ^{99}Tc initially reduced by strong reductants such as zero valent iron (ZVI, Hepure Technologies), sulfur modified iron (SMI-PS Inc.), and calcium polysulfide (CPS) in batch scale experiments under sequential anaerobic conditions followed by aerobic conditions. In FIU Year 2, experimental work was extended to investigate the reoxidation behavior of ^{99}Tc in in the presence of collocated uranyl (UO_2^{2+}) and nitrate (NO_3^-) ions.

Sediment samples obtained from the Hanford Site Ringold Formation were sieved and the ≤ 2 mm size fraction was used in the batch experiments. The batch experiments were conducted in two phases: Phase 1 – reduction of ^{99}Tc collocated with NO_3^- and UO_2^{2+} in the presence of strong reductants, 1.0 % ZVI or 1.0 % SMI, under anaerobic conditions for 4 weeks; and Phase 2 – re-oxidation of reduced ^{99}Tc and other contaminants, NO_3^- and UO_2^{2+}, under aerobic conditions for 5 weeks. Two contacting solutions were used in these experiments: (1) a synthetic perched water solution amended with 10 µg/L (34 pCi/L) of ^{99}Tc collocated with 150 mg/L of U(VI) and (2) a synthetic groundwater solution amended with 420 µg/L (122.3 pCi/L) of ^{99}Tc collocated with 124 mg/L NO_3^-.

Subtask 1.2: Objectives

The objective of this subtask is to study re-oxidation kinetics of perched and groundwater contaminants, such as ^{99}Tc(VII) comingled with NO_3^- and UO_2^{2+} that have been initially reduced by strong reductants such as 1.0% ZVI and 1.0% SMI, in batch-scale experiments under anaerobic initial conditions followed by aerobic conditions. This report presents results on Tc reduction and reoxidation behavior when ^{99}Tc is comingled with UO_2^{2+} in perched water and NO_3^- in groundwater solutions.

Subtask 1.2: Methodology

These batch experiments studied re-oxidation behavior of reduced forms of technetium [^{99}Tc$^{(IV)}$ oxides and/or sulfides] in the presence of UO_2^{2+} and NO_3^- after treatment with strong reductants, including ZVI and SMI. Ringold Formation non-contaminated sediment samples sent from PNNL were obtained near the Hanford Site. The sediment was dried in an oven at 30˚C for 48 hours and sieved through a 2 mm sieve (Saslow et al., 2018).

The ≤ 2 mm sediment fraction was used in the batch experiments conducted in two phases: Phase 1 - Reduction of ^{99}Tc comingled with UO_2^{2+} and NO_3^- in the presence of strong reductants under anaerobic conditions for 4 weeks; and Phase 2 - Identification of the re-oxidation rates of reduced ^{99}Tc comingled with UO_2^{2+} and NO_3^- under aerobic conditions for 5 weeks.

Initial set up

Ultrapure deionized water (> 18 MΩ-cm, DIW, 5 L) was purged with N_2 for 30 minutes and transferred into the anaerobic chamber (Coy Laboratory) to prepare 2.5 L of each of the two contacting simulant solutions of synthetic perched and groundwater solutions. An anaerobic CAM-12 meter inside the anaerobic chamber monitored oxygen (ppm) and hydrogen (%) levels. The anaerobic glove box was connected to two cylinders: (i) high purity nitrogen and (ii) nitrogen (95%) mixed with hydrogen (5%). The level of H_2 was kept as ~2% and O_2< 50 ppm. A palladium catalyst in the anaerobic chamber was replaced and regenerated weekly by heating in the oven at 180^{o}C for 4-5 h. The pH adjustment solutions were prepared based on the information presented in Table 1.

Table 1. HCl Volume (mL) to Prepare 100 mL of pH-Adjustment Solutions

MW_{HCl} =36.46 g/mol, density 1.18 g/cm^3, purity- 35-38%		
0.1 M	1 M	2 M
0.835 mL	$V = \frac{36.46 * 100 * 100}{1.18 * 37 * 1000} = 8.35\, mL$	16.7 mL

The perched water (PW) and groundwater (GW) simulants were prepared inside the glovebox, using salts defined in Table 2, and diluted using the previously created DIW purged with N_2. These solutions were then pH-adjusted by using small quantities of hydrochloric acid from Table 2 (HCl, TraceMetal™ Grade, 0.1 M, 1 M and 2 M) to a pH of 7.8 ± 0.1 and 8.2 ± 0.1 for the artificial GW and PW solutions, respectively. During pH adjustments, simulants were swirled gently. The pH electrode was calibrated using three buffers (pH: 4.01, 7.00, and 10.01) immediately before measuring the pH of the solutions.

Table 2. Recipes for Simulant Solutions (Saslow et al., 2018)

Synthetic Perched Water (PW) Recipe (~pH 8.2)			
Chemical	mmol/L	g/L	Mass to prepare 2.5 L solution, g
$NaHCO_3$	10.708	0.9	2.25
$KHCO_3$	0.310	0.031	0.0775
(anhydrous) $MgSO_4$	2.703	0.325	0.8125
$CaSO_4$ $2H_2O$ (dite)	0.561	0.097	0.2425
Na_2SO_4	1.744	0.248	0.62
NaCl	3.3006	0.193	0.4825
Add 100 µL of 2M HCl to 1L solution to lower pH to ~8.2			

Artificial Groundwater (GW) recipe (~pH 7.8)			
Chemical	mmol/L	g/L	Mass to prepare 2.5 L solution, g
$NaHCO_3$	1.586	0.133	0.3325
$KHCO_3$	0.123	0.012	0.03
$MgSO_4$	0.366	0.090	0.225
$MgCl_2$ $6H_2O$	0.247	0.050	0.125
$CaCl_2$ $2H_2O$	1.071	0.157	0.3925

100 mL of GW and 100 mL of PW were set aside for control samples without contaminants. The remaining simulant solutions (GW and PW) were spiked with contaminants of concern, 150 mg/L U and 10 µg/L ^{99}Tc were added to the PW while 420 µg/L of ^{99}Tc in addition to 124 mg/L $NO_3^{- -}$ were added to the GW. These Tc, U, and NO_3^- concentrations are consistent with previous work conducted at PNNL (Lawter et al., 2018) and experiments conducted in FY Year 1 (2021) by FIU (Table 3).

Table 3. Amounts of U, NO_3^- and Tc Added from Stock Solutions to 2.5 L of Artificial GW or PW Solutions

Volume of stock to prepare 2.5 L solution	**Tc (stock concentration 4.217 mM/417.483 mg/L)**	**U [uranyl acetate solution (depleted U)], $UO_2(OCOCH_3)_2{\cdot}2H_2O$, stock solution, 2%)***	**$NaNO_3^-$, 0.01 M** (0.62 g/L of NO_3)**
Groundwater (420 µg/L of ^{99}Tc and 124 mg/L NO_3^-	2515 µL		500 µL
Perched water (150 mg/L U and 10 µg/L ^{99}Tc)	59 µL	33.52 mL	

*****2% of $UO_2(OCOCH_3)_2{\cdot}2H_2O$ solution (MW= 424.14 g/mol) is 0.047 mol/L. This requires 13.4 mL per L to have 0.15 g/L of U.

******0.01 M $NaNO_3$ (MW= 90.104) requires 0.0901 g of salt dissolved in 100 mL D IW.

Twelve 250 mL bottles were given 10 ± 0.01 g of sieved homogeneously mixed sediment. This will provide a 1:10 solid to liquid ratio. Six bottles were given the specified amount of ZVI reductant in Table 4. The other six bottles were given the specified amount of SMI in Table 4. Two sediment-free control samples with 100 mL GW and PW synthetic solutions containing the same concentrations of ^{99}Tc, U, and NO_3^- as those used in the experimental samples were prepared inside the glovebox. These sediment-free control samples were treated the same as the experimental samples to determine the initial content of ^{99}Tc, U and NO_3^- in GW and PW solutions. In addition, two control bottles of 100 mL GW and PW amended with reductants and provided with sediment but without contaminants were prepared for solid characterization studies to compare iron products formed with and without contaminants. These contaminant-free samples were treated the same as other experimental samples and were set aside earlier in the experiment. Two reductant-free control samples were created containing contaminants and sediment. Each of the tested reductants were weighed to prepare for batch experiments within ± 0.01 g (1.0 % ZVI and 1.0 % SMI (Table 4 and Table 5).

Table 4. Mass of reductants in GW and PW bottles

Reductant per 100 mL	ZVI	SMI
GW (Tc=420 µg/L), 1.0%	1000 mg, Tc/Fe molar ratio=0.0023	1000 mg, Tc/Fe molar ratio=0.0023
PW (Tc= 10 µg/L), 1.0%	1000 mg, Tc/Fe molar ratio=0.000056	1000 mg, Tc/Fe molar ratio=0.000056

Table 5. The amount of experimental and control bottles

	ZVI	SMI
GW, 1.0%	**3** experimental bottles. Monitored changes in pH, oxidation reduction potential (ORP), dissolved oxygen (DO), and contaminant concentrations (Tc, NO_3^-). Use for solid characterization studies after the completion of reoxidation experiments	**3** experimental bottles. Monitored changes in pH, ORP, DO, and contaminant concentrations (Tc, NO_3^-). Use solids for the characterization studies after the completion of reoxidation experiments
	1 reductant- free GW control monitored changes in pH, ORP, DO, and contaminant concentrations	
	1 sediment-free control monitored changes in contaminant concentrations	**1** sediment-free control monitored changes in contaminant concentrations
	1 contaminant-free control to be used for solid characterization at the end of experiment	**1** contaminant-free control to be used for solids characterization at the end of experiment
	1 bottle of sacrificial control with contaminants for solid characterization after phase 1 in anaerobic glove box	**1** bottle of sacrificial control with contaminants for solid characterization after phase 1 in anaerobic glove box
PW, 1.0%	**3** experimental bottles. Monitored changes in pH, ORP, DO, and contaminant concentrations (Tc, U). Use for solid characterization studies after the completion of reoxidation experiments	**3** experimental bottles. Monitored changes in pH, ORP, DO, and contaminant concentrations (Tc, U). Use for solid characterization studies after the completion of reoxidation experiments
	1 reductant- free PW control to monitor changes in pH, ORP, DO, and contaminant concentrations (Tc, U)	
	1 sediment-free control to monitor changes in contaminant concentrations (Tc, U)	**1** sediment-free control to monitor changes in contaminant concentrations (Tc, U)
	1 contaminant-free control to be used for solids characterization	**1** contaminant-free control to be used for solids characterization
	1 bottle of sacrificial control with contaminants for solid characterization after phase 1 in anaerobic glove box	**1** bottle of sacrificial control with contaminants for solid characterization after phase 1 in anaerobic glove box

	ZVI	SMI
Total experimental	6	6
Total controls	8	6
Total bottles	26	

Phase 1: ^{99}Tc reduction experiment

Triplicate samples with sediment and reductant in 250 mL bottles were transferred into an anaerobic glovebox for 48 hours before contacting with 100 mL of deoxygenated synthetic GW and PW solutions amended with ^{99}Tc, UO_2^{2+} and NO_3^-. Samples were manually shaken several times per day for a period of 30 days (Saslow et al., 2018). An aliquot of 0.4 mL was collected at variable times, including 7 days, 15 days, 21 days and 28 days until nearly all ^{99}Tc, U and NO_3^- removal was achieved. Collected samples were filtered via 0.2 µm syringe filters and stored in a refrigerator (4°C) until analysis. Anions (NO_3^-, NO_2^-, and SO_4^-) were analyzed by ion chromatography (IC, Integrion Dionex), and ^{99}Tc, U, and Fe were measured by inductively coupled plasma mass spectrometry (ICP-MS, Thermo Fisher Scientific, iCAP RQ). Tc and U samples were prepared in 2 % nitric acid and NO_3^-, NO_2^-, and SO_4^- samples were prepared in DIW. In addition, measurements were taken for ORP, DO, and pH at each sampling time. After completion of Phase 1, the supernatant was removed from the sacrificial samples containing sediment, contaminants, and reductants, and solids were dried in the vaccum oven at 35^{o}C to prepare for solid phase characterization by XRD and SEM-EDS. These analyses would suggest changes in sediment solid phases in the anaerobic conditions due to presence of ZVI, SMI and CPS reductants. The results will be compared with solid samples analyzed after the completion of the reoxidation experiments (Table 6).

Phase 2: Re-oxidation of redox sensitive contaminants

After the $Tc^{(VII)}$, $U^{(VI)}$ and NO_3^- reduction in Phase 1, experimental bottles, sediment-free controls, reductant-free, and contaminant-free controls were removed from the anaerobic glovebox to study the re-oxidation behaviour of redox sensitive contaminants under aerobic conditions. The experiment was continued under a fume hood in FIU ARC's radiation laboratory. Capped samples were placed on a shaker for proper mixing (110 rpm, ThermoScientific) and kept for 45 days under slow aeration to allow sufficient oxygen presence in the aqueous phase throughout Phase 2 experiments, and for slow re-oxidation of the redox sensitive contaminants. Samples of 0.4 mL were collected once a week at 1 day, 7 days, 14 days, 21 days, 28 days, 35 days and 45 days and filtered via 0.2 µm syringe filters before being refrigerated (4°C) until analysis. Measurements were continued for the solution pH, ORP and DO at each sampling event in aerobic conditions conducted on the bench.

Liquid Analysis (ICP-MS, LSC, IC)

<u>Anion analyses by IC</u>**:**

Ion chromatography (IC, Integrion Dionex) was used to analyze anions, NO^-_3, NO_2^- and SO_4^-. Calibration standards were prepared from a solid sodium nitrate, sodium nitrite and sodium sulfate in DIW using special IC vials. The concentrations of NO_3^- and NO_2^- in the combined stock solution were 100 mg/L. The concentration ranges for NO_3^- and NO_2^- calibration standards were 100 – 1,500 µg/L for the sample volume of 5 mL.

The Dionex IonPac AS11 analytical column (2x250 mm) and an Anion Dynamically Regenerated Suppressor (ADRS) (2 mm) were used for analyses.

ICP-MS analyses for Tc, U and Fe

^{99}Tc calibration standards ranged from 0.005 µg/L to 50 µg/L through a serial dilution from 1mg/L stock solution that was prepared from 4.217 mM (417.483 mg/L) stock solution (Table 6).

Table 6. Preparation of Tc standards

Standard concentration, µg/L	Volume from the stock, µL	Volume of 2 % HNO_3, µL Total volume 40 mL
1.0 mg/L	96	39,904
50 (from 1 mg/L stock)	2,000	38,000
25 (from 1 mg/L stock)	1000	39,000
10 (from 1 mg/L stock)	400	39600
5 (from 10 µg/L std)	20,000	20,000
1 (from 5 µg/L std)	8,000	32,000
0.5 (from 1 µg/L std)	20,000	20,000
0.01 (from 0.5 µg/L std)	800	39,200
0.005 (from 0.01 µg/L std)	20,000	20,000

ICP-MS U standards were prepared from 1,000 mg/L commercial uranyl nitrate stock solution purchased from High Purity Standards by the dilution to 1 mg/L stock (0.01 -500 µg/L).

The remaining aqueous fraction of contaminant (unitless) was calculated as the ratio of concentration in the solution to the initial concentration.

Calculation of rate constants

The oxidation rate constants for Tc^{VII} were calculated using the first-order and second-order rate equations according to Eqns. 1 and 2, respectively (H Scott, 2006). Other kinetic models to calculate reoxidation rate constants will be also considered.

$$ln\left(\frac{[C_t]}{[C_0]}\right) = -K_t \qquad (1)$$

$$\frac{1}{[Ct]} - \frac{1}{[C0]} = Kt \qquad (2)$$

Where C_t = concentration at the time, t, in mol L^{-1}
C_0 = initial concentration, mol L^{-1}
t =time, min
K = pseudo-first-order rate, min^{-1} for Eq. 1 and pseudo-second-order rate, $M^{-1}min^{-1}$ for Eq. 2.

Subtask 1.2: Results and Discussion

Tc$^{(VII)}$, U$^{(VI)}$, and NO_3^- are redox sensitive contaminants and the reduction of Tc$^{(VII)}$ to Tc$^{(IV)}$, U$^{(VI)}$ to U$^{(IV)}$ and NO_3^- to NH_4 is described by the following equations 1-4 (Fiedor et al., 1998; Kobayashi et al., 2013; Yang and Lee, 2005)

$$2Fe^0 + TcO_4^- + 4H_2O = TcO_2(s) + 2Fe(OH)_3(s) + 2H^+ \qquad \text{Eq.1}$$

$$3Fe^{2+} + TcO_4^- + 7H_2O = TcO_2(s) + 3Fe(OH)_3(s) + 5H^+ \qquad \text{Eq.2}$$

$$Fe^0 + 1.5UO_2^{2+} + 6H^+ = Fe^{3+} + 1.5U^{4+} + 3H_2O \qquad \text{Eq. 3}$$

$$NO_3^- + 4Fe^0 + 10H = 4Fe^{2+} + NH_4 + 3H_2O \qquad \text{Eq. 4}$$

This study assessed the ability of ZVI and SMI to simultaneously reduce Tc(VII) in the presence of U(VI) and NO_3^- in groundwater or perched water typical for Hanford Site. ZVI is readily oxidized in an anaerobic Fe^0-H_2O system by the following reactions (Agrawal and Tratnyek, 1995):

$$Fe^0 + 2H^+ = Fe^{2+} + H_2 \qquad \text{Eq. 5}$$

$$Fe^0 + 2H_2O = Fe^{2+} + H_2 + 2OH^- \qquad \text{Eq. 6}$$

Under aerobic conditions, dissolved oxygen is the electron acceptor and the primary reaction yields OH^- (Zhao et al., 2016):

$$2Fe^0 + O_2 + 2H_2O = 2Fe^{2+} + 4OH^- \qquad \text{Eq. 7}$$

Precipitation of ferrous iron releases protons during initial oxidation (Su and Puls, 2004):

$$Fe^{2+} + O_2 + 10H_2O \rightarrow 4Fe(OH)_3(s) + 8H^+ \qquad \text{Eq. 8}$$

Sediment Sieving and Fraction Analysis

Most of the Ringold Formation non-contaminated sediment collected at Hanford was classified as a fine sand. Table 7 depicts the results from the fraction analysis. Fine sediment particles with 500 µm-63 µm size present the largest fraction ~87 %. The clay fraction was the smallest fraction measured by a significant margin.

Table 7. Fraction Analysis of the Background Ringold Formation sediment

Fraction	Soil Weight (g)	Weight Percentage
2000µm-500µm (Sand)	7.52	7.5
500µm-63µm (Sand)	87.15	87.2
63µm-20µm (Silt)	4.06	4.1
<20µm (Clay)	1.22	1.2

Aqueous Removal of ^{99}Tc by different reductants

Under anaerobic conditions, reduction of ^{99}Tc in the presence of $U^{(VI)}$ and NO_3^- occurred very quickly (Figure 1 and Figure 2). Before entering the aerobic phase of the experiments, all batches had less than 1% of Tc remaining as $Tc^{(VII)}O_4^-$ in the aqueous phase. The results obtained for triplicate GW sediment-amended samples in anaerobic conditions revealed that remaining aqueous concentrations of Tc after 1.0 % of ZVI and SMI treatment were measured as 0.0195±0.003 µg/L and 0.013±0.0006 µg/L, respectfully. The remaining aqueous concentrations of Tc after treatment of PW with 1.0 % of ZVI and SMI were measured as 0.007±0.001 and 0.006±0.0006, respectively. These concentrations correspond to aqueous fractions of Tc after treatment with ZVI of GW and PW as 0.00005±0.000009 and 0.0005±0.00007. For PW, the corresponding aqueous fractions were calculated as 0.0005±0.00007 and 0.0004±0.00005 for ZVI and SMI (Figure 1 and Figure 2). SMI was a slightly more effective reductant than ZVI in anaerobic conditions. Reoxidation of Tc(VII) increased after samples were exposed to aerobic conditions via aeration, but then Tc concentrations were decreased. Tc(VII) re-oxidation in GW increased to 0.5-0.7 µg/L for ZVI and 0.6-0.9 µg/L for SMI. In PW, Tc(VII) concentrations increased to 0.02-0.03 µg/L for ZVI and 0.04-0.07 µg/L for SMI. This suggests that in aerobic conditions, ZVI was barely more effective in resisting reoxidation compared to SMI. Therefore, sediment-containing samples treated with ZVI and SMI showed an increase in the Tc aqueous fraction remaining in the solution after samples were exposed to aerobic conditions. Then the Tc aqueous fraction slowly decreased and stabilized at the level of 0.001-0.002 for GW and 0.002-0.005 for PW. The remaining fractions of Tc in GW ZVI-treated samples showed lower values compared to measure in SMI-treated samples (0.001 vs. 0.002) by day 68 at the end of sampling in aerobic conditions (Figure 1). In PW the tendency was similar as in GW calculating the remaining fractions of Tc in ZVI-treated samples vs. SMI-treated samples as 0.002 vs. 0.005 (Figure 2). These values are at least 10 times less compared to the remaining aqueous fraction estimates obtained in experiments using 0.1% ZVI and 0.1% SMI.

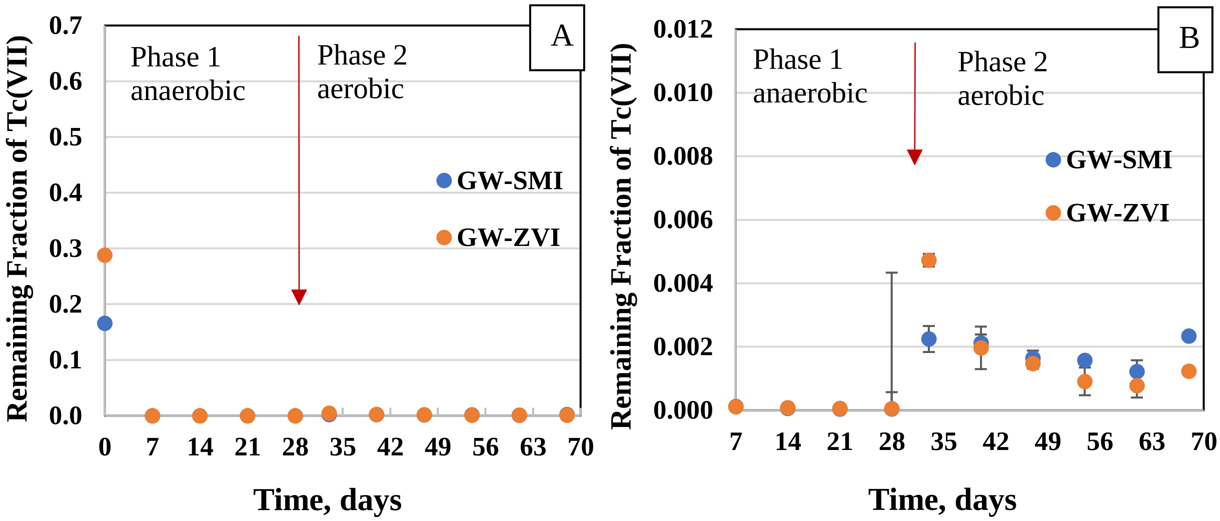

Figure 1. Reductive removal of Tc over time in aerobic and anaerobic conditions in GW samples amended with 1.0 % of ZVI or SMI. A) from day 0 – 68; B) from day 7 to 68. Note: The remaining aqueous fraction of Tc (Y-axis, unitless) was calculated as the ratio of Tc concentration in the solution to the initial Tc concentration in the control.

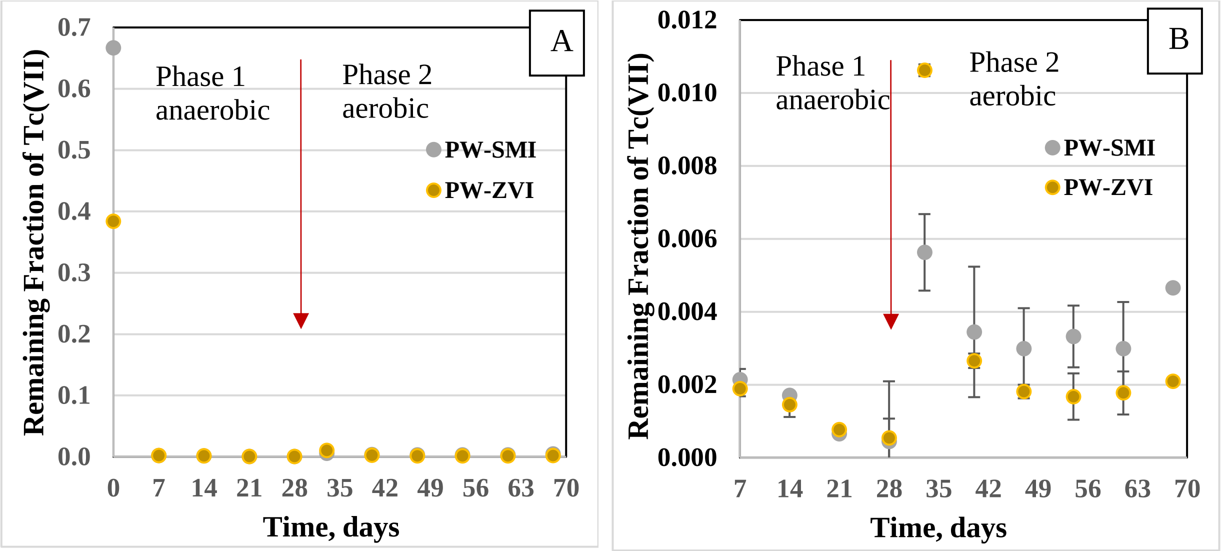

Figure 2. Reductive removal of Tc over time in aerobic and anaerobic conditions in PW samples amended with 1.0 % of ZVI or SMI. A) from day 0 – 68; B) from day 7 to 68. Note: The remaining aqueous fraction of Tc (Y-axis, unitless) was calculated as the ratio of Tc concentration in the solution to the initial Tc concentration in the control.

This tendency was the same in sediment-free PW samples suggesting that ZVI and SMI were effective reductants in anaerobic conditions, while ZVI was marginally more effective in resisting re-oxidation in aerobic conditions. The remaining aqueous fractions of Tc were very close in values gaging 0.001 at the end of the aerobic sampling period in ZVI- treated samples compared to ~0.003 remaining in sediment-free SMI samples (Figure 3B).

For GW solutions, both reductants were effective in reducing Tc to less than 0.00003 of the remaining aqueous fraction in the anaerobic conditions and effective in resisting reoxidation with an aqueous fraction calculated between 0.0003-0.0005 (Figure 3A).

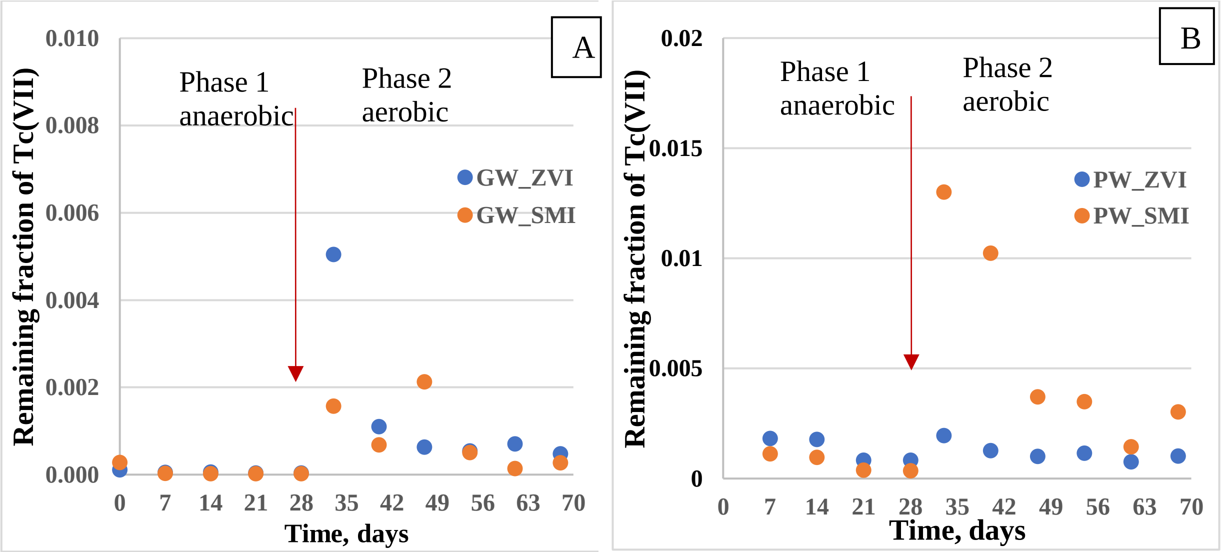

Figure 3. Reductive removal of Tc over time in aerobic and anaerobic conditions. A) in GW sediment-free

samples amended with 1.0% ZVI or 1.0% SMI; B) in PW sediment-free samples amended with 1.0% ZVI or 1.0% SMI. Note: The remaining aqueous fraction of Tc (Y-axis, unitless) was calculated as the ratio of Tc concentration in the solution to the initial Tc concentration in the control.

The remaining aqueous fractions using 1.0 % ZVI and SMI were one-two order of magnitude lower compared to counterparts at 0.1% ZVI and SMI. The results obtained using 1.0 % ZVI or SMI amended samples have not suggested any priority for SMI in resisting reoxidation compared to ZVI as it was noted in 0.1% SMI and ZVI treatments (Figure 3).

Evaluation of U(VI) reduction from the synthetic PW solutions in the presence of 1.0% SMI suggested that the initial U(VI) concentration of 157212±9734 µg/L was reduced to 46.7±14.0 µg/L in sediment-amended samples in anaerobic conditions, leaving a remaining aqueous fraction of ~0.0003±8.9E-05 by the end of anaerobic Phase 1. In the same conditions, ZVI was more effective in the U(VI) reduction. The remaining concentration in ZVI-treated PW samples was measured as 11.06±9.32 µg/L that correlated to the uranium remaining aqueous fraction as 7.03E-05± 5.9E-05 by the end of the anaerobic sampling period of 7 days (Phase 1) (Figure 4). In aerobic conditions, ZVI was also more effective than SMI in resisting re-oxidation. The remaining U(VI) concentration in ZVI samples was measured as 791.8± 77.9 µg/L which corresponds to the remaining aqueous fraction as 0.005±0.0005 by day 68 at the end of the aerobic sampling period (Phase 2). However, the remaining concentration of U(VI) in SMI–treated samples was increased to 6427.7±441 leaving an aqueous fraction of U as 0.040±0.003 by day 68 at the end of the aerobic Phase 2 (Figure 4).

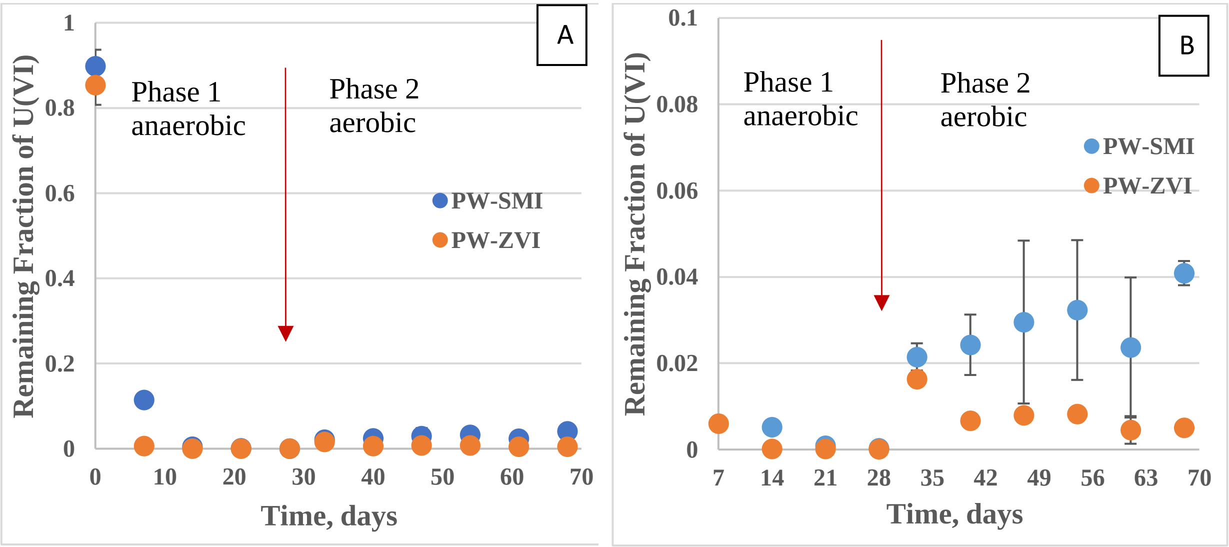

Figure 4. Reductive removal of U(VI) over time in aerobic and anaerobic conditions in PW samples amended with 1.0 % of ZVI or 1.0% SMI. A) from day 0 – 68; B) from day 7 to 68. Note: The remaining aqueous fraction of U(VI) (Y-axis, unitless) was calculated as the ratio of U concentration in the solution to the initial U concentration in the control.

In the sediment-free samples, ZVI and SMI showed similar behavior in reducing U to 0.15 µg/L in anaerobic conditions which corresponds to a remaining aqueous fraction <0.00001 by the end of Phase 1. The remaining U concentration in sediment-free SMI-amended samples in aerobic conditions was measured at 2222.1 µg/L with a corresponding remaining aqueous fraction of U 0.014 by the end of sampling in Phase 2 at day 68 (Figure 5). In similar conditions, the remaining U concentration in sediment-free ZVI-amended samples was gauged as 4707.7µg/L with a corresponding remaining aqueous fraction of U 0.03 by the end of Phase 2 at day 68 (Figure 5). SMI also more efficiently resisted reoxidation of Tc in sediment-free PW samples compared to ZVI at 1% in the solution (Figure 6). So, MSI at 1% in sediment-free PW solutions resisted to reoxidation of U and Tc to a greater degree compared to ZVI (Figure 5, Figure 6). The concentration of re-oxidized U in the PW sediment-free solution still persisted very high that requires additional methods to sequester U.

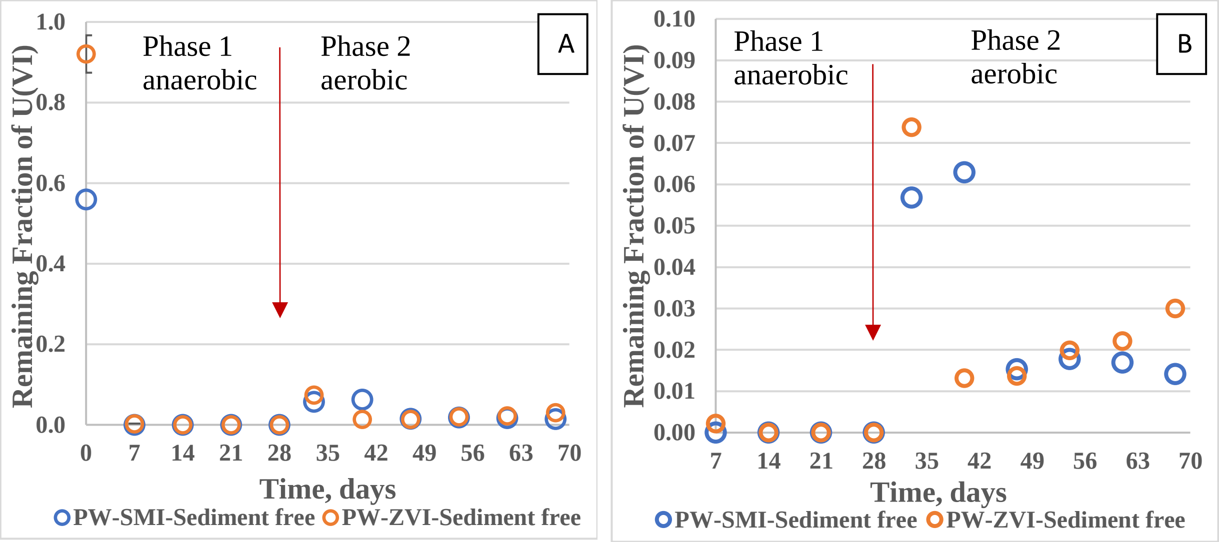

Figure 5. Reductive removal of U(VI) over time in anaerobic and aerobic conditions in sediment-free PW samples amended with 1.0 % of ZVI or 1.0% SMI. A) from day 0 – 68; B) from day 7 to 68. Note: The remaining aqueous fraction of U(VI) (Y-axis, unitless) was calculated as the ratio of U(VI) concentration in the solution to the initial U concentration in the control.

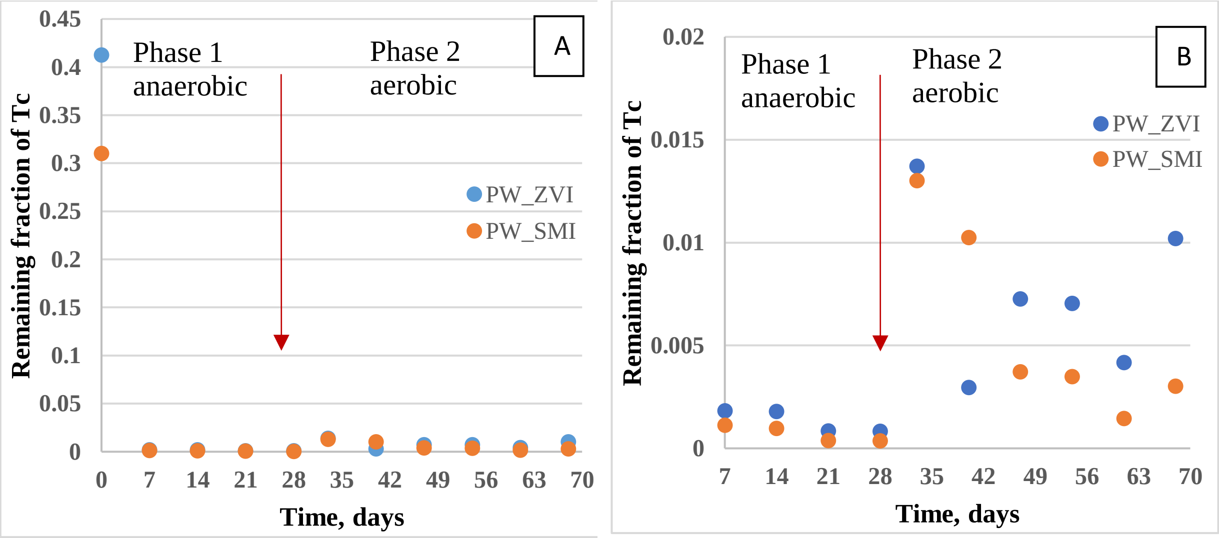

Figure 6. Reductive removal of Tc over time in anaerobic and aerobic conditions in sediment-free PW samples amended with 1.0 % of ZVI or 1.0% SMI. A) from day 0 – 68; B) from day 7 to 68. Note: The remaining aqueous fraction of Tc (Y-axis, unitless) was calculated as the ratio of Tc concentration in the solution to the initial Tc concentration in the control.

MSI at 1% in sediment-free GW solutions showed the same tendency for more efficient resistant reoxidation compared to ZVI (Figure 7).

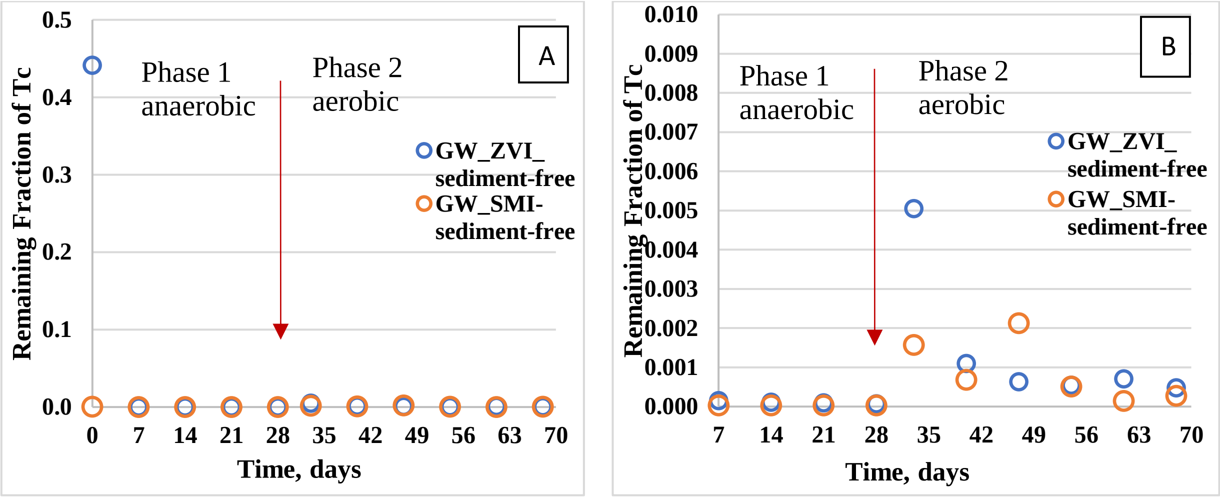

Figure 7. Reductive removal of Tc over time in anaerobic and aerobic conditions in sediment-free GW samples amended with 1.0 % of ZVI or 1.0% SMI. A) from day 0 – 68; B) from day 7 to 68. Note: The remaining aqueous fraction of Tc (Y-axis, unitless) was calculated as the ratio of Tc concentration in the solution to the initial Tc concentration in the control.

Further analysis was conducted for the kinetic behavior of Tc in sediment-free GW & PW samples amended with 0.1% ZVI and SMI. The kinetic behavior was determined as first-order with respect to Tc. Sediment-free control samples revealed that Tc steadily oxidized in ZVI-containing samples in aerobic conditions, while Tc SMI-containing samples resisted re-oxidation to a greater degree (Figure 8).

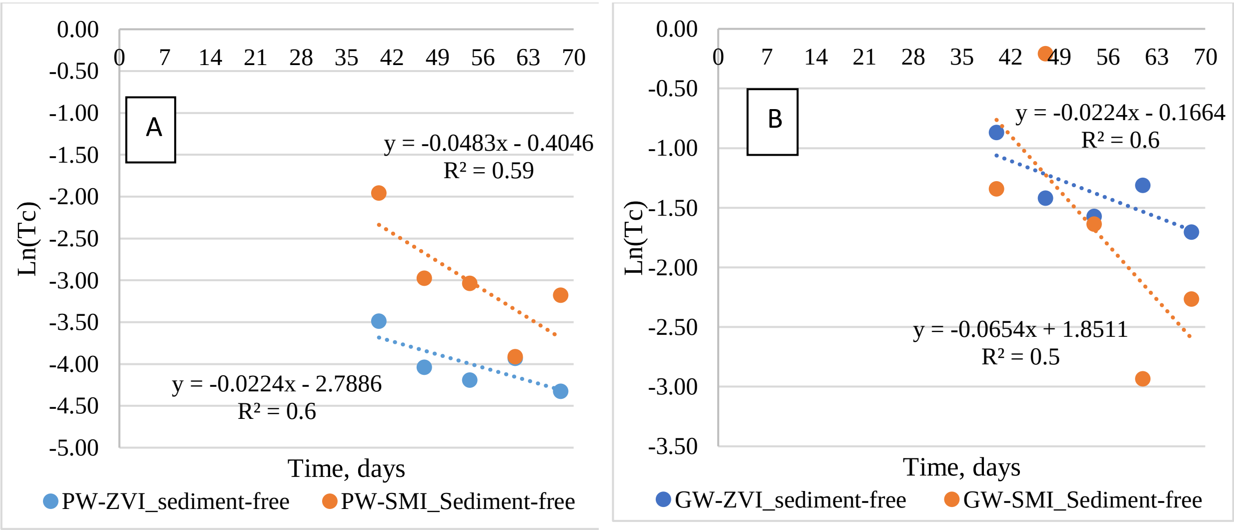

Figure 8. Re-oxidation behavior of Tc in PW and GW sediment-free samples. A) PW sediment- free samples; B) GW sediment-free samples.

The results for the anion analysis by IC to evaluate the amount of NO_3^-, NO_2^-, & SO_4^{2-} in GW samples amended with NO_3^- collocated with Tc during treatment with ZVI and SMI are presented in Figure 9 - Figure 11. ZVI was more effective in $NO3^-$ removal by the end of the anaerobic Phase 1 compared to SMI. The concentrations of NO_2^- were similar in samples amended with ZVI or SMI at the end of Phases 1 and 2.

Data for the concentrations of nitrate showed it re-oxidized in Phase 2 (Figure 10, Figure 9). This might be due to accumulation of nitrite in Phase 1 that was subsequently re-oxidized to nitrate in aerobic conditions (Figure 11). Overall, nitrate reoxidation was larger compared to samples treated with 0.1% ZVI and SMI. The potential analytical errors might be a high dilution factor for these samples due to a low sample amount. In addition, only ~2/3 (0.310 g) of the required sodium nitrate salt was added to the solution to have a nitrate concentration of 124 mg/L at the beginning of the experiment. The required weight of sodium nitrate needed to make 2.5 L of 124 mg/L nitrate was calculated as 0.480 g. These samples will likely need to be analyzed once more through IC.

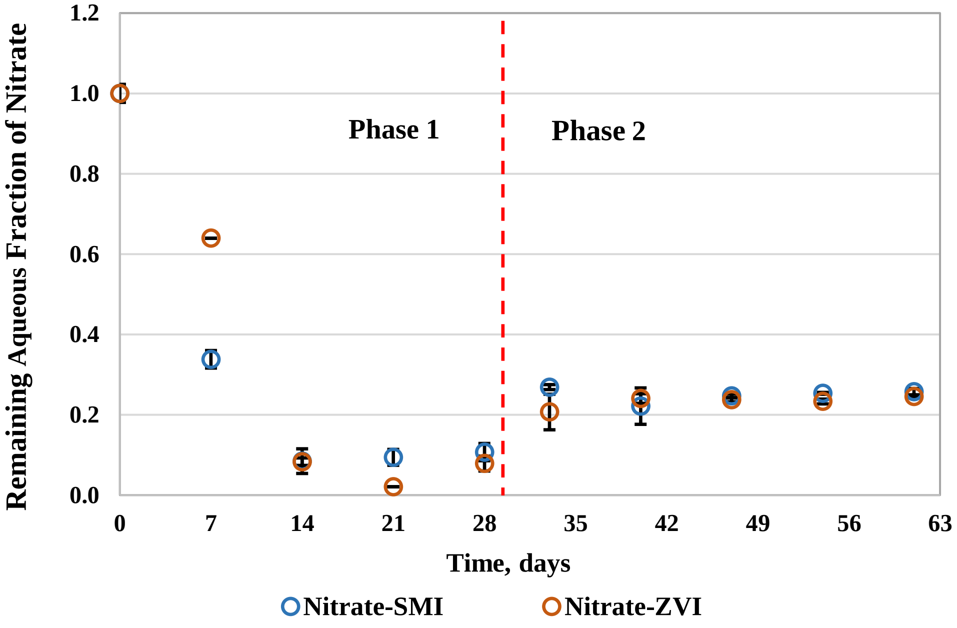

Figure 9. Remaining Aqueous Fraction of Nitrate in GW (1% ZVI &SMI) samples. The remaining aqueous fraction of NO_3^- (Y-axis, unitless) was calculated as the ratio of NO_3^- concentration in the solution to the initial NO_3^- concentration in the control.

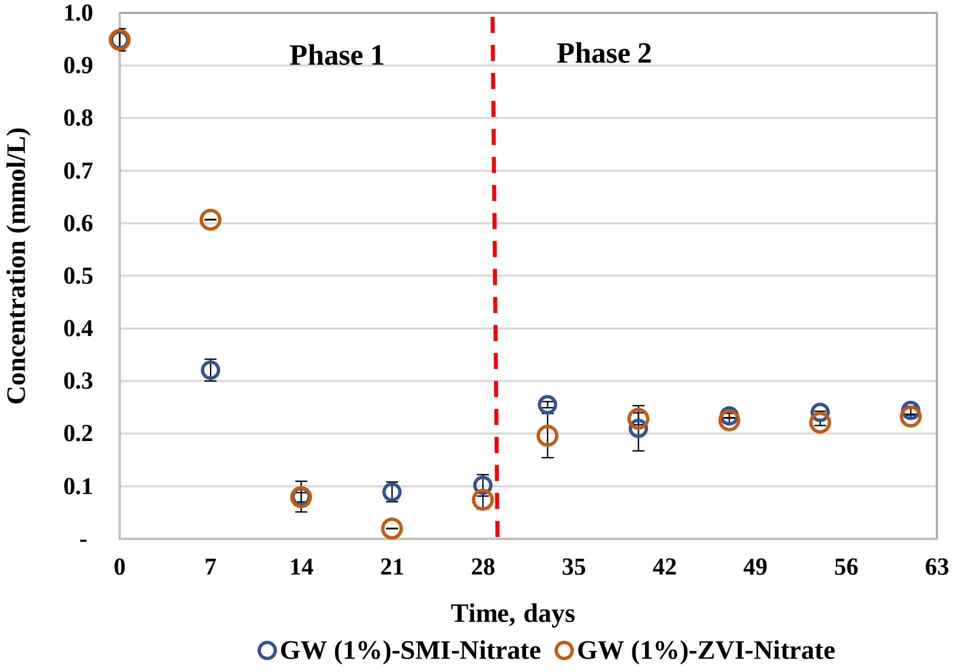

Figure 10. Concentration of Nitrate vs. time in GW (1% ZVI &SMI) samples.

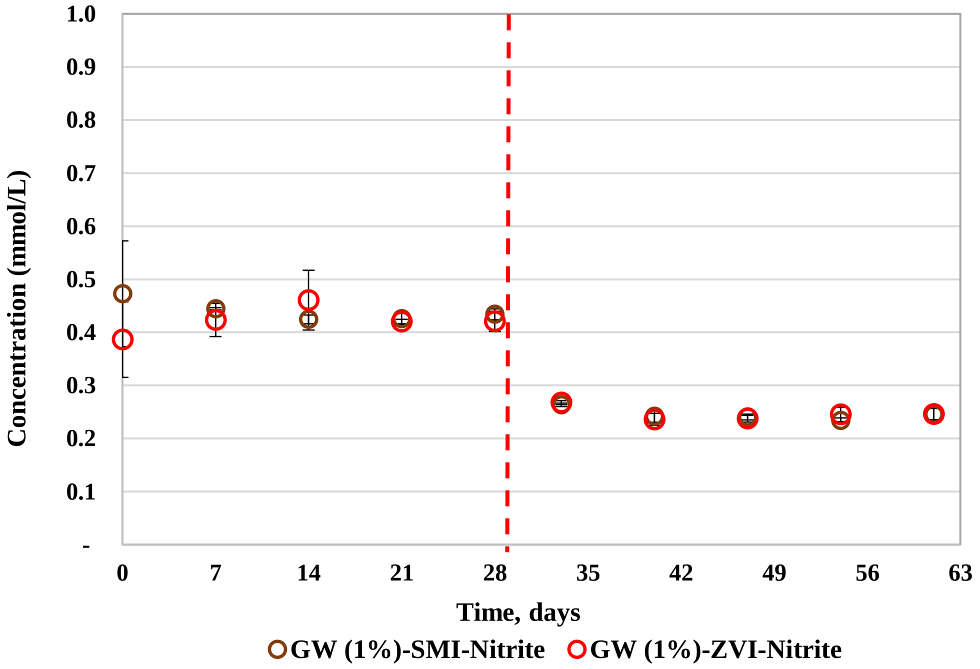

Figure 11. Concentration of nitrite vs. time in GW samples amended with 1% ZVI and SMI.

The concentration of sulfate was found to be higher in SMI-amended samples throughout both phases of the experiment (Figure 12). This is likely due to the presence of sulfur in SMI, which can be oxidized to sulfate. SMI is treated during its production by powdered elemental sulfur or other sulfur compounds such as sulfide. SMI includes about 2-8% of sulfur that may oxidize in aerobic conditions to SO_4^{2-}. The presence of sulfur in the SMI is likely the reason why the concentration of sulfate was increased two times by the end of Phase 2 compared to SMI-amended samples at the beginning of the experiment. In SMI-treated samples, the concentration of SO_4^{2-} was increased from an average value of 2.4±0.03 mmol/L at day 28 to 2.9-3.0 mmol/L by the end of the experiments (Figure 12).

In ZVI-treated samples, the concentration of SO_4^{2-} was approximately on the level of 0.9-1.0 mmol/L but decreased to 0.7±0.12 mmol/L by the end of the experiment.

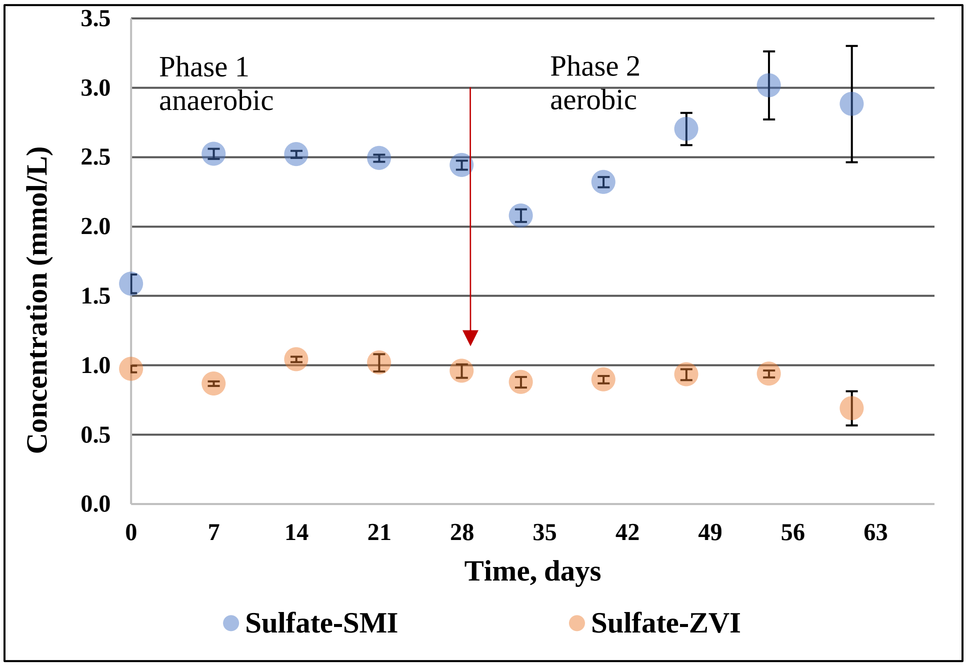

Figure 12. SO_4^{2-} **concentrations over time in groundwater samples treated with 1.0% SMI and 1.0% ZVI.**

Oxidation Reduction Potential (ORP), pH and Dissolved Oxygen (DO)

Readings for pH, ORP, and DO are presented in Figure 13. The initial pH of the PW of 7.7-8.1 decreased after 7 days to pH 7.6-7.9 and then gradually increased during 28 days in the anaerobic conditions to pH 7.9± 0.15 for SMI and 8.4±0.2 for ZVI. These values were not changed under aerobic conditions by the end of the experiment measuring pH 7.9±0.03 and 8.5±0.11 for SMI and ZVI, respectively. For GW samples, pH was decreased from an initial 7.8±0.14 to 7.2±0.01 and 7.5±0.04 after 7 days under anaerobic conditions for SMI and ZVI, respectively. By the end of Phase 1 at day 28, pH values were stabilized at 7.6±0.26 and 8.3±0.25 for both SMI and ZVI, respectively. After switching to aerobic conditions, the pH gradually decreased to 7.4±0.04 and 8.1±0.13 by day 68 for SMI and ZVI, respectively.

Measuring the ORP can provide information about the reductive/oxidative behavior of species in the system. The observed trend ORP for GW (1.0% iron reductant amended samples) solutions revealed values ranging from about -300 to -400 mV during the anaerobic period, indicating that reducing conditions were present throughout. The ORP values measured during the aerobic phase were consistent with oxidizing conditions, yielding ORP values ranging from about +200 to +400 mV. The observed trend of the DO concentrations throughout the anaerobic period revealed very low concentrations of about 0.03-0.05 mg/L, while the trend observed throughout the aerobic period revealed an increase of DO concentrations up to 5-6 mg/L (Figure 13).

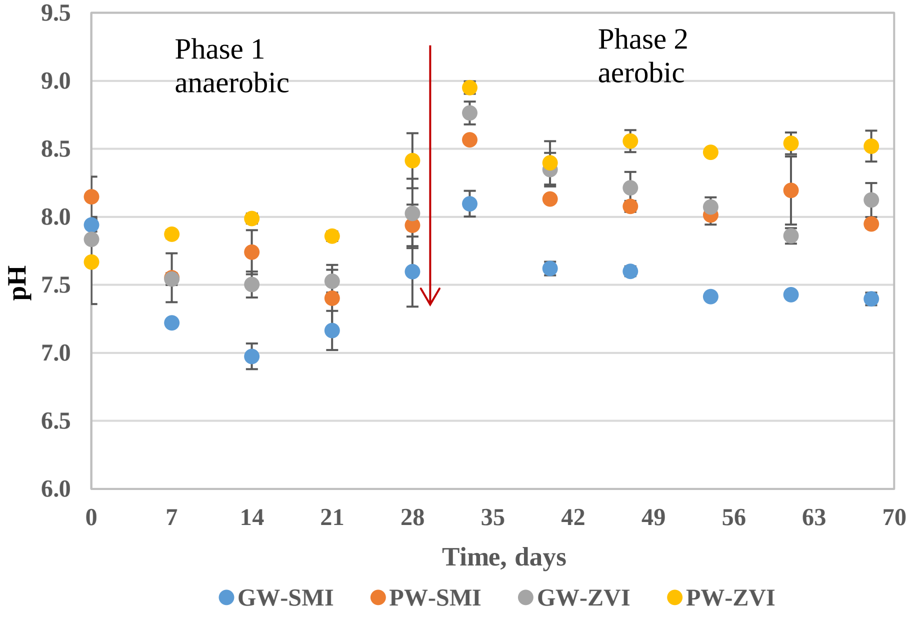
Phase 1
anaerobic
Phase 2
aerobic
pH
9.5
9.0
8.5
8.0
7.5
7.0
6.5
6.0
0
7
14
21
28
35
42
49
56
63
70
Time, days
GW-SMI
PW-SMI
GW-ZVI
PW-ZVI

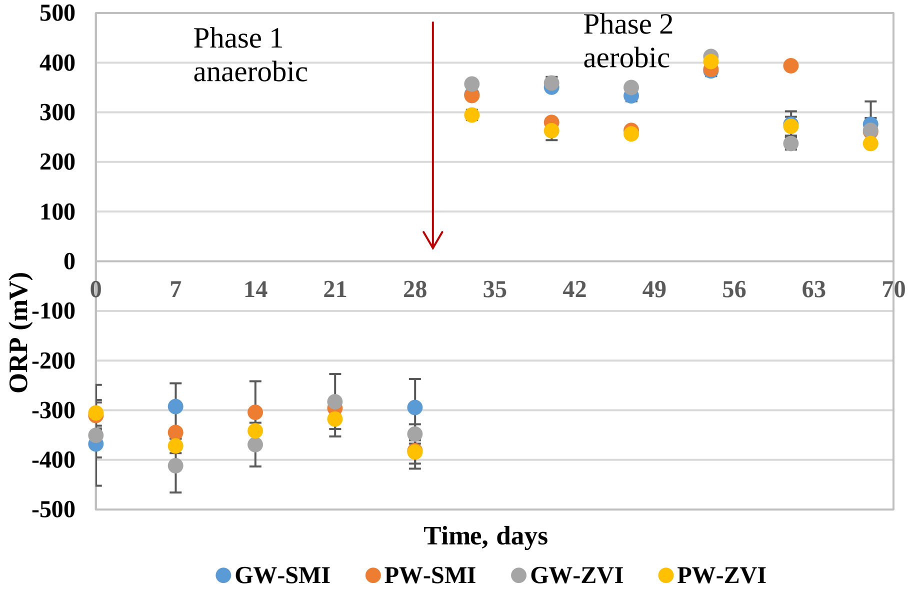
Phase 1
anaerobic
Phase 2
aerobic
ORP (mV)
500
400
300
200
100
0
-100
-200
-300
-400
-500
0
7
14
21
28
35
42
49
56
63
70
Time, days
GW-SMI
PW-SMI
GW-ZVI
PW-ZVI

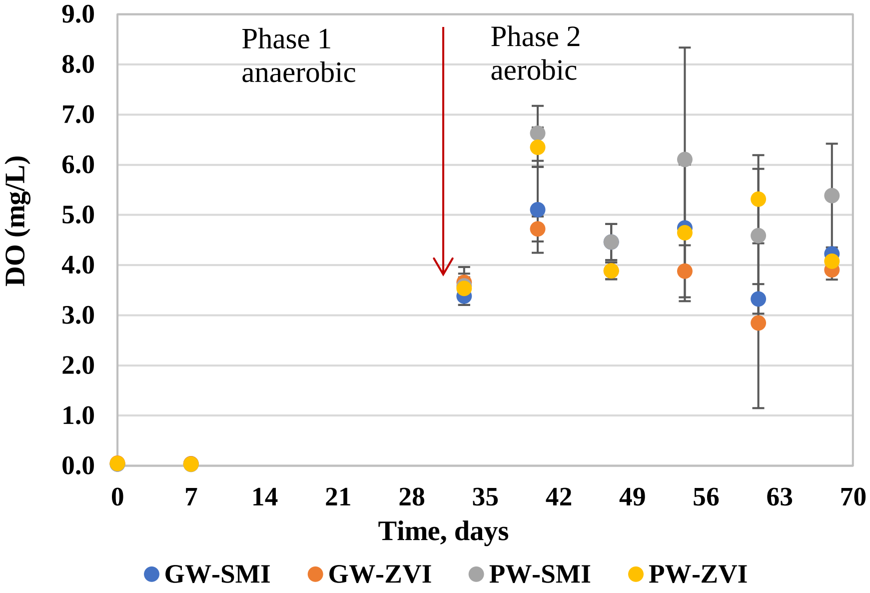

Figure 13. Changes in pH, ORP, and DO content over time. The ORP values were measured against Ag/AgCl reference electrode.

Scanning Electron Microscope

Measurements from the scanning electron microscope (SEM) were used to evaluate the elemental composition in each of the dried solid samples. SEM provides an accurate assessment, which helps with mineralogical analysis using other methods like X-ray diffraction. The elemental composition showed an increase in iron content in samples amended with 0.1 % from 15-20% compared to 1.0% ZVI to 30-48%, which might lead to the formation of iron oxide phases within the sediment. Low concentrations of TcO_4^- used in this study did not allow for Tc identification via EDS analysis. SEM has not identified typical iron oxide crystals resembling octahedral for magnetite or needle-like for goethite in samples amended with ZVI and SMI. SEM/EDS provided mapping of elements such as Ca, Fe, Na, Si, Al, and U that allow visualization of elements for the comparison of the elemental associations on the sample surface.

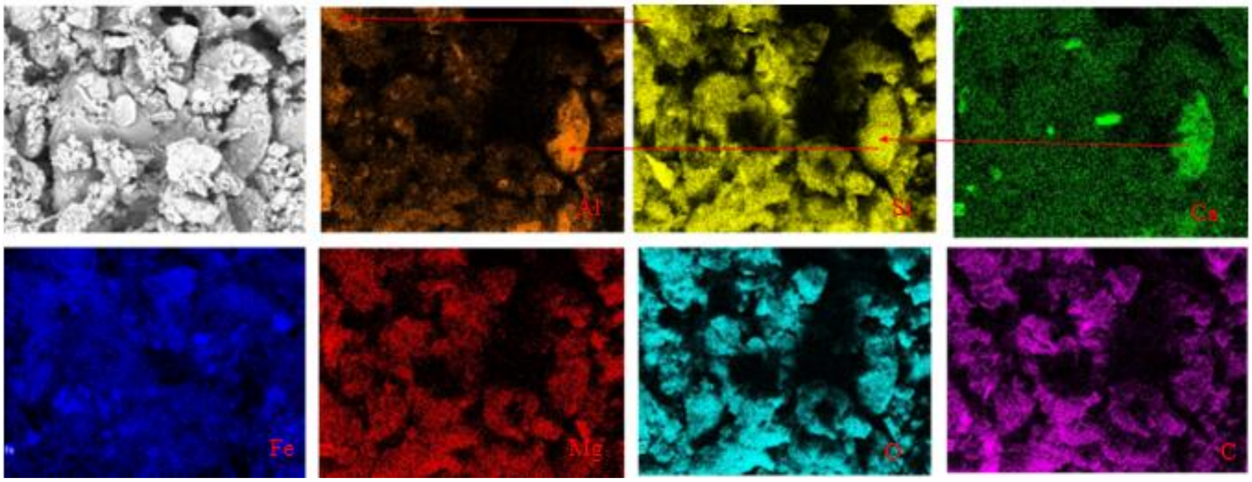

Figure 14. EDS maps of GW sample treated with 1%ZVI

PW sample treated with 1% ZVI showed alignment between Ca, Al, Na, and Si maps. Uranium is on the background level but a couple of bright spots on the U map were aligned with a Fe map (Figure 15).

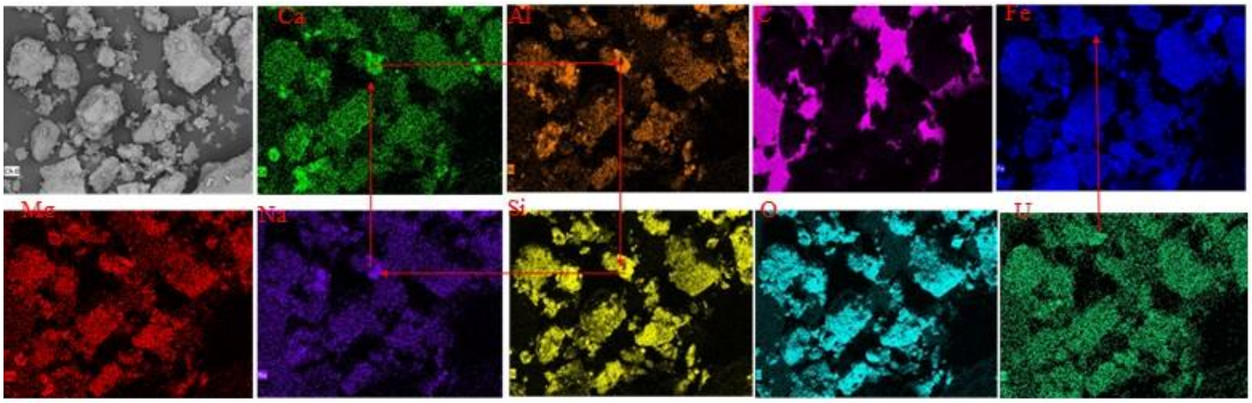

Figure 15. EDS maps of PW sample treated with 1% ZVI

Uranium alignment with a Fe map is also visible on a PW sample treated with 1% SMI and then sacrificed for solids recovery to conduct solids characterization after Phase 1 (Figure 16A). A larger magnification of U and Fe maps demonstrated the presence of a uranium-rich particle on the surface of a fine sediment grain (Figure 16B). This U-rich particle is a newly reduced UO_2 that is precipitated on the surface of sediment in anaerobic conditions and does not have alignment with any elemental maps based on the EDS analysis.

A) Elemental maps

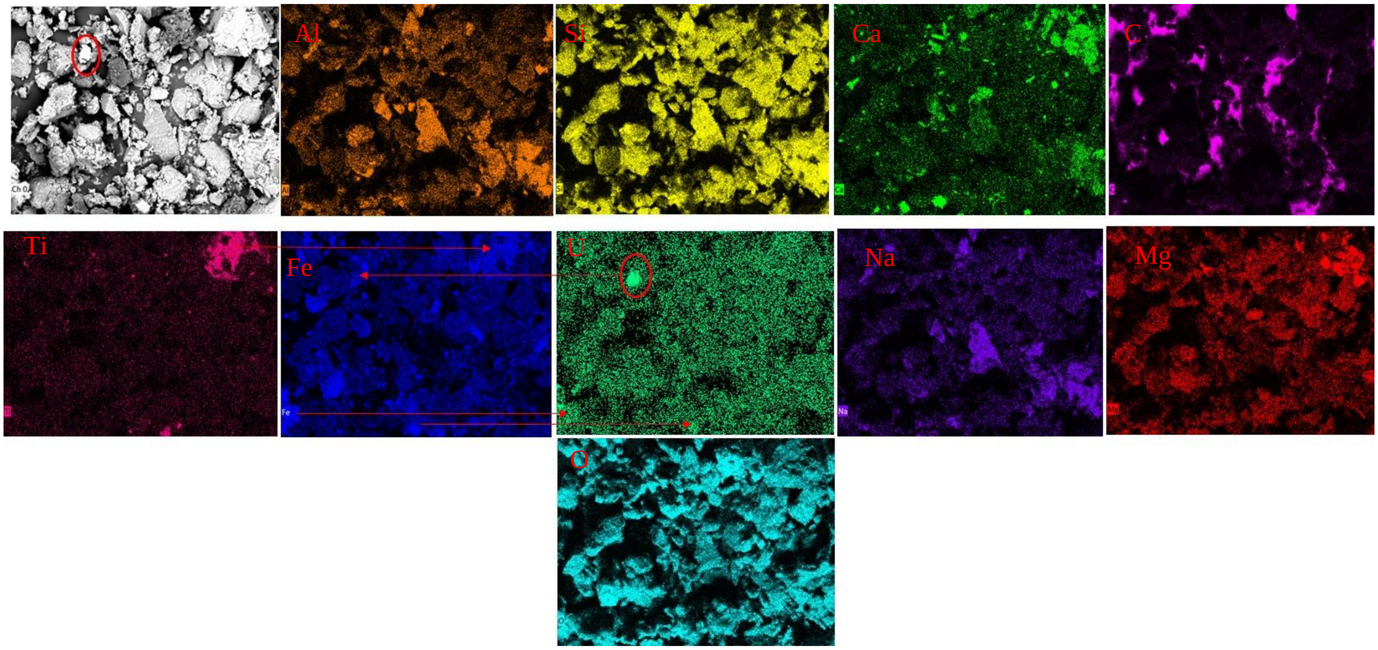

B) U and Fe maps

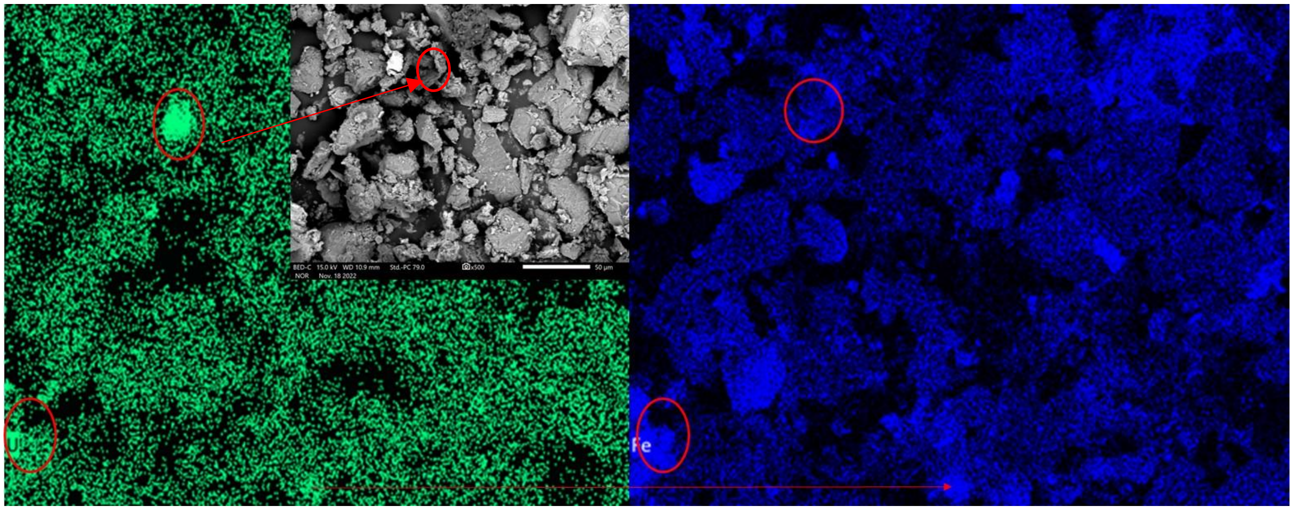

Figure 16. EDS maps of PW sample treated with 1% SMI sacrificed after Phase 1. A) Elemental maps; B) U and Fe maps.

A formation of similar U-rich particles that are precipitated on the surface of sediment in anaerobic conditions and do not have alignment with any elemental maps was noted in another sample's spot (Figure 17).

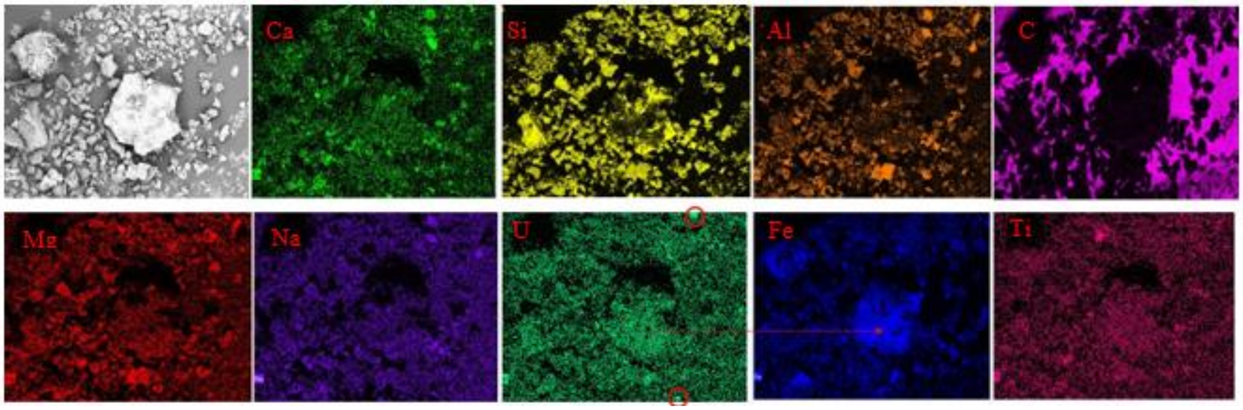

Figure 17. EDS maps of spot #2 on the same PW sediment sample treated with 1% SMI and sacrificed after anaerobic Phase 1. Note: U-rich particles circled in red do not have alignment with any elemental maps. A red arrow shows alignment of U and Fe maps.

X-Ray Diffraction Analysis

Each of the solid samples was run in duplicate to assure replicability. Lack of homogeneity in the sieved sediment samples with size fraction < 2 mm caused inconsistent matches for the mineralogy of the obtained X-ray patterns. ZVI- and SMI-treated sediment samples did not show presence of iron oxide phases like magnetite or goethite which might be due to relatively low weight percentage of ZVI and SMI in the sediment or potential incorporation of iron oxides to the sediment's alumosilicate mineral structures.

Table 8. Solid Phases Matched in1% Sulfur Modified SMI-Treated Sediment in Artificial Ground Water

	Name	ID	Formula	Percentage
GW SMI 1%-contaminant-free S1	Quartz, syn	PDF 04-008-7651	Quartz, SiO_2	22.6
	Quartz-alpha Fe-doped brown	PDF 04-007-0522	60.9	60.9
	Nontronite	PDF 00-058-2026	(Na,Ca)0.3Fe2(Si,Al)4)10(OH)2xH2O	14.9
	Albite, ordered	PDF 00-041-1480	(Na, Ca)Al(SiAl)3O8	2.3
GW SMI 1%-contaminant-free S2	Quartz, syn	PDF 04-008-7651	Quartz, SiO2	42.9
	Quartz-alpha Fe-doped brown	PDF 04-007-0522	SiO2	18.5
	Nontronite	PDF 00-058-2026	(Na,Ca)0.3Fe2(Si,Al)4)10(OH)2xH2O	37.0
	Albite, ordered	PDF 00-041-1480	(Na, Ca)Al(SiAl)3O8	1.5
GW SMI 1% S1	Lagalyite	PDF 00-050-0015	Ca2Mn14O27xH2)	18.7
	Quartz, syn	PDF 04-008-7651	SiO2	28.0
	Illite	00-058-2015	(K,H30)Al2(Si3Al)O10(OH)2xH2O	19.7
	Muscovite	PDF 00-002-0467	KAl2(Si3Al0O10(OH,F)2	2.4
	Montmorillonite	PDF 00-003-0009	Si3.74Al2.03Fe0.03Mg0.20O11	2.2
	Goethite	PGF 00-001-0401	Fe2O3H2O	2.6
	Anorthoclase, disordered	PDF 00-009-0478	(Na,K)(Si3Al)O8	12.7
	Albite, Ca-bearing, ordered	PDF 00-041-1480	(Na,Ca)Al(Si,Al)3O8	13.7
GW SMI 1.0% S2	Anorthoclase, disordered	PDF 00-009-0478	(Na,K)(Si3Al)O8	5.8
	Lagalyite, syn	PDF 00-050-0015	Ca2Mn14O27·xH2O	8.6
	Muscovite-2M1	PDF 00-058-2035	KAl2(Si,Al)4O10(OH)2	10.0
	Illite-2M2 (NR)	PDF 00-058-2015	(K,H30)Al2(Si3Al)O10(OH)2·xH2O	10.4
	Albite, Ca-bearing, ordered	PDF 00-041-1480	(Na,Ca)Al(Si,Al)3O8	21.2
	alpha-Si O2, quartz-alpha Fe-doped brown, syn | Silicon Oxide	PDF 04-007-0522	SiO2	34.4

	Quartz, syn	PDF 00-046-1045	SiO2	9.7
GW SMI 1.0%-sacrificial-S1	Quartz, syn	PDF 00-046-1045	SiO2	86.3
	Albite, calcian, ordered	PDF 00-041-1480	(Na,Ca)Al(Si,Al)3O8	19.9
	Anorthoclase, disordered	PDF 00-009-0478	(Na,K)(Si3Al)O8	2.2
GW SMI 1.0%-sacrificial-S2	Quartz, syn	PDF 04-008-7651	SiO2	13.7
	Albite, Ca-bearing	PDF 01-083-1938	Na0.622Ca0.368Al1.29Si2.71O8	13.0
	Muscovite-2M1	PDF 00-058-2035	KAl2(Si,Al)4O10(OH)2	11.4
	Nontronite	PDF 00-058-2026	(Na,Ca)0.3Fe2(Si,Al)4O10(OH)2·xH2O	21.5
	Quartz, syn	PDF 00-046-1045	SiO2	40.5

Table 9. Solid Phases Matched in1% ZVI-Treated Sediment in Artificial Ground Water

	Name	ID	Formula	Percentage
GW ZVI 1%-contaminant-free S1	α-Si O2, quartz-alpha Fe-doped brown, syn | Silicon Oxide	PDF 04-007-0522	Quartz, SiO2	62.0
	Anorthite, Na-bearing	PDF 01-084-2723	Ca0.66Na0.34(Al1.66Si2.34O8)	19.6
	Albite, ordered	PDF 00-020-0554	NaAlSi3O8	10.4
	muscovite	PDF 04-017-7272	KAl3Si3O11	8.0
GW ZVI 1%-S1	alpha-Si O2, quartz-alpha Fe-doped brown, syn | Silicon Oxide	PDF 04-007-0522	Quartz, SiO2	49.1
	quartz-alpha, syn | Germanium Silicon Oxide	PDF 04-018-2594	SiO2	20.9
	Albite/anorthoclase low	PDF 04-025-6532	K0.06Na0.88Ca0.03AlSi3O8	20.4
	Lagalyite, syn	PDF 00-050-0015	Ca2Mn14O27·xH2O	9.0
	hemicalcium undecaoxohydroxodialumotetrasilicate, montmorillonite | Calcium Aluminum Silicon Oxide Hydroxide	PDF 01-076-8291	Ca0.5(Al2Si4O11(OH))	0.5
GW ZVI-1.0%-sacrificial-S1	Quartz, syn	PDF 00-046-1045	SiO2	60.6
	calcium mica | Calcium Aluminum Silicate	PDF 00-046-0744	Al3Ca0.5Si3O11	13.7
	Albite, Ca-bearing, ordered	PDF 00-041-1480	(Na,Ca)Al(Si,Al)3O8	17.3
	Nontronite	PDF 00-058-2026	(Na,Ca)0.3Fe2(Si,Al)4O10 (OH)2·xH2O	8.4

GW ZVI-1.0%-sacrificial-S2	α-Si O2, quartz-alpha Fe-doped brown, syn | Silicon Oxide	PDF 04-007-0522	SiO2	54.5
	Quartz, syn	PDF 04-008-7651	SiO2	19.7
	Calcium Zinc Silicate	DF 00-054-0604	CaZnSi3O8	11.2
	Albite, disordered	PDF 00-010-0393	Na(Si3Al)O8	9.8
	Muscovite-2M1	PDF 00-058-2037	KAl2(Si,Al)4O10(OH)2	4.8

Table 10. Solid Phases Matched in 1% Sulfur Modified SMI-Treated Sediment in Artificial Perched Water

	Name	ID	Formula	Percentage
PW SMI 1%-contaminant-free S1	Quartz, syn	PDF 04-008-7651	Quartz, SiO2	83.4
	Muscovite-2M1, glycolated	PDF 00-058-2036	KAl2(Si,Al)4O10(OH)2	8.3
	Sodium Aluminum Silicate	DF 04-016-0707	NaAlSi2O6	5.0
	Albite, ordered	PDF 00-009-0466	NaAlSi3O8	3.3
PW SMI 1% S1	Quartz, syn	PDF 04-008-7651	SiO2	31.7
	Quartz, syn	PDF 00-046-1045	SiO2	33.5
	Microcline	PDF 04-016-1525	K0.964Na0.036AlSi3O8	13.5
	Albite, ordered	PDF 00-020-0554	NaAlSi3O8	12.6
	Montmorillonite-chlorite	PDF 00-007-0027	Na-Ca-Al-Si4O10-O	4.4
	Maghemite	PDF 00-025-1402	Fe2O3	4.3
PW SMI 1.0%-sacrificial-S1	α-Si O2, quartz-alpha Fe-doped brown, syn | Silicon Oxide	PDF 04-007-0522	SiO2	80.3
	Sanidine	PDF 04-016-1657	K0.42Na0.58Ca0.03AlSi3O8	8.4
	Anorthite, Na-bearing	PDF 04-015-4238	Na0.5Ca0.5Al1.5Si2.5O8	5.9
	Muscovite	DF 00-058-2034	KAl2(Si,Al)4O10(OH)2	2.8
	Albite, ordered	PDF 00-009-0466	NaAlSi3O8	2.5

Table 11. Solid Phases Matched in 1% ZVI-Treated Sediment in Artificial Perched Water

	Name	ID	Formula	Percentage
PW ZVI 1%-contaminant-free S1	Quartz-alpha Fe-doped brown	PDF 04-007-0522	Quartz, SiO2	89.3
	Albite, ordered	PDF 00-009-0466	NaAlSi3O8	7.2
	Muscovite	PDF 00-058-2034	KAl2(Si,Al)4O10(OH)2	3.5
PW ZVI-1%-contaminant-free S2	Quartz, syn	PDF 00-046-1045	Quartz, SiO2	57.5
	Muscovite	PDF 00-058-2035	KAl2(Si,Al)4O10(OH)2	20.3
	Albite, ordered	PDF 01-083-1938	Na0.622Ca0.368Al1.29Si2.71O8	13.1
	Nontronite	PDF 00-058-2026	(Na,Ca)0.3Fe2(Si,Al)4O10(OH)2·xH2O	9.1
PW ZVI 1% S1	Quartz, syn	PDF 00-046-1045	SiO2	45.9
	Muscovite	PDF 00-058-2034	KAl2(Si,Al)4O10(OH)2	30.2

	Albite, Ca-bearing	PDF 01-083-1938	Na0.622Ca0.368Al1.29Si2.71O8	23.9
PW ZVI 1.0% S2	Anorthite, Na-bearing	DF 01-085-0878	Na0.48Ca0.52(Al1.52Si2.48O8)	15.4
	Muscovite-2M1, glycolated	PDF 00-058-2036	KAl2(Si,Al)4O10(OH)2	9.0
	Quartz, syn	PDF 00-046-1045	SiO2	53.1
	Albite, ordered	PDF 00-020-0554	NaAlSi3O8	22.4
PW ZVI 1.0%-sacrificial-S1	quartz-alpha, syn | Germanium Silicon Oxide	PDF 04-018-2596	Ge0.13Si0.87O2	35.3
	α-Si O2, quartz-alpha Fe-doped brown, syn | Silicon Oxide	PDF 04-007-0522	SiO2	40.6
	Anorthite, Na-bearing	PDF 01-084-2723	Ca0.66Na0.34(Al1.66Si2.34O8)	15.7
	Albite, Ca-bearing	PDF 01-079-1254	(Ca0.38Na0.62)(Al1.38Si2.62O8)	5.4
	U1 | Potassium Uranium	DF 00-048-0823	Na-Ca-Al-Si4O10-O	2.1
	Magnetite, Ti-bearing, syn	PDF 04-016-9466	Ti0.096Fe2.904O4	0.8
PW ZVI 1.0%-sacrificial-S2	quartz-alpha, syn | Germanium Silicon Oxide	PDF 04-018-2596	Ge0.13Si0.87O2	36.5
	α-Si O2, quartz-alpha Fe-doped brown, syn | Silicon Oxide	PDF 04-007-0522	SiO2	42.0
	Anorthite, Na-bearing	PDF 01-084-2723	Ca0.66Na0.34(Al1.66Si2.34O8)	17.4
	U1 | Potassium Uranium	DF 00-048-0823	Na-Ca-Al-Si4O10-O	3.3
	Magnetite, Ti-bearing, syn	PDF 04-016-9466	Ti0.096Fe2.904O4	0.8

Subtask 1.2: Conclusions

These experiments provided insights into the re-oxidation behavior of immobilized ^{99}Tc, ^{238}U, and NO_3^- with 0.1% ZVI and SMI. Experimental data revealed that the reduction of all contaminants occurred in the presence of both reductants when in anaerobic conditions. The results obtained through ICP-MS analyses showed that in sediment-bearing samples, ZVI and SMI were effective reductants in anaerobic conditions, while ZVI was marginally more effective in resisting re-oxidation in aerobic conditions. Sediment-free PW samples treated at 1% MSI resisted to reoxidation of U and Tc to a greater degree compared to ZVI. The concentration of re-oxidized U in the PW sediment-free solution still persisted very high which requires additional methods to sequester U.

Both ZVI and SMI were effective in NO_3^- removal by the end of the anaerobic Phase 1. The results showed the reoxidation at the end of aerobic Phase 2 which might be due to the accumulation of nitrite in Phase 1 that was subsequently re-oxidized to nitrate in aerobic conditions. Measurements of total SO_4^{2-} concentrations in aerobic and anaerobic conditions suggested a decrease of SO_4^{2-} content from the initial value in the GW simulant.

Results obtained through measurements of ORP (mV) in anaerobic conditions supported this data, with average ORP values ranging from -300 to -400 mV; indicating strong reducing conditions. Similarly, the average ORP values in aerobic conditions ranged from +200 to +400 mV, indicating that oxidizing conditions were present throughout.

Future work will complete characterization studies of solid samples recovered from batch solutions at the end of each phase and the initiation of the next round of batch experiments using a 0.5% and 5% calcium polysulfide liquid ratio in GW and PW solutions.

Subtask 1.2: References

Agrawal, A., and Tratnyek, P. G., 1995, Reduction of nitro aromatic compounds by zero-valent iron metal: Environmental Science & Technology, v. 30, no. 1, p. 153-160.

Boglaienko, D., Emerson, H. P., Katsenovich, Y. P., and Levitskaia, T. G., 2019, Comparative analysis of ZVI materials for reductive separation of 99Tc (VII) from aqueous waste streams: Journal of hazardous materials, v. 380, p. 120836.

Emerson, H. P., Gebru, A., Boglaienko, D., Katsenovich, Y. P., Kandel,['{: S., and Levitskaia, T. G., 2020, Impact of zero valent iron aging on reductive removal of technetium-99: Journal of Environmental Chemical Engineering, v. 8, no. 3, p. 103767.

Fiedor, J. N., Bostick, W. D., Jarabek, R. J., and Farrell, J., 1998, Understanding the mechanism of uranium removal from groundwater by zero-valent iron using X-ray photoelectron spectroscopy: Environmental science & technology, v. 32, no. 10, p. 1466-1473.

Gephart, R. E., 2003, A short history of Hanford waste generation, storage, and release: Pacific Northwest National Lab.(PNNL), Richland, WA (United States).

Gu, B., Liang, L., Dickey, M., Yin, X., and Dai, S., 1998, Reductive precipitation of uranium (VI) by zero-valent iron: Environmental Science & Technology, v. 32, no. 21, p. 3366-3373.

H Scott, F., 2006, Elements of chemical reaction engineering, Prentice Hall Profesional.

Kobayashi, T., Scheinost, A. C., Fellhauer, D., Gaona, X., and Altmaier, M., 2013, Redox behavior of Tc (VII)/Tc (IV) under various reducing conditions in 0.1 M NaCl solutions: Radiochimica Acta, v. 101, no. 5, p. 323-332.

Lawter, A. R., Garcia, W. L., Kukkadapu, R. K., Qafoku, O., Bowden, M. E., Saslow, S. A., and Qafoku, N. P., 2018, Technetium and iodine aqueous species immobilization and transformations in the presence of strong reductants and calcite-forming solutions: remedial action implications: Science of the Total Environment, v. 636, p. 588-595.

Pearce, C. I., Cordova, E. A., Garcia, W. L., Saslow, S. A., Cantrell, K. J., Morad, J. W., Qafoku, O., Matyáš, J., Plymale, A. E., and Chatterjee, S., 2020, Evaluation of materials for iodine and technetium immobilization through sorption and redox-driven processes: Science of The Total Environment, v. 716, p. 136167.

Reinsch, B. C., Forsberg, B., Penn, R. L., Kim, C. S., and Lowry, G. V., 2010, Chemical transformations during aging of zerovalent iron nanoparticles in the presence of common groundwater dissolved constituents: Environmental science & technology, v. 44, no. 9, p. 3455-3461.

Saslow, S. A., Lawter, A. R., Gartman, B. N., Zhang, Z., Snyder, M., Zhong, L., Cantrell, K. J., and Brown, C. F., 2018, Evaluation of Perched Water Post-Extraction Remedy

Technologies: Interim Status Report: Pacific Northwest National Lab.(PNNL), Richland, WA (United States).

Su, C., and Puls, R. W., 2001, Arsenate and arsenite removal by zerovalent iron: effects of phosphate, silicate, carbonate, borate, sulfate, chromate, molybdate, and nitrate, relative to chloride: Environmental science & technology, v. 35, no. 22, p. 4562-4568.

Su, C., and Puls, R. W., 2004, Nitrate reduction by zerovalent iron: effects of formate, oxalate, citrate, chloride, sulfate, borate, and phosphate: Environmental science & technology, v. 38, no. 9, p. 2715-2720.

Szecsody, J. E., Jansik, D. P., McKinley, J. P., and Hess, N. J., 2014, Influence of alkaline co-contaminants on technetium mobility in vadose zone sediments: Journal of environmental radioactivity, v. 135, p. 147-160.

Szecsody, J. E., Truex, M. J., Zhong, L., McKinley, J. P., Qafoku, N. P., Lee, B. D., and Saurey, S. D., 2015, Remediation of technetium in vadose zone sediments using ammonia and hydrogen sulfide gases: Vadose Zone Journal, v. 14, no. 7, p. 1-12.

Yang, G. C., and Lee, H.-L., 2005, Chemical reduction of nitrate by nanosized iron: kinetics and pathways: Water research, v. 39, no. 5, p. 884-894.

Zhao, X., Liu, W., Cai, Z., Han, B., Qian, T., and Zhao, D., 2016, An overview of preparation and applications of stabilized zero-valent iron nanoparticles for soil and groundwater remediation: Water research, v. 100, p. 245-266.

Subtask 1.3: Evaluation of Competing Attenuation Processes for Mobile Contaminants in Hanford Sediments

Subtask 1.3: Introduction

Weapons production at the Hanford Site has created large volumes of legacy radioactive and chemical waste. Some contaminants were released to the environment through discharges to liquid disposal sites, cribs and trenches, or accidental leakages from single-shell tanks. Contaminants, including uranium (U), technetium-99 (^{99}Tc), iodine-129 (^{129}I), chromium (Cr) and nitrate (NO_3^-), migrated to the vadose zone creating subsurface plumes at the Hanford 200 Area located in the Central Plateau. The mobile contaminants persist in the subsurface and have potential to enter the groundwater via downward migration through the vadose zone. If allowed to reach the groundwater, contaminants will flow towards the Columbia River, a major water resource in the Pacific Northwest and a path for public exposure. U is in the hexavalent form [U(VI)] primarily existing as tertiary neutral and anionic carbonate complexes ($Ca_2UO_2(CO_3)_3$ aq, $CaUO_2(CO_3)_3^{2-}$) in the natural oxic vadose zone environment at solution pH of ~ 8 (Gorman-Lewis et al. 2009). Tc is primarily in the form of anionic mobile pertechnetate (TcO_4^-) under oxidizing conditions (Peretyazhko et al. 2012). Chromium is present in the hexavalent form, the most mobile form of chromium, [Cr(VI)] as chromate (CrO_4^{2-}) (Zachara et al. 2004). Major aqueous species of I have been distributed as 76% IO_3^-, 22% organo-iodine, and 2% I^- (Xu et al. 2015). NO_3^- is stable and mobile in oxygenated environments (Martin 2011).

These co-contaminants in subsurface plumes at the 200 Area are currently being remediated with pump and treat technology. Once active remediation is completed, a transition to more passive approaches, such as monitored natural attenuation (MNA) will be investigated. This will allow the determination as to whether the concentrations of these contaminants are behaving as predicted and if mobility is reduced by natural processes. Effective MNA requires a thorough understanding of the contaminant immobilization processes that keep the contaminants stable and resistant to remobilization during any changes in environmental conditions or groundwater chemistry. Quantifying contaminant attenuation processes via competitive adsorption mechanisms on vadose zone sediment will assess competitive attenuation processes. This was initiated by FIU by conducting geochemical modeling, batch adsorption studies of Cr and U in artificial groundwater (AGW) onto Hanford formation sediment, a competition batch study with Cr and U in AGW onto Hanford formation sediment with two sets of concentrations, and a column study with U and U+Cr that is currently in progress.

Many studies have been conducted to understand the adsorption mechanisms of U(VI) onto a variety of different minerals and even natural sediment. Their findings have indicated that in the pH range of 6-9, the presence of calcium carbonate in sediment (from calcite) reduces U (VI) ability to sorb. This is due to the blockage of reactive sites by Ca^{2+} and the formation of neutral uranyl complexes [$Ca_2UO_2(CO_3)_3^0(aq)$] (Stewart, Mayes, and Fendorf 2010), (Zheng, Tokunaga, and Wan 2003),(Dong et al. 2005), (Fox, Davis, and Zachara 2006). However, there is still a need to incorporate the presence of collocated contaminants into these studies to understand the true adsorption capacity of sediment present at the Hanford Site. These contaminants include Tc-99, iodate, Cr (VI), and NO_3^- which may compete for reactive sites on the same minerals in the vadose zone. There, mineralogy is mainly comprised of quartz and feldspars; the finer-grained sediment includes a variety of phyllosilicates (Um et al. 2010). This assessment will support the development of site conceptual models with co-located contaminants and identify relevant contaminant fate and transport parameters. Understanding of contaminant sorption behavior is also important for assessing the viability of long-term MNA.

Subtask 1.3: Objectives

This research is focused on competitive adsorption between contaminants of concern onto the Hanford Formation vadose zone sediment as an assessment of their mobility and fate.

Uncontaminated sediments were collected at the Tristate Asphalt gravel pit in Pasco, WA and separated into different size fractions for physical, chemical and mineralogical characterization. Previous research by Zachara et al. (2007) noted that iron-rich vadose zone sediment contains magnetite ($Fe^{II}Fe_2^{III}O_4$), ilmenite ($FeTiO_3$), Fe(II)/Fe(III) phyllosilicates, Fe(III) oxides (ferrihydrite [$5Fe_2O_3 \bullet 9H_2O$]), and goethite [α-FeO(OH)]) (Gee et al. 2007). The finer grained sediments might also include the higher weight percentage of clay mineral phases such as illite (a dominant mineral in the clay-size fraction), smectite, biotite and chlorite. Physical analysis of sediment fractions included evaluation for dry bulk density, particle density, and porosity. Surface areas of each fraction were determined using the Brunauer–Emmet–Teller (BET) method. Elemental composition, surface morphology, and mineralogy of the sediment prior to and post U and Cr treatment in batch studies were analyzed using scanning electron microscopy-energy dispersive spectroscopy (SEM-EDS) and powder X-ray diffraction (XRD).

The U+Cr competitive sorption capacity of the sediment was studied in batch experiments at a sediment:water ratio as 1:1 with two sets of concentrations. Results were compared with data when each contaminant was used for adsorption experiments separately. The competitive sorption capacity is currently being further investigated with U and U+Cr column experiments.

Geochemical speciation modeling was conducted to determine the distribution of uranyl aqueous species and to analyze the saturation state of U in artificial groundwater used in batch and column experiments.

Further details on methodology and results of experiments described above can be found in a draft manuscript included in Appendix B.

Subtask 1.3: References

Dong, Wenming, William P. Ball, Chongxuan Liu, Zheming Wang, Alan T. Stone, Jing Bai, and John M. Zachara. 2005. "Influence of Calcite and Dissolved Calcium on Uranium(VI) Sorption to a Hanford Subsurface Sediment." *Environmental Science and Technology* 39 (20): 7949–55. https://doi.org/10.1021/es0505088.

Fox, Patricia M., James A. Davis, and John M. Zachara. 2006. "The Effect of Calcium on Aqueous Uranium(VI) Speciation and Adsorption to Ferrihydrite and Quartz." *Geochimica et Cosmochimica Acta* 70 (6): 1379–87. https://doi.org/10.1016/j.gca.2005.11.027.

Gee, G. W., M. Oostrom, M. D. Freshley, M. L. Rockhold, and J. M. Zachara. 2007. "Hanford Site Vadose Zone Studies: An Overview." *Vadose Zone Journal* 6 (4): 899–905. https://doi.org/10.2136/vzj2006.0179.

Gorman-Lewis, Drew, Tatiana Shvareva, Karrie-Ann Kubatko, Peter C Burns, Dawn M Wellman, Bruce Mcnamara, Jennifer E S Szymanowski, Alexandra Navrotsky, and Jeremy B Fein. 2009. "Thermodynamic Properties of Autunite , Uranyl Hydrogen Phosphate , and Uranyl Orthophosphate from Solubility and Calorimetric Measurements." *Environ. Sci. Technol.* 43 (19): 7416–22. https://doi.org/10.1021/es9012933.

Martin, C J. 2011. "Overview of Hanford Hydrogeology and Geochemistry."

Peretyazhko, T S, J M Zachara, R K Kukkadapu, S M Heald, I V Kutnyakov, C T Resch, B W Arey, et al. 2012. "Pertechnetate (TcO4-) Reduction by Reactive Ferrous Iron Forms in Naturally Anoxic, Redox Transition Zone Sediments from the Hanford Site, USA." *Geochimica et Cosmochimica Acta* 92: 48–66. https://doi.org/10.1016/j.gca.2012.05.041.

Stewart, Brandy D., Melanie A. Mayes, and Scott Fendorf. 2010. "Impact of Uranyl - Calcium - Carbonato Complexes on Uranium(VI) Adsorption to Synthetic and Natural Sediments." *Environmental Science and Technology* 44 (3): 928–34. https://doi.org/10.1021/es902194x.

Um, Wooyong, Jonathan P. Icenhower, Christopher F. Brown, R. Jeffery Serne, Zheming Wang, Cleveland J. Dodge, and Arokiasamy J. Francis. 2010. "Characterization of Uranium-Contaminated Sediments from beneath a Nuclear Waste Storage Tank from Hanford, Washington: Implications for Contaminant Transport and Fate." *Geochimica et Cosmochimica Acta* 74 (4): 1363–80. https://doi.org/10.1016/j.gca.2009.11.014.

Xu, Chen, Daniel I. Kaplan, Saijin Zhang, Matthew Athon, Yi Fang Ho, Hsiu Ping Li, Chris M. Yeager, et al. 2015. "Radioiodine Sorption/Desorption and Speciation Transformation by Subsurface Sediments from the Hanford Site." *Journal of Environmental Radioactivity* 139: 43–55. https://doi.org/10.1016/j.jenvrad.2014.09.012.

Zachara, John, Calvin Ainsworth, Gordon Brown, Jeffrey Catalano, James McKinley, Odeta Qafoku, Steven Smith, James Szecsody, Sam Traina, and Jeffrey Warner. 2004. "Chromium Speciation and Mobility in a High Level Nuclear Waste Vadose Zone Plume." *Geochimica et Cosmochimica Acta* 68 (1): 13–30. https://doi.org/10.1016/S0016-7037(03)00417-4.

Zheng, Zuoping, Tetsu K. Tokunaga, and Jiamin Wan. 2003. "Influence of Calcium Carbonate on U(VI) Sorption to Soils." *Environmental Science and Technology* 37 (24): 5603–8. https://doi.org/10.1021/es0304897.

Subtask 1.4: Experimental Support of Lysimeter Testing

Subtask 1.4: Introduction

Vitrification is a well demonstrated technology for the immobilization of radioactive wastes. Vitrification involves melting waste materials with glass-forming additives to immobilize contaminants in the structure of the final vitreous product. Borosilicate glasses are the most commonly researched and demonstrated class of glasses used for radioactive wastes as they are able to immobilize larger quantities of actinides (Grambow, 2006; Ojovan and Lee, 2011). While borosilicate glass is a dense material, there are several different processes that can lead to the apparent dissolution rate measured by the release of aqueous species to the bulk solution depending on the glass composition and chemical and physical conditions near the glass surface (Gin et al., 2013). The chemical durability of borosilicate glasses expressed as a dissolution rate, k (g $m^{-2}day^{-1}$), is the most important requirement for acceptance of glass waste forms for geological disposal (Jantzen et al., 2010).

The corrosion of glass is traditionally evaluated using ASTM Method C1662-18, *Standard Practice for Measurement of the Glass Dissolution Rate Using the Single Pass Flow Through (SPFT) Test Method* and the static Product Consistency Test (PCT) (Standard, 2014). The rate of corrosion can be calculated using a model based on the transition state theory (TST) equation (Eyring, 1935). Resulting from the dissolution of the glass and interaction with dissolved species in the near field various secondary phases may precipitate (Cailleteau et al., 2008; Cailleteau et al., 2011). These processes can affect chemical and physical properties at the altered glass surface and create a ‘protective’ precipitate layer on a glass surface (Icenhower et al., 2004; Pierce et al., 2008) (Standard, 2014) or these phases can serve as “sinks” for dissolved species acting to suppress the dissolution rate. As the precipitates form, the concentration of controlling species is reduced, and in turn, the corrosion rate can increase.

One of the planned configurations at Hanford’s Field Lysimeter testing units is the co-disposal of grout waste forms above glass waste forms. The grout waste forms placed above the glass is expected to strongly affect both the glass corrosion mechanisms and rate. It is presumed that the alkaline water resulting after contact with the grout waste forms may increase the dissolution rate of the glass waste forms below and pre-experimental modeling suggested such behavior. The grout-contacted water has elevated pH (~12) and contains dissolved species from the grout (e.g., Si, Al, Ca, K) that may affect the rate of glass dissolution through a common ion effect or precipitation reactions. If the pore water composition contacting the glass is dominated by the grout, the formation of calcium-silicate-hydrates is expected due to a very strong affinity between calcium and silica gels in alkaline media (Armelao et al., 2000).

Kaspar et al., used spectroscopic ellipsometry (SE) and cross-sectional secondary electron microscopy to evaluate the thickness and optical properties of the alteration layer formed on glass coupons exposed to aqueous solutions with various pH. The authors obtained a quantitative agreement of alteration layer thickness between SE and cross-sectional SEM imaging (Kaspar et al., 2018). Changes in the alteration layer composition observed by EDS cross-sections demonstrated a decrease in the concentration of Na compared to a pristine glass as previously noted by (Conradt, 2008; Jantzen et al., 2010). A field lysimeter test is currently ongoing at the

Hanford site in which glass and cementitious waste forms are placed within disposal backfill near the planned disposal facility (Bacon et al., 2018).

Subtask 1.4: Objectives

The objective of this study is to determine the effect of temperature, pH and dissolved components on the borosilicate glass dissolution rate in the presence of grout-contacted solution. This would help to evaluate if the dissolution behavior of the glass is controlled by a pH-mediated effect by the sediment or by the chemical makeup of the grout-contacted groundwater. The results of these experiments will provide information to support the design of future FTLF units to investigate the dissolution of waste forms at the Hanford Site Integrated Disposal Facility (IDF).

Subtask 1.4: Methodology

Materials

The glass used in this study was borosilicate ORLEC28 glass which is one of the two glasses being tested in the FLTF (Neeway et al., 2018). The grout used to prepare the grout-contacted solutions was Cast Stone which is used to immobilize simulated LAW and its fabrication is described elsewhere (Asmussen et al. 2018). Buffer solution with pH 12 was prepared by dissolving LiCl and LiOH in DI water. Sodium metasilicate nonahydrate was used to prepare silicon-amended solution (~ 5 mg/L Si) and ACS grade 67-70 wt. % HNO_3 reagent was used for solution preparation and analytical measurements.

Preparation of glass and grout- and grout/sediment-contacted solutions

The bulk glass was crushed with an agate mortar and pestle and sieved to the desired size fraction 149 - 74 μm (-100 to +200 mesh). Glass powder was washed with DI water and ethanol according to the *Section 19.6* of *ASTM C1285-14* to remove fines. The glass particles were then dried in an oven overnight at 90°C and, finally, tested by SEM for the absence of any fines adhered to the surface of glass particles. The grout-contacted solution was prepared by first crushing the bulk grout sample with a hammer and sieving the powder to < 2 mm particle size. DI water (1,000.0 g) was contacted with of the powdered grout (25.0 g) for 7 days on a mechanical shaker. The filtrate with pH 11.52 ± 0.08 was used as a grout-contacted solution. Sediment-contacted solution was prepared using the same procedure as for grout-contacted solution except for using as-received sediment sample without grinding and sieving. Grout/sediment-contacted solution was prepared by passing using peristaltic pump grout-contacted solution through a column filled with sediment. Figure 18 shows the experimental setup used for grout/sediment contacted solution preparation. The pH of the grout/sediment-contacted solution was found to be lowered (8.3) compared with the pH of the grout-contacted solution. Table 12 compares the pH of three prepared solutions.

Figure 18. Column for preparation of grout/sediment-contacted solution.

Table 12. pH of Grout-, Sediment-, and Grout/Sediment-Contacted Solutions

Solution	pH
Grout-contacted	11.52
Sediment-contacted	8.68
Grout/sediment contacted	8.3

Collection and analysis of samples

The PCT tests were performed at 90 ^{o}C with different solutions. The PCT tests were performed in triplicate and reported results are average values of three separate reactors. In addition, three control reactors were tested without glass to monitor the stability of solutions at 90 ^{o}C. Reactors were 60 mL PFA jars with closures (Savillex, Minnetonka, MN). This test continued for 7 days at 90±1 ^{o}C with ratio V_{soln}/m_{solids} = 10:1 (11.0 mL solution and 1.1 g of glass), which corresponds to S/V ratio of 2000 m^{-1}. After the experiment, reactors were removed from the oven one by one, weighed, and opened for sampling. The weight change due to evaporation was less than 3% for the test duration. Immediately after opening five reactors, 0.250 mL of sample aliquots were collected from hot leachate and diluted by 6.0 mL of 2 % HNO_3. The pH in each reactor was measured after cooling down the solution to room temperature. The pH measurements were done by an Orion Star A215 meter with Orion 8156BNUWP Ross Ultra electrode. The pH electrode calibration was conducted before pH measurements using standard pH buffers (pH 4.01, 7.00 and 10.01, Thermo Scientific).

The concentrations of B and Re, which is a chemical surrogate of Tc, in the samples and blanks were measured by the inductively coupled plasma mass spectroscopy (Thermo Fisher Scientific, iCAP RQ ICP-MS). The concentration of Si was measured by the inductively coupled plasma optical emission spectroscopy (ICP-OES, Perkin Elmer, Optima 7300 DV). The ICP-MS estimated limits of quantification (LOQ) for B and Re as 9.2 µg/L and 0.13 µg/L, respectively. The LOQ for Si by the ICP-OES was determined as 50 µg/L. Solutions were diluted with 2% HNO_3 before analysis. Micrographs and elemental analysis of used glass from each experiment were taken from a JEOL JSM-5900LV scanning electron microscopy/energy-dispersive X-ray spectroscopy (SEM/EDS) at 25.0 kV and a takeoff angle of 35.0°. SEM/EDS study was done on the powdered glass samples mounted in epoxy resin and polished using Al_2O_3 abrasive powder. Specimens were coated with gold using cold sputter coater to avoid charging of the surface under electron beam. The Brunauer-Emmett-Teller (BET) specific surface area measured via Micromeritics TriStar II 3020 instrument was $2.04 \times 10^{-2} \pm 0.005$ m^2/g. Glass bulk density is 2.74 g/cm^3 (Bacon et al., 2018).

Subtask 1.4: Results and Discussion

SEM/EDS analyses of glass samples treated at 90^{o}C in pH 12 buffer, grout-contacted and Ca-amended solutions

Glass samples treated at 90 ^{o}C for 7 days in the static PCT test in three different solutions (pH 12, Ca-amended and grout-contacted solutions) were visualized via SEM/EDS. Examination of the glass at higher magnification revealed that the degree of glass corrosion was different in each of three studied samples. Glass treated in the pH 12 buffer solution featured corrosion pockets in the form of deep holes with an approximate diameter of 200-300 µm which covered the surface of the glass particles (Figure 19A). Glass particles treated in the Ca-amended solution, showed no sign of surface corrosion compared to the untreated glass sample (Figure 19B). Finally, glass particles treated in the grout-contacted solution, featured only slight corrosion defects in the form of shallow craters of irregular shape with average diameter of about 500 µm (Figure 19D). These craters were observed only on a limited number of glass particles (Figure 19D).

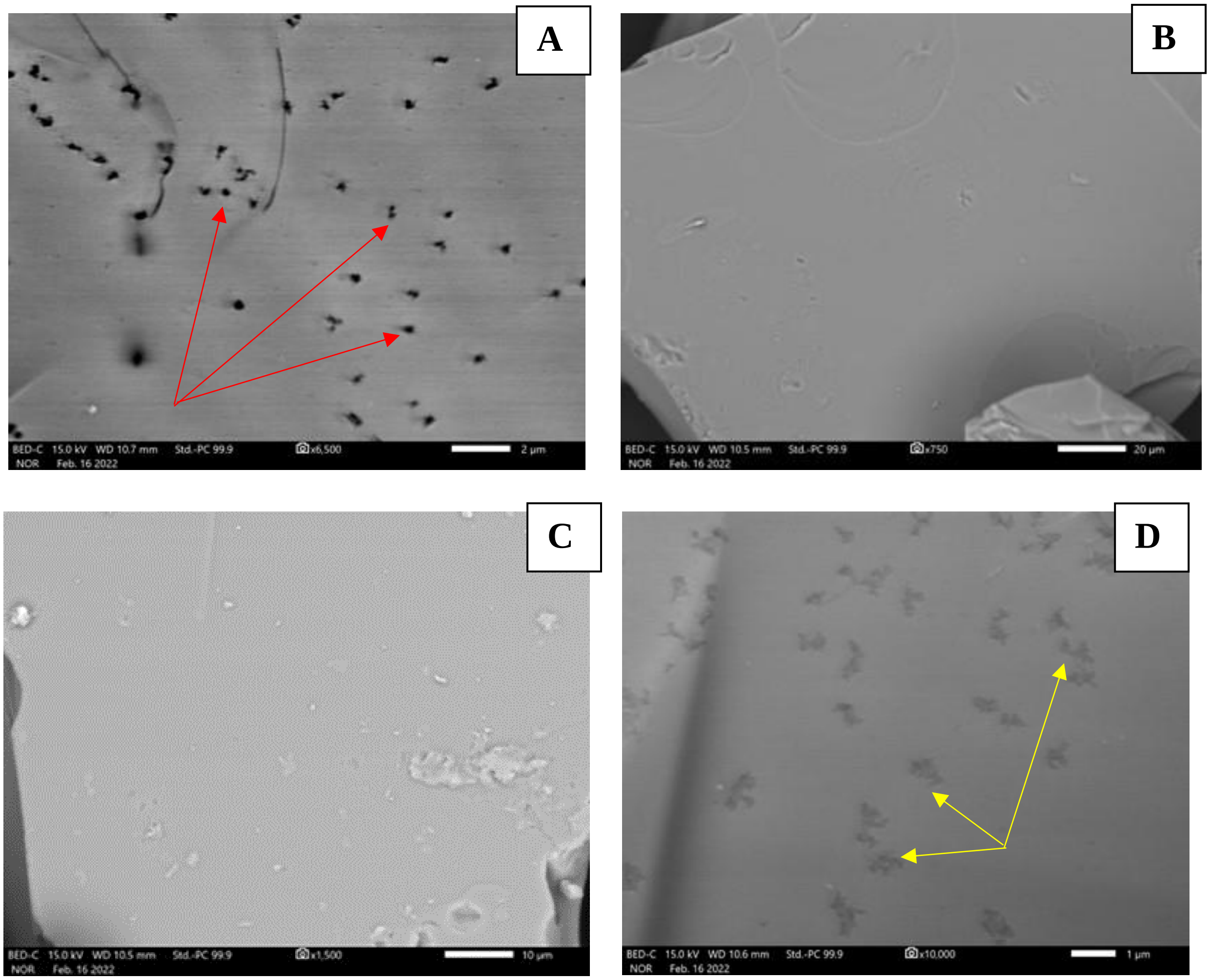

Figure 19. SEM images of glass particles used in the static PCT test. A) deep corrosion pockets on the surface of glass treated with pH 12 buffer solution (red arrows); B) Ca^{2+} solution buffer solution; C) with grout-contacted solution; D) minor corrosion defects on the surface of glass particles used in the static PCT test with grout-contacted solution (yellow arrows).

The results of SEM testing showed a drastic decline of glass corrosion defects after treatment in grout or Ca-amended leaching solutions. This positively correlates with a significant decrease of glass pore size cumulative volume measured by the BJH adsorption procedures. Precipitates with crystal cubic morphology were detected on the surface of glass particles treated in a grout-contacted solution (Figure 20). This correlates with previous results that corrosion of silicate glasses matrix in contact with aqueous solutions is strongly influenced by the ion exchange mechanism involving Na^+, OH^- via interaction of a leaching solution with glass components, the formation of solid alteration products, and a strongly bonded CSH layer on the glass surface (Armelao et al., 2000; Conradt, 2008; Vienna et al., 2013).

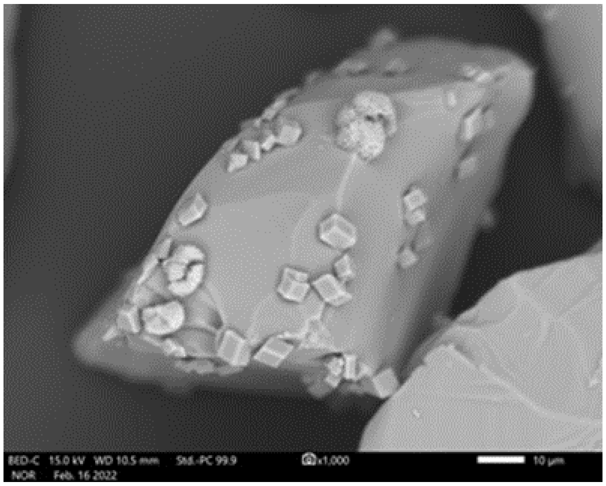

Figure 20. Precipitates on the surface of glass particles used in the static PCT test using grout-contacted solution.

Static PCT test with sediment- and grout/sediment-contacted solutions

Table 13 shows results of ICP-MS and ICP-OES analysis of the grout-, sediment- and grout/sediment-contacted solutions. Passing grout-contacted solution through a column with sediment leads to significant increase in the concentration of Re, Mg, Si and decrease in the concentration of Al. Concentrations of B and K moderately decrease, while concentration of Ca increases. The pH of the solution drops to 8.66 compared with 11.85 for grout-contacted solution.

Sediment before and after passing the grout-contacted solution through it was analyzed by powder XRD. Results of the phase analysis are shown in Figure 21. Major phases detected in the sediment sample are quartz and albite. No change in the phase composition of the sediment after the contact with grout-contacted solutions is detected.

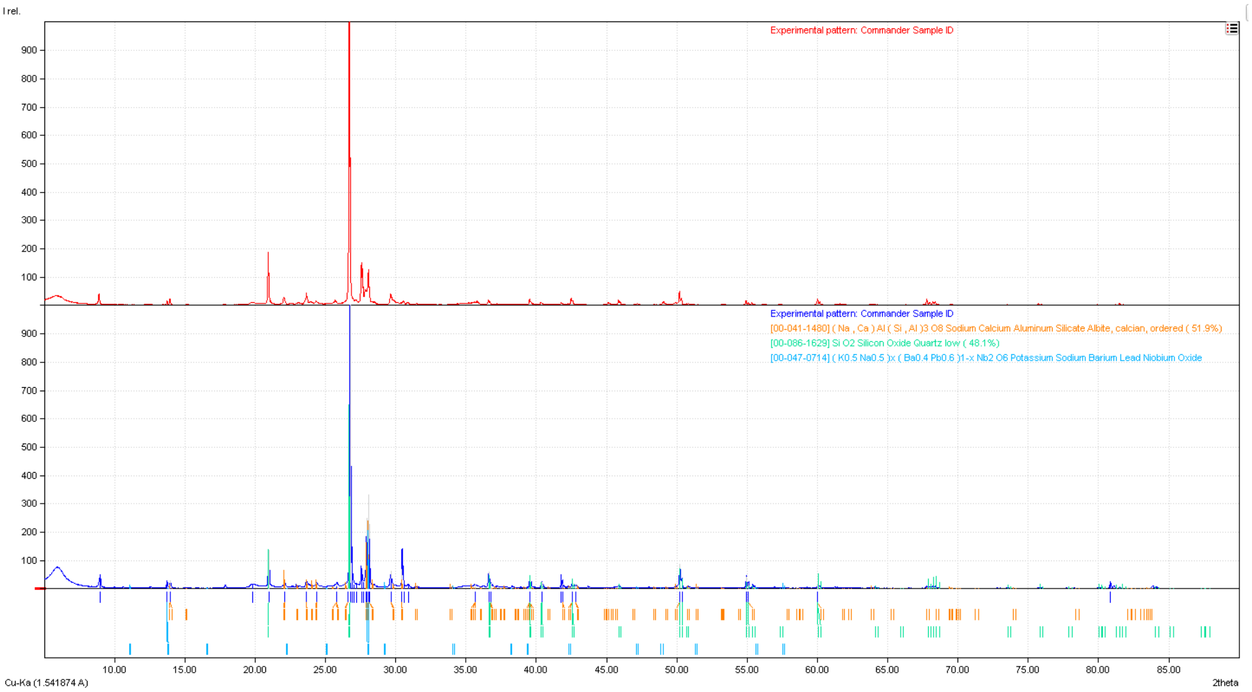

Figure 21. XRD analysis of pristine sediment powder (bottom) and after contact with grout-contacted solution (top).

Table 13. Compositions of Grout-, Sediment-, and Grout/Sediment-Contacted Solutions According to ICP-MS (B, Re) and ICP-OES (Si, Al, Ca, Mg, K and Fe) Analysis.

Element	**Concentrations, μg/L**		
	Grout-contacted	**Sediment-contacted**	**Grout/sediment-contacted**
B	172(6)	2.8(6)	112.1(9)
Re	0.052(4)	0.006(3)	0.08(9)
Si	6397(83)	22711(443)	22719(199)
Al	423(118)	391(24)	18(5)
Ca	111506(2312)	2934(45)	48634(449)
Mg	33(2)	106(5)	24821(259)
K	3064(226)	6037(347)	18947(1084)
Fe	0	291(66)	0

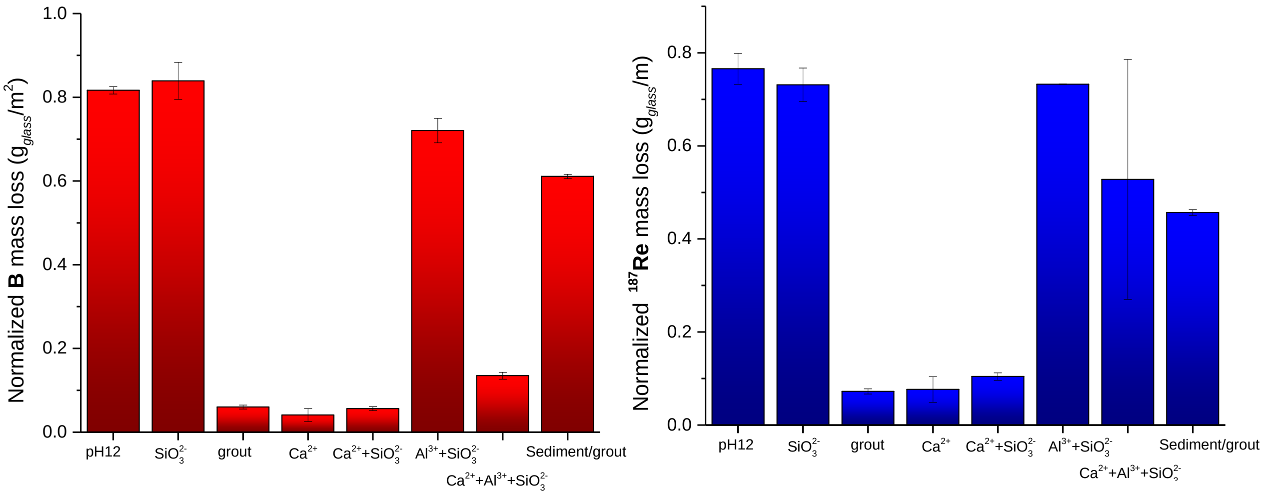

a) b)

Figure 22. Normalized B (a) and Re (b) losses calculated after analysis of the leachates collected in 7 days PCT static test at 90ºC in sediment/grout-contacted solution. Results for other solutions which were tested previously are plotted for comparison.

Figure 22 shows results of ICP-MS analysis for B and Re of leachates collected in the PCT test with sediment/grout-contacted solution. As seen, glass dissolution rate increases in the sediment/grout-contacted solution compared to the grout-contacted or Ca-amended solution, but it is still lower compared with the pH-12 buffer or Si-amended solutions. However, the latter observation might be related to the lower pH of the sediment/grout-contacted solution rather than to the difference in the chemical composition of the solutions.

Long-term static PCT test with pH 12 buffer, grout-contacted and Ca-amended solution

The static long-term PCT experiment was initiated with three solutions: pH 12 buffer, Ca^{2+} (130 ppm) in pH 12 buffer and grout-contacted solutions. Each solution is triplicated. In addition to the glass powders, the reactors contain two polished glass coupons for SEM/EDS study. Table 4 shows the schedule of the experiment. After completion of the experiment, the following samples will be prepared for characterization of corrosion stability of borosilicate glass in three solutions of the interest: polished glass coupons corroded for 0.5, 1, 2, 3, 4.5 and 6 months (SEM/EDS study) and glass powders (corroded for 1, 3 and 6 months) for SEM/EDS and BET studies.

Glass coupons were cut from ORLEC-28-LYS-062-08 bulk sample (provided by PNNL) using a diamond saw blade. Two sides of the coupons were polished, using for the final polishing Al_2O_3 abrasive powder (1.0 and 0.3 µm). Figure 23 shows a photo of the prepared coupons.

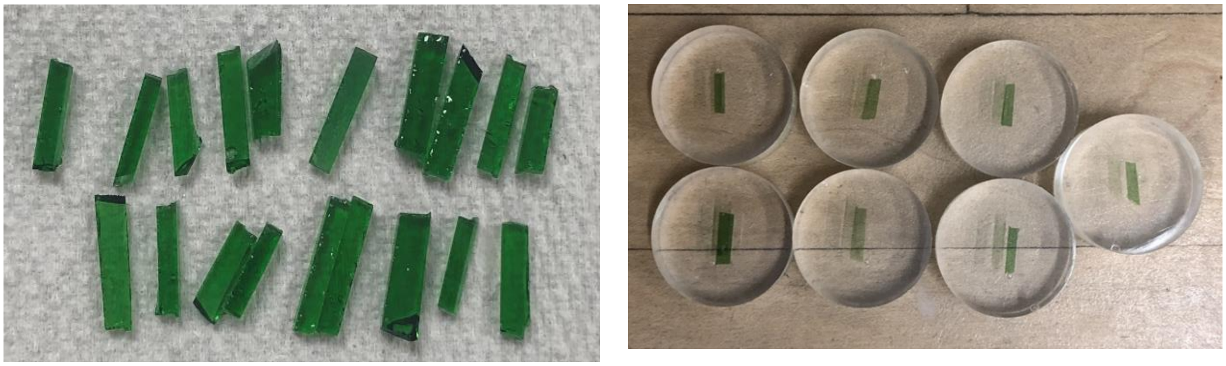

a) b)

Figure 23. (2) Polished glass coupons for the long-term static PCT test and mounted in the epoxy resin and (b) polished glass coupons after 2 and 4 weeks of the static PCT test.

Table 14. Schedule of the Long-Term Static PCT Test.

Time	Sample
2 weeks	1st glass coupon is removed from each reactor #1 for SEM/EDS study
4 weeks	2nd glass coupon and glass powder are removed from each reactor #1 for SEM/EDS study
8 weeks	1st glass coupon is removed from each reactor #2 for SEM/EDS study
16 weeks	2nd glass coupon and glass powder are removed from each reactor #2 for SEM/EDS study
28 weeks	1st glass coupon is removed from each reactor #3 for SEM/EDS study
40 weeks	2nd glass coupon and glass powder are removed from each reactor #3 for SEM/EDS study

Figure 24 depicts normalized elemental mass losses for B, Re, Si and Al as functions of time in the long-term static PCT test at 90°C with pH 12 buffer, grout-contacted and Ca-amended solutions. The highest losses are detected in pH 12 buffer solution, and they increase with time for B and Re. On the contrary, concentrations of Al and Si in leachates decrease over time. The latter might be indicative of precipitation of Al and Si from the solution. Elemental losses of Re, B and Si by the glass are lower in grout-contacted and Ca-amended solutions compared to the pH 12 buffer, however, they show significant increase over a period of time between 8 and 16 weeks. Aluminum concentrations in the leachates for the grout-contacted and Ca-amended solution do not vary significantly. These trends shown by Al and Si could indicate that the precipitates might be aluminosilicates which start precipitating after Si concentration in the solution reaches the precipitation limit.

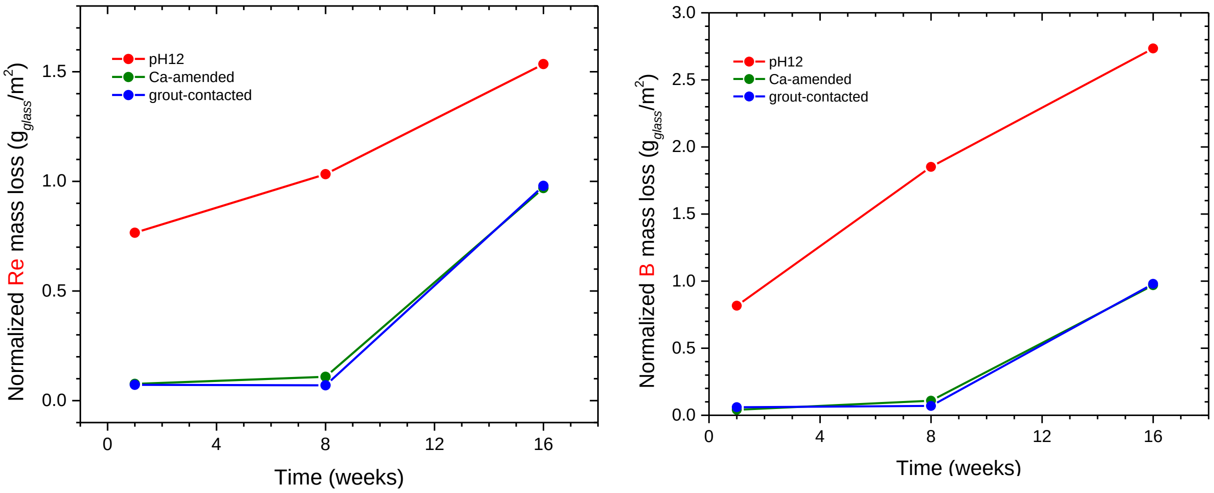

a) **b)**

Figure 24. Normalized elemental release rates for Re (a) and B (b) as functions of time in long-term static PCT test.

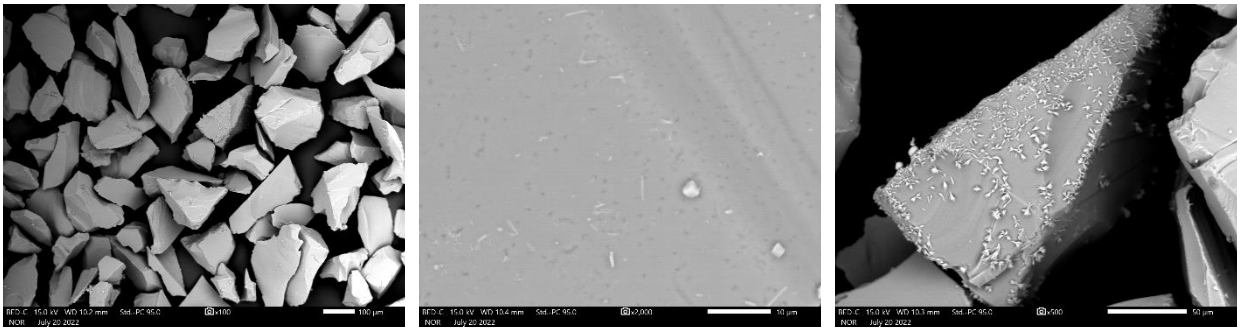

a) pH 12 buffer solution

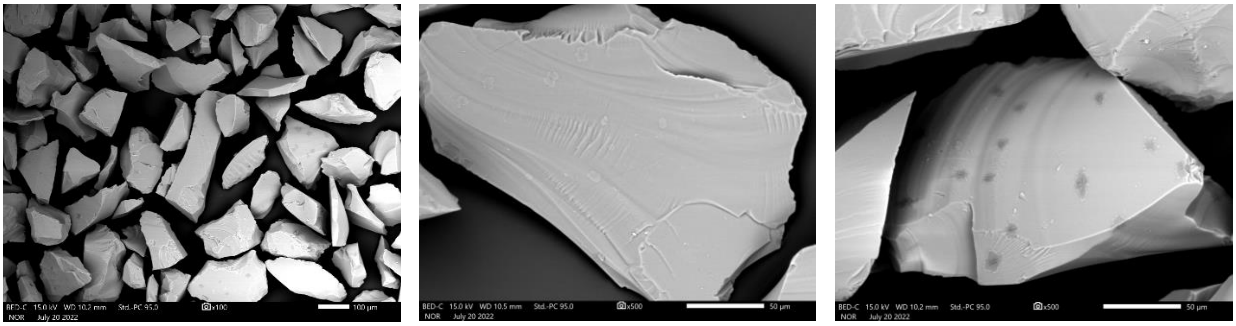

b) Ca^{2+}-amended solution

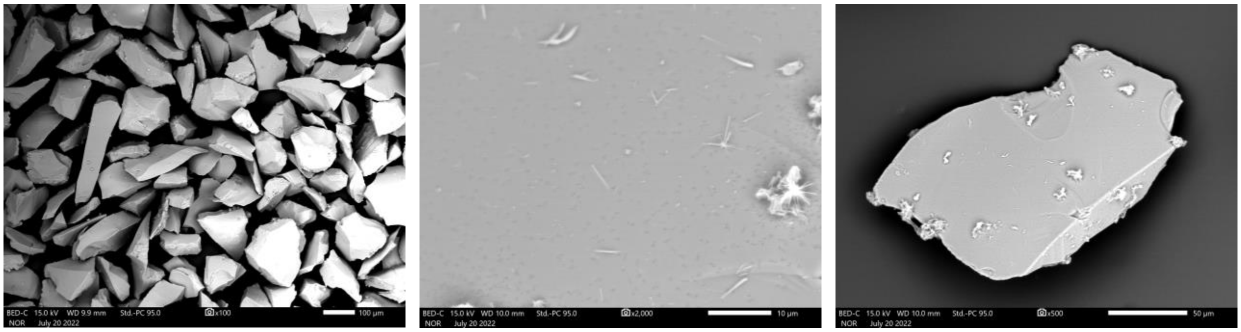

c) grout-contacted solution

Figure 25. SEM images at different magnifications of three ORLEC28 glass powders treated at 90°C for 4 weeks (PCT test) in pH 12 buffer, Ca^{2+}-amended and grout-contacted solution.

Glass powders collected and tested in the long-term PCT test (4 weeks) at 90°C in pH 12 buffer, Ca-amended and grout-contacted solutions were studied by SEM analysis. SEM micrographs at different magnifications are shown in Figure 25. Observed corrosion behavior in three solutions after 4 weeks of the test is very similar to that after 1-week of the test. The majority of glass particles treated in the pH 12 buffer have corrosion features in the form of small 200-300 µm and deep craters in the surface of glass particles. Corrosion features seen on the glass particles treated in the grout-contacted solution are present in much smaller amounts and are less deep compared to the pH 12 buffer. Glass particles treated in the Ca-amended solution shows almost no sign of surface corrosion. Precipitates of acicular-type crystal habit are observed in large amounts on the glass particles treated in the pH 12 buffer solution.

Glass particles tests in the grout-contacted and Ca-amended solutions show similar corrosion features in the form of ~1 µm craters on the surface of the glass. This observation can be an indication of pitting corrosion. Meanwhile, the corrosion of glass in pH 12 buffer is more uniform. Another feature observed to a large extent for the latter glass is a well-developed network of the crack lines.

Figure 26 shows SEM images collected on glass powders tested for 16 weeks in the static PCT experiment at 90°C. A large number of flake-like precipitates was detected on the surface of glass particles tested in all three solutions. Precipitates which form in the pH 12 buffer solution are of submicron size. Larger precipitates form in grout-contacted solution and precipitates from the Ca-amended solution are the biggest in size (>1 µm).

pH 12 buffer solution (a-d)

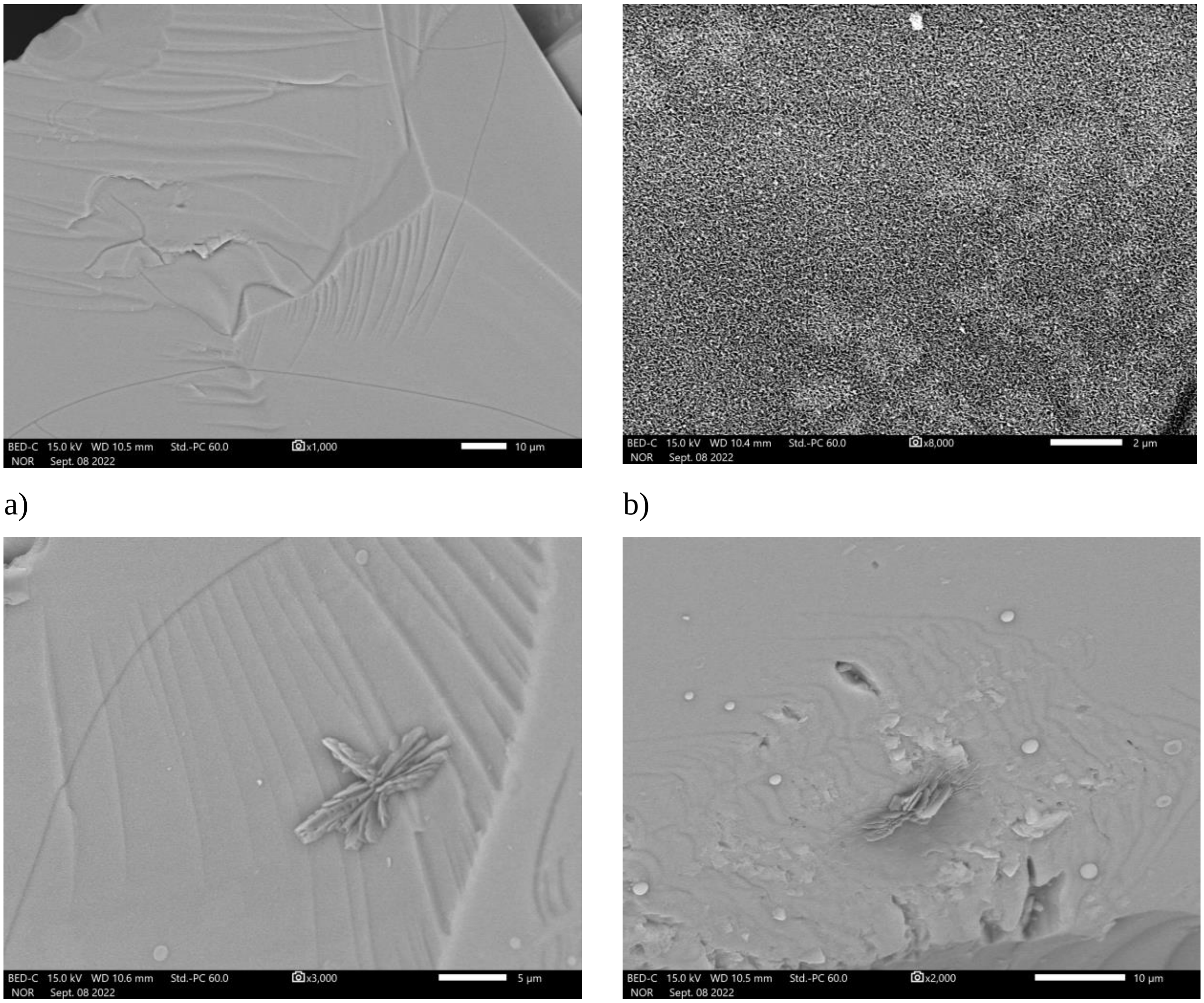

a) b)

c) d)

Ca-amended solutions (e-h)

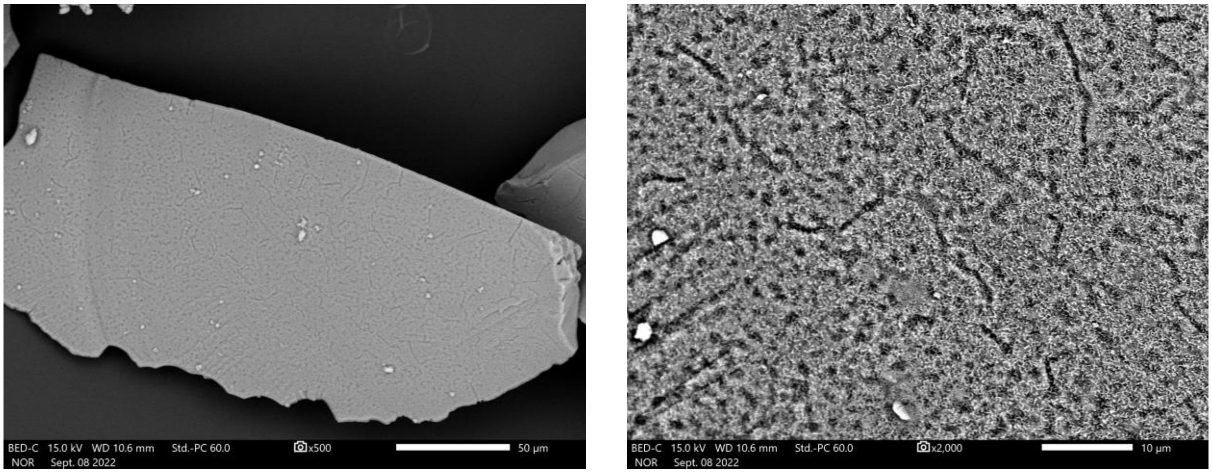

e) f)

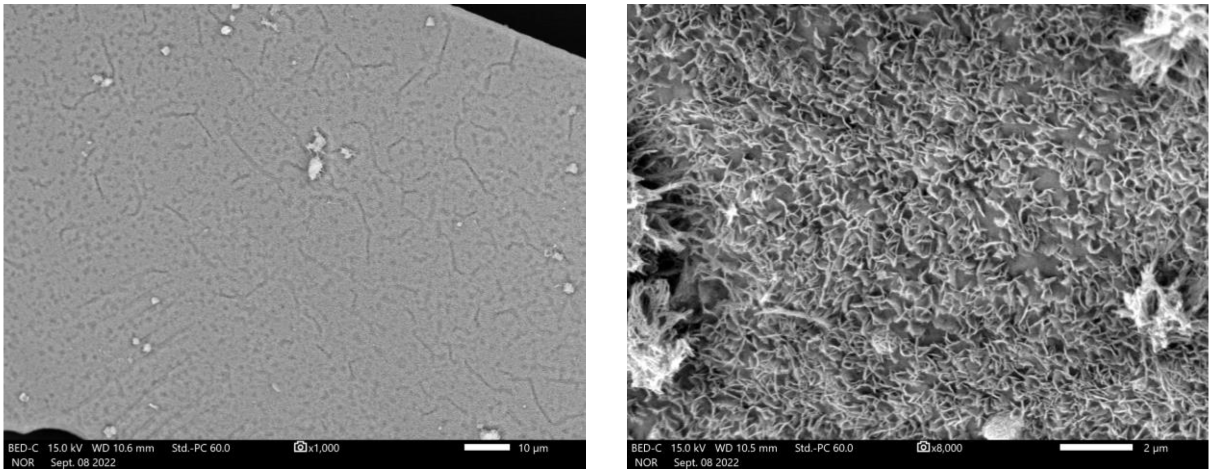

g) h)

Grout-contacted solution (i-l)

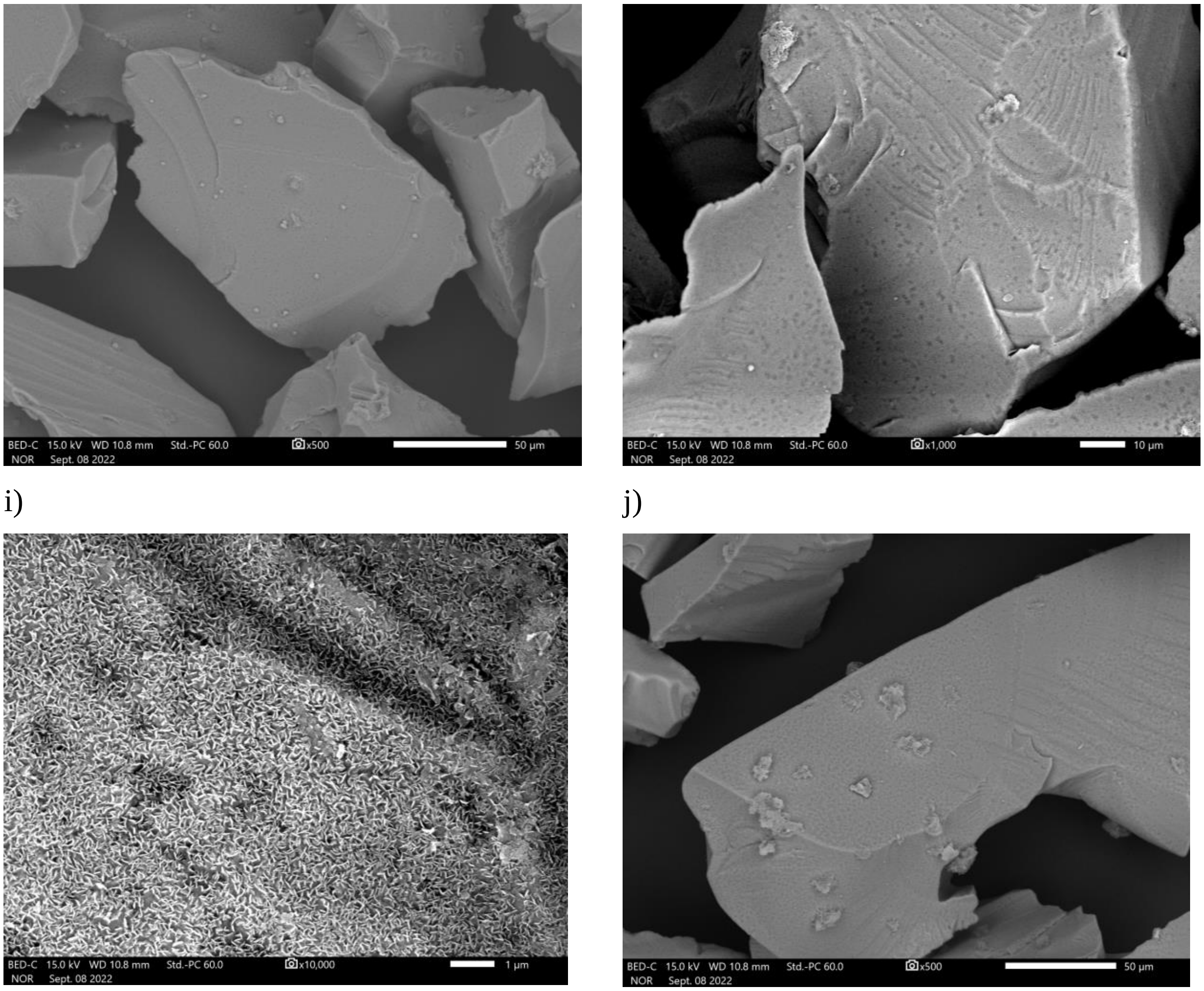

k) l)

Figure 26. SEM micrographs of glass treated for 16 wks in pH 12 buffer, Ca-amended and grout-contacted solutions.

These glass samples tested for 16 weeks were examined by X-ray diffraction to reveal the nature of precipitates observed in the SEM/EDS study. Collected XRD patterns are shown in Figure 27. As seen, no crystalline secondary phases are detected by the X-ray diffraction method. It can be concluded that the amount of precipitates is below the detection limit of the method or they are amorphous.

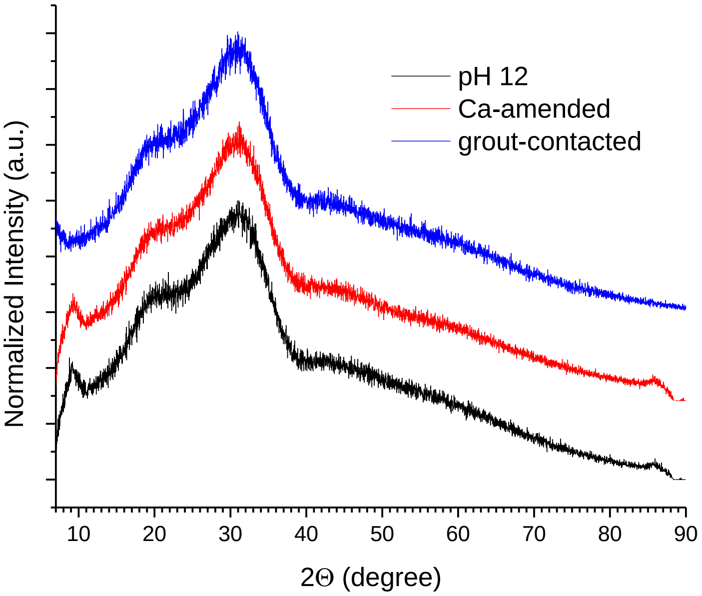

Figure 27. X-ray diffraction patterns of glass powders treated in different solutions for 16 weeks.

Subtask 1.4: Conclusion

The BET surface area and pore size measurements performed on the pristine ORLEC28 glass powder and several glass powders used in the static PCT test with pH 12 buffer, grout-contacted and Ca-amended solutions showed pore voids “sealing” in the presence of Ca^{2+} ions, which might be due to the precipitation of calcium silicate hydrate (CSH) or other corrosion products such as calcium carbonate saturated from the grout solution. This conclusion is supported by SEM studies on the glass powders after treatment in a PCT test with the same solutions. A long-term static PCT test using a pH 12 buffer, grout-contacted and Ca-amended solution was initiated to study glass corrosion behavior over an extended period of time (40 weeks). Preliminary data indicates a diminishing effect of calcium on the glass dissolution kinetics. Dissolution behavior of borosilicate glass in grout/sediment-contacted solution has been investigated using a static PCT test at 90^{o}C. Glass dissolution rate increases in the sediment/grout-contacted solution compared to the grout-contacted or Ca-amended solution, but it is still lower compared to the pH 12 buffer or Si-amended solutions.

Subtask 1.4: References

ASTM (2018). Standard practice for measurement of the glass dissolution rate using the single-pass flow-through test method (Designation: C1662-18). Philadelphia, PA: ASTM

Armelao, L., Bassan, A., Bertoncello, R., Biscontin, G., Daolio, S. and Glisenti, A., 2000. Silica glass interaction with calcium hydroxide: a surface chemistry approach. Journal of Cultural heritage, 1(4): 375-384.

Bacon, D.H., Meyer, P.D., Neeway, J.J., Fang, Y., Asmussen, R.M. and Strickland, C.E., 2018. Field-Scale Lysimeter Studies of Low-Activity Waste Form Degradation, Pacific Northwest National Lab.(PNNL), Richland, WA (United States).

Cailleteau, C., Angeli, F., Devreux, F., Gin, S., Jestin, J., Jollivet, P. and Spalla, O., 2008. Insight into silicate-glass corrosion mechanisms. Nature materials, 7(12): 978-983.

Cailleteau, C., Devreux, F.o., Spalla, O., Angeli, F. and Gin, S., 2011. Why do certain glasses with a high dissolution rate undergo a low degree of corrosion? The Journal of Physical Chemistry C, 115(13): 5846-5855.

Conradt, R., 2008. Chemical durability of oxide glasses in aqueous solutions: a review. Journal of the American Ceramic Society, 91(3): 728-735.

Eyring, H., 1935. The activated complex in chemical reactions. The Journal of Chemical Physics, 3(2): 107-115.

Gin, S., Abdelouas, A., Criscenti, L.J., Ebert, W.L., Ferrand, K., Geisler, T., Harrison, M.T., Inagaki, Y., Mitsui, S. and Mueller, K.T., 2013. An international initiative on long-term behavior of high-level nuclear waste glass. Materials Today, 16(6): 243-248.

Grambow, B., 2006. Nuclear waste glasses-How durable? Elements, 2(6): 357-364.

Icenhower, J.P., Samson, S., Lüttge, A. and McGrail, B.P., 2004. Towards a consistent rate law: glass corrosion kinetics near saturation. Geological Society, London, Special Publications, 236(1): 579-594.

Jantzen, C.M., Brown, K.G. and Pickett, J.B., 2010. Durable glass for thousands of years. International Journal of Applied Glass Science, 1(1): 38-62.

Kaspar, T.C., Reiser, J.T., Ryan, J.V. and Wall, N.A., 2018. Non-destructive characterization of corroded glass surfaces by spectroscopic ellipsometry. Journal of Non-Crystalline Solids, 481: 260-266.

Maraghechi, H., Rajabipour, F., Pantano, C.G. and Burgos, W.D., 2016. Effect of calcium on dissolution and precipitation reactions of amorphous silica at high alkalinity. Cement and Concrete Research, 87: 1-13.

Ojovan, M.I. and Lee, W.E., 2011. Glassy wasteforms for nuclear waste immobilization. Metallurgical and Materials Transactions A, 42(4): 837-851.

Pierce, E.M., Rodriguez, E.A., Calligan, L.J., Shaw, W.J. and McGrail, B.P., 2008. An experimental study of the dissolution rates of simulated aluminoborosilicate waste glasses as a function of pH and temperature under dilute conditions. Applied Geochemistry, 23(9): 2559-2573.

Standard, A., 2014. C1285-14, Standard Test Methods for Determining Chemical Durability of Nuclear, Hazardous, and Mixed Waste Glasses and Multiphase Glass Ceramics: The Product Consistency Test (PCT). ASTM International, West conshohocken, PA.

Vienna, J.D., Ryan, J.V., Gin, S. and Inagaki, Y., 2013. Current understanding and remaining challenges in modeling long-term degradation of borosilicate nuclear waste glasses. International Journal of Applied Glass Science, 4(4): 283-294.

TASK 2: REMEDIATION RESEARCH AND TECHNICAL SUPPORT FOR THE SAVANNAH RIVER SITE

Subtask 2.1: Environmental Factors Controlling the Attenuation and Release of Contaminants in the Wetland Sediments at Savannah River Site

Subtask 2.1: Introduction

The Savannah River Site (SRS) is a nuclear separation facility built in the 1950's to refine nuclear materials for the production of nuclear weapons (Kaplan, Roberts et al. 2011, Otosaka, Schwehr et al. 2011). The SRS F-Area Seepage Basins consists of three unlined basins that received low-level radioactive wastewater originating from the reprocessing of uranium sludge and irradiated fuel in the F-Area Separation Facility. The waste was acidic due to the presence of an elevated concentration of nitric acid (Killian, Kolb et al. 1987). Over the years, ^{129}I and other radionuclides migrated through the vadose zone to the saturated zone and contaminated the groundwater, where it was transported and discharged to the wetlands associated with a local stream, Fourmile Branch (Schwehr, Santschi et al. 2009, Emerson, Xu et al. 2014, Kaplan, Zhang et al. 2014, Zhang, Ho et al. 2014, Neeway, Kaplan et al. 2019). F-Area wetlands have been an important sink for ^{129}I and other contaminants, but changes in biogeochemical conditions such as variations in microbial activity, redox conditions, soil temperature, soil moisture and pH could cause the release of ^{129}I into the surrounding areas (Otosaka, Schwehr et al. 2011, Xu, Zhang et al. 2011). Previous field sampling events have indicated that ^{129}I is being accumulated in the topsoil (Kaplan, Zhang et al. 2014).

Exposure to radioiodine has a negative impact on public health (Davis, Kopecky et al. 2004, Cardis, Vrijheid et al. 2005, Stone, Stanford et al. 2013), water quality, and ecosystems. Several remediation techniques were applied at the F-Area seepage basin including pump-and-treat and funnel-and-gate with base and silver chloride injections to help control the mobilization of radionuclides, including ^{129}I, and the acidity in the groundwater in an attempt to reduce exposure and any associated health risk. However, these techniques have some limitations on the remediation of ^{129}I at the wetland due to the presence of organic matter, vegetation, and other factors, hence an effective remediation method is urgently needed to control the mobilization of IO_3^- and organo-iodine species in the wetland. Iodide and iodate have been found to bind strongly to the natural organic matter in the environment resulting in the formation of organo-iodide in the Fourmile Branch wetlands (Kaplan, Xu et al. 2019, Li, Xu et al. 2019, Neeway, Kaplan et al. 2019).

The goal of this study is to evaluate the use of organoclays as a potential remediation technology for ^{129}I at the wetland. In the present study, wetland soils were collected from a background area along the Fourmile Branch wetlands that has not been affected by site operations. A sequential extraction of SRS wetland soil was conducted to understand the iodine bounded to different fractions of the soil samples. In order to mitigate the mobility and release of ^{129}I at the Fourmile Branch, the use of two low cost and environmentally friendly organoclays PM-199 and MRM were investigated as potential sorbents for the sequestration of ^{129}I in the wetland at SRS. The outcome of these studies will provide SRS and the DOE with the ability to remediate I-129 from the F-Area more effectively.

Subtask 2.1: Objectives

The research objective of this study is to better understand the dominant attenuation mechanisms for ^{129}I in the wetlands, how strong is the attenuation, and what conditions would reverse it. The potential findings of this study will improve the understanding of the effect of environmental factors on the adsorption and release of iodine species and determine if organoclays are feasible amendments for in-situ remediation of iodine species in the SRS wetland environments. The study will also determine conditions for optimal iodide, iodate, and organo-iodine removal from the aqueous phase.

Subtask 2.1: Methodology

Chemicals:

Commercially available organoclays PM-199 and MRM were obtained from CETCO Inc. Iodide standard (I^-, 1000 µg/mL) and rhenium (Re, 1000 µg/mL) were purchased from SPEX CertiPrep. The VeriSpec^{TM} iodate standard (IO_3^-, 1000 ppm) and VeriSpec® Tellurium concentration was obtained from Rica Chemical. Tetramethylammonium hydroxide (TMAH, 25%) and sodium chloride (NaCl) were obtained from Fisher Scientific. Ammonium acetate (NH_4OAc) and hydroxylamine hydrochloride $(NH_3OH)_2 \cdot HCl$ were purchased from Alfa Aesar. Millipore water (MilliQ water, resistivity~18.0 $M\Omega \cdot cm^{-1}$ at 22 °C) was used for sample and standard preparation unless indicated otherwise.

Sequential extraction of SRS topsoil:

Sequential extraction of iodine from the SRS wetland soil was studied by preparing two sets of triplicate samples of 100 g/L SRS wetland soils that were equilibrated with 0.01 M NaCl for a week. The pH of the samples was adjusted to 5.5±0.2 to represent the wetland pH condition. To understand the interaction of iodine and SRS's wetland soil, the stock solutions of iodide and iodate (10 ppm) were then added into the soil suspension samples to achieve the final concentration of 400 ppb. The samples were placed on a platform shaker for a week, and the pH values were monitored and kept at 5.5±0.2 during the contact time. The samples were centrifuged at 4,500 rpm for 30 minutes to separate the solid phase from the aqueous phase, and the supernatants were analyzed for total iodine by Inductively Coupled Plasma Mass Spectrometry (ICP-MS)

To be able to compare the influence of 0.01 M NaCl background solution to the release of iodine, two sets of control samples of 100 g/L SRS wetland soil were prepared in DI water and in 0.01 M NaCl. The pH of those samples was adjusted to 5.5±0.2 to represent the wetland pH condition. The samples were placed on a platform shaker for a week and the pH values were monitored and kept at 5.5±0.2 during the contact time by adding 0.1 M NaOH/HCl. The sequential extraction method was obtained from Kohler et al. (Köhler, Riebe et al. 2019) and the procedure is as follows:

1. Water soluble fraction: The deionized water was added to the samples and placed on a shaker at 100 rpm for 2 hours at room temperature to extract water soluble components. The supernatants were collected.
2. Ion-exchangable fraction: 13.5 mL of 1.0 M ammonium acetate was added to the solid samples and shaken for 2 hours. The supernatants were collected.
3. Organic bound fraction: 13.5 mL of 10 mM sodium hydroxide was added to the samples. The samples were heated in a water bath at 80°C for 6 hours. The supernatants were collected.

4. Metal-oxides fraction: 13.5 mL of 40 mM hydroxylamine hydrochloride was added to the solid samples. The samples were placed in a water bath at 80°C for 6 hours. The supernatants were collected.

Effects of pH and dissolved organic matter on the attenuation/release of Iodine:

To understand the factors controlling the attenuation and release mechanisms of I, FIU investigated the effect of pH and dissolved organic content on the adsorption/desorption of iodide and iodate on wetland soils. Based on the results from the sediment depth profile study conducted by Savannah River National Laboratory (SRNL), the following depth intervals were chosen for the batch experiments: 0 - 1.5 feet, 5 - 6 feet, and 13 - 14 feet, representing the organic layer (high organic carbon content), intermediate layer (intermediate organic carbon content), and the aquifer layer (low organic carbon content) as shown in Table 15. Triplicate background soils (1.0 g/L) of 13 - 14 feet depth interval were equilibrated with the 0.01 M NaCl background solution for a week. The pH values of suspension samples were adjusted by adding 0.1 M NaOH/HCl during the contact time to 4, 5, 6, 7, and 8, respectively. Then, the samples were spiked with 10 mg/L stock solution of iodide and iodate to achieve the final concentration of 100 µg/L of iodide and iodate. A control study was also conducted to monitor the effect of pH on the wetland soil as well as release of natural iodine incorporated in the soil (if any) during the experiment. Finally, the samples were shaken at 100 rpm for 7 days then the samples were centrifuged at 2700 rpm for 30 min to separate the solid phase from the aqueous phase. The aqueous solutions were transferred into new vials and analyzed by ICP-MS.

Table 15. Parameters of Soil at 5 Different Depth Intervals (Data received from SRNL).

Soil depth interval (ft)		pH	Total Organic Carbon (mg/kg)	Aluminum (mg/kg)	Iron (mg/kg)	Silicon (partially dissolved) (mg/kg)
0 - 1.5	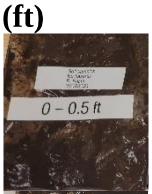	4.79 ~ 4.81	25300-119000	5310-7130	1340-8940	431-701
5 - 6		5.05	41700	4310	215	1260
13 - 14		5.49	350	2920	180	712

Adsorption experiments of iodine by organoclays:

A stock solution of 20 mg/L of iodide was prepared in MilliQ water. A series of iodate standard solutions ranging from 0.5 to 15 µg/L in 0.1% TMAH solution was prepared using VeriSpec™ iodate standard for the ICP-MS calibration curve of total iodine. A series of control solutions and working standards were prepared by dilution of stock solution. Kinetic experiments were performed in triplicate by adding 0.0135 g of organoclays PM-199/MRM into 13.5 mL of 50 µg/L I^- solutions in the 15 mL centrifuge tubes. The adsorption studies were conducted at room temperature and at solution pH of 5.5 ± 0.2. The mixtures were placed in the platform shaker at the agitation rate of 100 rpm and samples were collected at predetermined time intervals throughout and filtered with a 0.45 μm of syringe filter.

The adsorption capacities of organoclays PM-199 and MRM were calculated using Equation 1.

$$q_e = \frac{(C_0 - C_e) \times V}{m}$$ **Equation 1**

Where:

q_e is the equilibrium adsorption amount (mg/kg),
C_0 is the initial concentration (mg/L),
C_e is theequilibrium concentration (mg/L) of I^-,
V is the volume of I^- solution (L), and
m is the mass of organoclays PM-199 or MRM (kg).

Subtask 2.1: Results and Discussion

Sequential extraction of SRS topsoil:

FIU observed that natural iodine leached out into the solution in the initial step of the extraction process (Figure 28). The supernatants collected from each extraction step were analyzed using ICP-MS for the total iodine in the solution. To be able to compare the release of iodine during each extraction step from various sample matrices (DI water and 0.01 M NaCl), the residual concentration of total iodine in the solution was normalized to the total iodine leachate concentration of each sample matrix, as reported in Figure 29. As shown in Figure 29, under our experimental conditions, the water-soluble fraction extraction step has the highest extracted iodine concentration of ~ 80% while the ion-exchangeable fraction extraction step has the least extracted iodine concentration of ~ 1%. The organic bound iodine was approximately 15% of the total extracted iodine while the metal oxides fraction accounted for ~ 3% of the total extracted iodine concentration. The speciation of iodine study was carried out to understand which dominant species was leached out from the water soluble fraction of the soil. The iodide species is the dominant species that had leached out from the water-soluble fraction while the remaining iodine species are organo-iodine, and/or iodate.

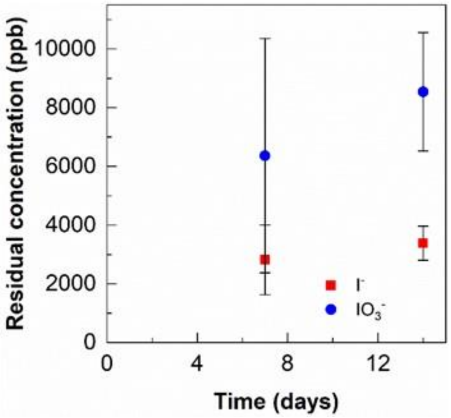

Figure 28. Residual concentrations of total iodine in the respective samples: (■) spiked iodide samples and (●) spiked iodate samples.

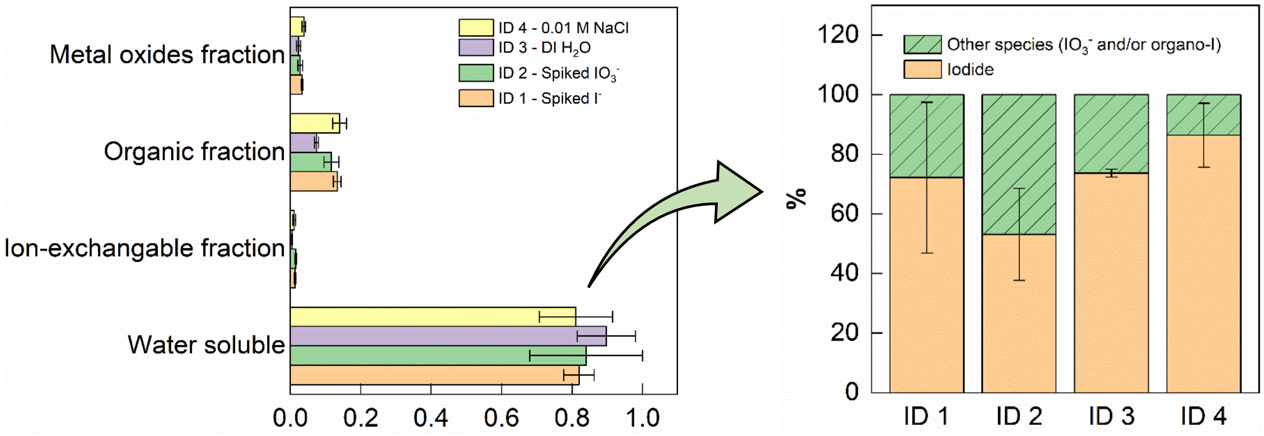

Figure 29. Distribution of iodine in SRS F-Area wetland soils in DI H_2O and 0.01 M NaCl matrices (left) and the speciation of iodine in water soluble fraction (right).

Effects of pH on the attenuation/release of Iodine-129:

The data collected from the ICP-MS analysis show that there was no sorption of iodide nor iodate on the 5-6 ft and 13-14 ft soils at pH 4 - 8 (Figure 30). The laboratory experiment is in agreement with the field sampling data as the iodine accumulated in the top 2 ft of wetland soil where the pH does not influence the sorption/release of iodine-129 at the wetland.

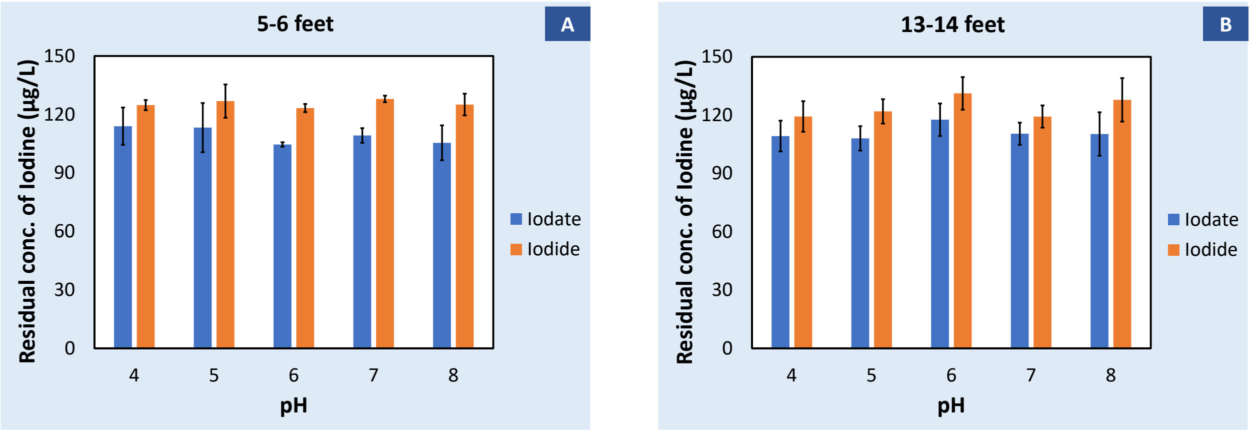

Figure 30. Residual concentration of iodide and iodate in solution after a week of sorption onto SRS wetland's soils at A) 5-6 feet and B) 13-14 feet depth intervals.

Adsorption kinetics:

The kinetic sorption experiments of iodide with organoclays were performed at the relatively low concentrations within the range of iodine concentration found at the Savannah River Site F-Area seepage basin. Furthermore, the sorption reactions are site-limited and strongly dependent on the diffusion processes, therefore it is important to conduct the experiments at environmentally relevant conditions (Schwehr, Santschi et al. 2009, Choung, Kim et al. 2014). Kinetic results obtained from the ICP-MS analyses showed that the adsorption of iodine on the surface of organoclays PM-199 increased with time and reached adsorption equilibrium within 24 hours with > 95% of iodide was adsorbed from the initial concentrations of 50 µg/L (Figure 31). Sorption is a combination of different processes such as external mass transfer, film diffusion, intraparticle diffusion, and sorption (Gonzalez-Raymat, Anagnostopoulos et al. 2018). The kinetic data were fit to both pseudo-first order and pseudo-second order kinetic models (Equations 2 & 3, respectively) and compared, to provide insights of adsorption mechanisms such as mass transfer and chemical reaction.

The non-linear pseudo-first-order kinetic model was formulated as follows:

$$qt = qe(1 - e^{-kt}) \qquad \textbf{Equation 2}$$

Where:

k_1 (hour^{-1}) is the first-order rate constant,
qe (mg/kg) is the amount of iodide adsorbed at equilibrium, and
qt (mg/kg) is the amount of iodide adsorbed at any time.

The parameters k_1 and qe were determined from the non-linear pseudo-first fitting.
The pseudo-second-order kinetic model is expressed by equation 3, as shown below.

$$qt = \frac{k_2 q_e^2 t}{1 + k_2 q_e t} \qquad \textbf{Equation 3}$$

Where:

k_2 (g/mg min) is the second-order rate constant,
qe (mg/kg) is the amount of iodide adsorbed at equilibrium,
qt (mg/kg) is the amount of iodide adsorbed at any time.
The values of k_2 and qe are determined from the non-linear pseudo-second fitting.

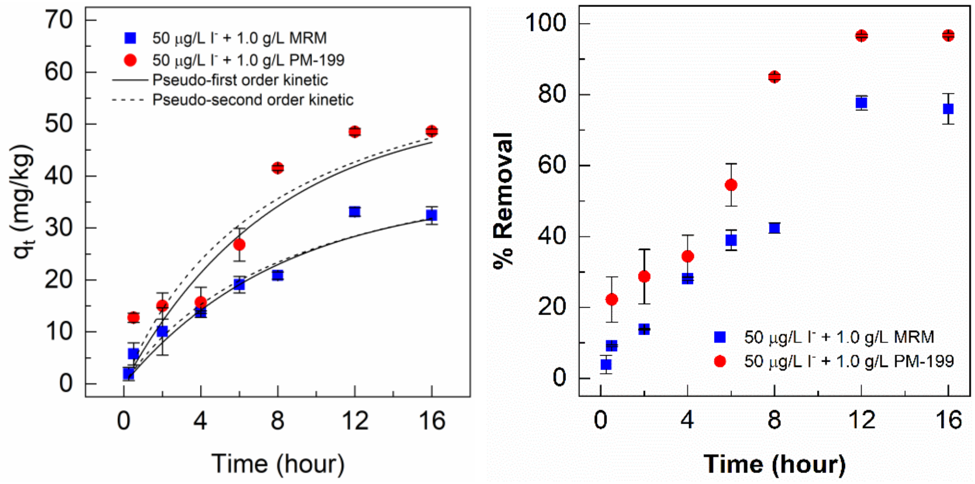

Figure 31. Pseudo-first and pseudo-second order fitting for adsorbed I$^-$ on organoclays PM-199 and MRM.

The pseudo-first-order kinetic model generally fits better to the initial stage of processes with rapid adsorption (Ho and McKay 1998), while the pseudo-second-order model considers adsorption behavior over longer contact times, consistent with chemisorption as the rate-controlling step (Bhattacharyya and Sharma 2004, Bulut, Özacar et al. 2008). Table 16 shows the kinetic parameters derived from pseudo-first-order and pseudo-second-order models. The adsorption of iodide by organoclays PM-199 and MRM follows the pseudo-first-order kinetic model with good linearity and agrees with the experimental and calculated q_e values. The pseudo-first-order rate constants (k_1) are calculated as 0.128±0.066 and 0.120±0.0382 hr^{-1}, for PM-199 and MRM, respectively. These results suggested that the adsorption of iodide on organoclays PM-199 and MRM is mainly physical sorption and likely occurs through the electrostatic and Van de Waals interactions of iodide and organoclays.

To further explore the sorption processes of iodide on the surface of organoclays, PM-199 and MRM, the kinetic data were also fitted into the Weber and Morris intraparticle diffusion model (Weber and Morris 1963). The intraparticle diffusion model expresses that the solute uptake (q_t)

has a linear correlation with respect to the square root of time as described by Equation 4.

$$q_t = k_d \times t^{1/2} + C \qquad \textbf{Equation 4}$$

Table 16. Parameters of the Pseudo-First-Order and Pseudo-Second-Order Models

		Pseudo 1st order			Pseudo 2nd order		
Organoclays	qe,expt. (mg/kg)	k_1 (hr^{-1})	q_{e1} (mg/kg)	R^2	k_2 (kg mg^{-1} hr^{-1})	q_{e2} (mg/kg)	R^2
PM-199	48.6±0.47	0.128±0.066	53.4±13.9	0.85	0.0018±0.0017	70.7±21.2	0.85
MRM	32.4±1.72	0.120±0.0382	37.2±6.11	0.95	0.0022±0.0013	50.0±9.76	0.95

Where Q_t is the amount of adsorbed iodide on the surface of organoclays PM-199 and MRM at a given time, k_d is the intraparticle diffusion rate constant, and C is the intercept which reflects the resistance in mass transfer at the boundary layer (Weber and Morris 1963, Gonzalez-Raymat, Anagnostopoulos et al. 2018). The kinetic data of 50, 100, and 150 µg/L iodide is used to fit this model to investigate the existence of different phases in the adsorption process. If the intercept $C = 0$, intraparticle diffusion is the rate-limiting step, whereas if the intercept $C \neq 0$, intraparticle is not the rate-controlling step, and film diffusion has a greater effect on the sorption process. A plot of Q_t vs $t^{1/2}$ (Figure 32) yielded a linear relationship which did not pass through the origin, $C \neq 0$, suggesting that intraparticle diffusion is involved in the overall data with the Weber-Morris intraparticle diffusion plot.

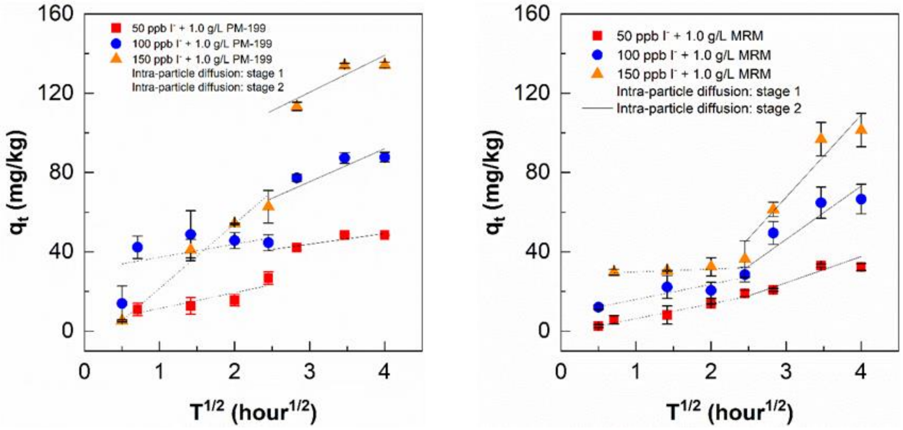

Figure 32. Intraparticle diffusion model of iodide on organoclays a) PM-199 and b) MRM.

Subtask 2.1: Conclusions

A sequential extraction of the SRS wetland's soil was conducted to understand the iodine bounded to different fractions of the soil samples. The sequential extraction of background topsoil collected from the F-Area seepage basin of the SRS showed that ~ 80% of iodine are bounded to the water-soluble fraction while ~ 20% of iodine are bounded to the organic fraction. In our iodine speciation study, ~ 40 – 60% of iodine extracted from thr water-soluble fraction is in the form of iodide and ~ 40% of iodine is in the form of iodate and/or organo-iodine. The pH does not influence the attenuation and release of ^{129}I from the wetland soils at different depth intervals. The organoclays

PM-199 and MRM were investigated as a potential remediation amendment for ^{129}I. Iodide was effectively separated from aqueous solution and the fast removal of it is mostly driven by the strong adsorption onto the organoclays showing high removal capacity for ^{129}I at the wetland's ambient conditions. The results of the study suggested that the organoclays could be used to facilitate iodine species adsorption to control the mobility of iodine species in the Fourmile Branch wetlands. Investigations of adsorption kinetics suggests that the adsorption mainly occurs through electrostatic interactions.

Subtask 2.1: References

Bhattacharyya, K. G. and A. Sharma (2004). "Azadirachta indica leaf powder as an effective biosorbent for dyes: a case study with aqueous Congo Red solutions." Journal of Environmental Management 71(3): 217-229.

Bulut, E., M. Özacar and İ. A. Şengil (2008). "Equilibrium and kinetic data and process design for adsorption of Congo Red onto bentonite." Journal of Hazardous Materials 154(1): 613-622.

Cardis, E., M. Vrijheid, M. Blettner, E. Gilbert, M. Hakama, C. Hill, G. Howe, J. Kaldor, C. R. Muirhead, M. Schubauer-Berigan, T. Yoshimura, F. Bermann, G. Cowper, J. Fix, C. Hacker, B. Heinmiller, M. Marshall, I. Thierry-Chef, D. Utterback, Y.-O. Ahn, E. Amoros, P. Ashmore, A. Auvinen, J.-M. Bae, J. B. Solano, A. Biau, E. Combalot, P. Deboodt, A. D. Sacristan, M. Eklof, H. Engels, G. Engholm, G. Gulis, R. Habib, K. Holan, H. Hyvonen, A. Kerekes, J. Kurtinaitis, H. Malker, M. Martuzzi, A. Mastauskas, A. Monnet, M. Moser, M. S. Pearce, D. B. Richardson, F. Rodriguez-Artalejo, A. Rogel, H. Tardy, M. Telle-Lamberton, I. Turai, M. Usel and K. Veress (2005). "Risk of cancer after low doses of ionising radiation: retrospective cohort study in 15 countries." BMJ 331(7508): 77.

Choung, S., M. Kim, J.-S. Yang, M.-G. Kim and W. Um (2014). "Effects of Radiation and Temperature on Iodide Sorption by Surfactant-Modified Bentonite." Environmental Science & Technology 48(16): 9684-9691.

Davis, S., K. J. Kopecky, T. E. Hamilton, L. Onstad, Hanford Thyroid Disease Study Team and the (2004). "Thyroid Neoplasia, Autoimmune Thyroiditis, and Hypothyroidism in Persons Exposed to Iodine 131 From the Hanford Nuclear Site." JAMA 292(21): 2600-2613.

Emerson, H. P., C. Xu, Y.-F. Ho, S. Zhang, K. A. Schwehr, M. Lilley, D. I. Kaplan, P. H. Santschi and B. A. Powell (2014). "Geochemical controls of iodine uptake and transport in Savannah River Site subsurface sediments." Applied Geochemistry 45: 105-113.

Gonzalez-Raymat, H., V. Anagnostopoulos, M. Denham, Y. Cai and Y. P. Katsenovich (2018). "Unrefined humic substances as a potential low-cost amendment for the management of acidic groundwater contamination." Journal of Environmental Management 212: 210-218.

Ho, Y. S. and G. McKay (1998). "A Comparison of Chemisorption Kinetic Models Applied to Pollutant Removal on Various Sorbents." Process Safety and Environmental Protection 76(4): 332-340.

Kaplan, D. I., K. A. Roberts, K. A. Schwehr, M. S. Lilley, R. Brinkmeyer, M. E. Denham, D. DiPrete, H.-P. Li, B. A. Powell, C. Xu, C. M. Yeager, S. Zhang and P. H. Santschi (2011). "Evaluation of a Radioiodine Plume Increasing in Concentration at the Savannah River Site." Environmental Science & Technology 45(2): 489-495.

Kaplan, D. I., C. Xu, D. Li, P. Lin, W. Xing, R. Nichols, K. Schwehr and P. H. Santschi (2019). "Iodine speciation in cementitious environments." Applied Geochemistry 103: 15-22.

Kaplan, D. I., S. Zhang, K. A. Roberts, K. Schwehr, C. Xu, D. Creeley, Y.-F. Ho, H.-P. Li, C. M. Yeager and P. H. Santschi (2014). "Radioiodine concentrated in a wetland." Journal of Environmental Radioactivity 131: 57-61.

Killian, T., N. Kolb, P. Corbo and I. Marine (1987). "Environmental information document F-area seepage basins." EI du Pont de Nemours and Company, Savannah River Laboratory, Aiken, SC.

Köhler, F., B. Riebe, A. C. Scheinost, C. König, A. Hölzer and C. Walther (2019). "Sorption of iodine in soils: insight from selective sequential extractions and X-ray absorption spectroscopy." Environmental Science and Pollution Research 26(23): 23850-23860.

Li, D., C. Xu, C. M. Yeager, P. Lin, W. Xing, K. A. Schwehr, N. Chen, Z. Arthur, D. I. Kaplan and P. H. Santschi (2019). "Molecular Interaction of Aqueous Iodine Species with Humic Acid Studied by I and C K-Edge X-ray Absorption Spectroscopy." Environmental Science & Technology 53(21): 12416-12424.

Neeway, J. J., D. I. Kaplan, C. E. Bagwell, M. L. Rockhold, J. E. Szecsody, M. J. Truex and N. P. Qafoku (2019). "A review of the behavior of radioiodine in the subsurface at two DOE sites." Science of The Total Environment 691: 466-475.

Otosaka, S., K. A. Schwehr, D. I. Kaplan, K. A. Roberts, S. Zhang, C. Xu, H.-P. Li, Y.-F. Ho, R. Brinkmeyer, C. M. Yeager and P. H. Santschi (2011). "Factors controlling mobility of 127I and 129I species in an acidic groundwater plume at the Savannah River Site." Science of The Total Environment 409(19): 3857-3865.

Schwehr, K. A., P. H. Santschi, D. I. Kaplan, C. M. Yeager and R. Brinkmeyer (2009). "Organo-Iodine Formation in Soils and Aquifer Sediments at Ambient Concentrations." Environmental Science & Technology 43(19): 7258-7264.

Stone, M. B., J. B. Stanford, J. L. Lyon, J. A. VanDerslice and S. C. Alder (2013). "Childhood Thyroid Radioiodine Exposure and Subsequent Infertility in the Intermountain Fallout Cohort." Environmental Health Perspectives 121(1): 79-84.

Weber, W. J. and J. C. Morris (1963). "Kinetics of Adsorption on Carbon from Solution." Journal of the Sanitary Engineering Division 89(2): 31-59.

Xu, C., S. Zhang, Y.-F. Ho, E. J. Miller, K. A. Roberts, H.-P. Li, K. A. Schwehr, S. Otosaka, D. I. Kaplan, R. Brinkmeyer, C. M. Yeager and P. H. Santschi (2011). "Is soil natural organic matter a sink or source for mobile radioiodine (129I) at the Savannah River Site?" Geochimica et Cosmochimica Acta 75(19): 5716-5735.

Zhang, S., Y.-F. Ho, D. Creeley, K. A. Roberts, C. Xu, H.-P. Li, K. A. Schwehr, D. I. Kaplan, C. M. Yeager and P. H. Santschi (2014). "Temporal Variation of Iodine Concentration and Speciation (127I and 129I) in Wetland Groundwater from the Savannah River Site, USA." Environmental Science & Technology 48(19): 11218-11226.

Subtask 2.2: Humic Acid Batch Sorption Experiments with SRS Soil

Subtask 2.2: Introduction

Savannah River Site (SRS) is a 310 square mile area located in west central South Carolina near the boundary of Georgia that was developed during the middle of the 1950's for use in the production of materials such as tritium, plutonium, and special nuclear materials for national defense, medicine, and space programs. During the Cold War, from 1953 to 1988, SRS produced a large amount of radioactive and hazardous acidic waste from the production of plutonium and irradiated fuel (Evans, et. al., 1992). The F-Area Seepage Basins received approximately 1.8 billion gallons of low level acidic waste solutions that contained nitrate, metals, and several radionuclides. At that time, it was believed that most of the radionuclides present in the waste solution would bind to the soil, precluding the migration of the radionuclides. Some of these contaminants including tritium, uranium isotopes, strontium-90, and iodine-129, over a period, were able to pass through the soils at the bottom of the basins, through the vadose zone and into the saturated zone. Once in the groundwater, these contaminants migrated downstream and resurfaced at seeps in wetland areas associated with Fourmile Branch. Specifically, Fourmile Branch and its associated wetlands have been impacted for more than thirty years by the outcropping of contaminated groundwater coming from the F-Area Seepage Basins. The groundwater remains acidic with uranium concentrations surpassing the Environmental Protection Agency (EPA) maximum contaminant levels (Dong et. al., 2012). In an effort to remove the contaminants from the groundwater, pump-and-treat and re-inject systems were implemented in 1997. Downgradient contaminated groundwater was pumped up to a water treatment facility, treated to remove metals (through osmosis, precipitation/flocculation, and ion exchange), and then re-injected upgradient within the aquifer. The pump-and-treat water treatment unit eventually became less effective generating large amounts of radioactive waste. The maintenance of the pump-and-treat water treatment unit was very expensive, and this prompted the research for new remedial alternatives. In 2004, the pump-and treat system was replaced by a funnel and gate system in order to create a treatment zone via injection of a solution mixture composed of two components, sodium hydroxide and carbonate. The injections were done directly into the gates of the F-Area groundwater to raise pH levels. The purpose of the treatment zone was to reverse the acidic nature of the contaminated sediments, thereby producing a more negative net charge on the surface of sediment particles and enhancing the adsorption of cationic contaminants. This amplified the adsorption of cationic contaminants on the sediment and resulted in the decrease of Sr-90 and U-238 concentrations but had no effect on the treatment of iodine. To maintain the pH neutral within the treatment zone, systemic injections were required. Carbonate forms strong complexes with uranium and could remobilize uranium that was already adsorbed within the treatment zone (Gudavalli et. al., 2013).

Humic substances (HS) are major components of soil organic matter, which are polyfunctional organic macromolecules that are formed from the decomposition of biomass or dead organic matter (Trevisan, et. al., 2010). Humic substances can be divided into three main fractions: humin, which is insoluble at all pHs; humic acid (HA), soluble at pHs greater than 3.5; and fulvic acids, which are soluble at all pHs (Choppin et. al., 1992). Humic acid is an important ion exchange and metal complexing ligand with a high complexation capacity, allowing it to chemically bind to metals and influence their migration behavior (Davis et. al., 2002). Previous studies suggest that the sorption of U(VI) in the presence of humic acid is a complex process (Perminova et. al., 2002). Ivanov et al (2012) studied U(VI) sorption onto bentonite with and without humic acid and proved enhanced uranium sorption at pHs lower than 3.8, while it was reduced at pHs above 3.8. In another study, U(VI) sorption proved to be influenced by pH, the U(VI) concentration, humic acid, and inorganic carbon species (Krepelova et al., 2007).

Chemically modified humate materials, commercially known as KW-15 and KW-30, are being tested for its use in remediation techniques to reduce the mobility of uranium in the subsurface at SRS. This project focuses on studying the characterization of humate materail and the sorption of uranium in the presence of humate onto SRS sediments, with parameters set to evaluate the effect of pH, time, and concentrations of U and HA. This study aims to determine if humic substances containing humic/fulvic acids of different molecular weights can be used to control uranium mobility and to understand the different interactions and mechanisms occurring in the presence of the modified humic acid. These interactions affect the adsorption of uranium onto the sediments that impacts U(VI) mobility in SRS groundwater. This study evaluates if humic substances could be used for in-situ remediation of uranium in acidic environments and determines the optimal conditions for U(VI) removal from the aqueous phase.

This research also suggests if modified humic substances can be used as potential amendments at other DOE sites, where soil and groundwater conditions are less acidic compared to SRS.

Subtask 2.2: Objectives

The objective of this research is to investigate the sorption behavior of humic substances via batch experiments and evaluate the effect of sorbed humic (KW-30) substances on uranium sorption to support groundwater remediation strategies. The outcome of these studies will help to determine approaches to deploy humate technology under varying site-specific conditions.

Subtask 2.2: Methodology

Materials:

This study utilized sediment samples that were collected from the F-Area at SRS (FAW1 70-90 ft) and sieved through a 2mm sieve. The fraction ≤ 2 mm was used in the experiments. This sediment was chosen due to its comparability to the soil composition in the uranium-contaminated aquifer layer. For U(VI), a commercial 1,000 ppm uranyl stock solution in 2% nitric acid was used. A humate stock solutions (KW-30) consisting of 1,000 mg in 1,000 mL of deionized water (DIW) was prepared for use in the experiments. The pH of the samples was adjusted using 0.1 M HCL or 0.1 M NaOH.

Experimental Procedures:

Humate Sorption

For sorption experiments, dried SRS sediment (200 milligrams) was mixed with 20 mL of humic acid (KW-30) at a concentration of 50 mg/L. The samples were adjusted to pH 4.0 using 0.1 M HCl and 0.1 M NaOH before and during the sorption period. The samples were placed on the platform shaker at 100 rpm for 5 days to reach equilibrium. Then, the samples were centrifuged at 2,700 rpm for 30 minutes to separate the solid from the aqueous phase. The supernatants were transferred to clean centrifuge tubes for humic acid measurement by a UV-Vis spectrophotometer.

Uranium Sorption isotherms

Sediment coated with humic acid was then contacted with U(VI) solution at pH 4. Similar to the sorption of HA step, the pH of the samples was adjusted to pH 4 daily for 7 days. After 7 days, samples were centrifuged for 30 minutes at 2700 rpm, supernatant was carefully removed, and unfiltered samples as well as samples filtered through 0.45 µm filters were analyzed via ICP-MS.

Subtask 2.2: Results and Discussion

Sorption of KW-30 and Uranium

Figure 33 shows the sorption of humate (mg/kg) in each sample at pH 4. The KW-30 amended sediment samples were then introduced with fresh DIW spiked with a range of U(VI) concentrations (0.025, 0.05, 0.1, 0.25, 0.5, 1 ppm). The samples were pH adjusted to pH 4 and placed on the platform shaker for 7 days, then centrifuged at 2,700 rpm for 30 minutes. The supernatant was removed and analyzed on the UV-Vis for humate concentrations to estimate the amount of humate desorbed during the uranium sorption process. Figure 34 displays the concentration of humate remaining on the sediment when spiked with U(VI). The trend is similar to the sorption of humate without the presence of U(VI).

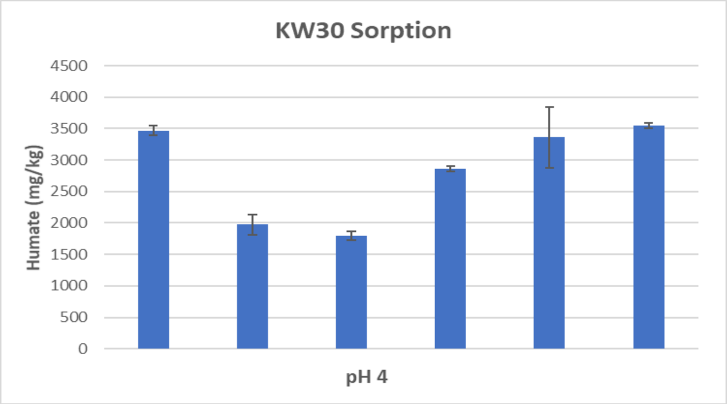

Figure 33. KW30 humate sorption onto SRS sediments.

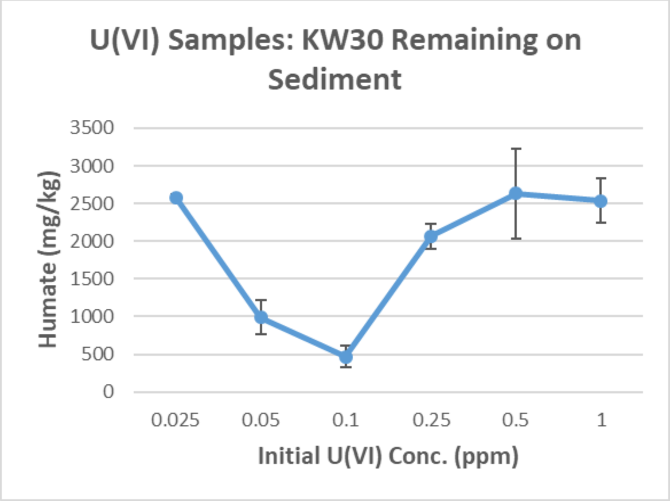

Figure 34. Humate remaining on SRS sediment in the presence of U(VI).

A new set of samples to study the sorption of uranium on humate (KW-30) coated sediments were prepared. As shown in Figure 35, inconsistent results for Samples 1 through 3 were possibly due to human error. These samples are excluded in the second part of the rest of the sample (4-12) and were used to study the sorption of uranium onto humate-coated sediments (~2300 mg/kg).

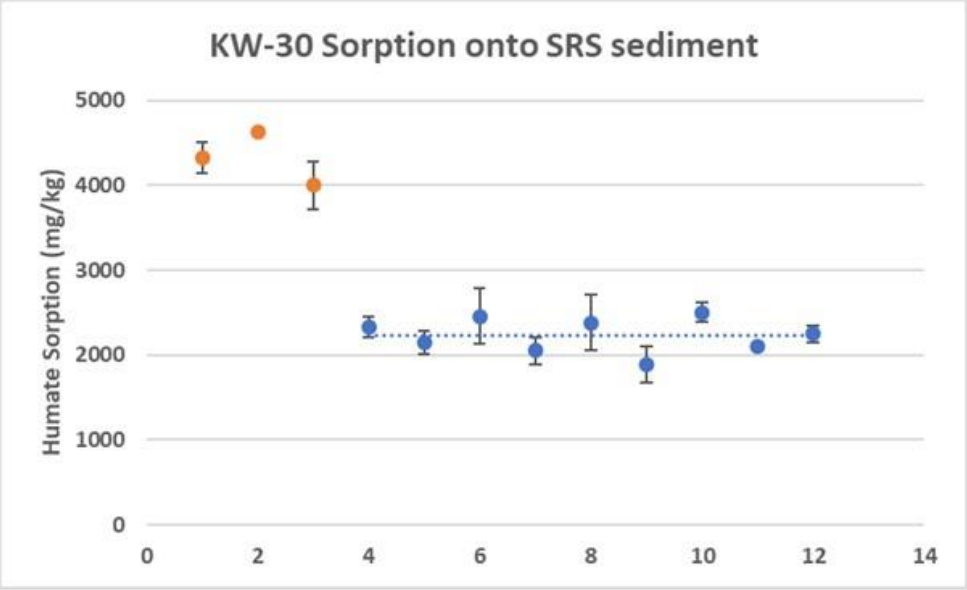

Figure 35. Sorption of KW-30 onto SRS sediment.

A volume of 20 mL of fresh uranium solution in the range of 200, 300, 400, 500, 600, 700, 800, 900, and 1000 ppb was introduced into vials containing sediment coated with KW-30. Figure 36Figure shows the removal of uranium with respect to equilibrium uranium concentrations was increased with an increase in uranium concentrations, however, the removal of uranium has not reached an equilibrium.

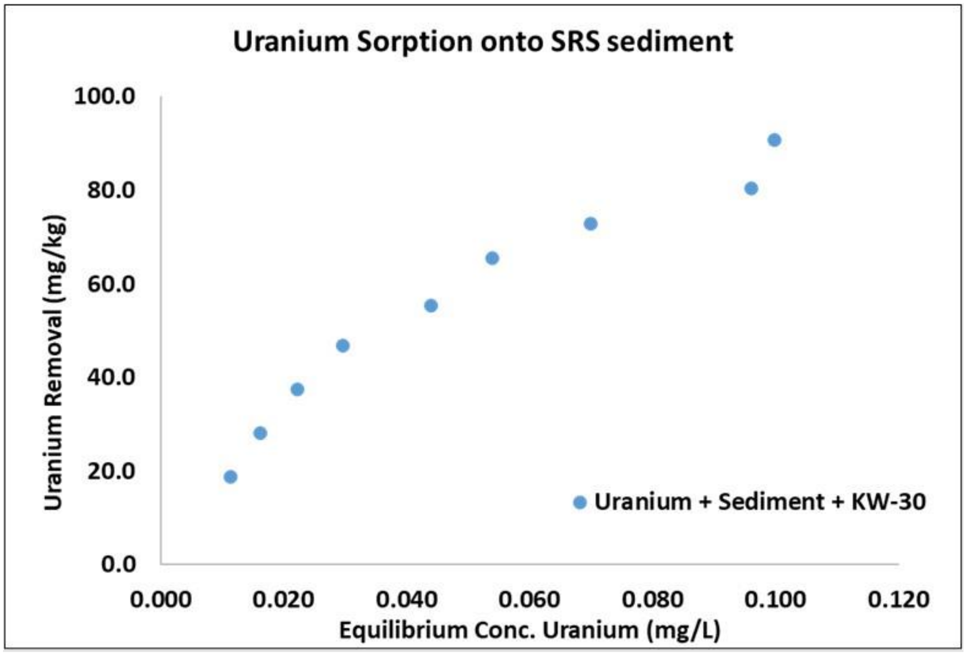

Figure 36. Sorption of uranium onto humate (KW-30)-coated SRS sediment.

Comparison of data obtained from humate-free, Huma-K and KW-15 uranium sorption data with KW-30 sorption data is shown in Figure 37. Sorption of uranium onto SRS sediment coated with KW-30 is much higher compared to mod-HA (KW-15) and Huma-K coated sediment. As evident in Figure 37, the sorption of uranium in the presence of KW-30 is yet to reach equilibrium. Experiments will be conducted to extend the range of initial uranium concentration up to 20 ppm. The current data shows sorption of uranium for the initial uranium concentration in the range of 200 ppb - 1 ppm.

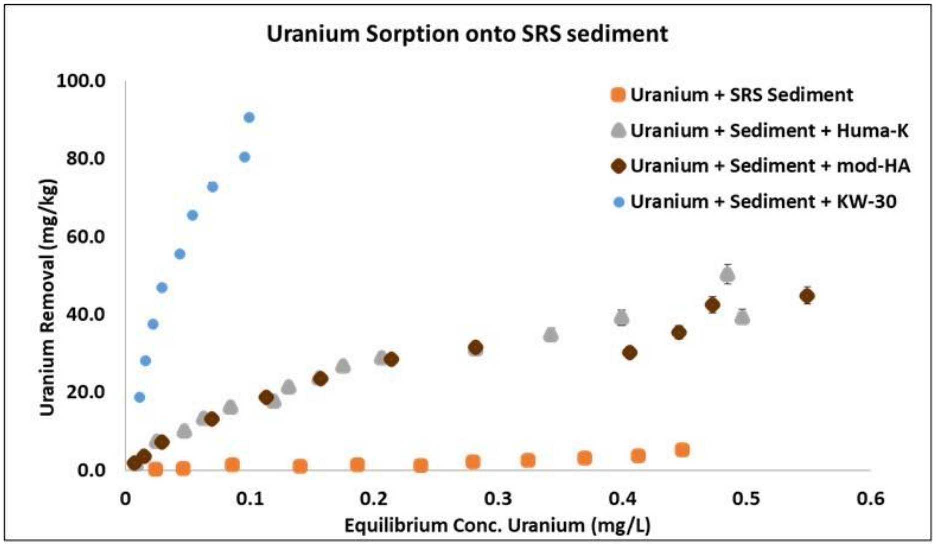

Figure 37. Sorption of uranium onto humate-coated sediment and plain sediment.

The sorption of humate KW-30 onto the SRS sediment is ~ 2,000 – 3,000 mg/kg as shown in Figure 38. Since the humate sorption onto SRS sediments was consistent with previous observations, the second step of the experiment was initiated. The solid samples were spiked with uranium stock solution to make 20, 40, 60, 80, and 100 ppm uranium samples and the ionic strength of the solution was kept at 0.01 M using perchlorate solution. The samples were adjusted to pH 4.0 using 1M NaOH and 1M HCl and placed on the platform shaker at 100 rpm for 7 days. Then, the samples were collected and analyzed using ICP-MS.

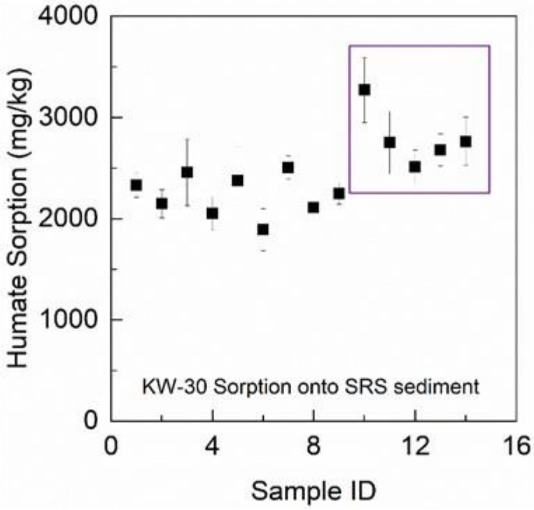

Figure 38. Sorption of 50 ppm humate KW-30 onto 10 g/L of SRS sediments.

The sorption of uranium onto KW-30-coated SRS sediments was shown in Figure 38. The collected data was combined with previous data for the isotherm fitting. The data was fitted to Langmuir and Freundlich isotherms. The Langmuir isotherm assumes that monolayer adsorption occurs on homogeneous adsorbent surface and there is no interaction between the adsorbate molecules (Wang and Wang 2018). The Langmuir adsorption isotherm is represented below in Equation (1),

$$Q_e = \frac{Q_m K_L C_e}{1 + K_L C_e} \tag{1}$$

where Q_m (mg/g) is the maximum adsorption capacity to form a complete monolayer on the surface of adsorbate, and K_L (L/mg) is the Langmuir constant.

The Freundlich isotherm, on the other hand, describes the heterogeneity of the adsorbent surface with non-uniform distribution of adsorption heat and affinities as well as the formation of a multilayer during the adsorption process (Wang and Wang 2018). The mathematical expression of the Freundlich isotherm is represented below, Equation (2),

$$Q_e = K_F C_e^{1/n} \tag{2}$$

where K_F ((mg/g)(mg/L)$^{-1/n}$) is the Freundlich constant that represents the quantity of adsorbate adsorbed onto the adsorbent for a unit equilibrium concentration, and n is the dimensionless exponent of the Freundlich equation indicating how favorable the adsorption process is.

The observed data was fitted into both Langmuir and Freundlich isotherm models. Based on the statistical analysis of sum square means, the Langmuir isotherm model is a better fit to our observed data.

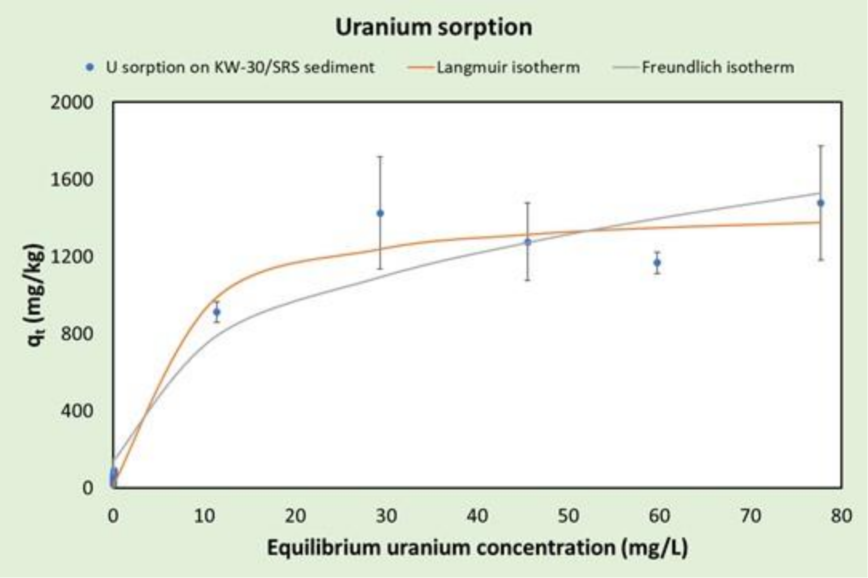

Figure 39. Sorption of 0-100 ppm uranium onto 10 g/L of 50 ppm humate KW-30-coated SRS sediments.

FIU focused on comparing the uranium removal by sediment coated with KW-30 with data previously obtained with KW-15 and plain sediment. Figure 40 shows the sorption of KW-15 and KW-30 onto SRS sediment. The average sorption for KW-15 was observed to be around 500 mg/kg, while KW-15 average sorption was 5 times that of KW-15 and was around 2,500 mg/kg.

Humate-coated SRS sediment and plain SRS sediments were used to study the sorption/removal of uranium isotherms. Figure 41 shows the removal of uranium with and without humate coated SRS sediment. Figure 41a shows the removal of uranium for samples with an initial uranium concentration up to 1.0 ppm, while the uranium removal for plain sediment and sediment coated with KW-15 appears to reach equilibrium. Uranium removal in the case of sediment coated with KW-30 still appears to not have reached equilibrium. The isotherm experiment was extended to include an initial uranium concentration up to 100 ppm, as seen in Figure 41b. Removal of uranium with KW-30-coated SRS sediment reached equilibrium. Figure 42 shows the log uranium removal as the removal of uranium at high initial uranium concentration overshadows the removal at lower concentrations.

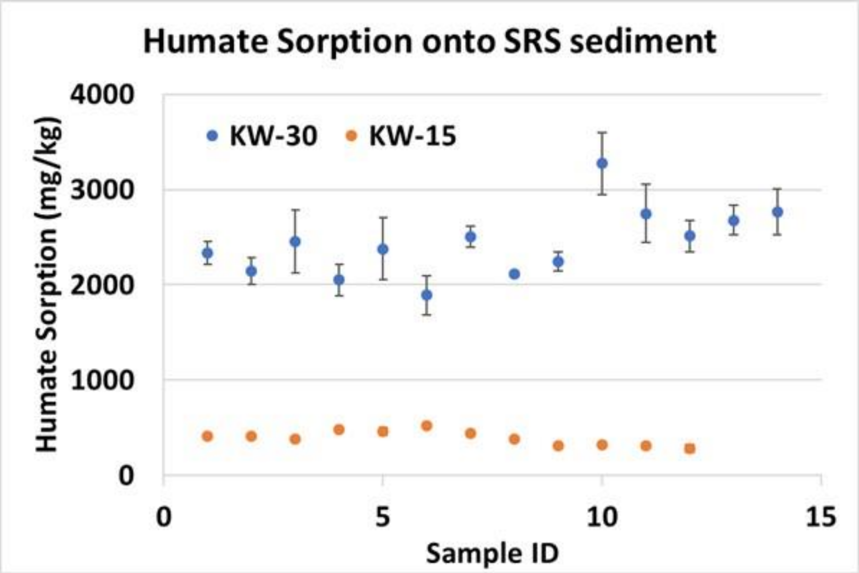

Figure 40. Sorption of humate material onto SRS sediment.

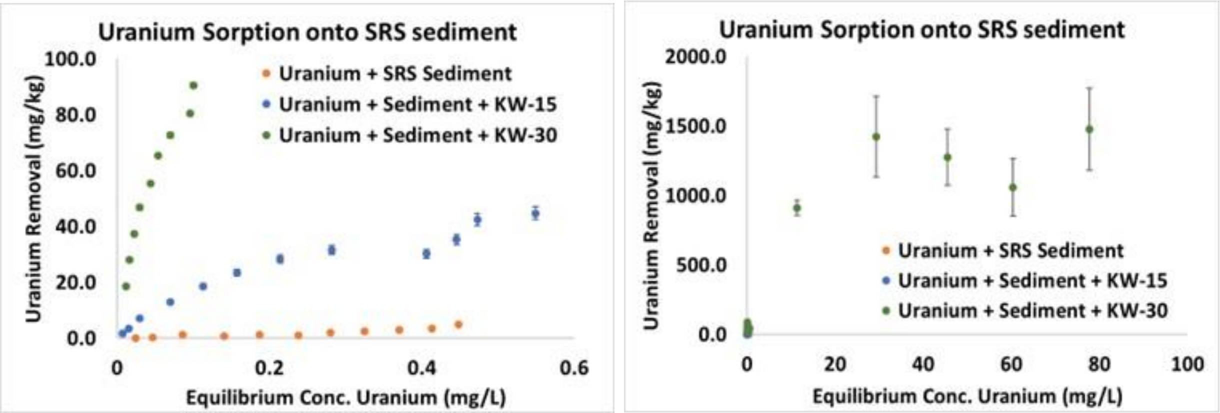

Figure 41. Removal of uranium with and without humate-coated SRS sediment: 0-1ppm U (left), 0-100 ppm U (right).

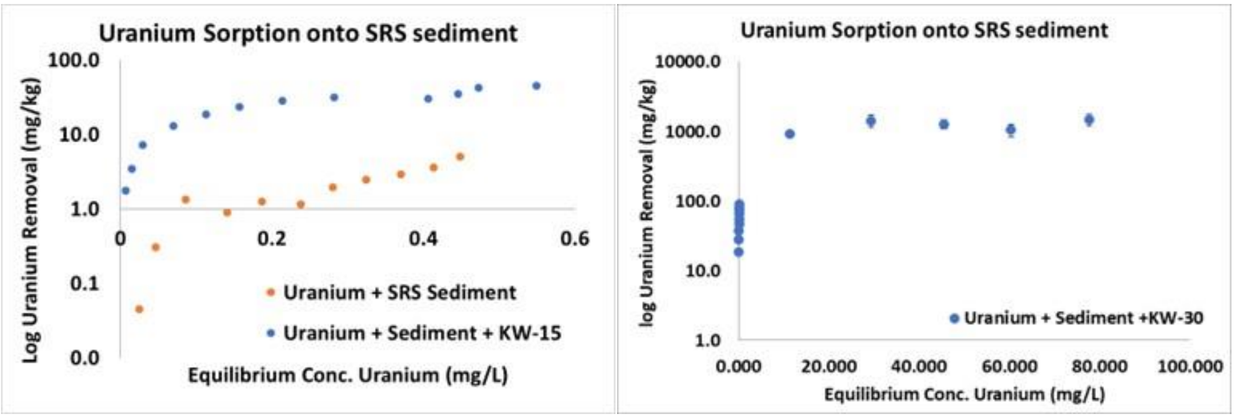

Figure 42. Log Uranium removal with and without humate-coated SRS sediment: 0-1ppm U (left), 0-100 ppm U (right). Table 17 shows the summary of the data. KW-30 sorption increased 5 times compared to KW-15, while the uranium removal increased 30 times for KW-30-coated sediment compared to KW-15-coated sediment, the overall uranium removal increased 300 times for KW-30 compared to plain SRS sediment.

Table 17. Comparison of Sorption of Humate Material and Uranium Removal

	Average Humate Sorption (mg/kg)	Average U Removal (mg/kg)	Max U Removal (mg/kg)
Sediment	NA	1.9	5.00
Sediment + KW-15	393	24	44.82
Sediment + KW-30	2435	474	1478

Subtask 2.2: Conclusions

KW-30 is able to sorb more on the sediment compared to KW-15 and other humate materials tested. KW-30 is also shown to improve uranium removal compared to plain sediment and KW-15. Additional experiments are needed to study the influence other contaminants have on KW-30 sorption and uranium removal.

Subtask 2.2: References

Choppin, G.R., 1992. The role of natural organics in radionuclide migration in natural aquifer systems. *Radiochim. Acta* 58/59, 113.

Davis. J.A., Adsorption of natural dissolved organic matter at the oxide/water interface, 1982, 2002. Geochim. Cosmochim. Acta 46, 2381-2393.

Dong, W., Tokuanga, T. K., Davis, J. A., Wan, J., (2012). Uranium(VI) Adsorption and Surface Complexation Modeling onto Background Sediments from the F-Area Savannah River Site. Environ. Sci. Technol. 46, 1565-1571.

Evans, A.G., Bauer, L.R., Haselow, J.S., Hayes, D.W., Martin, H.L., McDowell, W.L., Pickett, J.B., 1992. Uranium in the Savannah River Site environment. Westinghouse Savannah River

Co., Aiken, SC (United States), p. 95.

Gonzalez-Raymat, H., Anagnostopoulos, V.; Denham, M.; Cai, Y.; Katsenovich, Y. P., Unrefined humic substances as a potential low-cost amendment for the management of acidic groundwater contamination. Journal of Environmental Management 2018, 212, 210-218.

Gudavalli, R., Katsenovich, Y., Wellman, D., Idarraga, M., Lagos, L., Tansel, B., 2013. Comparison of the kinetic rate law parameters for the dissolution of natural and synthetic autunite in the presence of aqueous bicarbonate ions

Hay, M. B., Myneni, S. C. B., Structural environments of carboxyl groups in natural organic molecules from terrestrial systems. Part 1: Infrared spectroscopy. Geochimica et Cosmochimica Acta 2007, 71 (14), 3518-3532.

Ivanov, P., Griffiths, T., Bryan, N.D., Bozhikov, G. and S. Dmitriev, 2012. The effect of humic acid on uranyl sorption onto bentonite at trace uranium levels. *J. Environ. Monit.*, 14, 2968 - 2975.

Jiang, W., Cai, Q., Xu, W., Yang, M., Cai, Y., Dionysiou, D. D., O’Shea, K. E., Cr (VI) adsorption and reduction by humic acid coated on magnetite. Environmental science & technology 2014, 48 (14), 8078-8085.

Kimmig, S. R., C. Thompson, S. Baum and C. F. Brown (2021). "Evaluation of iodine speciation and 129I/127I ratios at low concentrations in environmental samples using IC-ICP-MS." Journal of Radioanalytical and Nuclear Chemistry 327(2): 929-937.

Köhler, F., B. Riebe, A. C. Scheinost, C. König, A. Hölzer and C. Walther (2019). "Sorption of iodine in soils: insight from selective sequential extractions and X-ray absorption spectroscopy." Environmental Science and Pollution Research 26(23): 23850-23860.

Krepelova. A., 2007. Influence of Humic Acid on the Sorption of Uranium(VI) and Americium(III) onto Kaolinite (Dissertation).

Largitte, L. and R. Pasquier (2016). "A review of the kinetics adsorption models and their application to the adsorption of lead by an activated carbon." Chemical Engineering Research and Design 109: 495-504.

Perminova, I.V, Hatfield, K., Hertkorn, N., 2002. Use of humic substances to remediate polluted environments: from theory to practice. In the proceedings of the NATO Advance Research Workshop, Springer, P.O Box 17, 3300 AA Dordrech, The Netherland.

Trevisan, Sara, et al. “Humic Substances Biological Activity at the Plant-Soil Interface.” *Plant Signaling & Behavior*, vol. 5, no. 6, 2010, pp. 635–643., doi:10.4161/psb.5.6.11211.

Wang, W. and J. Wang (2018). "Comparative evaluation of sorption kinetics and isotherms of pyrene onto microplastics." Chemosphere 193: 567-573.

Zhou, T., S. Huang, D. Niu, L. Su, G. Zhen and Y. Zhao (2018). "Efficient Separation of Water-Soluble Humic Acid Using (3-Aminopropyl)triethoxysilane (APTES) for Carbon Resource Recovery from Wastewater." ACS Sustainable Chemistry & Engineering 6(5): 5981-5989.

TASK 3: CONTAMINANT FATE AND TRANSPORT MODELING FOR THE SAVANNAH RIVER SITE

This task involves the development and application of integrated hydrological, hydraulic and contaminant transport models for studying the fate of priority pollutants in the stream systems at SRS. For Year 2, specific focus has been on contaminant transport modeling during extreme storm events with emphasis on interactions between solute and sediment transport in Tims Branch (Subtask 3.1). The aim is to examine the response of this stream to historical discharges and environmental management remediation actions and to provide a means of assessment, evaluation and post-closure long-term monitoring of water quality and environmental conditions following remedial activities. In addition, FIU began investigating the F-Area wetland hydrology to develop a detailed hydrological model to represent the flow of groundwater downslope of F-Area and its interaction with the seepage face and riparian zone adjacent to the braided Fourmile Branch river network (Subtask 3.2). Understanding the wetting and drying out of this seep line interface while interacting with the groundwater and developing a model will be critical and can ultimately help in understanding the flow and fate of contaminants migrating down-gradient towards the stream within the Fourmile Branch.

Subtask 3.1: Calibration of the Tims Branch Watershed Model and Scenario Analysis

Subask 3.1: Introduction

The Tims Branch ecosystem represents an important applied science opportunity as a result of significant past research by SREL and SRNL. Tims Branch has served as an ideal testbed for development of a flow and contaminant transport model of an SRS stream that was impacted by DOE operations for 50 years and which is now recovering. The Tims Branch model developed by FIU addresses the knowledge gaps related to the fate and transport of dissolved and sediment-bound contaminants at DOE EM sites during extreme hydrological events.

A MIKE SHE/MIKE 11 contaminant fate and transport model of the Tims Branch watershed was developed by FIU to better understand the impact of extreme atmospheric events on the remobilization, transport and redistribution of sediment-bound heavy metals and radionuclides such as uranium (U), tin (Sn) and nickel (Ni) in the Tims Branch watershed. Results from this study are key to evaluating the effectiveness of tin (II)-based mercury treatment of wetlands at the SRS site, and are also relevant to evaluating the potential of using this type of novel EM-developed remediation technology in other heavy metal- of radionuclide-contaminated stream systems at SRS to accelerate site closure.

For the Southeastern United States, climate change will result in wetter summers which will lead to increases in summer discharge, and possible increases in the frequency and magnitude of high-water events. This can occur via two distinguishable sources: (1) rain falling on already saturated soils in which soils cannot store the water, thus resulting in runoff; and (2) termed return flow which occurs if the rate of interflow entering a saturated area from the upslope exceeds the capacity for interflow to leave the area by flowing downhill through the soil (Cornell’s Soil and Water Lab, 2022). Such major storm events have been shown to have a strong impact on the runoff and sediment load observed inside the river network of Tims Branch watershed. More specifically for uranium, Batson et al., (1996) showed that during intense storm events, considerable amount of remobilization of sediment-associated uranium (U) from the contaminated floodplain into the Tims Branch stream occurs. This leads to much higher uranium concentrations in the river network compared to baseflow situations. As discharge-producing storm events are regularly observed in Tims Branch watershed (e.g. for the period 1985-1993 a total of 260 of these storms occurred), there is a need to gain an improved understanding on the fate and transport of historical contaminants under a variety of storm events and discharge scenarios. This will lead to an improved understanding on how heavy metal transport varies between stormflow and baseflow conditions. Therefore, the event-based MIKE SHE/MIKE 11 model previously developed in Year 1, during Year 2 was converted into a continuous model that allows for long-term simulations.

Knowledge acquired from this research can also support model development for other contaminated SRS stream systems such as Fourmile Branch where contaminants such as iodine-129 is of primary concern. This research will assist in developing cost-effective remediation plans integrated into the SRS Area Completion Project (ACP) and accelerate progress of the DOE EM environmental restoration mission.

Subtask 3.1: Objectives

The principal objective of this subtask is to develop and test a comprehensive transport model using available hydrological modeling software and geographical information systems (GIS) tools to examine the response of Tims Branch to historical discharges and environmental management remediation actions. FIU will use the calibrated model to study transport scenarios of heavy metal contaminants of concern under extreme hydrological conditions that provide information related to inter-compartmental transfers and the environmental conditions that result in mobilization of adsorbed heavy metals in sediment, and accumulation of priority contaminants of concern due to sedimentation.

Surface water contamination is a widespread problem across the DOE complex. Development of hydrological models can support DOE-EM’s long-term monitoring strategy by simulating the fate and transport of contaminants in impaired surface waters, paying particular attention to potential remobilization impacts as a result of climate change. Model development, however, can be a very cumbersome and time-consuming process, particularly when large-scale, site-specific information is required and the need is somewhat widespread at numerous DOE sites scattered across the US. FIU has therefore began developing scripts using ArcGIS and Python to automate and accelerate hydrological model development, emulating the process workflow used for developing the existing MIKE model of the Tims Branch watershed and Fourmile Branch Watershed (Subtask 3.2) at Savannah River Site. These scripts will fast-track the MIKE model development process for ANY basin of interest using publicly available information to enable the generation of a first version model as well as model results in a matter of days. Once this first model version has been developed and results have been evaluated, site specific information can subsequently be added to further enhance model performance. This process will lead to much faster model development, allowing FIU to provide DOE with complex-wide support as needed within a relatively short timeframe. The following section presents some of the initial steps performed during this performance period to automate the model generation process.

Subtask 3.1: Methodology

During FIU Year 2, FIU continued the execution of the final phase of the Tims Branch model development which involves model optimization to improve and verify the performance of the coupled hydrology and contaminant transport model. Sensitivity analysis, calibration and validation of the model as well as scenario analysis under extreme hydrological conditions that provide information related to intercompartmental transfers, stormflow impacts and downstream transport of priority contaminants of concern (e.g., uranium) was conducted. In FIU Year 1, the ECO Lab module was added to the MIKE 11 modeling framework. Initial results have shown that a parameterized ECO Lab module enables simulation of the historical uranium transport process in Tims Branch. The resuspension calibration parameters in ECO Lab was set based on the velocity profile obtained from the hydrodynamic module of the MIKE 11 modeling framework and the ECO Lab module was parameterized to simulate the contaminant transport process. For FIU Year 2, FIU focused on further optimization/calibration of the sediment transport process in ECO Lab for uranium based on the available field measurements for suspended sediment concentration. Specifically, FIU focused on a series of events observed in the 90’s for which both temporally varying flow and uranium concentrations were available. In FIU Year 2, FIU also worked on the migration of the data inputs from the Tims Branch model to an open source environment for easier integration with other DOE-EM modeling efforts.

Subtask 3.1: Results and Discussion

3.1.1. Hydrological modeling

During the first 6 months of FIU Year 2, the event-based calibrated hydrological-biogeochemical transport model of the Tims Branch watershed developed in MIKE SHE/MIKE 11 was converted to enable long-term simulations to support the SRS long-term monitoring strategy. The model currently takes about 7-10 years to spin-up and subsequent runoff simulations are heavily overestimated compared to in situ observations. Evaluations of model performance for multi-year simulations showed that the model overestimated discharge in the channel network of Tims Branch, which would lead to an overestimation of channel bed erosion and the transport of heavy metals by the model. In FIU Year 2 a number of analyses were performed to understand which model component resulted in the overestimation. The general water balance for Tims Branch watershed can be defined as:

$$dS = P - ET_A - Q_{river} - Q_{lat,gw} \qquad \text{(Eq. 3.1)}$$

where dS is the basin storage change, P the total amount of precipitation, ETA the total actual evapotranspiration rate, Qriver the total discharge through the river network at the basin outlet, and Qlat,gw the total lateral flow through the groundwater across the basin boundary. Note that all units are given in mm. It can be assumed that over long time periods, the storage change is negligible. Also, it is expected that little error exists in the precipitation used to force the model, as daily observations from an in-situ rain gauge were used to bias correct the hourly AORC forcing data. Therefore, to reduce the discharge simulations by the model, either actual evapotranspiration needs to be increased or lateral flow through the groundwater across the basin boundary needs to increase to close the water balance. Furthermore, the model’s ability to represent flow velocity variations was evaluated, as these are expected to play an important role in the transport and deposition of heavy metal particles.

As the land surface component of the previous version of the Tims Branch model predominantly used default parameters, the approach presented above was first used to generate automatic land surface parameters for MIKE SHE. To assess the potential of incorrect actual evapotranspiration estimates, daily simulated actual evapotranspiration amounts were compared with observations obtained from a database with nearby flux tower observations. Although the tower was not situated within Tims Branch, its nearby location (i.e., within a few kilometers) and similar land use characteristics made these observations useful for comparison.

Figure 43 shows the observed and simulated daily actual evapotranspiration rate as simulated for the period 2011-2013 using the updated vegetation parameter information. Generally, both model and observations show similar behavior with minimum values in winter well below 1 mm per day and maximum values in summer up to 5 mm. Some variations do occur although differences are small. A good model performance can also be observed from the KGE model statistic, where a value of 0.562 indicates reasonable model skill.

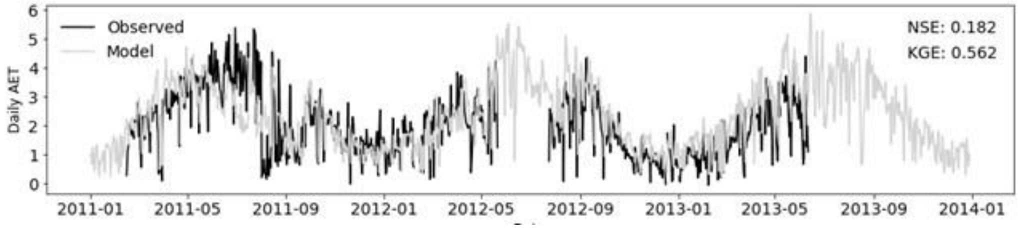

Figure 43. Daily actual evapotranspiration as observed from nearby fluxtower and simulated by MIKE SHE for Tims Branch watershed for the period 2011-2013. Top right shows the model performance as indicated by the Nash Sutcliffe and Kling Gupta efficiency.

In the scatterplot below (Figure 44), the same daily data is presented. Once again, it can be observed that both show a similar range of values with reasonable correction, r. It can also be observed from this figure that the model is slightly overestimating as compared to in situ observations (as indicated by α < 1).

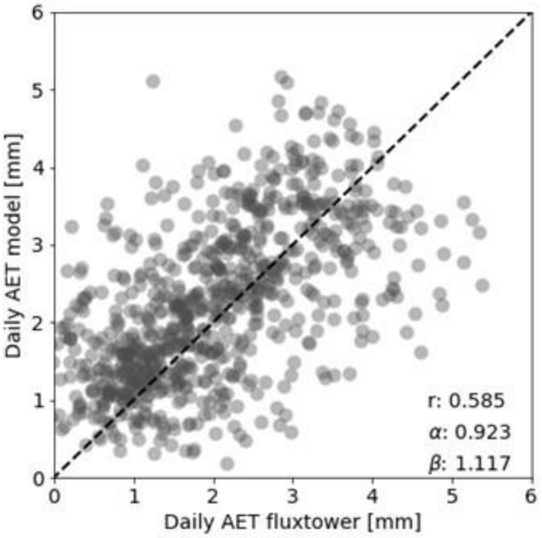

Figure 44. Comparison between observed and simulated daily actual evapotranspiration rate. Inset on bottom right shows correction, r, ratio of the mean α and ratio of the standard deviation, β.

Based on these results, it can be concluded that the model currently does not underestimate the actual evapotranspiration rate. As such, the hypothesis that an underestimation of the actual evapotranspiration would cause an overestimation of the simulated discharges is incorrect. In fact, the model does a reasonable job in simulating the observed daily actual evapotranspiration amounts. The figure below shows the various hydrological fluxes simulated for Tims Branch over the period 1982-2020. It can be observed that most of the precipitation leaves the catchment as actual evaporation and the flow through the boundary is limited (as expected). However, considerable variations in the yearly simulated discharge are observed. For the period 1998-2020, these long-term variations show good correlations with yearly changes in precipitation. However, for the increase in discharge during the first 10 years, they show no correlation with precipitation. To understand the increase in discharge during the initial 10-year period, one should focus on changes in the internal model states, as shown in the lower panel of Figure 45. This shows that during the initial 7-10 years a continuous positive change is observed, indicating rising groundwater levels. Once equilibrium is reached, the model simulated years with both positive and negative changes in internal model storage, as expected.

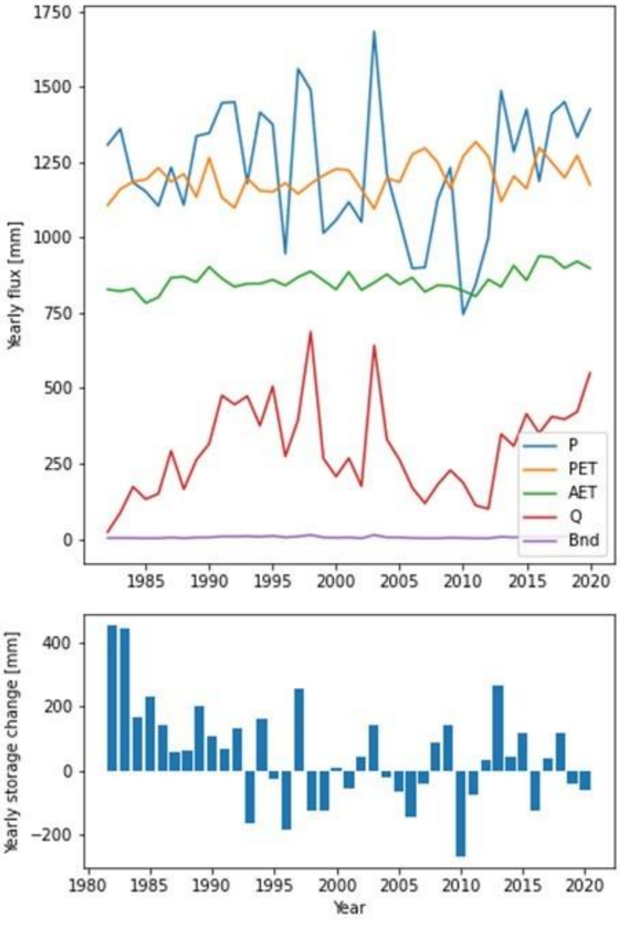

Figure 45. Upper panel: Yearly precipitation (P), potential evapotranspiration (PET), actual evapotranspiration (AET), discharge at the outlet (Q) and lateral unsaturated and saturated flow through the catchment boundary (Bnd); Lower panel: Yearly change in total saturated and unsaturated storage. All fluxes and states are presented in mm.

The amount of boundary flow simulated by the model is very small and close to zero on an annual basis. This is because the model currently assumes a zero-flow boundary for most of the watershed. Only for a small stretch close to the basin outlet some boundary flow occurs due to a constant head boundary condition. Literature review has revealed that considerable lateral flow occurs through the basin's boundary.

As a final component, the performance of the the MIKE SHE/MIKE 11 model to simulate the dynamics of the stream network within Tims Branch watershed was evaluated. More specifically, the ability of the model to represent flow velocity changes throughout the major channel network was assessed, as these changes will impact the erosion and deposition of suspended solids. A good understanding of this is necessary as this will enable the interpretation of the heavy metal simulations, which are currently being performed for uranium, tin and nickel. FIU's specific interest is to understand the role of various ponds (i.e., Steed Pond and the Beaver Ponds) and whether reduced velocities occur at these locations. Figure 46 shows the channel cross-section for various locations as implemented within MIKE 11. The top four locations up to Beaver Pond 1 show a broad network indicative of the braided riparian system, as observed between the confluence of the A-014 outflow with Tims Branch all the way down to Steed Pond. Such wider networks are expected to give rise to smaller flow velocities. Below Steed Pond the channel network is locally incised, increasing flow velocities. At Beaver Pond 3 (pink color) the river network widens, becoming more concise again lower down (gray), followed by a wider network between Beaver Ponds 4 and 5.

The MIKE SHE/MIKE 11 model was rerun for the period 1991-1993, focusing on the flow velocity variability. It should be noted that even though the model is not yet perfectly calibrated, results presented in our December report showed that for this period the MIKE runoff simulations correspond well with observed discharges.

In Figure 47 the simulated flow velocities and their temporal averages for different distances to the outlet are shown. From this figure, it is possible to observe that for the braided section between Beaver Pond 2 and Steed Pond, around Beaver Pond 3, and between Beaver Ponds 4 and 5, a reduction in flow velocities is indeed simulated. For the other sections of the channel network, flow velocities are considerably higher.

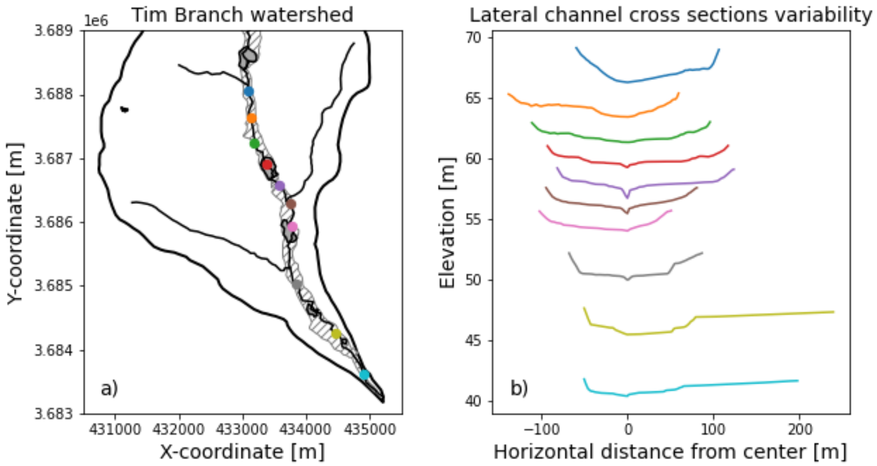

Figure 46. Panel a) shows the lower part of Tims Branch including the river network, various ponds and the riparian zone system. Panel b) shows the corresponding cross-section for each of the colored points in a), as used in MIKE 11.

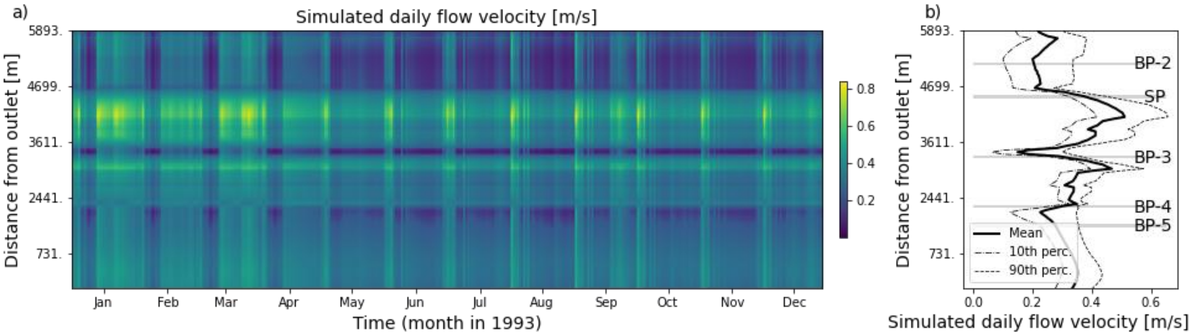

Figure 47. For the MIKE 11 simulation of the Year 1993, panel a) shows the temporal changes in simulated flow velocities for various distances from the outlet. In panel b) the average simulated flow velocity and the 10th and 90th percentile as a function of distance to the outlet are shown. Also presented in panel b) are the locations of Steed Pond and the various Beaver Ponds.

The above results reveal that in order to improve the performance of the MIKE SHE/MIKE 11 model to enable long-term simulations of hydrological flow and sediment transport, the groundwater component of the model needs to be altered to allow for lateral flow across the groundwater boundary. As such, there is a need to change the vertical aquifer system setup within the model. However, the long-term runtime makes it impossible to perform any type of recalibration within a reasonable amount of time. Therefore, during FIU Year 2 it was decided to redevelop the continuous MIKE SHE/MIKE 11 model. To enable this it was decided to develop an automated procedure that can subsequently be applied to other basins of interest (e.g. Fourmile Branch watershed in Subtask 3.2). To enable the generation of a continuous long-term model, the event-based MIKE SHE/MIKE 11 model previously developed for Tim Branch was converted from the original resolution of 50-m to 250-meter (250-m) resolution. A model grid resolution of 250-m is anticipated to lead to an increased run time performance, which will allow the recalibration of the model to improve its long-term performance. To generate these coarser resolution grids, FIU began developing a scripting approach using Python in combination with GIS, which would enable each of the steps to be repeated quickly within other basins (e.g., for Fourmile Branch in Task 3.2).

In GIS, a setup was generated to aggregate an originally 10-m resolution DEM to 250-m. Instead of taking the average per pixel, the minimum elevation of all 10-m pixels is taken. This was done to ensure that the flow direction at a 250-m resolution corresponds well to those obtained at a 10-m resolution (see Figure 49). The DEM .tif file and river network shapefile are subsequently processed by Python so that they can immediately be used within MIKE SHE. The left image of Figure 49 shows an example of this, where the derived elevation level at 250-m resolution as well as the river network at 10-m resolution are presented as shown in MIKE SHE.

After deriving the shape with the basin boundary, the river network, as well as a TIFF containing the DEM using GIS, a Jupyter notebook script in Python was developed to generate the various input arrays, parameter values and forcing components needed by MIKE (see Figure 48).

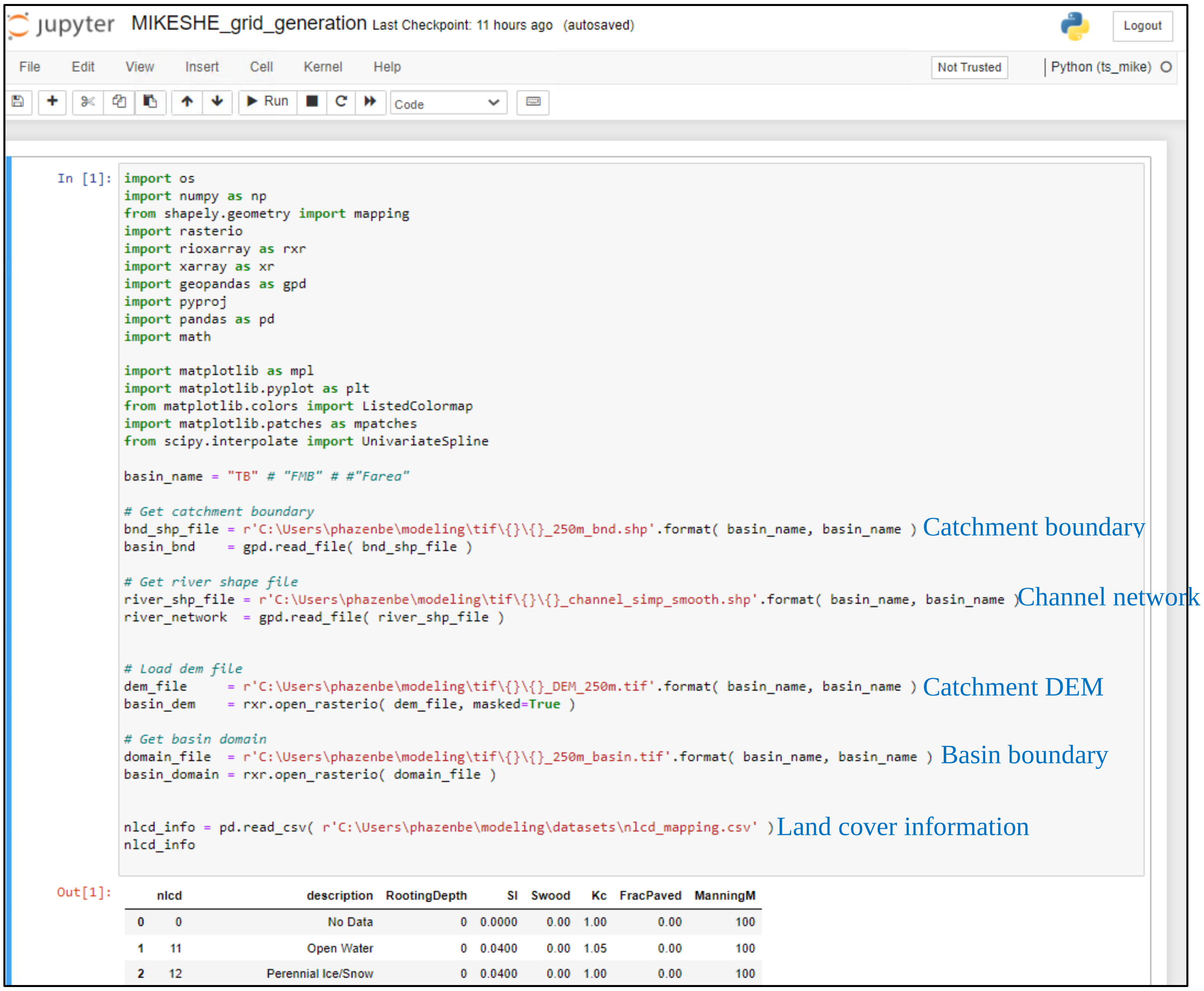

```
In [1]: import os
        import numpy as np
        from shapely.geometry import mapping
        import rasterio
        import rioxarray as rxr
        import xarray as xr
        import geopandas as gpd
        import pyproj
        import pandas as pd
        import math

        import matplotlib as mpl
        import matplotlib.pyplot as plt
        from matplotlib.colors import ListedColormap
        import matplotlib.patches as mpatches
        from scipy.interpolate import UnivariateSpline

        basin_name = "TB" # "FMB" # #"Farea"

        # Get catchment boundary
        bnd_shp_file = r'C:\Users\phazenbe\modeling\tif\{}\{}_250m_bnd.shp'.format( basin_name, basin_name )
        basin_bnd    = gpd.read_file( bnd_shp_file )

        # Get river shape file
        river_shp_file = r'C:\Users\phazenbe\modeling\tif\{}\{}_channel_simp_smooth.shp'.format( basin_name, basin_name )
        river_network  = gpd.read_file( river_shp_file )


        # Load dem file
        dem_file     = r'C:\Users\phazenbe\modeling\tif\{}\{}_DEM_250m.tif'.format( basin_name, basin_name )
        basin_dem    = rxr.open_rasterio( dem_file, masked=True )

        # Get basin domain
        domain_file  = r'C:\Users\phazenbe\modeling\tif\{}\{}_250m_basin.tif'.format( basin_name, basin_name )
        basin_domain = rxr.open_rasterio( domain_file )


        nlcd_info = pd.read_csv( r'C:\Users\phazenbe\modeling\datasets\nlcd_mapping.csv' )
        nlcd_info

Out[1]:
      nlcd         description  RootingDepth      SI  Swood    Kc  FracPaved  ManningM
   0     0             No Data             0  0.0000   0.00  1.00       0.00       100
   1    11          Open Water             0  0.0400   0.00  1.05       0.00       100
   2    12  Perennial Ice/Snow             0  0.0400   0.00  1.00       0.00       100
```

Figure 48. Starting point of Python Jupyter Notebook script that reads in various GIS files, which are subsequently used to produce a MIKE SHE/MIKE 11 model for the basin of interest.

The MIKE SHE/MIKE 11 model uses the DEM for model simulation. However, it can only interpret these files when stored in the.dfs2 format. Therefore, Python is used to convert the file into this format (see left panel of Figure 50).

The Python scripts use the DEM to subsequently obtain 1) long-term precipitation, potential evapotranspiration, and temperature information (as presented in the monthly report of December), 2) land use information (as shown during the monthly report of June), and 3) soil texture and van Genuchten parameter information (as shown during the monthly report of March). Furthermore, the river network information is used to set up the river network parameters as needed for MIKE 11 (see details below).

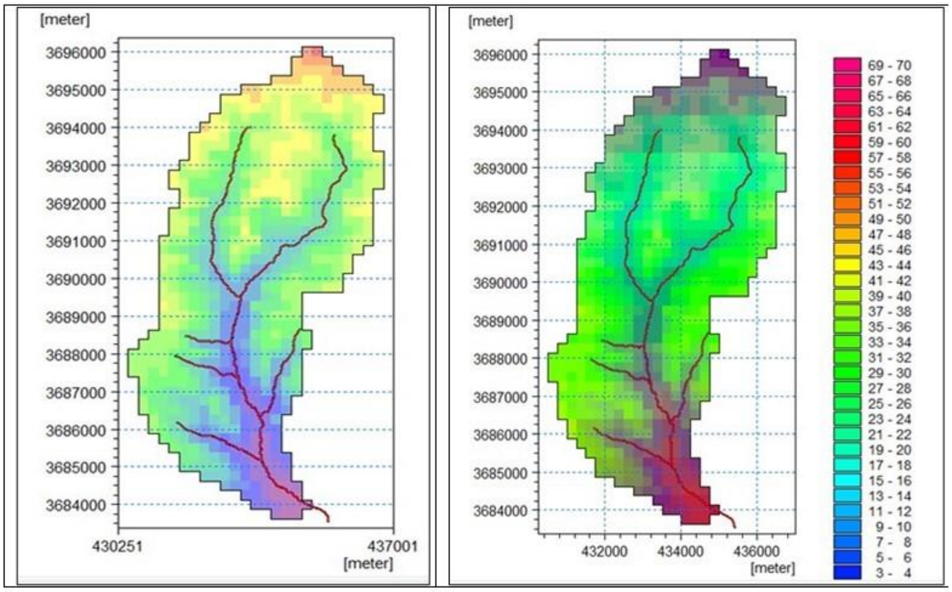

Figure 49. Left panel shows DEM at 250-m resolution and the location of the river network. For each 250-m grid pixel, the right image shows the corresponding soil texture location for which the van Genuchten parameters were derived.

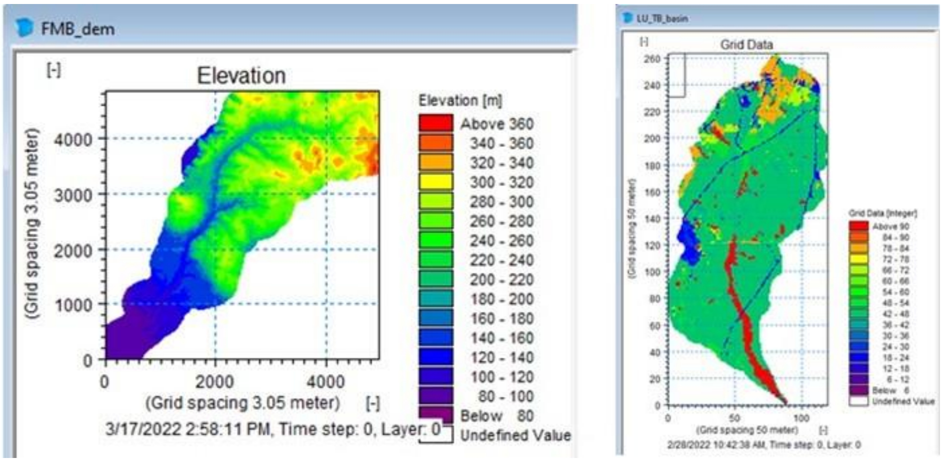

Figure 50. Left panel shows DEM for Fourmile Branch. Right panel show land use class information for Tims Branch. Both are generated in Python and stored in .dfs2 format interpretable by MIKE.

Generation of long-term atmospheric forcing - As sub-daily precipitation variability can have a considerable impact on the simulated runoff, it was decided to force the model with hourly precipitation, temperature and potential evapotranspiration data. For the first two model forcings, precipitation and temperature data available within the Analysis of Record for Calibration (AORC) was used. This long-term dataset was specifically created to contain continuous data to be used for model simulation and calibration, and covers the period 1979-2021 (Kitzmiller et al. 2018, AGU presentation). To ensure that AORC hourly precipitation data are representative for Tims Branch, the data was bias corrected using the daily in-situ observations. Given the uncertainty of what time daily rain gauge observations are recorded, Step 1 was to calculate and find the hourly timestep that maximizes the daily correlation between the locally observed data and daily AORC totals. Once the time shift has been identified on a correlogram, for Step 2, the ratio between the daily AORC data and rain gauge observation are calculated. Subsequently in Step 3, this daily ratio is used to bias correct the hourly AORC precipitation estimates. This ensures that the daily AORC precipitation totals are similar to the local daily rain gauge observations (Figure 51).

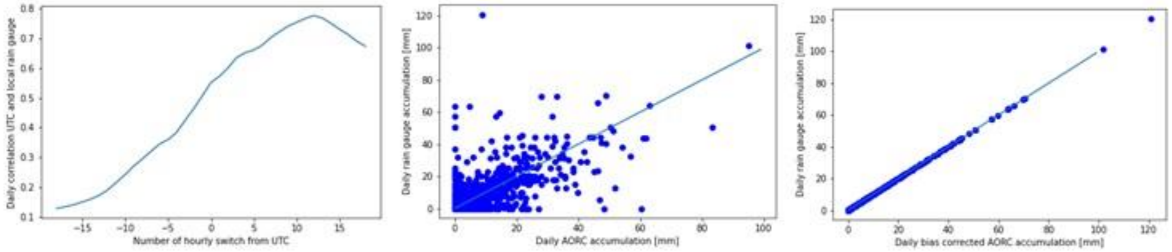

Figure 51. Focusing on period 1991-1993, left image shows the correlogram between daily AORC and local rain gauge observations where the hourly AORC data was shifted by various timesteps before aggregating to daily intervals. Middle image shows correspondence between daily AORC and rain gauge observations for hourly timesteps that maximizes correlation. Right image shows bias corrected AORC data to ensure that daily AORC totals correspond to rain gauge observations.

The AORC dataset also includes hourly temperature data which has been downscaled for Tims Branch. The MIKE model also uses hourly potential evapotranspiration as model forcing. It was decided to use the global hourly PET database as estimated from historical ERA5-Land data, recently developed by Singer et al. 2021 (Nature, Scientific Data). These global data with a grid resolution of 0.1 x 0.1 degrees were downloaded for the period 1982-2020 and the hourly average values for Tims Branch were extracted.

To automize the generation of model forcing, using the basin shapefile as input, a Python script was written to generate the hourly precipitation, temperature and potential evapotranspiration data using the procedure described above. Final results are being stored as (.dfs0) files to allow for immediate adoption by the MIKE model. An example of these results for the period June 1991 until October 1993 is shown below in Figure 52.

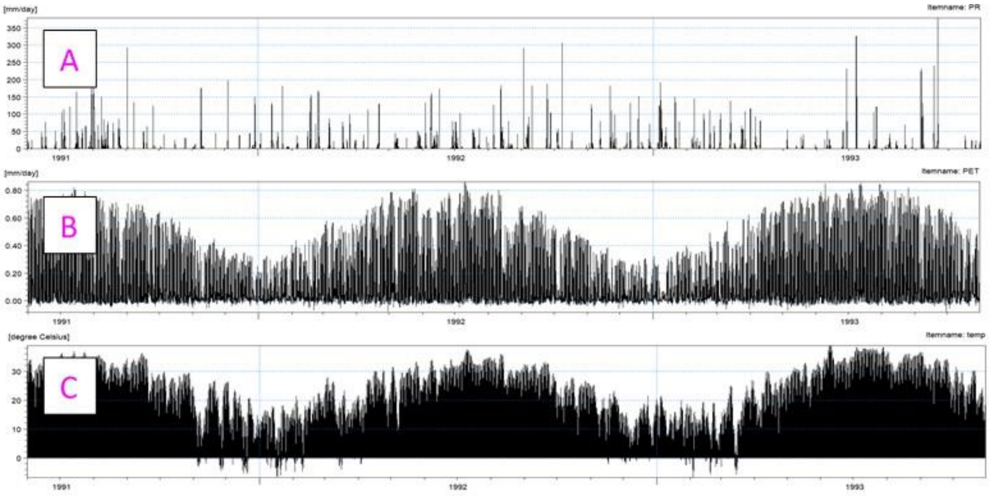

Figure 52. Example of generated hourly precipitation (A), temperature (B) and potential evapotranspiration (C) as available within the MIKE model.

Generation of land surface information - An important component within MIKE SHE is the simulation of actual evapotranspiration, for which the model makes use of gridded land use information with model parameters representative per land use class. In Python the basin shapefile is used to clip the National Land Cover Database (NLCD) grid, which contains land cover information at a resolution of 30 m, to the domain of interest and stored in .dfs2 format (see right panel Figure 53). Also, long-term Modis Leaf Area Index (LAI) observations for the domain of interest are clipped and subsequently averaged per land use class. Next, for each land use class the mean monthly LAI is estimated. The land use class and LAI are used in combination with a look-up table to subsequently develop the land use classification file, which contains information on the maximum surface interception, root depth and gridded paved area fraction (Figure 53).

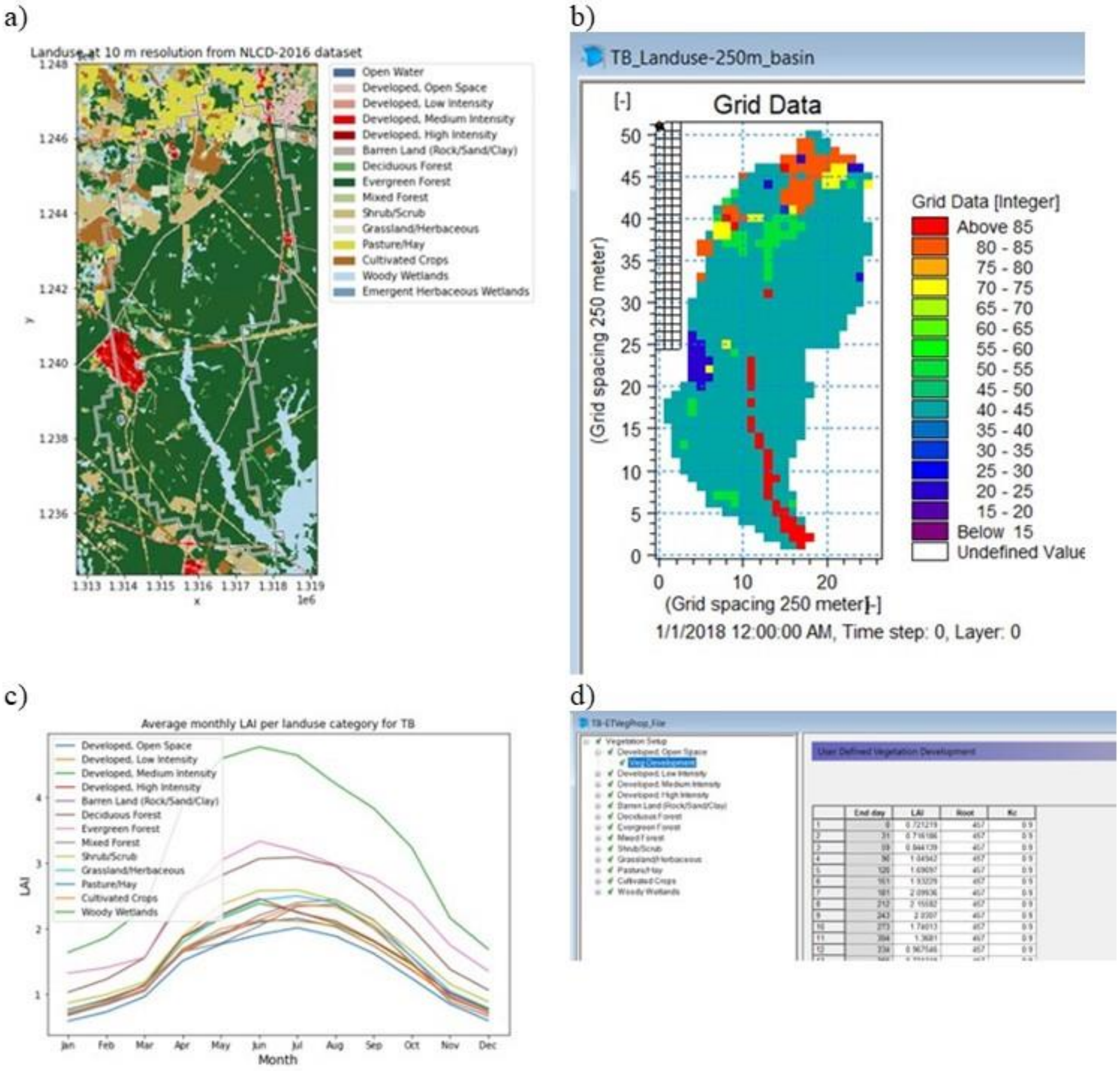

1/1/2018 12:00:00 AM, Time step: 0, Layer: 0

	End day	LAI	Root	Kc
1	0	0.721219	457	0.9
2	31	0.716186	457	0.9
3	59	0.844139	457	0.9
4	90	1.04942	457	0.9
5	120	1.69097	457	0.9
6	151	1.93229	457	0.9
7	181	2.09636	457	0.9
8	212	2.15582	457	0.9
9	243	2.0307	457	0.9
10	273	1.74013	457	0.9
11	304	1.3681	457	0.9
12	334	0.967546	457	0.9

Figure 53. Panel a) shows the land cover type for Tims Branch watershed from the NLCD 2016 dataset at 10-meter resolution. In panel b) this information is converted to 250-meter resolution and converted to a grid file (.dfs2) interpretable by MIKE. Panel c) shows for each land cover type within Tims Branch the observed average leaf area index (LAI) for a given month over the period 2002-2020 as observed from MODIS satellite observations. Using Python, in panel d) this information is subsequently translated into a MIKE SHE vegetation file (.vrt).

Generation of soil physical information - Besides land use for the vertical transport of water through the unsaturated and saturated zone, for each grid cell within the domain of interest, soil property information needs to be defined for MIKE SHE. In order to generate this, the global SoilGrids2.0 database (Hengl et al., 2015) was used, which contains soil texture information (e.g., sand, clay and silt content, bulk density, and pH for 7 different soil layer depths (0-5, 5-15, 15-30, 30-40, 40-60, 60-100, 100-200 cm), globally at 250-meter resolution. To reduce the amount of computational time within MIKE, the soil texture information was aggregated to 1,000-meter grid resolution, using first a vertically depth-weighted average and subsequently averaging over the pixels within a given 1,000x1,000 meter domain. The average soil texture information at 1,000-meter resolution was used to estimate the Mualem-van Genuchten soil retention parameters using the Rosetta pedotransfer model (see Figure 54a). The gridded soil information as well as the parameter values for a given 1,000-meter pixel were subsequently stored in the various MIKE soil column files (see Figure 54b).

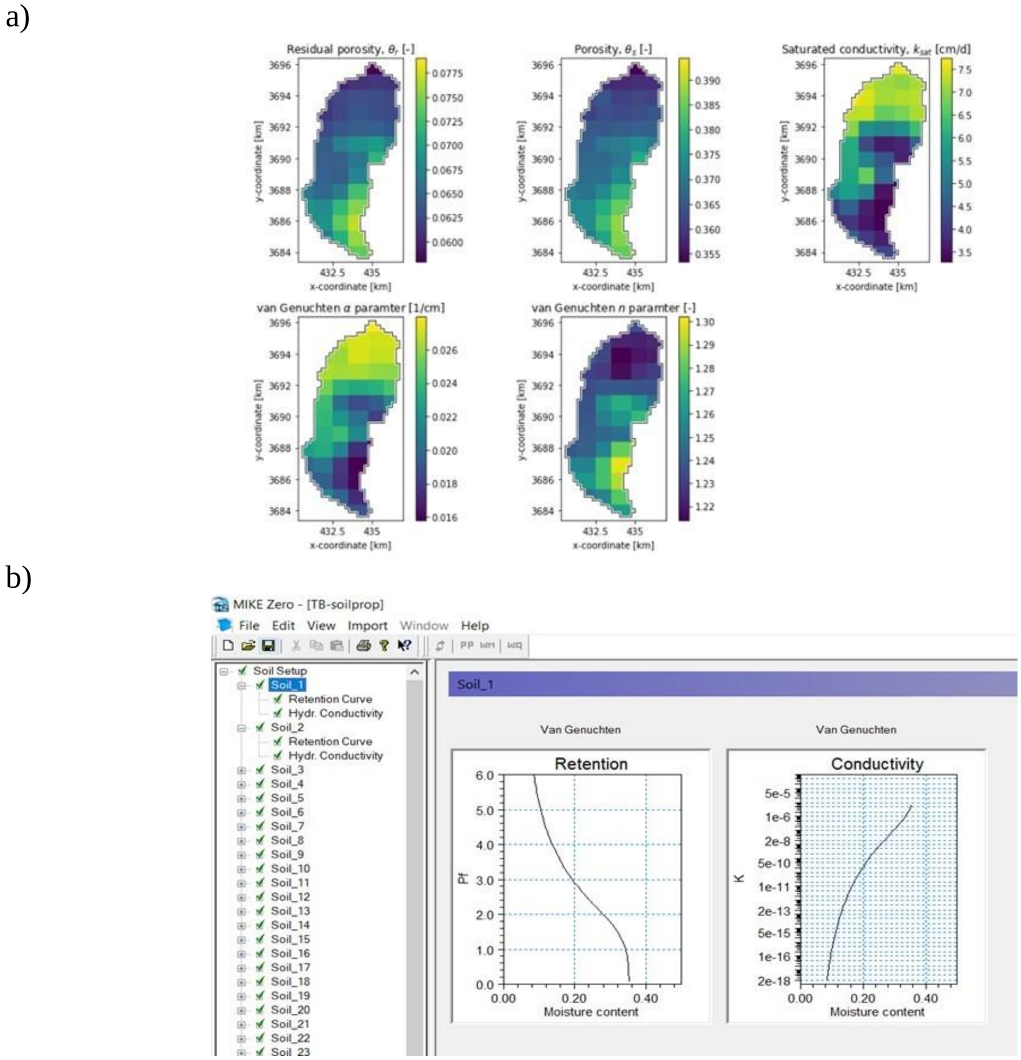

Figure 54. Panel a) shows the parameters of the Mualem-van Genuchten retention relationship as derived from upscaling the 250-meter SoilGrids2.0 soil texture dataset to ,1000-meter grid resolution and using the Rosetta PTF model to estimate the various parameter values (Schaap et al., 1998). In panel b) using Python a MIKE SHE soil property file is generated using this information.

Generation of river network information - Also within Python a process was developed to 1) extract the river network from a high 10-m resolution DEM, 2) identify locations where MIKE11 simulates discharge and water levels for the river network, and 3) derive the corresponding cross-sections. As indicated above, the river network is first delineated from a 10-meter DEM and its location evaluated with respect to satellite observations. Next the points along the river network where water levels and discharges will be simulated are derived, ensuring that each subsequent point downstream is 50-meters apart. Next, at each point, a reciprocal line is identified. A 1-meter DEM is then used to identify the river cross-section at the location of the reciprocal line at a 1-meter horizontal resolution. Python is used to identify the lowest point along this line as well as indicate the river network boundaries. The river network, cross-sectional information, upstream and downstream boundary and hydrodynamic parameter files are subsequently generated in Python in a format interpretable by MIKE 11. For Tims Branch, Figure 55 shows the river network and cross-sections as derived using this approach, presented in MIKE 11.

The Tims Branch river network contains various beaver ponds as well as a former farm pond (Steed Pond). It is anticipated that these ponds have an important impact on both the hydrological response and contaminant transport. This is because flow velocities are considerably lower compared to the river network, allowing for settlement of dissolved particles. As a result, heavy metal sediment loads are considerably higher within these ponds. The original MIKE model did not explicitly represent these ponds within the river network. Therefore, during the month of November, six ponds were included by extending the local width of the river network within as a new file in the Cross Sections folder of the MIKE 11 model. These ponds include Beaver Ponds 1 – 5 as well as Steed Pond. These ponds were incorporated as a new file in the Cross Sections folder of the MIKE 11 model.

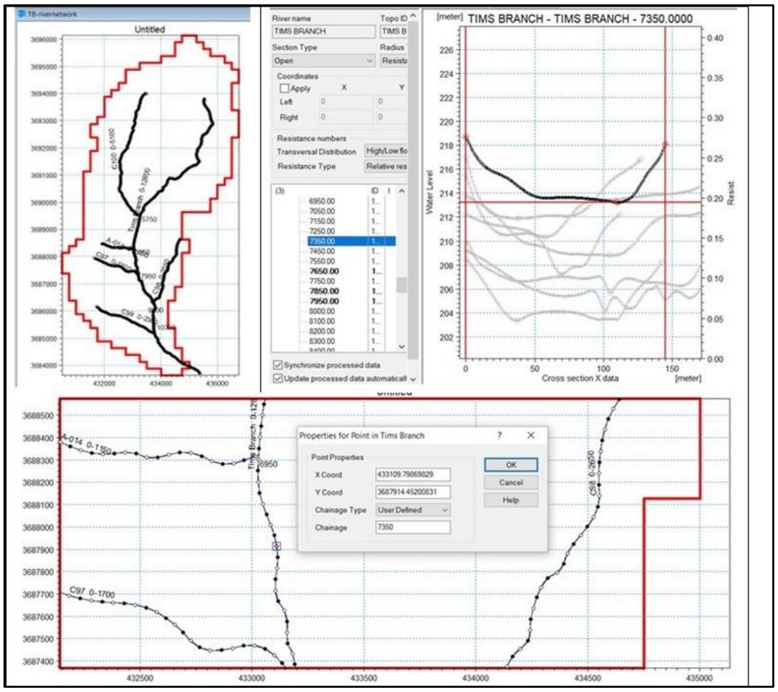

River name: TIMS BRANCH
Topo ID: TIMS B
Section Type: Open
Radius: Resista
Coordinates: ☐ Apply; Left X 0, Y 0; Right X 0, Y 0
Resistance numbers
Transversal Distribution: High/Low flo
Resistance Type: Relative res
☑ Synchronize processed data
☑ Update processed data automaticall

Properties for Point in Tims Branch
Point Properties
X Coord: 433109.79869829
Y Coord: 3687914.45200831
Chainage Type: User Defined
Chainage: 7350

Figure 55. Top left panel shows the river network and chainage locations. The bottom image shows a zoomed-in version of the top-left figure, where the white and dark dots indicate chainage points for which subsequently discharge and water levels are simulated. The top-right figure shows the corresponding cross-section as used by MIKE 11.

Finally, Python was used to automatically generate a MIKE SHE/MIKE 11 starting file containing all the information for a given catchment of interest. Figure 56 shows a newly generated MIKE model for Tims Branch, but it should be noted that this script can now also be applied to other basins, such as Fourmile Branch in Subtask 3.2.

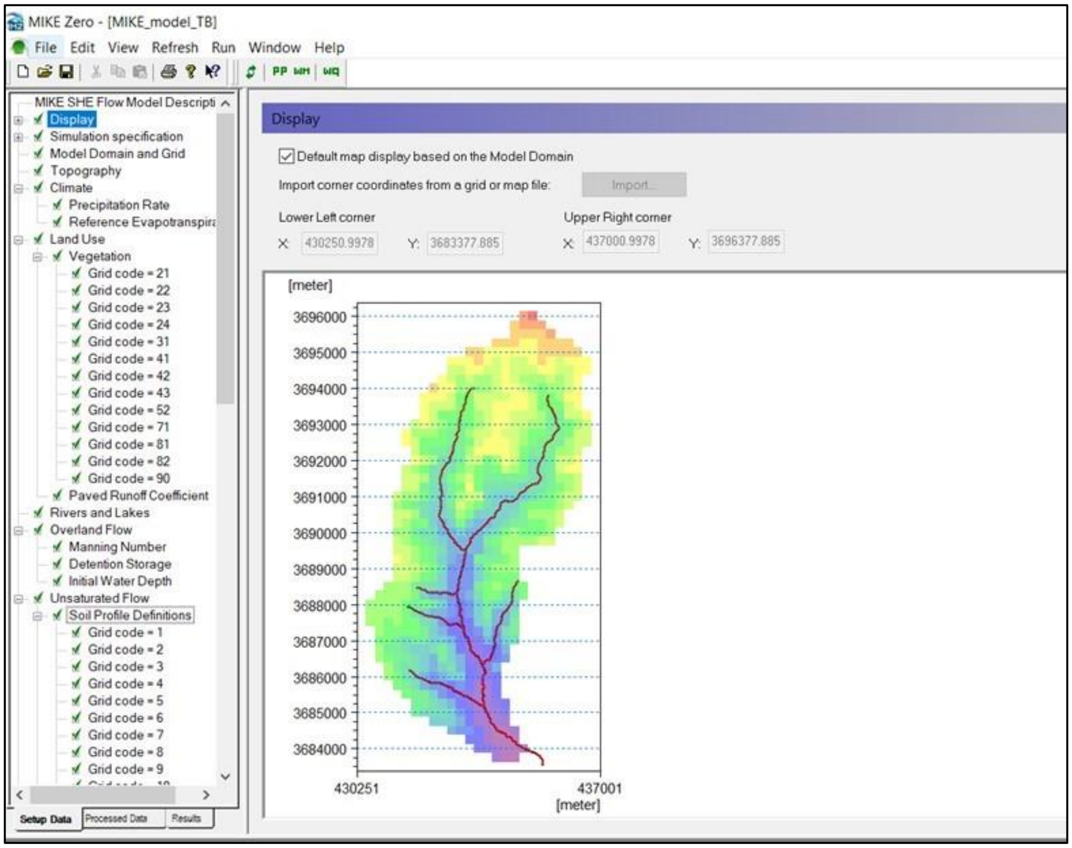

☑ Default map display based on the Model Domain

Import corner coordinates from a grid or map file:

Lower Left corner X: 430250.9978 Y: 3683377.885

Upper Right corner X: 437000.9978 Y: 3696377.885

Figure 56. Final MIKE SHE/MIKE 11 model for Tims Branch at 250-meter grid resolution as generated from Python script and publically available data sources.

The next step is to incorporate available historical observations into the model, which can then be subsequently used for the final model calibration. This will be the focus of FIU Year 3.

3.1.2. Evaluate the uranium transport during storm events from contaminated sediments that are subject to erosion.

To enable heavy metal transport simulations for uranium, tin and nickel within the MIKE model, the ECO Lab numerical template inside the MIKE Zero platform is used. The module or template can be modified according to whether one is modeling water quality, heavy metals, eutrophication, organic contaminants, or ecology. The module uses chemical, ecological, and biological processes and interactions between state variables to describe the mathematical state of a dynamic system (Promotionsausschuss, 2013). The transport of heavy metals discharged into the aquatic environment can be simulated and controlled using a simulated mechanism within the environment. The mechanisms are abundant, however on a macroscopic scale only a limited number govern transport processes (Promotionsausschuss, 2013). Listed below are the processes used for water quality modeling in the ECO Lab module accounting for four processes, while the advection-dispersion process is calculated by MIKE 11.

1) The sediment and resuspension of particle bound heavy metals.
2) Adsorption/desorption of heavy metals.
3) The diffusive transfer among dissolved heavy metal (sediment/water interface).
4) The transport of dissolved and particulate heavy metal in the water column by advection and dispersion.
5) Optional: biodegradation, photolysis, hydrolysis, and evaporation.

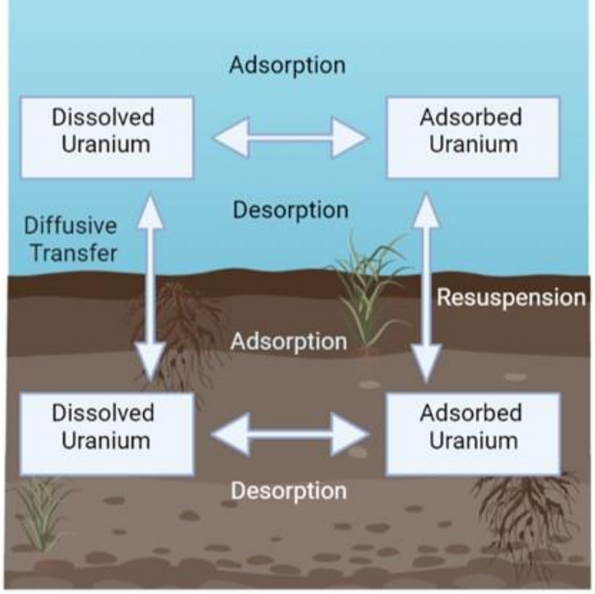

Figure 57. Processes of the heavy metal template in the MIKE ECO Lab module.

There are four main subdomains that can represent heavy metal concentration in different model production runs. These are dissolved in the water (SHM), absorbed in the water (XHM) (particulate), adsorbed in the sediment (XHMS), and dissolved in the sediment pore water (SHMS). Inside the MIKE 11 ECO Lab template, there are 3 processes in which advection-dispersion processes are calculated. This template uses a kinetic approach to identify the distribution of heavy metals in between particles and water. Here the adsorption and desorption terms define the transport of solute from the solution phase to a contiguous phase or in reverse (MIKE DHI, 2009). In the MIKE ECO Lab model, these terms are viewed as a combined process. The mechanisms describing the process are schematically summarized in Figure 57.

Long-term heavy metal water quality modeling will provide screening in ecological risk assessments for the transport and deposition of uranium, tin, nickel and other heavy metals released from former SRS hazardous waste management facilities. Based on the complexity between contaminants in both the solid and the aqueous phases, the data requirements for ECO Lab are complex and many of the variables contain uncertainty. During this quarter the ECO Lab heavy metal template initial transport variables used to model heavy metals in the Tims Branch surface waters were identified.

Table 18 lists all the ECO Lab input parameters for uranium as currently defined. It should be noted that a number of parameters still need to be estimated. As such, the following table presents the default values as defined within ECO Lab.

Table 18. Uranium / Heavy Metal Module Parameters

Parameter	Default/ Calculated	Value	Source	Units
Dissolved uranium in water column	Calculated	0.0014	(Applied Research Center, 2016; ARC, 2017)	mg/l
Adsorbed uranium	Calculated	0.21	(Pickett, 1990)	mg/l
Dissolved uranium in sediment pore water	Calculated	0.00001406	(Applied Research Center, 2016; ARC, 2017)	g/m^2
Adsorbed uranium in sediment	Calculated	0.0034	(Pickett, 1990)	g/m^2
Suspended solids	Calculated	1.91	(Applied Research Center, 2016)	mg/l
Mass of sediment	Calculated	1000		g/m^2
Organic- carbon partitioning coefficient	Calculated	833,333	(Applied Research Center, 2016; ARC, 2017; Betancourt et al., 2011)	l/kg
Desorption rate in water (sediment to pore water)	Default	0.1		per day
Fraction or organic carbon in suspended solids	Default	0.6		per day
Fraction of organic carbon in sediment	Calculated	0.042		dimensionless
Thickness of water film	Default	0.1		dimensionless
Ratio between thickness of diffusion layer in sediment	Default	0.2		mm
Factor for diffusion due to bioturbation etc.	Default	1		dimensionless
Moleweight of heavy metal	Calculated	238		dimensionless
ECO Lab time step	Calculated	30		g/mole
Density of dry sediment	Calculated	250		Seconds
Porosity of sediment	Default	0.8		kg/m^3 bulk
Settling velocity of SS	Calculated	0.1		m^3 H_20 / m^3 Bulk
Resuspension rate	Calculated	250		m/day
Particle production rate	Calculated	1		$gDW/m^2/day$
Critical current velocity for sediment resuspension	Calculated	0.32		$gDW/m^2/day$

In natural environments, heavy metals chemically react with the solid materials in which surface water comes into contact. Because heavy metal transport is a complex phenomenon governed by chemical and physical processes, our assumption between metal solutes and sorbents will be particularly dependent upon various geochemical characteristics of the water and soil.

Adsorption

The adsorption process is the enrichment of one or more components in an interfacial region because of unbalanced forces (Fernandes et al., 2013). In nature, heavy metals are found in the soils, suspended matter, and dissolved in the water. The extent by which a heavy metal is adhered to the suspended matter is different from metal to metal. Additionally, metal particles can remain attached to soils and can become resuspended during severe storm events (Batson et al., 1996).

In parallel, the movement or reaction of molecules from one phase to another is called partitioning. As such, a heavy metal induces chemical reactions with the solid media and are referred to as sorption reactions. Because of its low cost and great effectiveness, many remediation projects use adsorption isotherms to guide their theoretical foundation. The concept of adsorption isotherm modeling will provide FIU with an understanding of the mechanistic approach to the adsorption process, which is useful for adsorption system design in ECO Lab. Among the several adsorption mechanisms, the most common is chemical adsorption, which corresponds to the creation of chemical bonds, physical adsorption, which is related to the van der Waals force, and ion exchange (Wang & Guo, 2020). A description of the adsorption mechanisms can be seen in Figure 58.

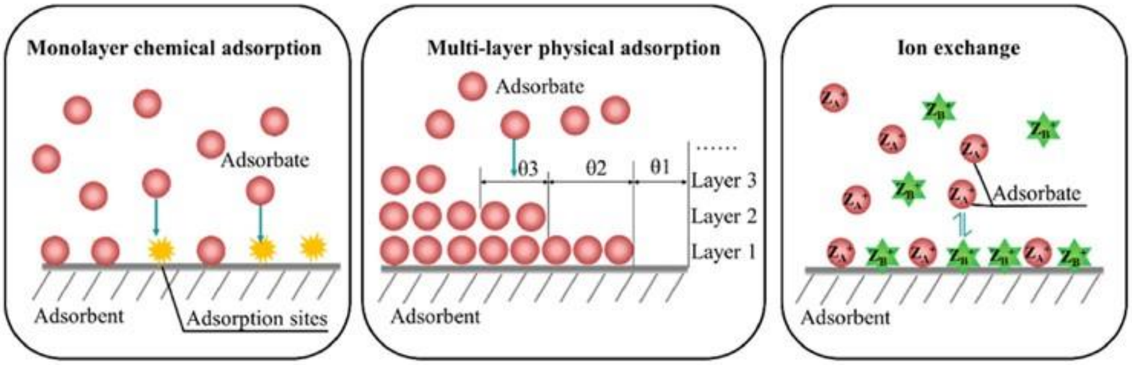

Figure 58. The possible adsorption mechanisms. (Review of adsorption isotherm models, Wang & Guo, 2020).

Isothermal modeling is the most convenient and extensively used method for determining the adsorption capacity. There are several methods for describing the mechanics in total. Some methods for describing absorption mechanics include characterization of the adsorbent before and after adsorption, investigation of molecular dynamics, and computation of the density functional theory (DFT) (Salim et al., 2021; Wang & Guo, 2020).

For the current project, the Freundlich isotherm model was used in terms of its empirical meaning, as well as to evaluate fitness using statistical metrics. This model assumes that the relationship between the amount of heavy metal adsorbed to the sediment q_e and the amount of heavy metal dissolved in water C_e can be described according to a power-law:

$$q_e = K_F C_e^{1/n}, \qquad \text{(Eq. 3.2)}$$

where K_F is the heavy metal partition coefficient following the Freundlich isotherm model, and n a fitting parameter. Equation 1 describes the non-linear Freundlich isotherm, where the K_F $\left(L^{\frac{1}{n}} * mg^{1-\frac{1}{n}} * g^{-1}\right)$, and n are constants. The Freundlich model will reduce the linear model when n=1. This equation can be linearized by taking rewriting the Freundlich equation in a logarithmic form.

$$log q_e = log K_F + \frac{1}{n} log C_e \qquad \text{(Eq. 3.3)}$$

As stated by Wang (2020), the Freundlich model is one of the most common isotherms to model adsorption.

In the Tims Branch watershed, both (field-applied) water samples (referred to as dissolved metal loaded samples) and "uncontaminated" water (referred to as baseline/background water) from a random trial site/stream (offsite) were sampled. The goal during the 2016 and 2017 summer field surveying was to sample and process stream water from Tims Branch, A-014, and A-011 outfall tributaries. This effort was funded by FIU's Applied Research Center under the DOE-FIU Cooperative Agreement #DE-EM0000598 and was carried out in collaboration with Dr. John Seaman of the University of Georgia's (UGA) Savannah River Ecology Laboratory (SREL) and Dr. Brian Looney of the Savannah River National Laboratory (SRNL). As a result, the following methods and results are documented below:

Water Sampling Methods - Fifteen (15) sampling sites were chosen: nine (9) from the outfall tributaries and six (6) from the mainstem surface waters running from the A-014 outfall (33°19'59.1"N 81°43'59.0"W) in the A/M area, Tims Branch watershed, Savannah River Site, SC to the Upper Three Runs river (33°17'07.4"N 81°41'43.1"W), including a field blank (collected at Beaver Pond 1). FIU was responsible for the timely and accurate documentation of field information in electronic and paper records, as well as the application of procedures and protocols to ensure the data's quality and measuring techniques. Water was sampled 500 to 1,000 meters apart inside the Tims Branch watershed (TIM/ TB, SP, A014, and A011) and collected using 3 calibration cups (Polyethene Terephthalate (PET) 200 ml bottles), adding to a total of 36 water samples specified as target locations (Figure 59). Before collection, all bottles were cleaned using the surface water at each location according to acceptable standard operating procedures (SOPs) and georeferenced using a GPS unit (USGS, Francesca, 2016).

Sample processing included the filtering of the water by placing the samples on a goose crucible assembly. The first 200 mL of water was filtered using a suction pump including a 0.2 µm filter to remove solids from the liquid. In total, 1L of water was filtered from each sample location. All samples were processed in triplicate applying standard QA/QC measures during the analysis. Lastly, the suspended solids were dried at (104°C) for approximately 1 hour and cooled in a desiccator. The values were recorded in the pro forma for each sample location.

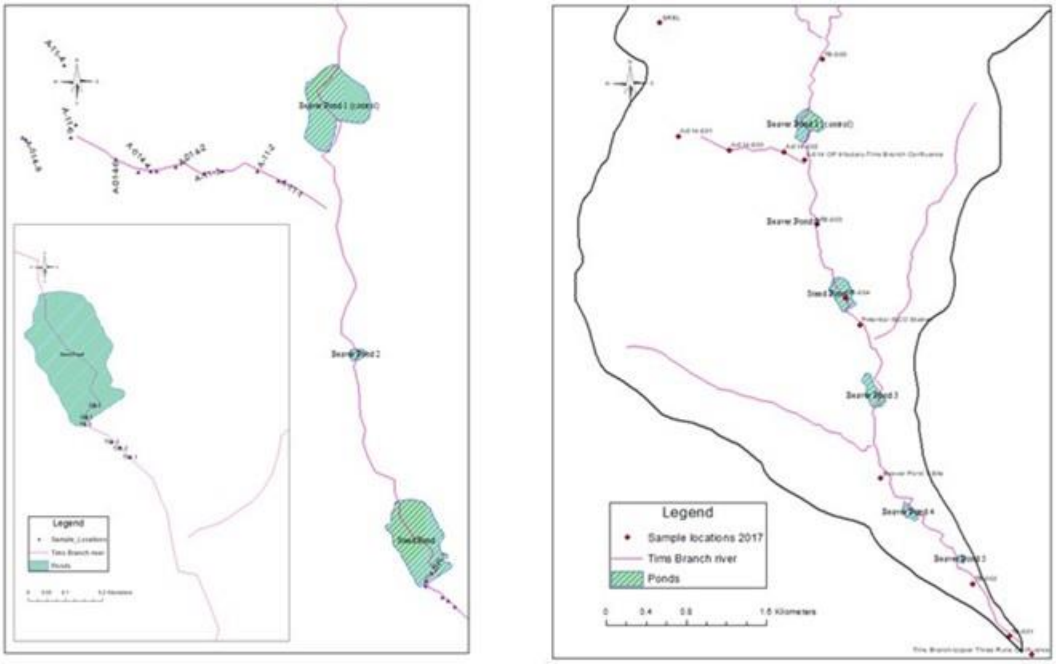

Figure 59. Sample locations from 2016 (left) and 2017 (right).

Water samples were collected by DOE Fellow Morales and analyzed by SREL using inductively coupled plasma-mass spectrometry (ICP-MS). The samples had been previously stored, therefore preservation and pretreatment measures were considered (EPA Method 200.8) (USGS, Francesca, 2016). The samples were examined for particles during the initial processing, and if any were found, the samples were re-filtered to avoid difficulties with the ICP-MS. As a solid type of sample, water containing 1% (w/v) suspended or particulate material was removed. After acidification, each sample was combined and stored for 16 hours before being validated to be at pH 2 just before removing an aliquot for processing. If the sample was found to have a high alkalinity level of more than 2, more acid was added, and the sample was maintained for an additional 16 hours until it was confirmed to have pH 2. To process each sample, at least 10mL of liquid had to be prepared.

FIU also constructed a field blank as if it were a sample and utilized the same preservation technique and storage procedure as the other samples. To estimate the total recoverable elements in the water, samples and field blanks were acidified with trace metal grade nitric acid to a concentration of 0.5 to 2 percent v/v. The sample was then filtered and acidified after the dissolved elements were determined. After the sample had been acidified, it was mixed and stored for a minimum of 16 hours before the ICP-MS analysis.

The following table and figure provide detailed information on the heavy metal concentrations in the Tims Branch River and its tributaries as obtained during the in 2016 and 2017 at the 15 different locations. These data were used to estimate the adsorption model parameters for uranium as discussed below.

Table 19. Discharge and Metal Concentrations in Water from the Tims Branch River and Tributaries, South Carolina, 2016-2017

		Metal concentration, (mg/L)															
Tims Branch	Discharge	Ni		Mg		Mn		As		Cd		Cu		Pb		U	
Tributaries		Tot	Filt	Tot	Filt	Tot	Filt	Tot	Filt	Tot	Filt	Tot	Filt	Tot	Filt	Tot	Filt
A014-3	0.011	<MDL	0.28	0.52	0.52	1.77E-03	1.58	<MDL	<MDL	<MDL	<MDL	3.21E-04	0.28	<MDL	<MDL	<MDL	<MDL
A014-6	0.004	3.77E-04	0.54	0.56	0.61	5.44E-03	5.37	<MDL	<MDL	<MDL	<MDL	1.07E-04	0.21	<MDL	<MDL	<MDL	1.34E-04
A014-8	0.004	3.71E-04	0.41	0.58	0.55	0.01	4.81	<MDL	<MDL	<MDL	<MDL	1.12E-04	<MDL	<MDL	<MDL	<MDL	<MDL
A-11-1	0.005	4.65E-04	0.41	0.51	0.53	0.01	1.38	1.15E-04	<MDL	<MDL	<MDL	7.05E-04	0.28	2.23E-04	<MDL	8.43E-04	<MDL
A-11-2	0.009	2.60E-04	0.58	0.52	0.54	1.90E-03	1.40	<MDL	<MDL	<MDL	<MDL	3.66E-04	0.34	4.31E-05	<MDL	6.67E-05	<MDL
A-11-3	0.008	2.62E-04	0.32	0.42	0.52	1.41E-03	1.15	<MDL	<MDL	<MDL	<MDL	3.26E-04	0.26	7.87E-05	<MDL	<MDL	3.85E-05
A014-001	0.011	4.08E-04	4.57E-04	0.62	0.63	0.01	0.01	2.80E-05	3.6E-05	8.7E-05	7.6E-05	1.68E-04	8.80E-05	8.67E-05	7.65E-05	2.85E-05	<MDL
A014-002	0.003	4.14E-04	0.28	0.59	0.52	2.27E-03	1.58	1.09E-04	6.3E-05	9.5E-05	9.2E-05	3.04E-04	0.28	9.48E-05	9.21E-05	6.75E-05	<MDL
A014-003	0.025	5.41E-04	0.54	0.57	0.61	2.69E-03	5.37	1.62E-04	6.1E-05	7.7E-05	9.3E-05	3.56E-04	0.21	7.69E-05	9.30E-05	4.28E-05	<MDL
Mainstream																	
SP1	-	<MDL	0.32	0.30	0.52	<MDL	1.15	<MDL	<MDL	<MDL	<MDL	<MDL	0.26	<MDL	<MDL	<MDL	1.01E-03
TIM-1	0.002	2.63E-03	4.78E-03	0.38	0.33	0.26	0.12	4.81E-03	9.22E-04	<MDL	<MDL	2.09E-04	3.19E-04	1.54E-04	8.24E-05	1.10E-03	<MDL
TIM-2	0.002	3.57E-03	3.11E-03	0.38	0.43	0.27	0.27	4.62E-03	2.77E-03	<MDL	<MDL	2.67E-04	1.00E-04	1.73E-04	7.55E-05	1.63E-03	1.16E-03
TIM-3	0.003	4.38E-03	3.10E-03	0.35	0.44	0.26	0.26	4.70E-03	2.54E-03	<MDL	<MDL	3.87E-04	1.56E-04	2.19E-04	1.06E-04	2.88E-03	4.17E-04
TB001	-	4.58E-03	3.17E-03	0.49	0.47	0.09	0.02	1.13E-03	6.40E-04	3.71E-06	3.8E-05	2.51E-04	2.30E-04	2.17E-04	2.97E-05	2.47E-03	5.04E-04
TB002	-	5.07E-03	3.50E-03	0.50	0.48	0.12	0.04	1.43E-03	6.53E-04	3.84E-06	9.1E-06	2.20E-04	1.45E-04	2.27E-04	5.25E-06	2.71E-03	9.08E-04
TB003	-	8.65E-03	3.99E-03	0.56	0.51	0.02	0.01	4.13E-04	2.28E-04	2.31E-05	7.8E-06	8.54E-04	3.15E-04	6.12E-04	4.05E-05	2.00E-02	9.37E-04
TB004	-	1.91E-02	1.53E-02	0.48	0.48	0.09	0.02	1.34E-03	7.14E-04	3.05E-05	2.1E-05	8.87E-04	5.67E-04	3.01E-04	2.75E-05	9.40E-03	2.37E-03

TB005	-	1.31E-03	9.69 E-04	0.36	0.36	0.05	0.01	1.45E-03	1.13E-03	<MDL	2.8E-05	5.12E-03	3.74E-03	7.25E-04	3.47E-04	1.89E-03	4.34E-03

Tot= total recoverable concentration, Filt = concentration in 0.2µm filtrate, Site abbreviations follow Figure 59.

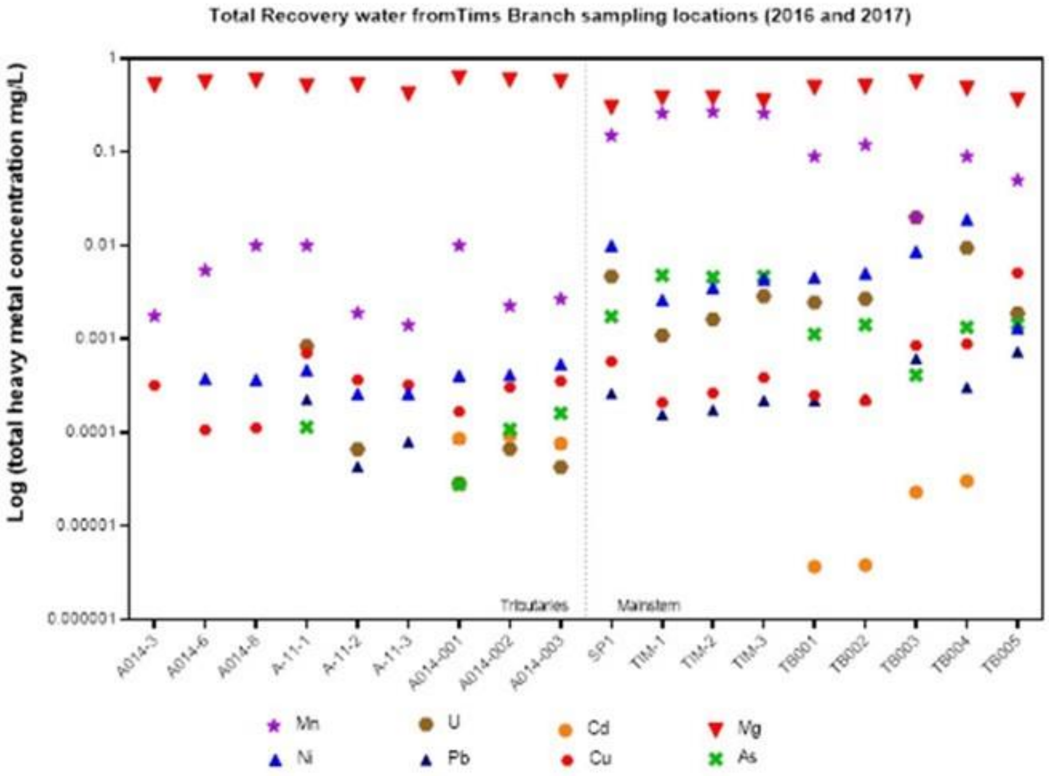

Figure 60. Log total heavy metal concentration from Tims Branch sampling locations (2016 and 2017).

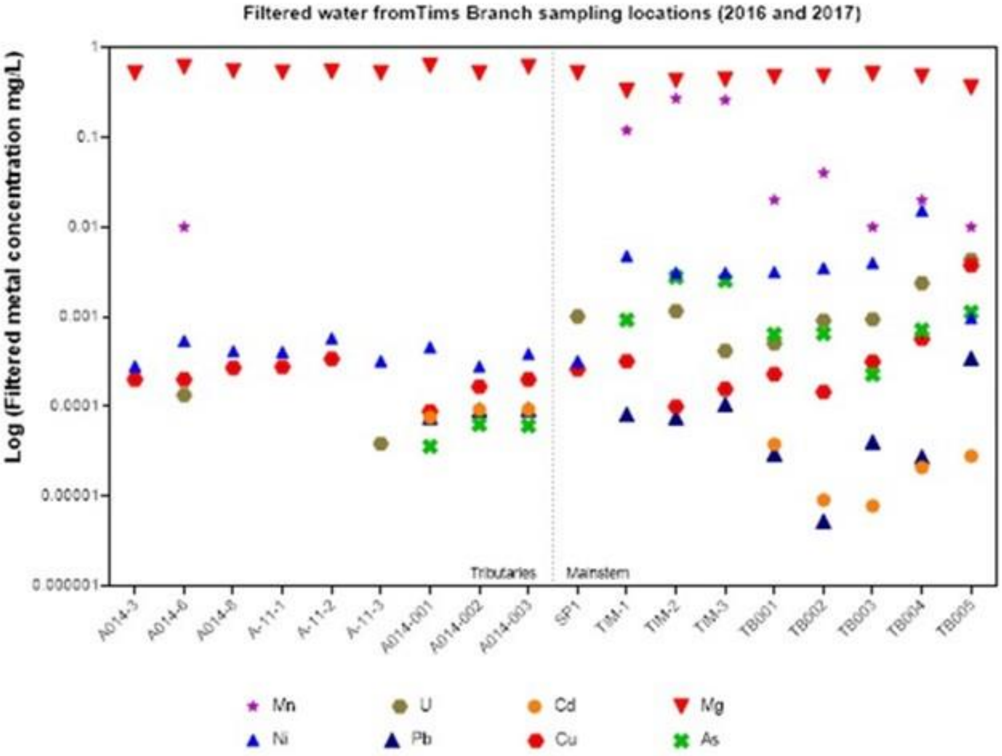

Figure 61. Log filtered heavy metal concentration from Tims Branch sampling locations (2016 and 2017).

Many transport models such as those using water quality pathways in surface waters incorporate the use of a metal partition coefficient (Kd). The partition or distribution coefficient (Kd) is the ratio of concentration of a compound in the two phases of a mixture of two immiscible (not forming a homogenous mixture when together) solvents at equilibrium. The Kd is important because this parameter measures the adsorption potential of a soil in contact with the dissolved contaminant.

Equation 3.4 expresses the ratio of the sorbed heavy metal concentration (expressed in mg of heavy metal per kg of sorbing material) divided by the dissolved metal concentration (expressed in mg of metal concentration per L of solution) source at equilibrium.

$$K_d = \frac{C\ solid\ (mg/kg)}{C\ liquid(mg/L)} \tag{Eq. 3.4}$$

In addition, the Kd value may be used to calculate the retardation factor (R_f). This is defined as the ratio of the average linear velocity of the water (m*s-1), divided by the average linear velocity of the heavy metal (m*s-1)(Kaplan & Serkiz, 2001) . Hence the retardation factor can be obtained by using the following equation:

$$R_f = \left(1 + \frac{K_d r_b}{h}\right) \tag{Eq. 3.5}$$

The uranium sorption coefficient K_d calculated using Eq. 3.4 is used for Eq. 3.3 in which the sorption coefficient $(K_d, l/Kg)$, being multiplied by the bulk density $(\rho_b, kg * m^{-3})$, is then divided by the porosity $(h, m^3 * m^{-3})$. Over the course of time, several assumptions have been imposed. Among these assumptions is that the sorption rate is equal to the desorption rate. This is seldom the case in natural sediments since desorption processes are usually significantly slower than sorption activities (Kaplan & Serkiz, 2001).

In MIKE ECO Lab, the state variable organic-carbon partition coefficient (K_{OC}) will be used to estimate the uranium sorption reactions and is considered the key transport parameter in the heavy metal modelling component. We found that in contrast to K_d , the K_{OC} is often expressed as the unit in which a chemical/heavy metal sorbs (adheres) to the organic portion of the soil/sediment. Given that the KOC can be referred to the organic carbon media in the soils, this parameter of interest can be calculated as the relationship between soil to water partitioning coefficient (K_d), divided by the fraction of organic carbon (foc).

Equation 3.6 describes the relationship and the formula in which K_{OC} can be calculated.

$$K_{OC} = \frac{K_d}{foc} \tag{Eq. 3.6}$$

Generally, K_{OC} is often indicated as a logarithmic value given the wide range of measured K_{OC} values reported. The table below shows how given KOC values can be interpreted.

Table 20. Interpretation of KOC Values

A low KOC (not tightly bound to soils)	A high KOC (tightly bound to soils)
1. Has the ability to leach/re-introduction to the soil.	1. Can reduce the amount of heavy metal in soil/ domain and thus cause degradation because less heavy metals are available to microorganisms.
2. The concentration in the soil of the surface level in reduced.	2. Removal from the water column via sorption to soil/sediment and particulate matter.
3. The contamination of surface water increases in storm runoff conditions	3. A high KOC (tightly bound to soils)

The proportion or fraction of organic carbon (foc) does not have a precise definition. It may, however, be conceived of as the amount of organic matter accessible to adsorb the organic pollutants of concern. The higher the organic carbon content, the more organic compounds that may be adsorbed to the soil and therefore ready to seep into groundwater. In the Risk Integrated System of Closure (RISC), a nondefault option is to employ foc in the Soil to Groundwater Partitioning Model to determine a site-specific migration to groundwater closure level (Allison et al., 2005). The relationship between the organic compound coefficient, K_d, the chemical-specific soil organic carbon water partition coefficient, K_{oc}, and the foc is shown in Equation 3.4.

Generally, the EPA's Soil Screening Guidance technical report suggests using 0.2 % (0.002 g/g) as a default concentration of organic carbon for subsurface soils as a good baseline for the fraction of organic carbon (foc). Any concentration > 0.02 % would need explanation of the source of organic carbon being reported (Soil Screening Guidance: Technical Background Document Second Edition, 1996) (Soil Screening Guidance: Technical Background Document Second Edition, 1996).

Another important parameter to set up for the heavy metal template in MIKE ECO Lab module is a desorption rate from sediment and suspended solids particles in water, K_W. The relationship between desorption rate and partition coefficient is:

$$K_d = \frac{K_a}{K_W} \quad \text{(Eq. 3.7)}$$

where:
K_W: desorption rate in water [day^{-1}]
K_a : adsorption rate [$m^3\ H_2O$/g DW/d]

where:

$$\text{Desorption} = K_W\ .\ X_{HM}$$

where X_{HM} : adsorbed heavy metal concentration in the water [gMe/m^3].

The section below presents a detailed overview on how the abovementioned parameters were estimated using both literature information and in situ observations.

Identifying the heavy metal partition coefficient, Kd - As a continuous effort to assign the corresponding values for ECO Lab module, FIU modeling team had searched for different methods through literature and the available field measuring data from Tims Branch (TB) to provide appropriate partitioning coefficient K_d values. The section below presents a detailed overview of how these various sources of data were used to estimate the partition coefficient.

Estimating Kd from scientific literature - A literature survey was conducted to obtain partition coefficients describing the partitioning between heavy metals in the soil, suspended matter, soil/water, surface waters, and between the dissolved and total organic carbon. Literature K_d for uranium show a wide variability, interestingly differing by three or four orders of magnitude. These vary according to pH and soil type (USEPA, 1999) These suggest the importance of carrying out actual field conditions of a particular site when carrying out specific K_d measurements. This ensures a reliable analysis of the solute transport.

Table 21. Results of the Literature Survey for Uranium Sorption Coefficients

Chemical	$Kd\ (L/Kg)$	Source	Comments
Uranium	600 - 1,600	(0. H. Thibault, M. I. Sheppard, 1990)	35mg/L- sand, 15 mg/L for silt, 1,600 mg/L for clay and 410 mg/L for OM.
	0.1 - 300	(Serkiz et al., 2007)	pH 3.1-7.1: Organic carbon <1 less or equal to the limit of detection
	2,100 - 6,900	(Kaplan et al., 2017)	At pH 5.5 (background) in sandy sediments ~700L/Kg; Clay reports at ~300 L/g.
	300	(Sheppard et al., 2006)	40 L/Kg- Observed geometric mean for sand, 200 L/kg for loam, 200 L/Kg for clay and 2000 L/Kg for OM. Recommended Kd was for soils with a pH 5.5 (regression equation)
	170 - 6,493	(Kaplan & Serkiz, 2001)	
	404	FIU- not published	Contaminated soils data from (Serkiz et al., 2007) was used to calculate the Kd. This was done using linear interpolation at pH 7.0

Outlined in Table 21, literature derived K_d values ranged from 0.1 to 6,900 L/Kg and were highly influenced by governing factors such as pH and organic matter. The only calculated K_d highlighted from contaminated soils in this table was done using linear interpolation, where a K_d of 404 L/Kg was determined.

Additionally, the Office of Air and Radiation at the United States Environmental Protection Agency (EPA) and Pacific Northwest National Laboratory (PNNL) have generated detailed documents to assist in understanding variation in partition coefficient (K_d) values, specifically:

a) Office of Air and Radiation, United States Environmental Protection Agency, 1999, Understanding Variation in Partition Coefficient, K_d, Values. Volume I.

b) Strenge, D.L., Peterson, S.R. (1989). “Chemical Databases for the Multimedia Environmental Pollutant Assessment System (MEPAS): Version 1”. Prepared for the U.S. Department of Energy under Contract DE-AC06-76RL01830. Pacific Northwest National Laboratory. ICF Northwest, Richland, Washington.

Within these reports an approach to a constant $\mathrm{K_d}$ model is presented, in which the $\mathrm{K_d}$ value varies as a function of environmental conditions (Delegard and Barney, 1983; Routson and Serne, 1972; Strenge and Peterson, 1989). This method identifies K_d using a 3-dimensional matrix depending on pH, clay content, aluminum and iron oxy-hydroxide, and the organic matter content of the sediment. The effect of adsorbent on the distribution coefficient was taken into account by dividing the total percent-by-weight composition of the clay, iron, aluminum oxy-hydroxide, and organic matter contents into three categories:

1. Those sediments with a total weight percent (of the aforementioned constituents) that is less than 10% (sandy soils).
2. Those sediments with a total weight percent (of the aforementioned constituents) that is 10-30% (loamy soils).
3. Those sediments with a total weight percent (of the aforementioned constituents) that is > 30% (clayey soils).

Using the abovementioned approach within the report of Strenge and Peterson (1989), the K_d values for tin, uranium, and nickel are provided in Table 22.

Table 22. K_d (ml/g) Values Based on Soil pH and Texture

		pH ≥ 9			pH 5-9			pH ≤ 5		
Total percent-by-weight composition of: 1. Clay 2. Iron 3. Aluminum oxy-hydroxide 4. Organic Matter Contents		< 10% (Sandy soils)	10-30% (Loamy soils)	> 30% (Clayey soils)	< 10% (Sandy soils)	10-30% (Loamy soils)	> 30% (Clayey soils)	< 10% (Sandy soils)	10-30% (Loamy soils)	> 30% (Clayey soils)
K_d (ml/g)	Uranium	0.0	5.0	50.0	0.0	50.0	500.0	0.0	5.0	50.0
	Tin	2.5	5.0	5.0	5.0	10.0	10.0	2.5	5.0	5.0
	Nickel	1.22	5.86	65.0	12.2	58.6	650.0	1.2	5.86	65.0

It should be noted that the values for uranium presented in the abovementioned table lie within the range of values as presented in the literature (see above), though values are on the lower end.

Estimating Kd from site observations – To estimate the heavy metal-specific partitioning coefficient, K_d, for uranium from in situ observations obtained in Tims Branch watershed, Eq. 3.2 is used. The sorbed heavy metal concentration ($C\ solid\ [\frac{mg}{kg}]$) was estimated from field samples collected by Betancourt et al. (2011). Betancourt et al. (2011) collected channel bed soil samples for various locations throughout Tims Branch and calculated the concentration of uranium, tin and nickel. For uranium, the samples collected from the field visit were sorted from lowest to highest concentration.

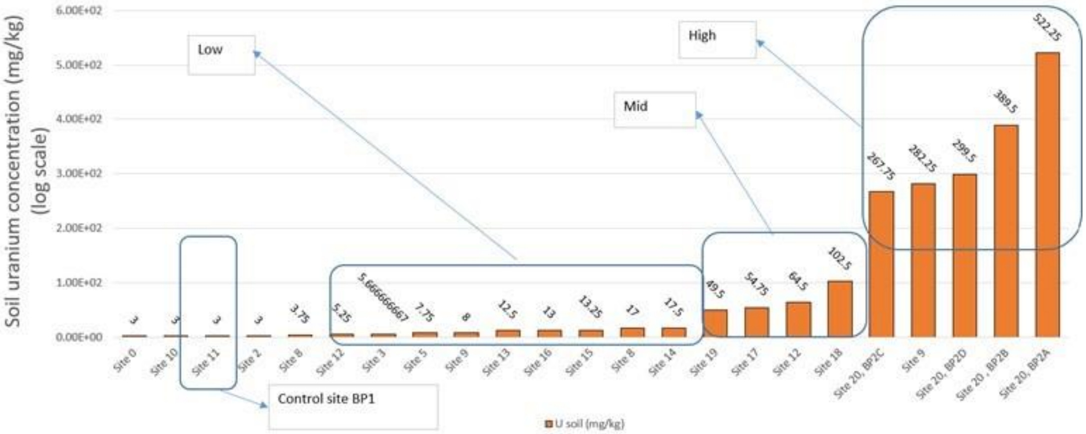

Figure 62. Soil uranium concentrations in (mg/kg). Data was extracted from Betancourt et al., 2011.

To derive the dissolved metal concentration of uranium ($C\ liquid[\frac{mg}{L}]$), observations from field summer surveys in 2016 and 2017 were used. The figure below presents the observations of aqueous uranium concentrations in Tims Branch stream. In line with the solid concentrations, observations are plotted from low to high (see Figure 63). The average concentration in the A-014 tributary was estimated at 0.000028 mg/L. Tims Branch stream, extending from downstream Beaver Pond 1 to the confluence of Upper Three Runs, contains an estimated average uranium concentration of 0.000754 mg/L. Lastly, the A-011 tributary contained an average uranium concentration of 0.00004 mg/L. The aqueous uranium concentrations along with sampling locations are highlighted below.

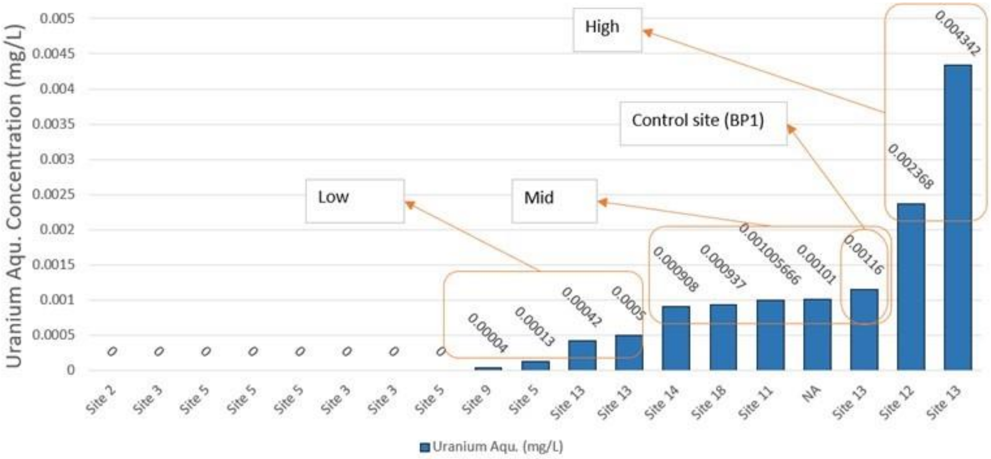

Figure 63. Aqueous uranium concentrations in (mg/L). Data was extracted from Applied Research Center, 2016; ARC, 2017.

The observations of sorbed heavy metal concentration in Table 23 and the observations of the dissolved heavy metal concentration of uranium in Table 24 were subsequently categorized in four classes for which the minimum and maximum uranium concentrations were estimated.

Table 23. Sorbed Uranium Concentration in Soil/Sediment (mg/kg)

Soil uranium concentration	Min (mg/kg)	Max (mg/kg)
Control site (Beaver Pond 1)	0	3
Low	5.23	17.5
Medium	49.5	102.5
High	267.75	522.25

Table 24. Aqueous Uranium Concentration (mg/L)

Aqueous uranium concentration	Min (mg/L)	Max (mg/L)
Control site (Beaver Pond 1)	0	0.00101
Low	0.00004	0.0005
Medium	0.00091	0.0.00116
High	0.00237	0.00434

These values are also presented in the figure below.

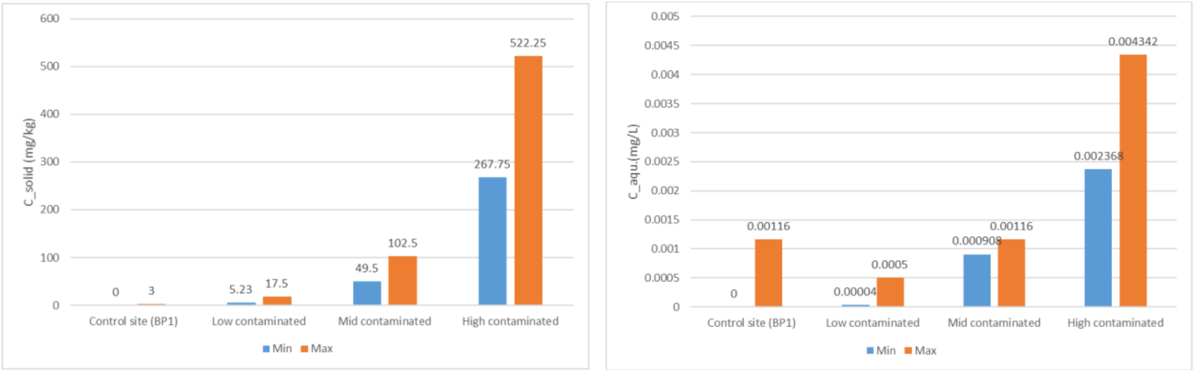

Figure 64. Soil/water concentrations used to determine the calculated partition coefficient.

Using Eq. 3.2 K_d values were determined at all sites, sorting the area of interest according to level of contamination (i.e., control, low, medium, and high contamination). The table below presents the derived K_d values for uranium. These results show that the partition coefficient ranges from 30-160 L/kg, with lowest values corresponding to the control location, while little difference between the low to high contaminated sites occur. These values correspond well to those observed in the literature (see above).

Table 25. Calculated K_d from in situ observations within Tims Branch

Class	K_d in (L/Kg)	log K_d in (L/Kg)	Area classification
Min	ND	ND	Control site (BP1)
Max	2,586	3.41	
Min	130,750	5.12	Low contaminated
Max	35,000 a	4.54	
Min	54,515	4.74	Mid contaminated
Max	88,362	4.95	

Min	113,070	5.05	High contaminated
Max	120,278	5.08	

a. Calculated K_d = 35,000 L/Kg . This was derived using Eq. 3.2, in which low uranium contaminated soils ($0.0175\,mg/g$) were divided by aqueous uranium contaminated averaged sample concentration ($0.0005\,mg/L$). The unit L/g was converted to L/kg by multiplying by the factor of 1000.

ND= Not detected

As indicated above, besides deriving K_d values for uranium directly from the data, also usage was made of the Freundlich isotherm model. All data from field uranium measurements were fitted to a Freundlich isotherm (see Eq. 3.1) to understand how the adsorbate particle distributes between the liquid phase and the solid surface of the adsorbent at equilibrium. Because of its low cost and great effectiveness, adsorption is a commonly used separation method, particularly in environmental cleanup. By taking the logarithm of the observed data and using Eq. 3.2, FIU fitted all samples for uranium soil/ water concentrations collected in 2011, 2016 and 2017.

Table 26. Tims Branch Watershed Soil/Water Uranium Concentrations Log Values used as Inputs for the Linear Freundlich Isotherm Model

a2011(q_e)	b2016(C_e)	c2017(c_e)	a$Log\ q_e$	b,c$Log\ C_e$
Site 9	A-11-3		-2.10	-4.40
Site 13	A-014-6		-1.90	-3.89
Site 16	TIM-2		-1.89	-3.38
Site 15	TIM-3		-1.88	-3.30
Site 8		TB001	-1.77	-3.04
Site 14		TB002	-1.76	-3.03
Site 19		TB005	-1.31	-3.00
Site 17	SP1		-1.26	-3.00
Site 12	TIM-1		-1.19	-2.94
Site 18		TB003	-0.99	-2.63
Site 20, BP2C		TB004	-0.57	-2.36

a. (Betancourt et al., 2011)

b. (Applied Research Center, 2016)

c. (ARC, 2017)

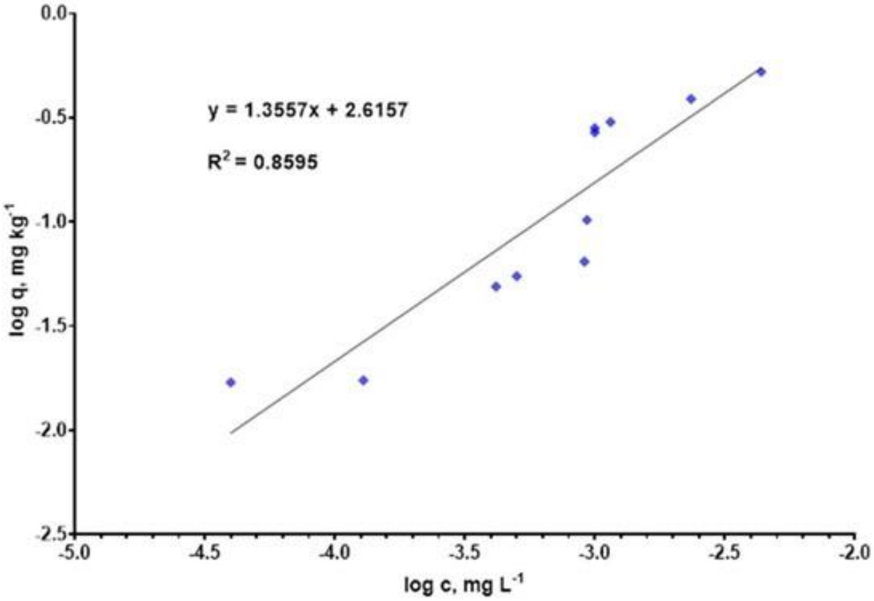

Figure 65. Freundlich adsorption isotherm for U ions.

Slope	Intercept	$K_F\ (L/g)$	$log\ K_F\ (L/g)$	$1/n$	R^2
1.3557	2.6157	412	2.6147	0.73866	0.8595

Using Eq. 3.2, plotting logq_e versus log C_e a linear line was fitted, which as indicated in for the observed data results in the slope = 1.3557 Figure 65 and $1/n$ = 0.73866. This corresponds to intercept Y $(logK)$ $logK_f = 2.6157$ and constant $K_f = 412$ L/g with an R2= 0.8595.

The values 1/n and n derived from Freundlich's equation were 0.73866 and 1.3557 respectively. Because the ratio of 1/n is between 0 and 1 and n>1, it suggests that the soil can successfully adsorb uranium. The Freundlich isotherm represents the data for uranium ion adsorption in Figure 65 with a regression coefficient of 0.8595.

The approach to estimate the partition coefficient for uranium was also applied for tin, although no variations between low to high concentrations were made. Betancourt and Looney (2011) estimated the average tin concentration for the top 3.5 inches of sediment depth in the riverine system from the A-014 Outfall downstream to the confluence of TB with Upper Three Runs Creek to be 26 $\mu g/g$. Looney et al. (2011) provided a theoretical tin concentration in treated groundwater from the M-1 Air Stripper System of 12.88 $\mu g\ Sn/L\ water$. Therefore, K_d can be calculated as:

$$K_d = \frac{26\ \mu g/g}{12.88\ \mu g\ Sn/Lit\ water} \approx 2{,}020\ ml/g$$

It can be noted that this observation-based estimate for tin is considerably higher compared to the range of values presented in Table 22.

FIU also possesses tin concentration observations from the water samples obtained during the field campaigns in the summer of 2016 and 2017. These observations will be used to provide a second method to estimate K_d for tin from observations within Tims Branch.

The fraction of organic carbon (foc) - To estimate the fraction of organic carbon (foc) for Tims Branch watershed, the Bechtel Environmental Integrated Data Management System (BEIDMS©) was used to evaluate historical seasonal trends of total and dissolved organic carbon concentrations in the A/M-Area riparian wetland. The data in BEIDMS goes back to 1984 and contains approximately 60 million records related to measurements made of environmental samples from the Savannah River Site. Using these observations enabled to the calculation of foc, which resulted in:

$$f_{OC} = 4.24\%.$$

The organic carbon partition coefficient (K_{OC}) - The organic carbon partition coefficient can be estimated using Equation 3.4 using the derived partition coefficient values, K_d and the fraction of organic carbon, foc. The section below presents how K_{OC} was estimated using literature observations for K_d in combination with the foc presented above, as well as using the in-situ observations.

Estimating $\mathrm{K_{OC}}$ from scientific literature – The literature values for $\mathrm{K_d}$ from the report of Strenge and Peterson (1989) (Table 22) were used to estimate the organic carbon partition coefficient using the estimated f_{OC} = 4.24%. These values are shown in Table 27 below.

Table 27. K_{OC} (ml/g) values tabulated based on K_d values provided by Strenge and Peterson (1989) and F_{OC} = 4.24%.

pH	pH ≥ 9			pH 5-9			pH ≤ 5		
Total percent-by-weight composition of 1. Clay 2. Iron 3. Aluminum oxy-hydroxide 4. Organic Matter Contents	< 10% (Sandy soils)	10-30% (Loamy soils)	> 30% (Clayey soils)	< 10% (Sandy soils)	10-30% (Loamy soils)	> 30% (Clayey soils)	< 10% (Sandy soils)	10-30% (Loamy soils)	> 30% (Clayey soils)
Tin	530	117.9	117.9	117.9	235.85	235.85	530	117.9	117.9
Nickel	28.8	138.2	1533.0	287.7	1382.0	15330	28.3	138.2	1533.0
Uranium	0.0	117.9	1180.2	0.0	1180.2	11792	0.0	117.9	1180.2

Estimating $\mathrm{K_{OC}}$ from site observations – Using the derived values for uranium, as observed within Tims Branch for the control site and the low, mid and high contaminated locations, the following table presents the estimated values of $\mathrm{K_{OC}}$ for uranium for the different sections.

Table 28. Calculated K_{OC} Values Used as Input Values for MIKE ECO Lab

Class	K_{OC} in (L/Kg)	$\log K_{OC}$ in (L/Kg)	Area classification
Min	ND	NA	Control site (BP1)
Max	61,576	4.79	
Min	3,113,095	6.49	Low contaminated

Max	833,333 b	5.92	
Min	1,297,986	6.11	Mid contaminated
Max	2,103,858	6.32	
Min	2,692,145	6.43	High contaminated
Max	2,863,777	6.46	

b. Calculated K_{OC} =833,333 L/Kg. This was derived using Eq. 3.4., in which $K_d = 35{,}000\ L/Kg$ was divided by the $foc = 0.042$ (unitless).
ND= Not detected

Similarly for tin, assuming a mean value for K_d of 2,020 ml/g (see above), the calculated value of the organic carbon partition coefficient for Tims Branch as derived from the in-situ observations becomes:

$$K_{OC} = \frac{2020\ ml/g}{0.0424} \approx 47{,}640\ ml/g \text{ or } 47{,}640\ lit/kg$$

The desorption rate in sediment and suspended sediment particles of water (K_W) - The desorption rate from sediment and suspended solids particles in water, K_W, was derived by calculating the adsorption rate, K_a, for tin using the observational data presented in the report by Betancourt and Looney (2011) and using Equation 3.5. The estimated average tin concentration in the sediments of Tims Branch watershed within the top 3.5 inches from the A-014 Outfall downstream to the confluence of TB with Upper Three Runs Creek on average had been estimated as 26 $\mu g/g$ after 1,369 days of releasing tin into the river system (from the start of the M-1 Air stripping system to the monitored date). Therefore, K_a rate for tin can be calculated as:

$$K_a = \frac{26\ \mu g/g}{1369\ days} \approx 0.0190\ \mu g/g \text{ per day}$$

The obtained value of K_a can subsequently be used to derive estimates of the desorption rate, K_W, using the K_d values presented above.

Estimating K_W from scientific literature – The literature values for K_d from the report of Strenge and Peterson (1989) (see Table 22) were used to estimate the organic carbon partition coefficient using the estimated K_a = 0.0190 $\mu g/g$ per day for tin. These values are shown in Table 29 below.

Table 29. K_W Values Tabulated from K_d Values Obtained from Strenge & Peterson (1989)

pH	pH ≥ 9			pH 5-9			pH ≤ 5		
Total percent-by-weight composition of: 1. Clay 2. Iron 3. Aluminum oxy-hydroxide 4. Organic Matter Contents	< 10% (Sandy soils)	10-30% (Loamy soils)	> 30% (Clayey soils)	< 10% (Sandy soils)	10-30% (Loamy soils)	> 30% (Clayey soils)	< 10% (Sandy soils)	10-30% (Loamy soils)	> 30% (Clayey soils)
Tin	7.6e-3	3.8e-3	3.8e-3	3.8e-3	1.9e-3	1.9e-3	7.6e-3	3.8e-3	3.8e-3

Estimating K_W from site observations – Using the derived value of K_d of 2,020 ml/g for tin (see above) for Tims Branch as obtained from the field observations from Betancourt and Looney (2011), the estimated value of the desorption rate in water, K_W, becomes:

$$K_W = \frac{K_a}{K_d} = \frac{0.0190\ \mu g/g \text{ per day}}{2020\ ml/g} \approx 9.41\text{e-}6\ \mu g/ml \text{ per day}$$

It should be noted that this value is considerably lower compared to the values shown in Table 29.

The section above presents a detailed overview of the geochemical factors that are most likely to impact the partition coefficient (K_d). Reported or calculated coefficients were also mentioned in this report, which included the aqueous and sorbed uranium concentrations, as well as weight fraction of particulate organic matter and other sorbing materials. During the month of January, FIU achieved successful identification of K_d, foc, K_{oc} and K_W values for uranium and tin and partially for nickel using both literature and in situ observations to derive estimates. The uncontaminated soil samples revealed uranium K_d values of ~700 L/kg, at a pH of 5.5 (Kaplan et al., 2017). The higher the organic carbon content, the greater the uranium adsorption to the soil and the less uranium that will be available in the water column.

Setting up the heavy metal transport simulations for uranium

As indicated above for uranium both literature and field uranium soil-water measurements to estimate the partition coefficient (K_d). Using this information, two different calibration methods were developed which will provide guidance to the assessment. For the part of the river network of interest for uranium, these two methods are: 1) Using spatially variable Kd coefficients corresponding to different sections of the channel network, and 2) Using a spatially uniform Kd coefficient (using the Freundlich isotherm model). For the upstream sections of the river network as well as for various sub-branches, uranium contamination was assumed to be low. Here, background Kd values will be used (see below). Figure 66 describes the motivation behind the calibration of the Tims Branch uranium model.

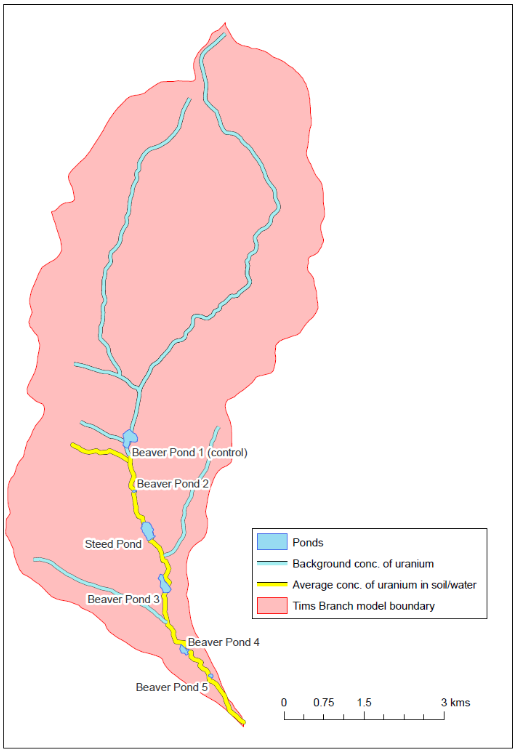

Figure 66. Adjusted soil and water uranium measurements from field and literature involving the calculation of partition coefficient using a variable Kd and an average Kd.

After setting up both methodologies, the next step is to initiate the calibration exercises using both the spatially variable and uniform Kd coefficient approaches. For the ECO Lab modeling setup, the parameter values derived above (i.e., Kd, foc, Kw, etc.) have been incorporated in the model. The figures below present this setup. Also, these simulations are currently being performed and the results will be evaluated in the coming months.

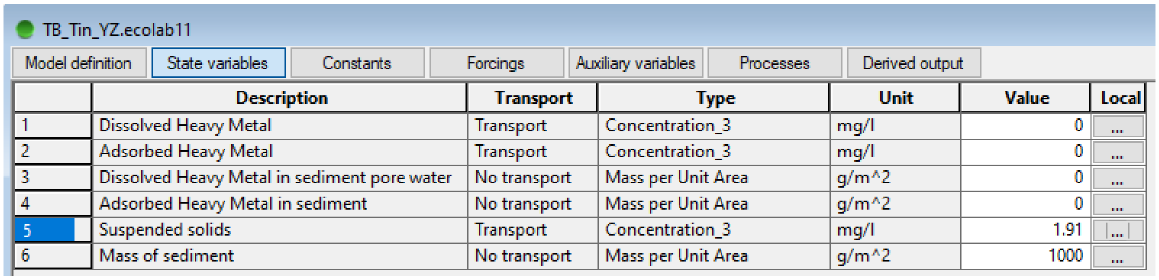

	Description	Transport	Type	Unit	Value	Local
1	Dissolved Heavy Metal	Transport	Concentration_3	mg/l	0	...
2	Adsorbed Heavy Metal	Transport	Concentration_3	mg/l	0	...
3	Dissolved Heavy Metal in sediment pore water	No transport	Mass per Unit Area	g/m^2	0	...
4	Adsorbed Heavy Metal in sediment	No transport	Mass per Unit Area	g/m^2	0	...
5	Suspended solids	Transport	Concentration_3	mg/l	1.91	...
6	Mass of sediment	No transport	Mass per Unit Area	g/m^2	1000	...

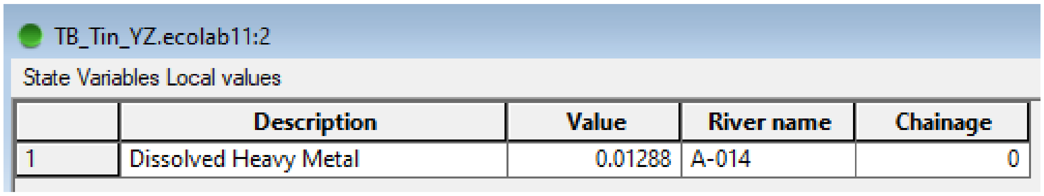

	Description	Value	River name	Chainage
1	Dissolved Heavy Metal	0.01288	A-014	0

Figure 67. Dissolved Heavy Metal (tin) concentration released as constant from A-014. Value obtained from Betancourt and Looney (2011).

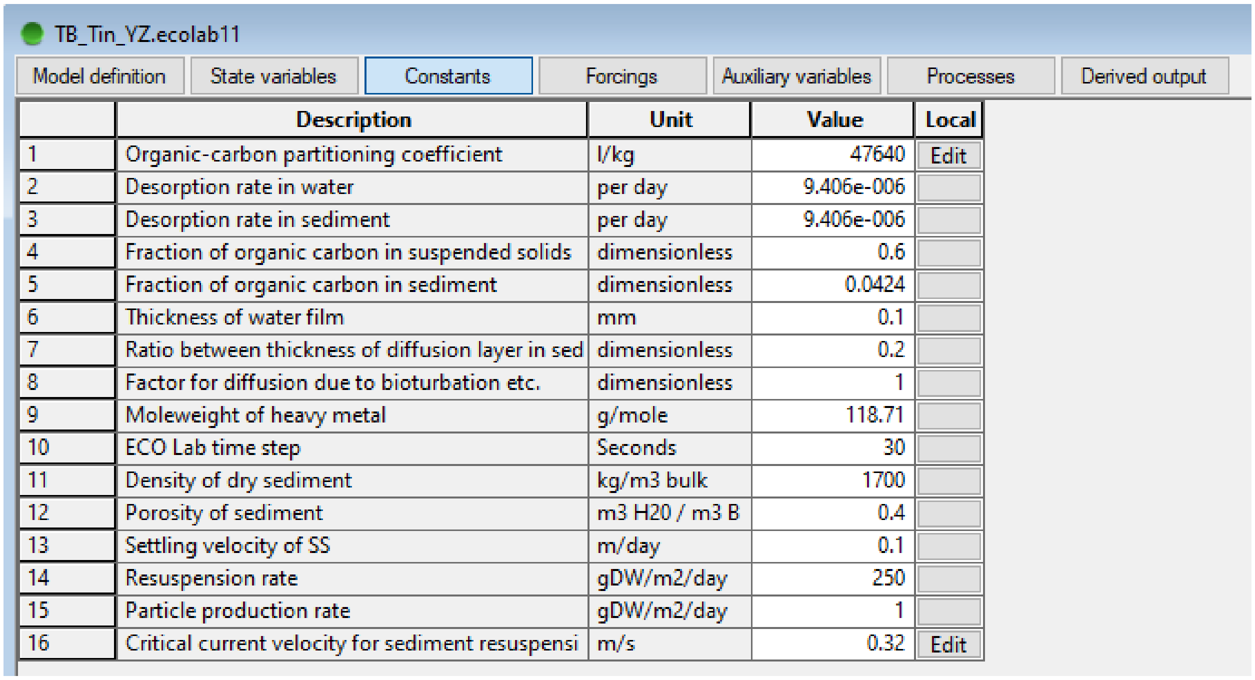

	Description	Unit	Value	Local
1	Organic-carbon partitioning coefficient	l/kg	47640	Edit
2	Desorption rate in water	per day	9.406e-006	
3	Desorption rate in sediment	per day	9.406e-006	
4	Fraction of organic carbon in suspended solids	dimensionless	0.6	
5	Fraction of organic carbon in sediment	dimensionless	0.0424	
6	Thickness of water film	mm	0.1	
7	Ratio between thickness of diffusion layer in sed	dimensionless	0.2	
8	Factor for diffusion due to bioturbation etc.	dimensionless	1	
9	Moleweight of heavy metal	g/mole	118.71	
10	ECO Lab time step	Seconds	30	
11	Density of dry sediment	kg/m3 bulk	1700	
12	Porosity of sediment	m3 H20 / m3 B	0.4	
13	Settling velocity of SS	m/day	0.1	
14	Resuspension rate	gDW/m2/day	250	
15	Particle production rate	gDW/m2/day	1	
16	Critical current velocity for sediment resuspensi	m/s	0.32	Edit

Figure 68. Constant values defined. K(oc), K(w), K(a), F(oc) were obtained in prior months and explained in previous reports. Density of sediment was obtained from Betancourt and Looney (2011). Critical current velocity was obtained through calibration from prior modelers.

Because the uranium soil and water quality measurements were obtained at different times, the calculated values for uranium were assumed to be uniformly distributed. The data at the contaminated locations were therefore grouped and the average calculated over a 3-year timespan to represent a uniformly spatially distributed measurement. Spatially uniform uranium model set-up

The field observational data were used to develop identify ECO Lab model parameters. It was decided to make use of both spatially uniform values as well as spatially distributed values within ECO Lab for the various chainage locations in Tims Branch. The following section provides specific details on the model parameter setup.

The MIKE SHE domain used in this setup was modified to 1 hour, with maximum allowed steps of 3 hours for the three modules: unsaturated and saturated zones, as well as overland flow. Meanwhile, MIKE 11 was set-up with 30 second time steps. This value reduces the instability errors in the advection dispersion (AD) courant number. The MIKE 11 results are stored hourly to evaluate the uranium concentrations hour by hour. Meanwhile, the results can be visualized both in a table and graph outlining hourly or daily measurements.

The boundary conditions in the water quality component of ECO Lab were included. In total, 564 transport initial uranium conditions were created and plotted in the domain, including a series of 282 spatially distributed dissolved uranium (in mg/L) values and 282 adsorbed uranium values in sediment (in g/m2). The soil uranium spatially distributed values are 1.82 g/m2 in the contaminated streambed and 0.05 g/m2 in the non-contaminated/ background areas.

The heavy metal template included in the ECO Lab module requires all the data at the same time interval. The heavy metal template uses 6 state variables, of which 3 are in the water phase, including (Transport) 1] Dissolved Heavy Metal, 2] Adsorbed Heavy Metal and 5] Suspended solids; and 3 of which are in the sediment phase (No Transport) 3] Dissolved Heavy Metal in pore water, 4] Adsorbed Heavy Metal in sediment and 6] Mass of Sediment.

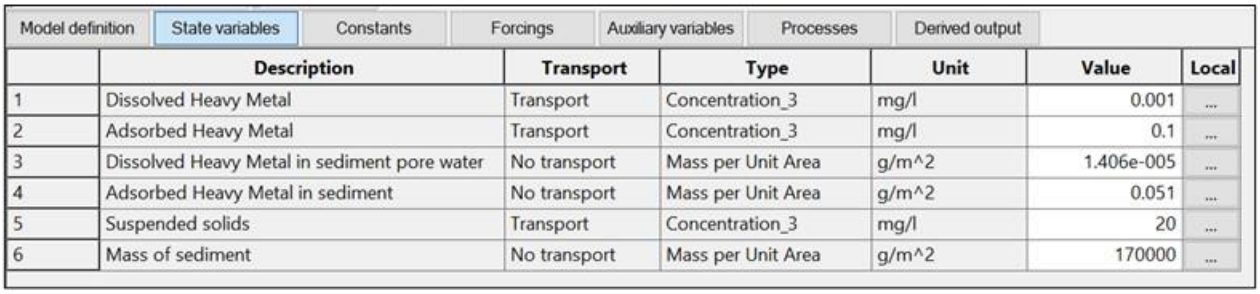

	Description	Transport	Type	Unit	Value	Local
1	Dissolved Heavy Metal	Transport	Concentration_3	mg/l	0.001	...
2	Adsorbed Heavy Metal	Transport	Concentration_3	mg/l	0.1	...
3	Dissolved Heavy Metal in sediment pore water	No transport	Mass per Unit Area	g/m^2	1.406e-005	...
4	Adsorbed Heavy Metal in sediment	No transport	Mass per Unit Area	g/m^2	0.051	...
5	Suspended solids	Transport	Concentration_3	mg/l	20	...
6	Mass of sediment	No transport	Mass per Unit Area	g/m^2	170000	...

Figure 69. State variables associated with the transport and non-transported uranium present in the Tims Branch model. Initial conditions in the state variables are associated with the spatially uniform model execution.

Spatially uniform uranium measurements for each variable [1,2, and 5] was needed. For this, it was assumed a uniform value as they are transported with the flow of water thus having a constant value for days without rain. Meanwhile, the uranium concentration increments will be based on:

- The amount of rainfall.
- Dissolved uranium in the water (SU): The spatially uniform values for the dissolved uranium used are 0.0013 mg/L in the uranium contaminated streams and 0.0010 mg/L in the non-contaminated/ background areas.
- Adsorbed uranium (XU): The spatially uniform value of 0.1 mg/L was assigned accounting the default value in the ECO Lab template.
- Suspended Solids (XSS): The state variables in ECO Lab were modified. Here the suspended solids parameter was obtained from field calculated observations in the summer of 2016, in which the mean observed suspended solids for Tims Branch stream is estimated to be 20 mg/L.

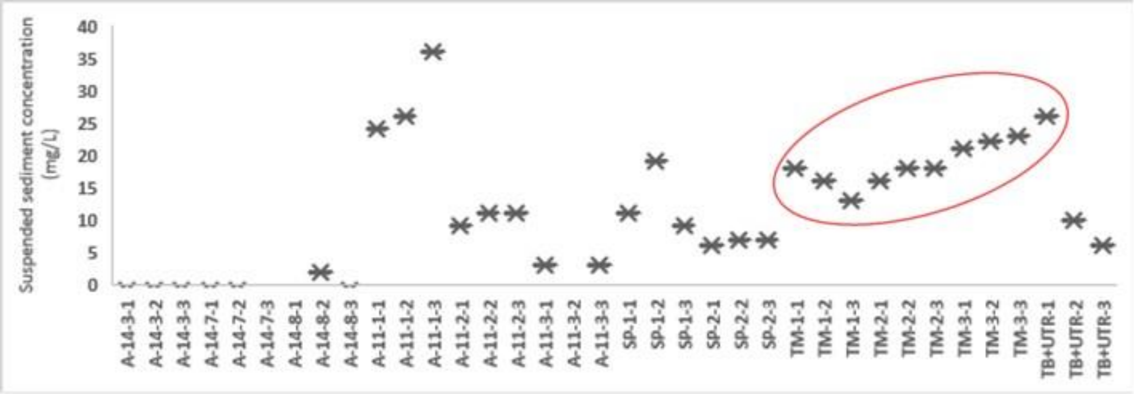

Figure 70. Suspended solids concentration from field calculated observations in summer 2016 at various monitoring points in Tims Branch.

For the non-transported state variables, the 4] adsorbed uranium in the sediment (XUS), the 3] dissolved uranium in pore water (SUS), and the 6] mass of the sediment (XSed), were adjusted using a spatially uniform value over time. In this exercise, the values were obtained from the different field observations, literature, and calculations.

- Adsorbed uranium in the sediment (XUS): The uranium values from (Betancourt et al., 2011; Pickett, 1990) were used as reference averages for the concentration of absorbed uranium in the sediments of Tims Branch watershed. Data from the top layer (3 inches) was used in this exercise following our assumption that the model uses a homogenous layer from the top 10 centimeters (MIKE DHI, 2009).
- Dissolved uranium in pore water SUS: The model default value of 1.406 E-5 g/m^2.
- Mass of sediment (XSED): It was estimated that the mass of sediment was 170,000 g/m^2 following the (Betancourt et al., 2011) environmental report where a value of 1.7 g/cm^3 is estimated.
- Constant variables

A resume of these parameters can be obtained from previous monthly reports. The parameters optimized were:

- Density of dry sediment in which 1,700 kg/m^3 was calculated from the environmental report (Betancourt et al., 2011).

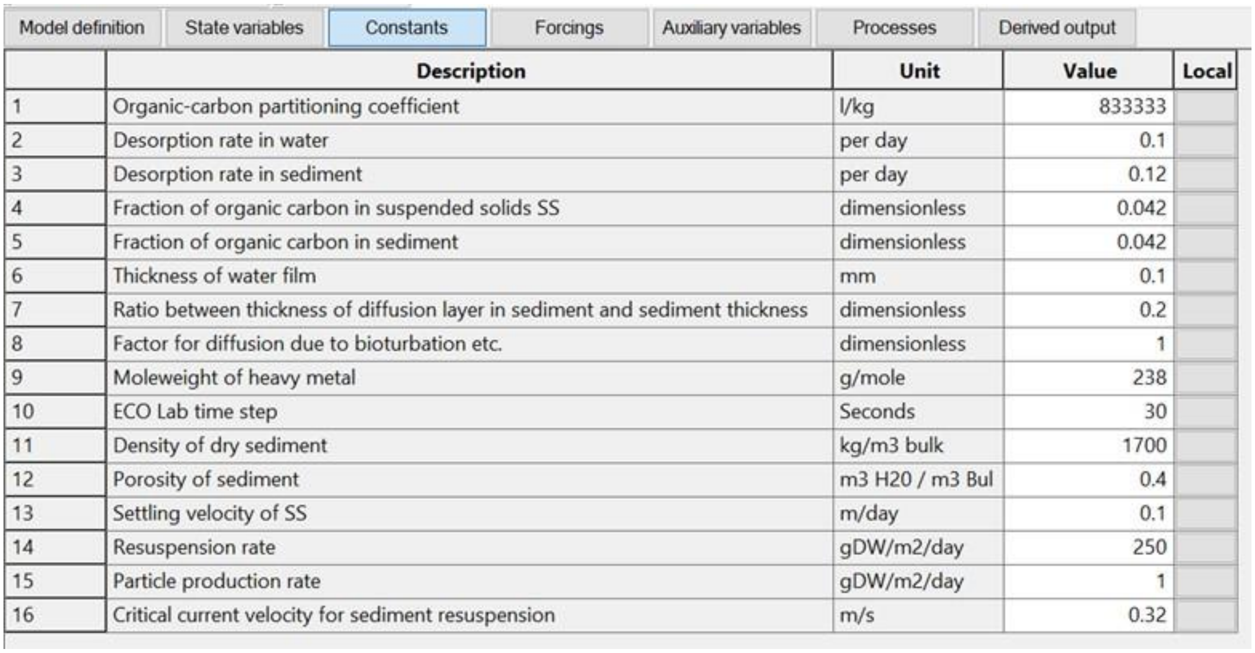

	Description	Unit	Value	Local
1	Organic-carbon partitioning coefficient	l/kg	833333	
2	Desorption rate in water	per day	0.1	
3	Desorption rate in sediment	per day	0.12	
4	Fraction of organic carbon in suspended solids SS	dimensionless	0.042	
5	Fraction of organic carbon in sediment	dimensionless	0.042	
6	Thickness of water film	mm	0.1	
7	Ratio between thickness of diffusion layer in sediment and sediment thickness	dimensionless	0.2	
8	Factor for diffusion due to bioturbation etc.	dimensionless	1	
9	Moleweight of heavy metal	g/mole	238	
10	ECO Lab time step	Seconds	30	
11	Density of dry sediment	kg/m3 bulk	1700	
12	Porosity of sediment	m3 H20 / m3 Bul	0.4	
13	Settling velocity of SS	m/day	0.1	
14	Resuspension rate	gDW/m2/day	250	
15	Particle production rate	gDW/m2/day	1	
16	Critical current velocity for sediment resuspension	m/s	0.32	

Figure 71. A resume with the constant ECO Lab model values as input in the setup.

The trend in suspended sediment concentrations, and discharge are important factors to understand the fate and transport of uranium-sorbed contamination in the Tims Branch stream. Nonetheless, trends in SSC and discharge can also have a high variability presently estimated because of seasonal river discharge changes, temperature changes, flow hysteresis, and changes in land use/

land cover (Mustard & Fisher, n.d.; Shen et al., 2013). The discharge and suspended sediment concentrations were investigated to identify the seasonal trends/variability if any. The method used in this exercise is the rating curve analysis.

Suspended sediment rating curves are commonly used to assess the patterns and trends in the river water quality. They are most often referred to as fitted relationships in between the river discharge (q) and the suspended -sediment concentrations (SSC) (Warrick, 2015.) These can also be used to estimate seasonal and long-term relationships among discharge and sediment. Statistically speaking, a poor correlation between the suspended sediment concentrations (SSC) and discharge (q) does not necessarily mean that a relationship does not exist. Meanwhile patterns associated with seasonal river discharge changes, flow hysteresis and changes in land cover can be the reason in this variability of the data (Mustard & Fisher, n.d.; Shen et al., 2013). Results of the rating curve are presented in the sections below.

FIU's suspended solid concentration data for 2016

Besides looking at observed data at the former USGS station in 1985, FIU also obtained SSC data during a 2016 field visit to Tims Branch stream (Applied Research Center, 2016). The sampling location is within the modeled area, and these samples were obtained using the gravimetric filtration system with paper filters. Records indicate that the average filter pore size was estimated at 6 microns.

Suspended Solids (XSS): The state variables in ECO Lab were modified. Here the suspended solids parameter was obtained from field calculated observations in the summer of 2016, in which the mean observed suspended solids concentration for Tims Branch stream was 20 (mg/L). These results were obtained during baseflow situations where flow rates were in the order of 0.3 m^3/s. The FIU SSC observations are of similar order of magnitude compared to those obtained during 1985, ranging from 5-20 mg/l (see Figure 72).

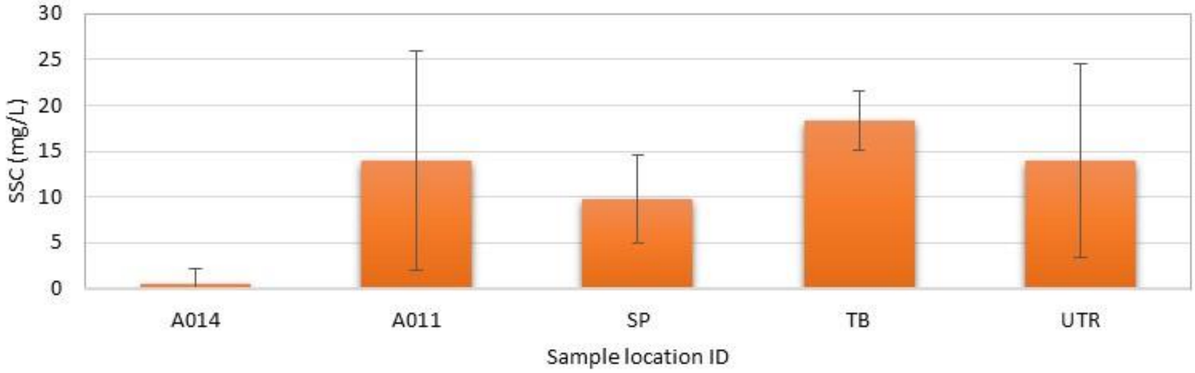

Figure 72. Average suspended sediment concentration data collected in Tims Branch watershed. Values collected represent baseflow conditions with an average stream velocity of 0.3 m^3/s.

It was determined that the temporal and spatial extent of the Tims Branch model was key to the calibration and model development. It was decided that the model for the Tims Branch stream reach branches from C98, C99, C100, A011, A014 and Tims Branch. Initial calibration focus was the Year 1993, which after providing good simulations, was extended to include the period 1991-1993.

The AD model was tested and calibrated over the period April to December 1993. The large quantity of model parameters in the AD module and the minimum amount of field observations typically complicate the model calibration/optimization. Many attempts were made to calibrate the AD model at Tims Branch, however the combined influence of thousands of computations proved to be too strong for the computing power available. Instead, a total of 40 continuous series of exercises were conducted to obtain corresponding similarities with the observed data values. The input parameters chosen for modification (i.e., mass of sediment, resuspension rate and critical current velocity) proved to be the controlling variables responsible for the SSC transport in ECO Lab. The simulation results were compared with the available observed and measured data, while adjusting the module input parameters with optimal ranges to provide the best agreement. The primary calibration parameters modified were mass of sediment, critical current velocity, and resuspension rate. During the experimental setup in the suspended sediment input data, it was expected that the simulated data would roughly follow significant peaks and lows in the measured suspended sediment concentration data, but not specifically directly corresponding to the data.

For the year 1993 it was possible to identify a set of model parameters that showed good correspondence with the observations. Figure 73 shows the sediment rating curves for both the historical observed and the best performing MIKE 11 simulations.

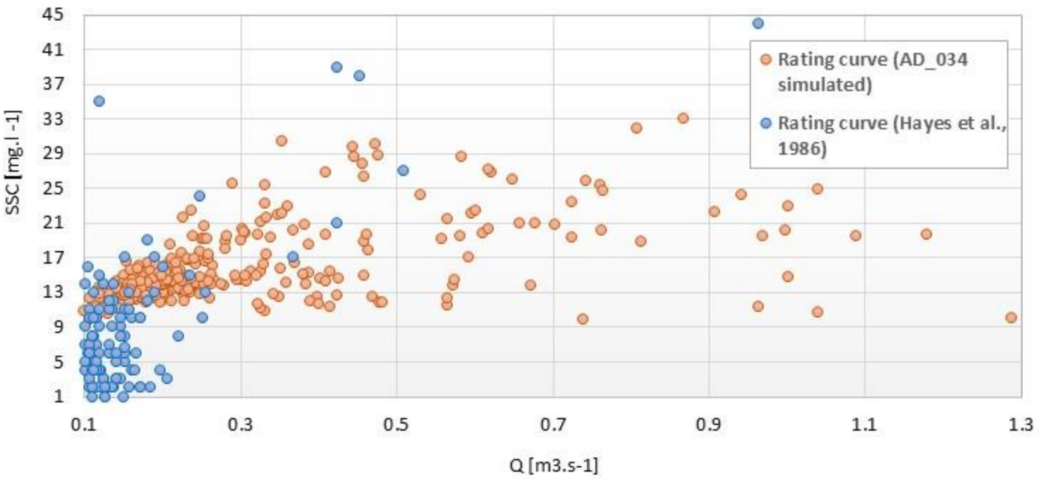

Figure 73. Rating curves at Tims Branch stream (09-10-1984 and 05-30-1985) in blue. Simulated suspended solid concentrations in orange for a short-term period.

In general, a good correspondence is shown between both datasets. The observational data shows that during baseflow conditions SSC are in the order of 5-15 mg/l, while during peak events these concentrations increase (10-45 mg/l). For the MIKE 11 model simulations baseflow SSC are in the order of 8-15 mg/l and increase as discharge increases, similar to the observations from 1984-1985. It should be noted that the observational dataset contained mainly winter groups of events. Also, the correlations between discharge and SSC are generally stronger at this group. A greater steepness of the slopes is observed, establishing a stronger correlation between the SSC and discharge. However, overall MIKE shows the correct relation with increasing SSC as flow rate increases and at a similar order of magnitude.

The simulated timeseries of the MIKE 11 model are given in the figure below, where the first four months are not taken into account as these are used for model spin-up.

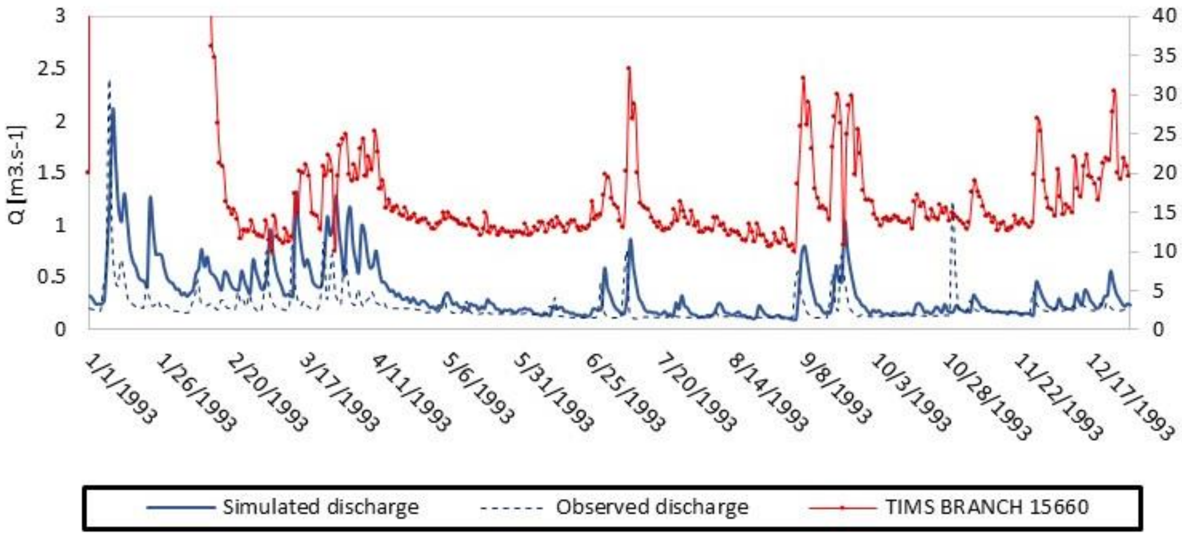

Figure 74. Time series of observed (dashed) and simulated discharge (blue) at Tim Branch outlet as well as simulated SSC (red).

Given the good model results, the impact of these parameters on the longer-term period from 1991-1993 is currently being reviewed (see Figure 75). Using the optimal parameter values, initial results show that for this longer period the simulated data are not in congruence with the lows and event peaks, especially during October 1992 through April 1993. The reasons for this behavior are currently being evaluated. These results will be presented in subsequent months.

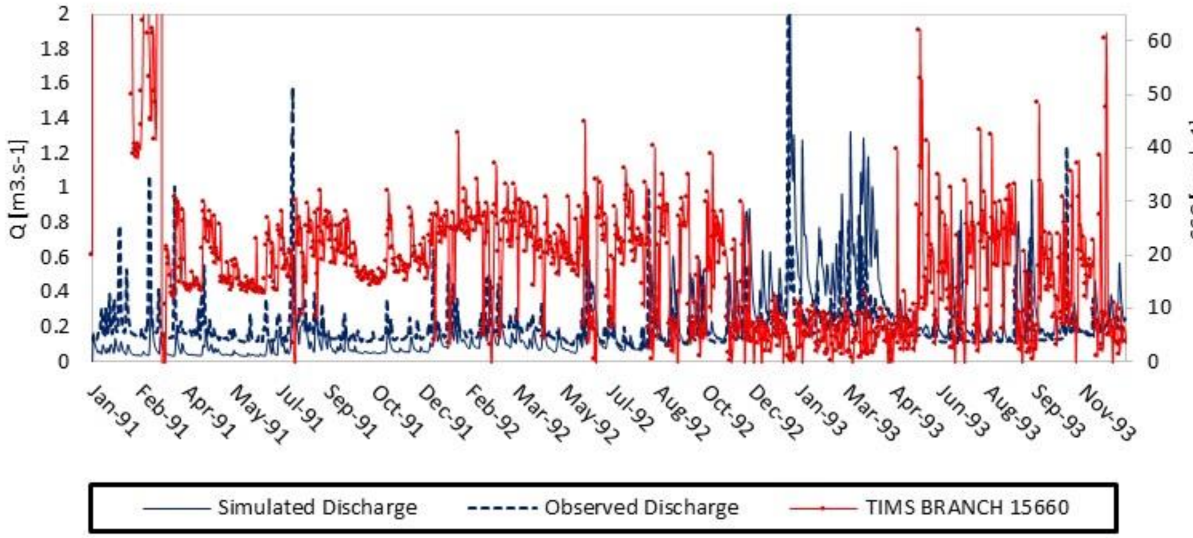

Figure 75. Similar to Figure 74 but for the period 1991-1993.

Uranium transport modeling

The various MIKE ECO Lab model parameters for uranium were estimated as indicated above, also from in-situ observations and from literature review. Using the previously defined model setup, Figure 76 and Figure 77 show the corresponding simulated uranium concentrations, both dissolved and absorbed to the suspended solids.The model simulations show that (almost) all uranium is attached to the suspended solid particles (comparing Figure 76 with Figure 77). Similar to the temporal suspended solid behavior, it can be observed that during storm events uranium concentrations increase, as can be observed from Figure 77.

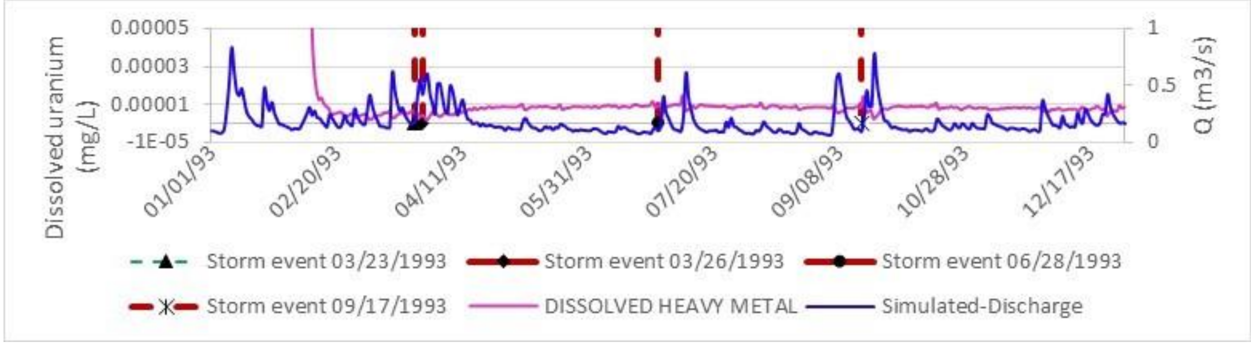

Figure 76. Simulated discharge by MIKE 11 (blue) and dissolved uranium concentration by MIKE 11 ECO Lab for Tims Branch for the year 1993.

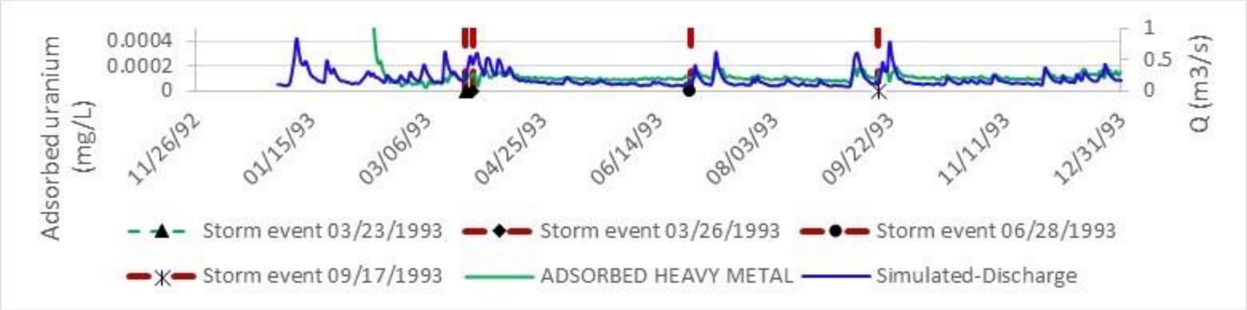

Figure 77. Simulated discharge by MIKE 11 (blue) and absorbed uranium concentration by MIKE 11 ECO Lab for Tims Branch for the year 1993.

The next step is to compare the results to those observed as well as vary the model parameters using maximum and minimum values as derived from observations. In addition, a spatially variable channel bed concentration of uranium will be used, which is more in line with observations.

Figure 78 shows the simulated dissolved and absorbed uranium concentrations using spatially uniform channel bed concentrations and ECO Lab parameter values. It can be observed from these results that uranium is much more present in the adsorbed phase as compared to the dissolved phase. Also, it can be observed that uranium concentrations increase with increases in runoff.

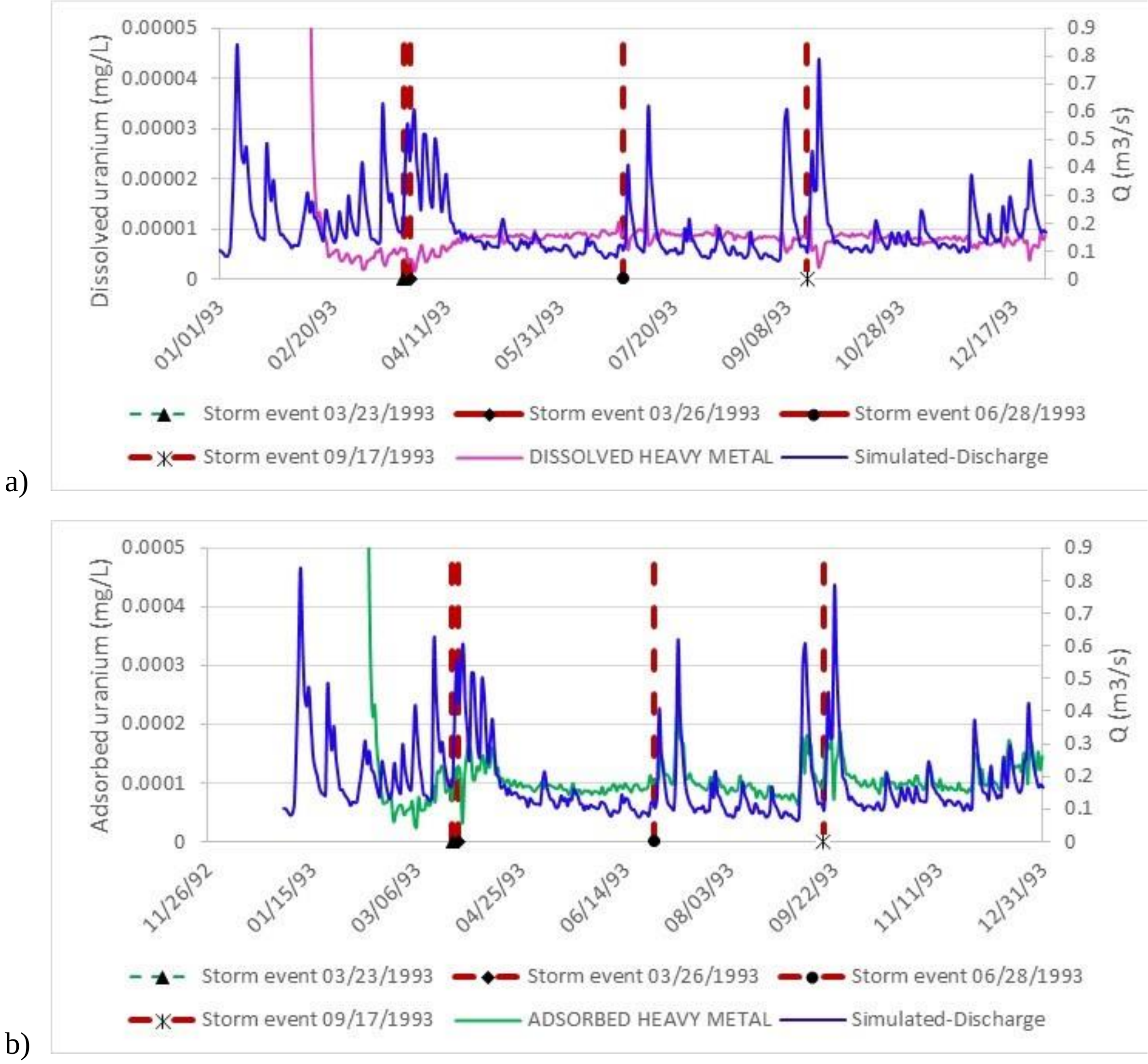

Figure 78. Simulated dissolved (panel a) and absorbed (panel b) uranium using spatially uniform MIKE ECO Lab parameter values.

Similarly, in Figure 79, the results are presented using a spatially variable modeling setup. Also, here more uranium is present in the adsorbed phase with increased concentrations during storm events. The next step is to compare these results as well as include additional ECO Lab modeling parameter values as previously derived and presented in earlier monthly reports. Also, FIU will zoom in to the four different flow events for which historical data is available. These results will be presented in future monthly reports.

a)

b)

Figure 79. Similar to Figure 78, simulation results after using spatially variable channel bed uranium concentration as well as spatially variable ECO Lab parameter values.

This subtask is currently delayed due to the departure of the DOE Fellow PhD student, Juan Morales, who was supporting these tasks and who had intent to use some of the results for his PhD dissertation. Efforts are currently focused on restructuring resources and finding support to complete this modeling effort.

Tin and Nickel transport modeling

The results above show that during FIU Year 2 we were able to identify the various ECOLab modeling parameter for tin and nickel. However, due to the fact that the Postdoc responsible for this part of the project, left during Year 2, it was decided in close interaction with SRNL collaborators to not focus further on the simulation of tin and nickel for Tims Branch.

Subtask 3.1: References

Baes, C. F., & Sharp, R. D. (1983). A Proposal for Estimation of Soil Leaching and Leaching Constants for Use in Assessment Models. Journal of Environmental Quality, 12(1), 17–28. https://doi.org/10.2134/jeq1983.00472425001200010003x

Batson, V.L., P.M. Bertsch, and B.E. Herbert. 1996. Transport of anthropogenic uranium from sediments to surface waters during episodic storm events. J. Environ. Qual. 25:1129–1137.

Bea, S. A., Wainwright, H., Spycher, N., Faybishenko, B., Hubbard, S. S., & Denham, M. E.

(2013). Identifying key controls on the behavior of an acidic-U(VI) plume in the Savannah River Site using reactive transport modeling. Journal of Contaminant Hydrology, 151, 34–54. https://doi.org/10.1016/j.jconhyd.2013.04.005

Betancourt, A., Looney, B. B. (2011) "Tin Distribution and Fate in Tims Branch at the Savannah River Site". U.S. Department of Energy Office of Environmental Management under Grant No. DE-EM0000598.

Campbell, J. (2011). Porosity. Complete Casting Handbook, V(xiii), 391–464. https://doi.org/10.1016/b978-1-85617-809-9.10007-6

Denham, M. E. (1999). SRS Geology/Hydrogeology Environmental Information Document. https://doi.org/10.2172/10526

DHI Water & Environment. (n.d.). Heavy Metal MIKE ECO Lab Template Scientific Description. Retrieved January 24, 2019, from www.mikepoweredbydhi.com

EPA, U., of Radiation, O., & Air, I. (1999). UNDERSTANDING VARIATION IN PARTITION COEFFICIENT, K d , VALUES Volume I: The K d Model, Methods of Measurement, and Application of Chemical Reaction Codes. https://www.epa.gov/sites/production/files/2015-05/documents/402-r-99-004a.pdf

Fetter, C.W. 1988. Runoff and streamflow. P. 37-61. In Applied hydrology. 2nd ed. Merrill Publ., Columbus, OH.

Freer J, Beven K, and Ambroise B, 1996. Bayesian estimation of uncertainty in runoff prediction and the value of data: an application of the GLUE approach. Water Resources Research, 32 (7), 2161–2173. doi:10.1029/95WR03723

Hall J, et al., 2005. Distributed sensitivity analysis of flood inundation model calibration. Journal of Hydraulic Engineering, 131 (2), 117–126. doi:10.1061/(ASCE)0733-9429(2005)131:2(117)

Hayes, D.W., and C.D. Ouzts. 1986. Sediment transport studies in Tims Branch. Rep. DPST-86-468. E.I. du Pont de Nemours & Co, Savannah River Laboratory, Aiken, SC.

Helsel, D.R. Less than obvious; statistical treatment of data below the detection limit. Environ. Sci. Technol 24(12);1767-1774.

Hornberger G and Spear R, 1981. An approach to the preliminary analysis of environmental systems. Journal of Environment Management, 12, 7–18.

Kaplan, D.I., Buettner, S.W., Li, D., Huang, S., Koster van Groos, P.G., Jaffé, P.R., et al. In situ porewater uranium concentrations in a contaminated wetland: Effect of seasons and sediment depth. Applied Geochemistry [Internet]. 2017 Oct 1 [cited 2019 Jan 26];85:128–36. Available from: https://www.sciencedirect.com/science/article/pii/S0883292716303626#tbl1

Killian, T.H., Kolb, N.L., Corbo, P., Marine, I.W., 1987. F-Area Seepage Basins: Environmental information document. E.I. du Pont de Neumors & Co., Aiken, SC 29808 .Long, S. (2009). An Integrated Flow and Transport Model to Study the Impact of Mercury Remediation Strategies for East Fork Poplar Creek Watershed, Oak Ridge, Tennessee. https://doi.org/10.25148/etd.FI09121604

Looney, B. B., Eddy, C. A., Ramdeen, M., Pickett, J., Rogers, V., Scott, M. T., & Shirley, P. A.

(1990). Geochemical and Physical Properties of Soils and Shallow Sediments at the Savannah River Site. May, 113.

Looney, B. B., Jackson, D. G., Peterson, M. J., Mathews, T. J., Southworth, G., Bryan, L., Paller, M., Eddy-Dilek, C., Halverson, N. (2010) "Assessing Potential Impacts of Stannous Chloride Based Mercury Treatment on a Receiving Stream Using Real-World Data from Tims Branch, Savannah River Site". Prepared for Karen Skubal, U.S. Department of Energy Environmental Management Office of Groundwater and Soil Cleanup (EM-32), Washington DC. SRNL-STI-2010-00393.

McCarthy, J. F., & Zachara, J. M. (1989). Subsurface transport of contaminants: binding to mobile and immobile phases in groundwater aquifers. Environmental Science & Technology, 23(5), 496–502. https://doi.org/10.1021/es00063a001

MIKE DHI. (2009). Heavy Metal Template. October.

Rheinheimer, D. S., Labanowski, J., Elsass, F., Cambier, P., & Tessier, D. (2007). Heavy metal transport modelling in soil : sorption / desorption phenomena , water fluxes and contaminant fate. Tópicos Em Ciência Do Solo, 5(1), 135–180.

Serkiz, S. M., Johnson, W. H., Wile, L. M. J., & Clark, S. B. (2007). Environmental Availability of Uranium in an Acidic Plume at the Savannah River Site. Vadose Zone Journal, 6(2), 354–362. https://doi.org/10.2136/vzj2006.0072

Soil Screening Guidance: Technical Background Document Second Edition. 1996.

United States Environmental Protection Agency, Region 3 Hazardous Waste Management Division Office of Superfund Programs 1650 Arch St. Philadelphia, PA 19103-2029.Batson, V.L., P.M. Bertsch, and B.E. Herbert. 1996. Transport of anthropogenic uranium from sediments to surface waters during episodic storm events. J. Environ. Qual. 25:1129–1137.

Subtask 3.2: Model Development for Fourmile Branch with Specific Focus on the F-Area Wetlands

Subask 3.2: Introduction

The F-Area wetlands at the U.S. Department of Energy's (DOE's) Savannah River Site (SRS) has been a primary area of concern due to the presence of low-level radiological contamination in the groundwater, which originated from the disposal of 1.8 billion gallons of acidic, low-level radioactive waste from 1955 to 1988 in three unlined basins, known as the F-Area Seepage Basins. While most of the dispositioned radionuclides such as plutonium isotopes and cesium-137 sorbed to the basin soil, other mobile contaminants such as uranium (U) isotopes, strontium-90 (Sr-90), iodine-129 (I-129), technetium-99 (Tc-99), tritium (3H), and nitrate (NO_3^-) migrated through the vadose zone into the aquifer zone contaminating the groundwater. Over time the contaminant plume migrated downstream extending from the basins approximately 600 m downgradient, resurfacing at outcrops (seep lines) in the adjacent wetlands and entering the Fourmile Branch stream system (see figure below). As such, Fourmile Branch and its associated wetlands have been impacted by the outcropping of contaminated groundwater coming from the F-Area Seepage Basins.

The groundwater-surface water interface is the region where contaminated groundwater emerges to the surface, which is often one of the major ecological and human health risk exposure pathways. In the F-Area, I-129 is one of the main contaminants of concern. Over the years at several surface water stations (e.g., FAS-091 and FAS-092), there has been seasonal variation of I-129, in which high concentrations were detected during summertime while low concentrations were detected during winter/spring. These seasonal variations have not been observed at upstream groundwater wells, such as FSP-47A, where I-129 concentrations have remained fairly constant and lower since 2010. The spikes in I-129 concentrations observed at surface water stations during the summer suggest that there are processes (e.g., geochemical, microbial, physical) releasing I-129 from wetland soils to surface waters that are still not well understood. The concerns exist, therefore, with the stability of I-129 and other radioactive contaminants that have attenuated in organic rich seepline sediments as geochemical conditions slowly return to baseline conditions over the next few decades.

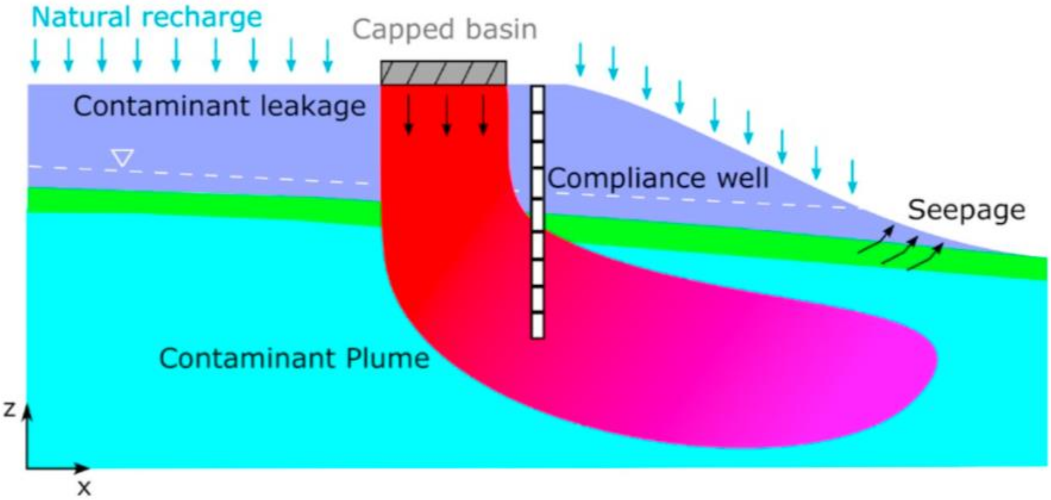

Figure 80. Schematic conceptual 2-D cross section of the F-Area focus domain and the existing residual contamination in the vadose zone and groundwater (from: Libera et al., 2019, JCH).

The F-Area Seepage Basins were closed and capped with a low-permeability material in 1988 after discharge operations ended. Furthermore, pump-and-treat remediation of contaminated groundwater was used to reduce to reduced dissolved phase contamination. In 2004, a funnel-and-gate system with groundwater flow barriers were constructed to decrease the groundwater gradient and enhance natural attenuation. Also, periodic base injections have been conducted at the gates to neutralize groundwater pH and cause the attenuation of uranium and Sr-90 by enhanced adsorption to mineral surfaces. Just upgradient of the base injection zones at the central gate, I-129 is being treated by injection of silver chloride particles. The particles react with I-129 that exist as iodide to form sparingly soluble silver iodide, removing I-129 from the groundwater. Currently, groundwater remains unnaturally acidic with high levels of various radionuclides and other contaminants upgradient of the funnel-and-gate.

Nowadays, remediation focuses on an enhanced monitored natural attenuation (MNA) approach, with periodically injecting a base solution to increase the sorption of cationic contaminants, making them less bioavailable. While these strategies are successful in sequestering the contaminants of concern, a long-term monitoring strategy is necessary at the zones of vulnerability of Fourmile Branch where there is potential for contaminant remobilization if changes in biogeochemical conditions occur that could potentially influence the release of contaminants.

Subtask 3.2: Objectives

FIU’s aim is to develop a hydraulic flow model for the Fourmile Branch riparian stream system near the SRS F-Area. This is critical for understanding the flow of contaminants to the down gradient stream. Currently, the Advanced Long-Term Environmental Monitoring Systems (ALTEMIS) project team has developed a detailed groundwater model using the Amanzi platform to model flow and reactive transport upstream of the seep line; however, the processes occurring beyond the seep line within the riparian zone and river network remains unclear. To understand the transport of contaminants from subsurface to surface and then to surface water, there is a need to improve the understanding of the groundwater-surface water dynamics occurring in the F-Area wetlands.

Currently, the ALTEMIS project is investigating the groundwater-surface water biogeochemistry dynamics occurring in the F-Area up to the seep lines in order to understand the I-129 transport from subsurface to surface, and then to surface water. These dynamics include groundwater table fluctuations as well as water temperature and chemistry to identify the extent of the water-saturated soil at the seepline as it migrates upslope under wetter conditions, as well as flow rate and the impact of precipitation on these controlling variables. Starting in 2022, a detailed monitoring network will be installed to measure the geochemisty at the surface water-groundwater interface along the seep line and its seasonal variability. Changes in moisture conditions at the seep line from unsaturated to saturated zones likely affect redox and microbial processes that strongly affect contaminant mobility.

The goal of FIU in FIU Year 2 was therefore to work with collaborators at Savannah River National Laboratory (SRNL) and Lawrence Berkeley National Laboratory (Berkeley Lab) to support the existing research being conducted under the ALTEMIS project and develop a detailed conceptual model of the hydrological flow processes occurring within the seepline over time in response to precipitation and throughout the different seasons (i.e. lateral (shallow) surface flow vs groundwater seepage) through a detailed assessment of in situ observations, and based on this conceptual understanding, build a hydrological model focusing on the flow of groundwater downslope through the funnel and gate system, and entering the seep line – riparian zone – river network using the MIKE model.

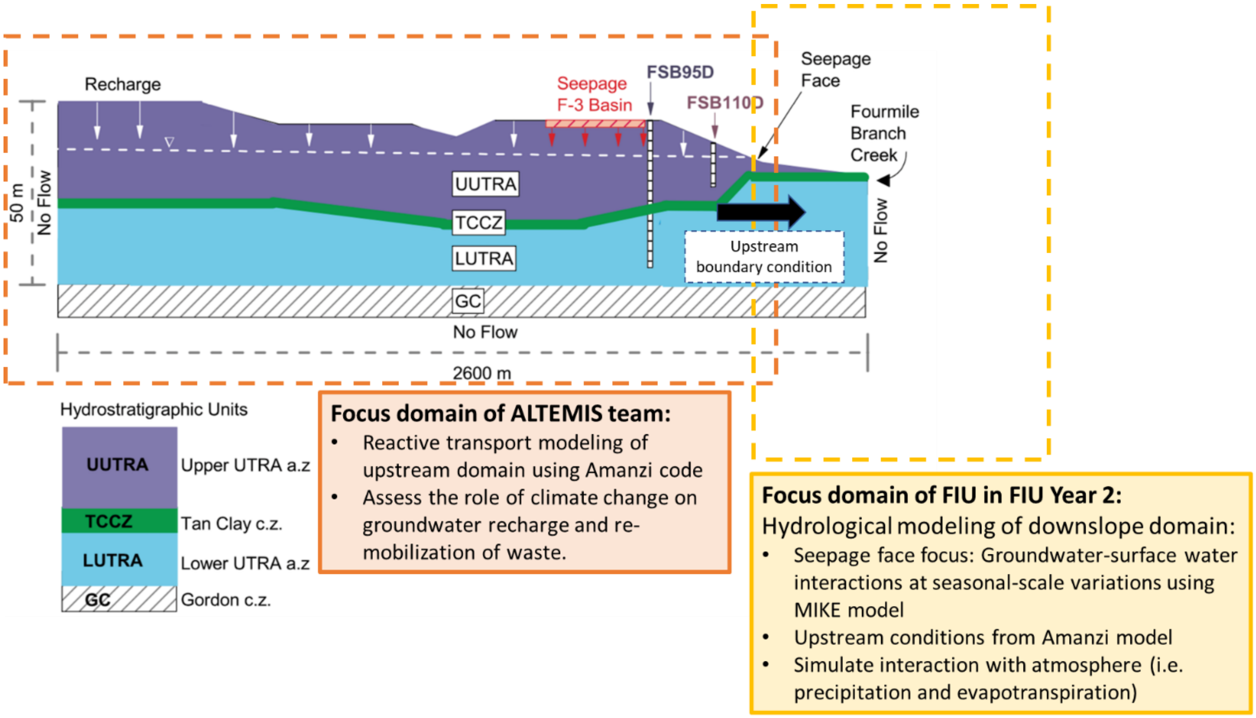

Focus domain of ALTEMIS team:

- Reactive transport modeling of upstream domain using Amanzi code
- Assess the role of climate change on groundwater recharge and re-mobilization of waste.

Focus domain of FIU in FIU Year 2:

Hydrological modeling of downslope domain:

- Seepage face focus: Groundwater-surface water interactions at seasonal-scale variations using MIKE model
- Upstream conditions from Amanzi model
- Simulate interaction with atmosphere (i.e. precipitation and evapotranspiration)

Figure 81. Lateral overview of the F-Area and how the domain of focus of the ALTEMIS project differs from FIU's proposed modeling effort under Subtask 3.2.

Initially a 2D version of the model will be created to obtain and increased understanding of the flow dynamics, followed by 3D modelling of the groundwater-seepline-river network system and the role of the funnel and gate system (see figure above). Subsequently (i.e. end of FIU Year 2 or Year 3), in close interaction with the SRNL and LBNL team, the model can be extended to include biogeochemistry focusing on the fate and transport of I-129 and other heavy metals (to be determined) in this contaminated region, focusing on remobilization of previous sequestered contaminants by temporal changes in hydrological conditions.

Subtask 3.2: Methodology

During FIU Year 2, FIU continued the data collection and pre-processing activities to support the development of an integrated surface/subsurface model to simulate the hydrological processes and the groundwater/surface interactions occurring at the SRS F-Area wetlands and Fourmile Branch. FIU also continued to review relevant literature and collect SRS site characterization data required for model development. Spatial and time series data collected in FIU Year 1 was processed and converted to compatible formats accepted by the MIKE hydrological model. The data includes but is not limited to (i) climatic data including rainfall and evapotranspiration, (ii) geospatial layers and associated databases including high resolution digital elevation models (DEMs), soil, geology and vegetation, (iii) hydrological conditions including records of river discharge and stage, locations of outfalls and hydraulic structures such as culverts, dams, etc., and (iv) water quality parameters relevant to transport and interactions of contaminants and sediment (such as partitioning coefficient, desorption rate, critical velocity and settling velocity). Training was provided to an FIU undergraduate student on collection of GIS data from federal, state and local online databases, GIS data management using ArcGIS geodatabases, as well as geoprocessing and visualization of GIS data using maps and graphs for reporting purposes. These data will enable the development of a conceptual understanding of the hydrological response of Fourmile Branch, which will subsequently result in the development of a detailed hydrological-hydraulic-transport model using the MIKE SHE/MIKE 11 and the ECO Lab module.

For **FIU Year 2,** FIU will develop an initial version of this detailed hydrological model of the seep line focusing specifically on the groundwater, riparian zone and river network interaction and the role of the funnel and gate system. The model will be forced within precipitation and weather data from nearby observations (as collected above). FIU will also incorporate water level data that can provide information of the groundwater flow patterns and discharges into the wetland areas. As a lateral upstream boundary condition, simulated water fluxes from the Amanzi model will be used, which will be provided by the Berkeley Lab team and ALTEMIS scientists (see Figure 81 above). Subsequently, the MIKE model can be extended to the 3D domain to gain an improved understanding of the ground water/riparian zone/river interface in the F-Area and upper portion of Fourmile Branch. Specifically, model results will be compared to in situ observations to be collected in the F-Area starting early 2022.

Subtask 3.2: Results and Discussion

The first step was to gain an improved understanding of the water balance and the size and variability of the various observations obtained at the F-Area site and the hillslope and riparian zone downslope.

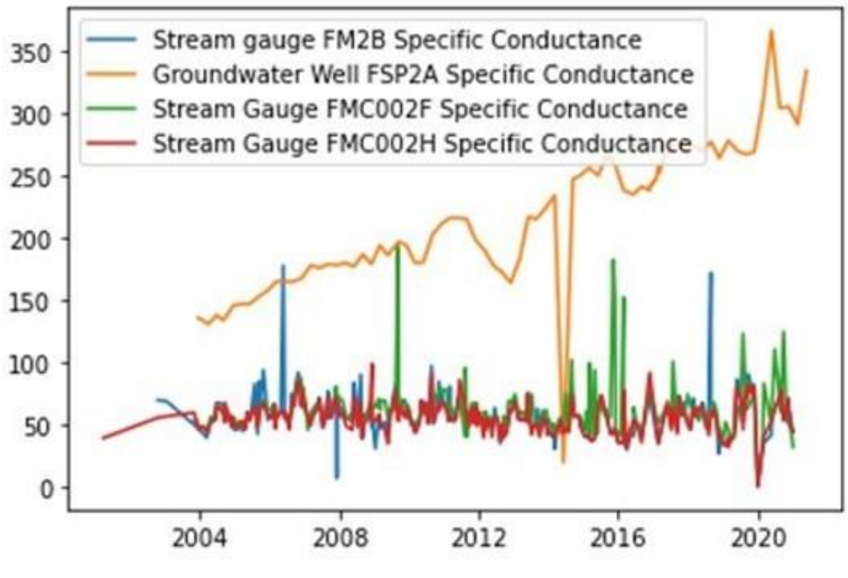

Figure 82. Example of observed specific conductance at three different locations within the river section downstream of the F-Area as well as the specific conductance within one of the groundwater wells.

The precipitation was analyzed from 1993 – 2020, during which the average rainfall was also calculated to be 47.02 inches. By looking at each yearly precipitation value, it can be observed that between 1999-2012 there was a decrease in rainfall totals. In recent years the total precipitation per year has since increased. The maximum yearly rainfall accumulation during this time period was recorded in 2003 and 2013 with over 60 inches of rain recorded in both years.

Besides looking at the yearly overview of the precipitation, the individual months were also observed to determine which months received the most rain, and which were the drier months. Figure 83 shows both the monthly average sum of precipitation for the 27-year time period, and the boxplot of each month which represents the median value of precipitation for each month. (Each month between 1993-2020 has a value of the sum of precipitation received. The values were then organized by month, and then the median value was found for each of the months).

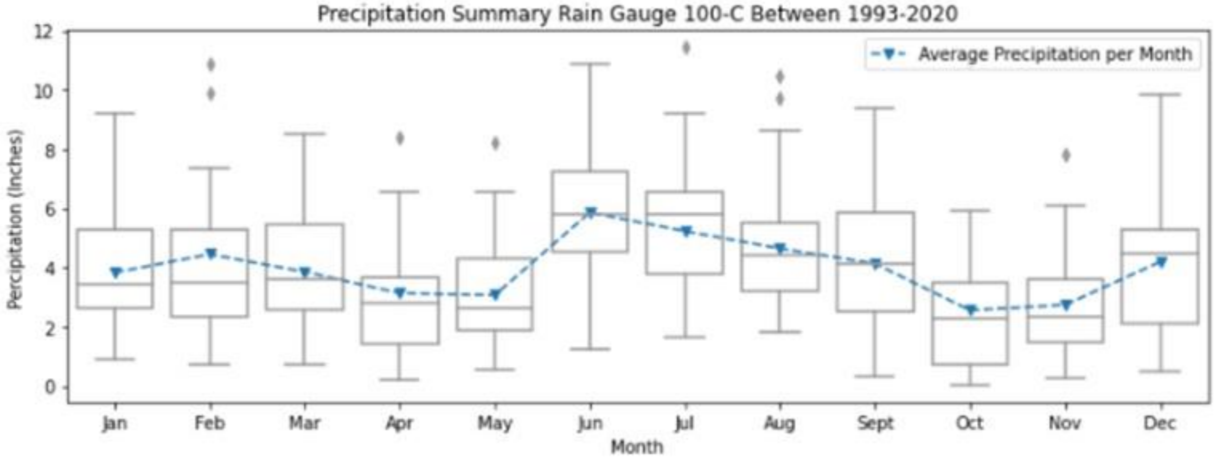

Figure 83. Monthly average precipitation between 1993-2020 at rain gauge 100-C (blue line) and a boxplot of each month showing the median value of precipitation for each month.

From the figures above the monthly precipitation recorded at this rain gauge are the highest during the summer months. Monthly precipitation peaks in June and declines in the following months. The months of October and November receive the least amount of rain. From the figure above, the outliers are seen to only be greater than the mean. There are no outliers below the mean. This shows that in the F-Area droughts or long periods without rain rarely occurred.

Boxplots were also completed for the air temperature recorded at the stream gauges within the F-Area of the Fourmile Branch watershed. Both the air and water temperature boxplots were organized in quarters due to the data being collected quarterly.

Q1 = Jan, Feb, Mar

Q2 = Apr, May, Jun

Q3 = Jul, Aug, Sept

Q4 = Oct, Nov, Dec

During the summer months in Q2 and Q3, the air temperature is shown to be the highest. The medians are similar between both quarters. Meanwhile, Q4 has the coldest air temperature. Not many outliers exist at either stream gauge, meaning that the IQR shown in the plots below shows a majority of the air temperature in the F-Area.

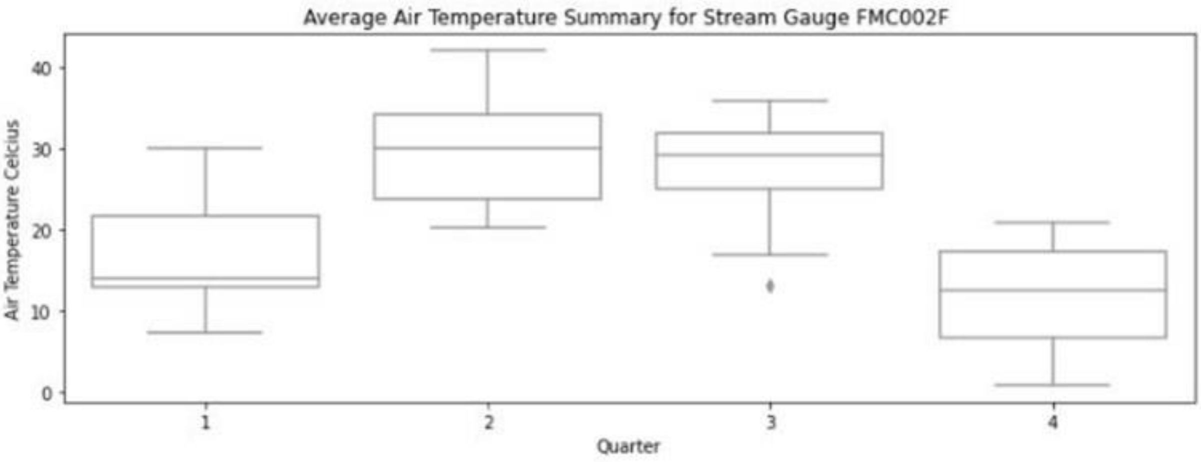

Figure 84. Average quarterly air temperature at stream gauge# FMC002F.

The boxplot of the water temperature data follows a similar pattern as the air temperature boxplots. Higher temperatures were recorded during the summer months whereas in the winter months the water temperatures are cooler. From comparing both the water and air temperatures, it does appear that neither data has high variability since not many outliers exist.

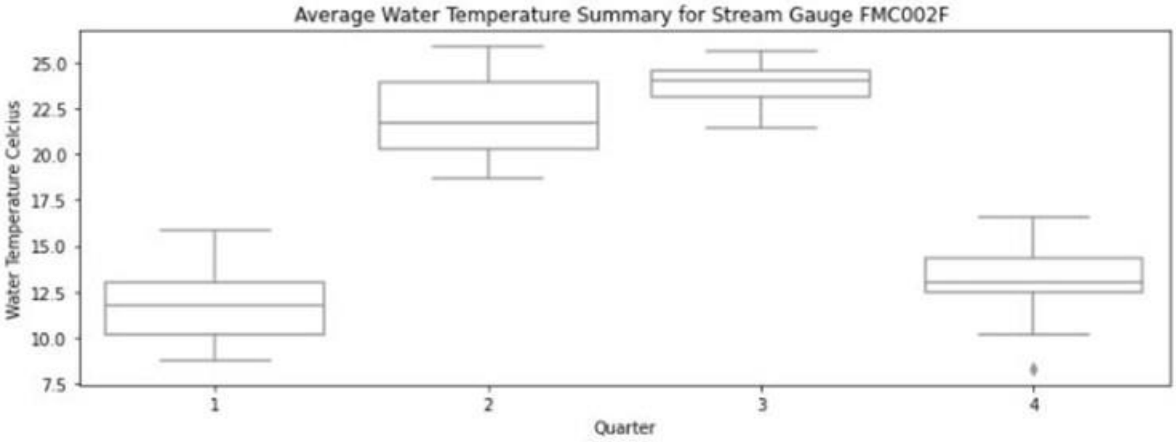

Figure 85. Average quarterly water temperature at stream gauge FMC002F.

Another parameter that was analyzed using boxplots was the flow rate at different stream gauges in the F-Area of Fourmile Branch watershed (Figure 86 and Figure 87). The flow rate averages in each quarter matched with the analysis that was done during the summer. March has the greatest flow rate while the flow rate throughout the rest of the year remains somewhat consistent. September and October have the lowest flow rate.

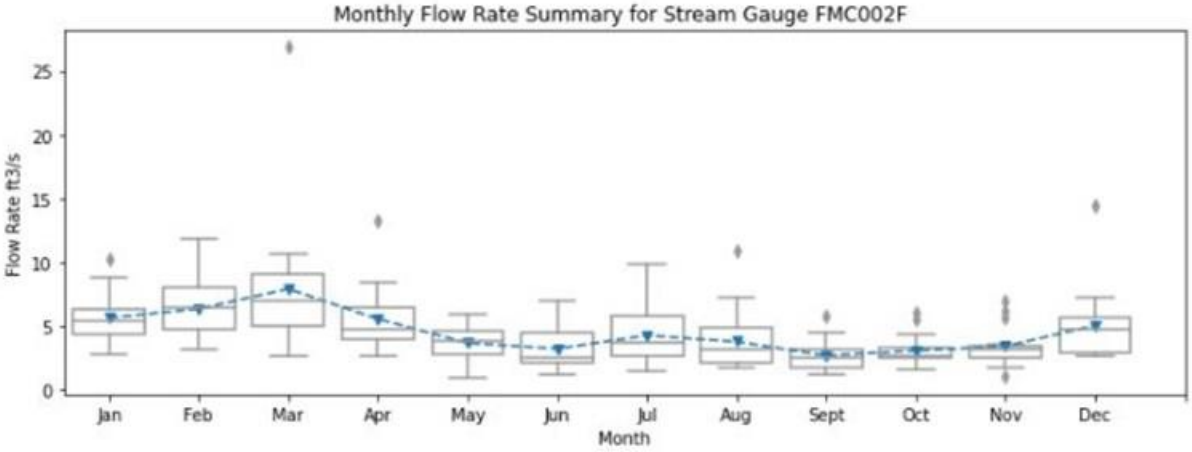

Figure 86. Monthly flow rate at stream gauge FMC002F.

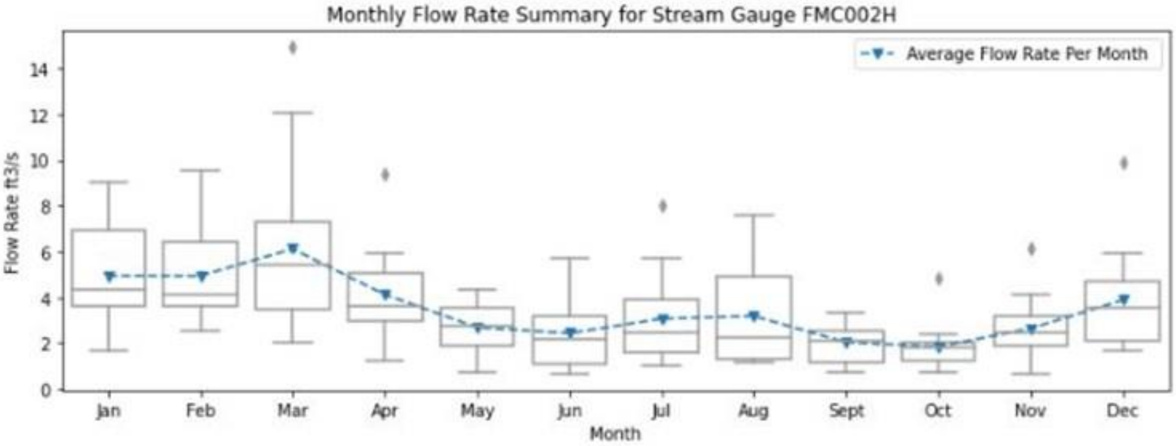

Figure 87. Monthly flow rate at stream gauge FMC002H.

In parallel, the GIS and hydrological modeling team also worked on delineating the Fourmile Branch watershed and hydrological features such as drainage lines, drainage points, catchments and rasters of flow direction and flow accumulation using a high resolution (3m) digital elevation model (DEM). Two delineation toolsets were compared, the ArcHydro toolset and the ArcGIS Pro Spatial Analyst Hydrology toolset. The delineation process was repeated several times using each toolset, varying the number of cells used to define the drainage lines (i.e., 5,000; 7,500; 10,000; and 64,492, which was the original default value used by ArcHydro, calculated as 1% of the maximum flow accumulation (6,449,295), a simple rule of thumb for stream determination threshold). As seen in (Figure 88 and Figure 89), the results were very similar for both toolsets, however, the decision was made to use ArcHydro as this toolset automatically generates the catchments and drainage points for the entire area and thus saves overall processing time.

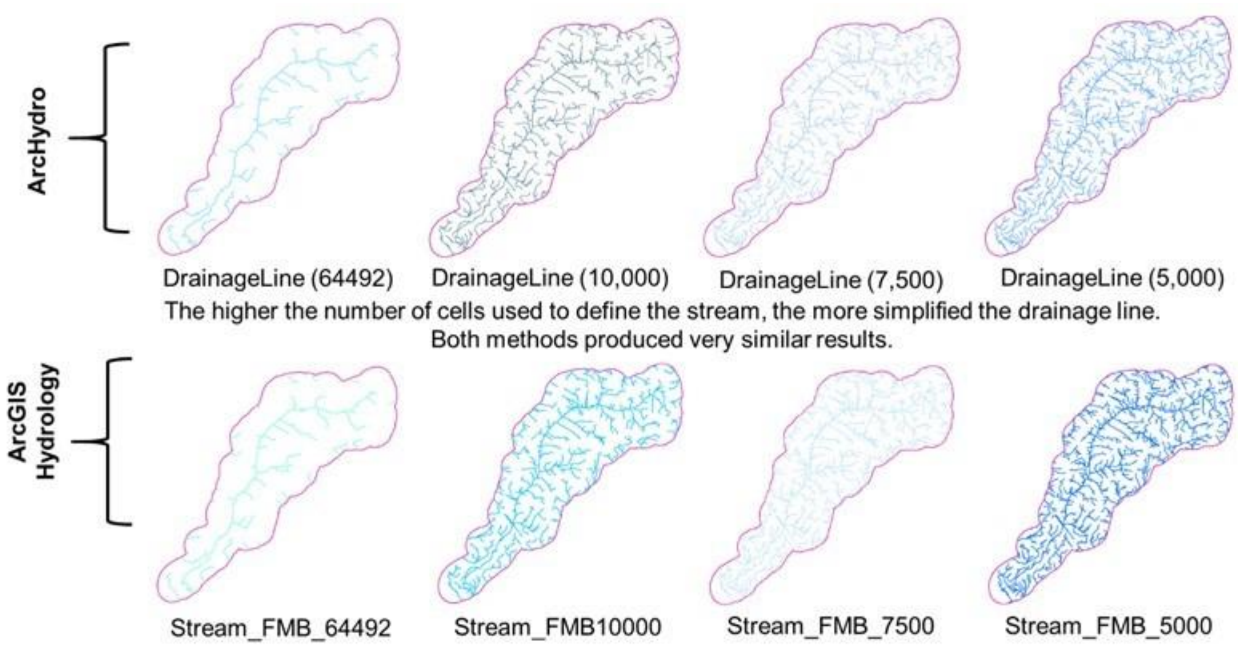

Figure 88. Comparison of the drainage line results using the ArcHydro and ArcGIS Pro watershed delineation toolsets with varying numbers of cells to define the drainage lines.

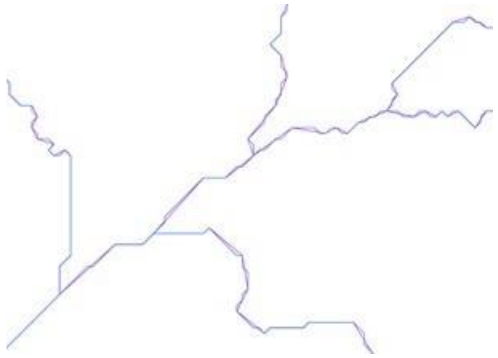

Figure 89. Drainage lines generated by ArcHydro (red line) and ArcGIS Hydrology (blue line) toolsets using same number of cells in each case for defining the drainage line.

ArcGIS ModelBuilder was also used to create a process flow model that automated the delineation process which also saved a lot of time (Figure 90). It was decided to make use of the ModelBuilder option to enable quick execution of this approach within other basins in the future. As such, the steps presented here become easily reproducible.

Figure 90. ArcGIS Pro ModelBuilder process flow model of ArcHydro watershed delineation.

The images in Figure 91 show some of the delineation results.

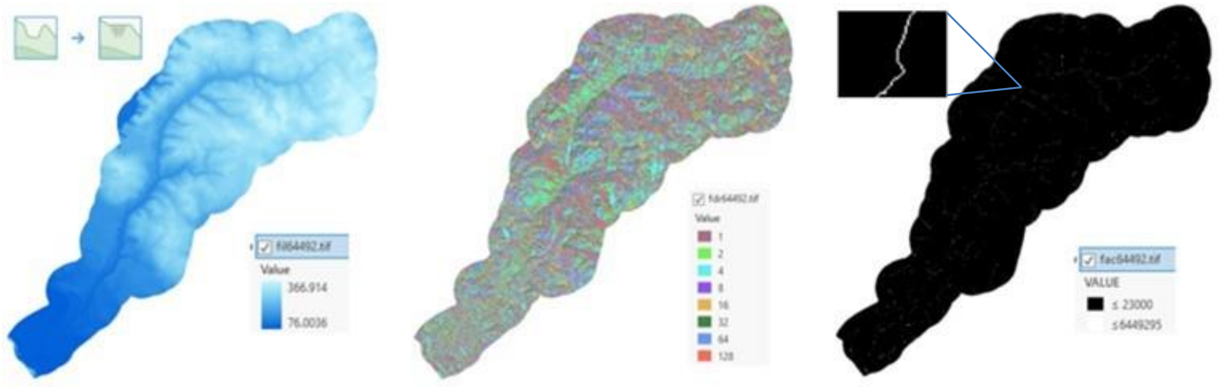

Fill Sinks DEM **Flow Direction Raster** **Flow Accumulation Raster**

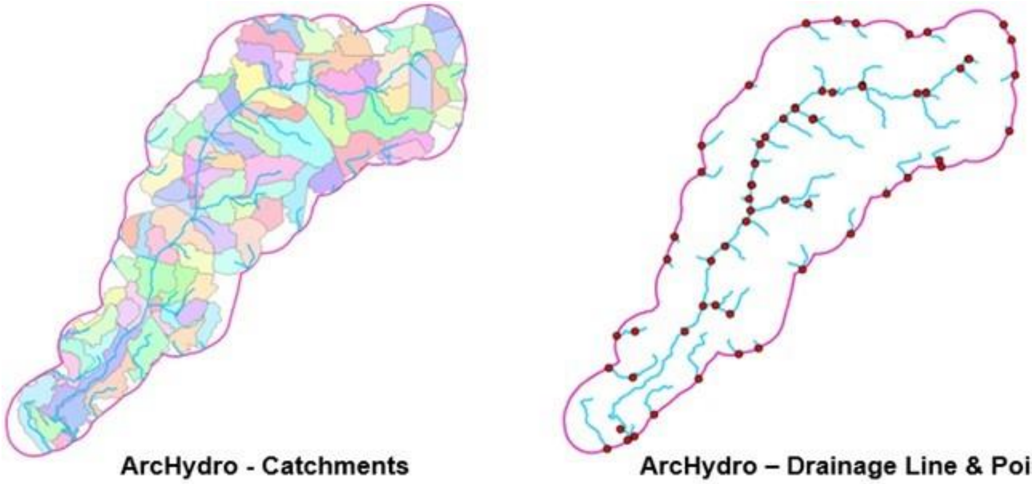

ArcHydro - Catchments **ArcHydro – Drainage Line & Points**

Figure 91. ArcHydro watershed delineation results for the Fourmile Branch watershed.

Once the delineation process was completed, further analyses were conducted focusing on the F-Area, specifically the region between the seepline and the FMB stream. A proximity analysis using the "Near" tool in ArcToolbox was conducted to determine the distance of each groundwater well in the F-Area to the main Fourmile Branch channel. In addition, the "Extract Multi Values to Points" tool was used to extract the flow direction and flow accumulation values from the delineated flow direction and flow accumulation rasters at each groundwater well location and incorporate the data in the attribute table of the groundwater well GIS shapefile as appended columns (Figure 92).

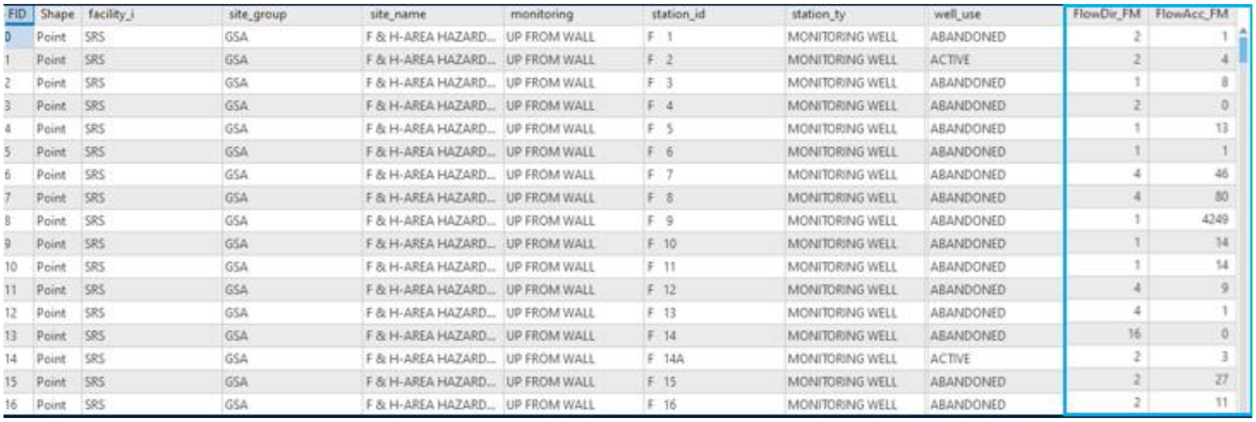

FID	Shape	facility_i	site_group	site_name	monitoring	station_id	station_ty	well_use	FlowDir_FM	FlowAcc_FM
0	Point	SRS	GSA	F & H-AREA HAZARD...	UP FROM WALL	F 1	MONITORING WELL	ABANDONED	2	1
1	Point	SRS	GSA	F & H-AREA HAZARD...	UP FROM WALL	F 2	MONITORING WELL	ACTIVE	2	4
2	Point	SRS	GSA	F & H-AREA HAZARD...	UP FROM WALL	F 3	MONITORING WELL	ABANDONED	1	8
3	Point	SRS	GSA	F & H-AREA HAZARD...	UP FROM WALL	F 4	MONITORING WELL	ABANDONED	2	0
4	Point	SRS	GSA	F & H-AREA HAZARD...	UP FROM WALL	F 5	MONITORING WELL	ABANDONED	1	13
5	Point	SRS	GSA	F & H-AREA HAZARD...	UP FROM WALL	F 6	MONITORING WELL	ABANDONED	1	1
6	Point	SRS	GSA	F & H-AREA HAZARD...	UP FROM WALL	F 7	MONITORING WELL	ABANDONED	4	46
7	Point	SRS	GSA	F & H-AREA HAZARD...	UP FROM WALL	F 8	MONITORING WELL	ABANDONED	4	80
8	Point	SRS	GSA	F & H-AREA HAZARD...	UP FROM WALL	F 9	MONITORING WELL	ABANDONED	1	4249
9	Point	SRS	GSA	F & H-AREA HAZARD...	UP FROM WALL	F 10	MONITORING WELL	ABANDONED	1	14
10	Point	SRS	GSA	F & H-AREA HAZARD...	UP FROM WALL	F 11	MONITORING WELL	ABANDONED	1	14
11	Point	SRS	GSA	F & H-AREA HAZARD...	UP FROM WALL	F 12	MONITORING WELL	ABANDONED	4	9
12	Point	SRS	GSA	F & H-AREA HAZARD...	UP FROM WALL	F 13	MONITORING WELL	ABANDONED	4	1
13	Point	SRS	GSA	F & H-AREA HAZARD...	UP FROM WALL	F 14	MONITORING WELL	ABANDONED	16	0
14	Point	SRS	GSA	F & H-AREA HAZARD...	UP FROM WALL	F 14A	MONITORING WELL	ACTIVE	2	3
15	Point	SRS	GSA	F & H-AREA HAZARD...	UP FROM WALL	F 15	MONITORING WELL	ABANDONED	2	27
16	Point	SRS	GSA	F & H-AREA HAZARD...	UP FROM WALL	F 16	MONITORING WELL	ABANDONED	2	11

Figure 92. Attribute table of F-Area groundwater well shapefile with flow direction and flow accumulation data at each well location in the appended columns to the far right outlined in blue.

Maps of the flow direction and flow accumulation at all the well locations were then created.

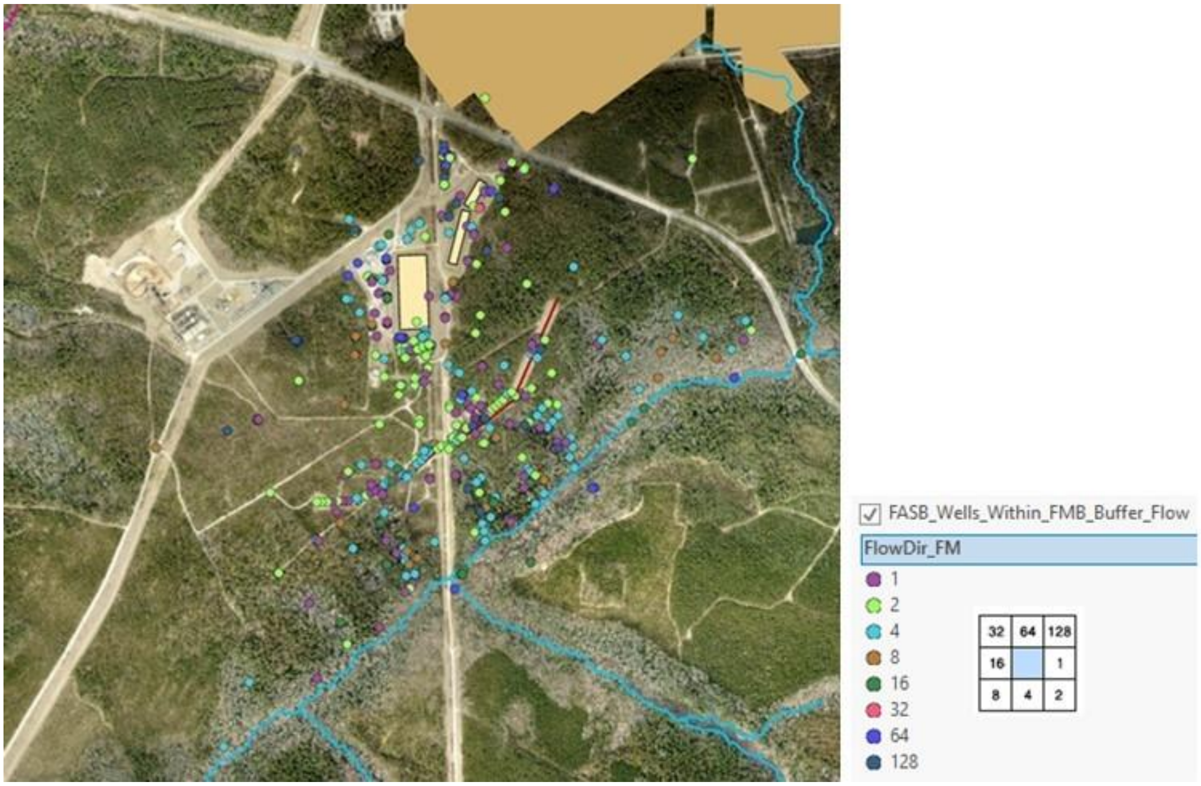

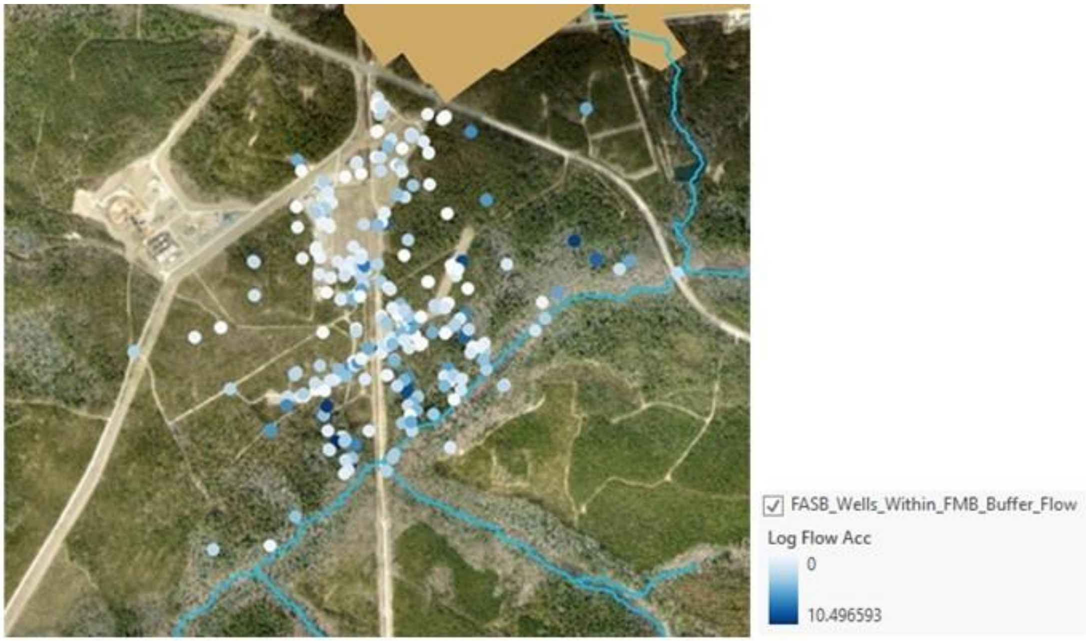

Figure 93. Maps of the flow direction (top) and flow accumulation (bottom) at each of the well locations in the F-Area.

A polygon of the region between the seepline and the FMB stream was also created and used to clip the well shapefile so that it will only include those wells within 5-m of the seepline-to-FMB stream polygon (Figure 94).

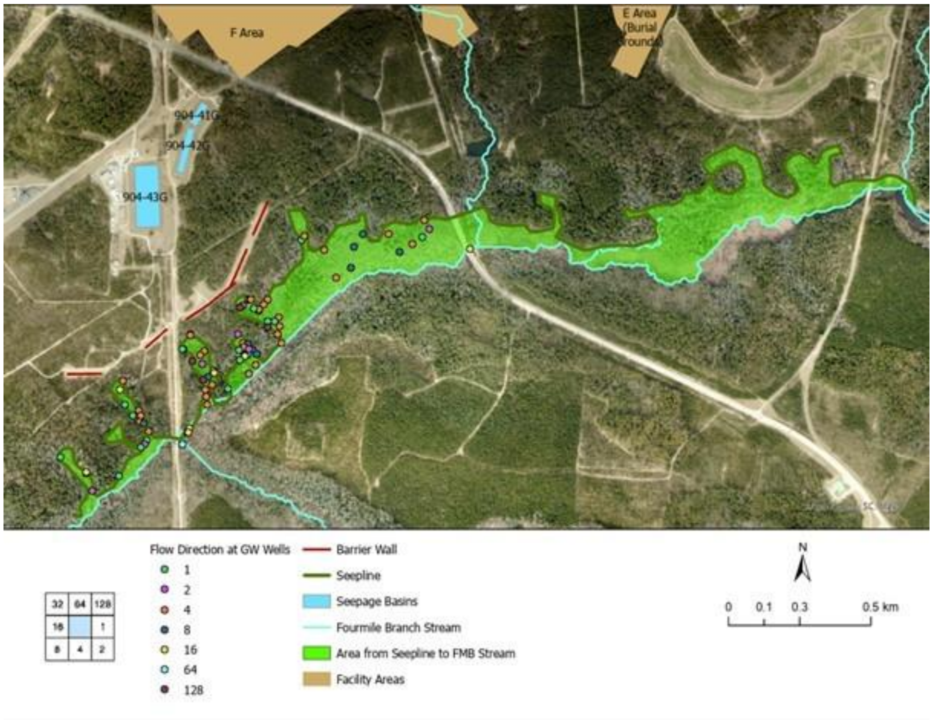

Figure 94. Map of the F-Area GW wells within 5 m of the seepline-to-FMB stream polygon. The image shows the flow direction at each of the wells.

The next step was to use the water level, temperature and pH data shown above and append it to the well shapefile so that similar maps can be generated for these parameters to examine their spatial variability as the proximity to the FMB stream increases. The main focus in the preliminary assessment was on completing the development of a python script to calculate the means and variances of several parameters recorded at 400 monitoring points in the F-Area, including groundwater wells and stream gauges. Each well and gauge had several data records of various parameters. For each well/gauge, the mean and variance of pH, water temperature and water level were calculated and then mapped using ArcGIS Pro to show the spatial variation of each parameter. FIU appended the water level, temperature and pH data being analyzed by the DOE Fellow working on this task to the attribute table of a well GIS shapefile, which enabled maps to be generated that provide a snapshot of the spatial variation of these parameters as they get closer to the main channel of the FMB stream.

Abandoned or inactive wells/gauges were excluded from the analysis by using a python script to filter, select and then remove them from the dataset. Wells/gauges with ‘no data’ for any of the parameters being investigated were also eliminated. After completing the script to filter the data, there were only between 170-185 wells/gauges remaining depending on the parameter.

Once calculation of the means and variances for each of the remaining wells/gauges was completed, a python script was developed to create scatterplots that show the relationship between the mean and variance values of the 3 parameters of focus (i.e., pH, water temperature and water level) and the proximity of the well to the main channel of the Fourmile Branch stream. The figure below shows the near distance vs the average water level at different gauges in the F-Area. The near distance is the distance from the gauge/well to the Fourmile Branch stream, and the water level is measured as the ground elevation minus the depth to water. Figure 95 shows a general trend that as the distance from Fourmile Branch increases the water level also increases. However, from the figure, two clusters of data points are shown. The second cluster of data points shows the water level decreasing as the distance from Fourmile Branch increases. This difference in trend is likely attributed to the fact that the wells extend into different aquifers and the variation in water level/head differs depending on the aquifer depth. The next step would be to further filter the wells according to their aquifer location to enable further analysis of the water level based on the aquifer depth.

Figure 95 shows the variation in average water level (head) in each aquifer as the distance from Fourmile Branch increases. The figure shows that the head increases as the distance from Fourmile Branch increases in both the LAZ and UAZ. In the GAU the opposite occurs, i.e., as the distance from Fourmile Branch increases, the head decreases. Water is known to travel from higher pressure to lower pressure. As such, it can be inferred that in both the LAZ and UAZ there is higher pressure further away from Fourmile Branch, causing the water to flow towards the stream. In the GAU there is higher pressure closer to the stream, and that causes the water to flow away from Fourmile Branch and into another stream system such as the Savanah River.

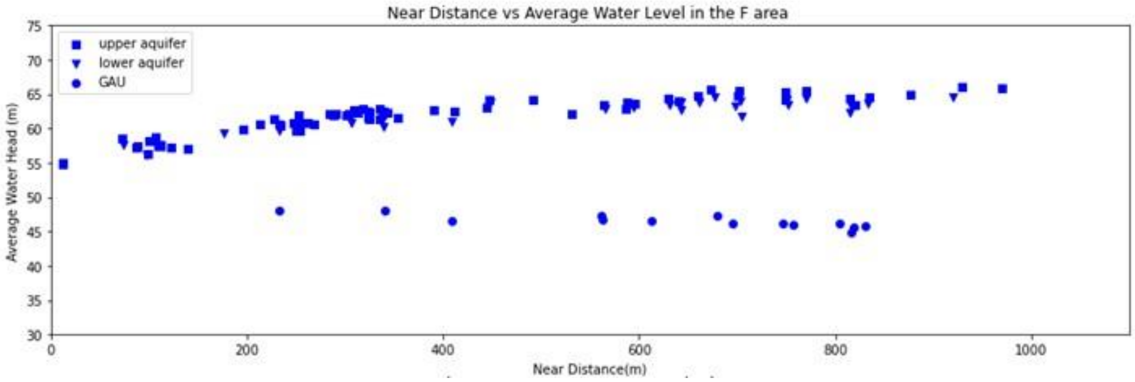

Figure 95. Near Distance vs Average Water Level in each aquifer in the F-Area.

In Figure 96 the relationship between water temperature and the distance from Fourmile Branch is examined in each aquifer. The average water temperature increases as the distance from Fourmile Branch increases in all three aquifers. Results indicate that the average water temperature increases with increasing aquifer depth.

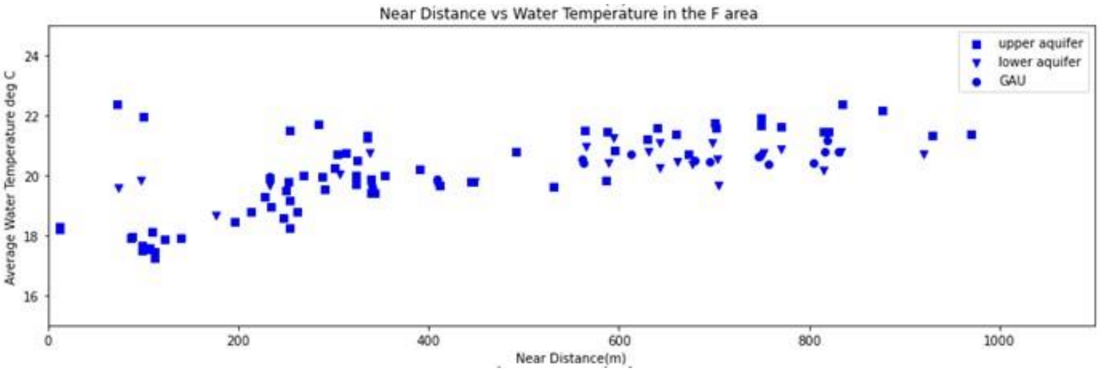

Figure 96. Near Distance vs Average Water Temperature in each aquifer in the F-Area

Figure 97 shows the relationship between pH and the well distance from Fourmile Branch. At first glance, it appears that the stations in the GAU have a near neutral pH while the pH values in the lower and upper aquifers are lower.

The calculated results confirm what is visualized in the graph (i.e., almost neutral pH in the GAU and more acidic pH in the UAZ and LAZ). This makes sense as the GAU, being the deepest aquifer, will be the least affected by the acidic waste derived from the seepage basins nearer the surface. Both the upper and lower aquifers are closer to the surface and the acidic waste thus has much more of an impact resulting in lower pH values.

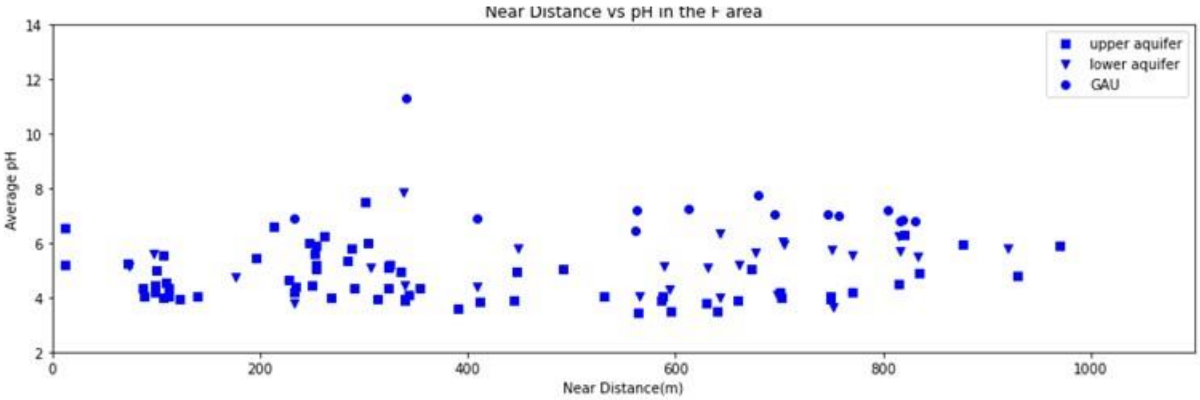

Figure 97. Near Distance vs pH in each aquifer in the F-Area.

Figure 98 to Figure 100 show the relationship between the three parameters and distance to FMB with respect to the type of station. Monitoring wells seem to be the most prominent station type in the F-Area based on the following scatterplots. There also seems to be very few extraction and injection wells. Besides showing the specific amount of each type of station in the F-Area, the three figures also show the most common locations of where these stations are placed. For example, the surface water stations are all within a few meters of Fourmile Branch. Seepline and piezometer wells are shown to be between 100-300 meters away from Fourmile Branch. Lastly, monitoring wells are the most common station type further than 300 meters away from the stream.

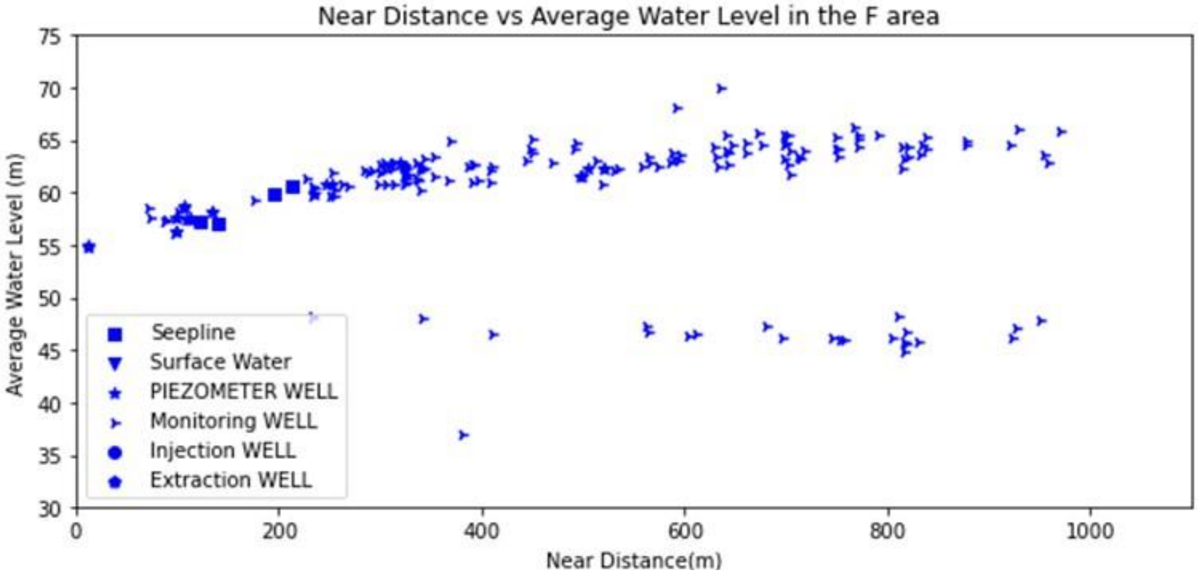

Figure 98. Near Distance vs Average Water Level based on the station type.

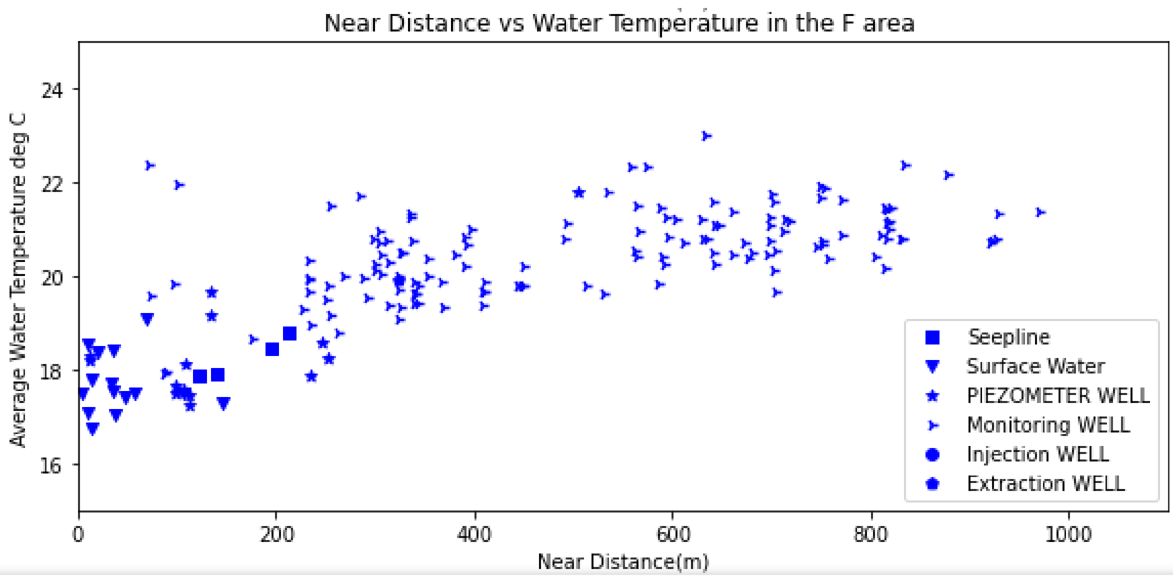

Figure 99. Near Distance vs Average Water Temperature based on the station type.

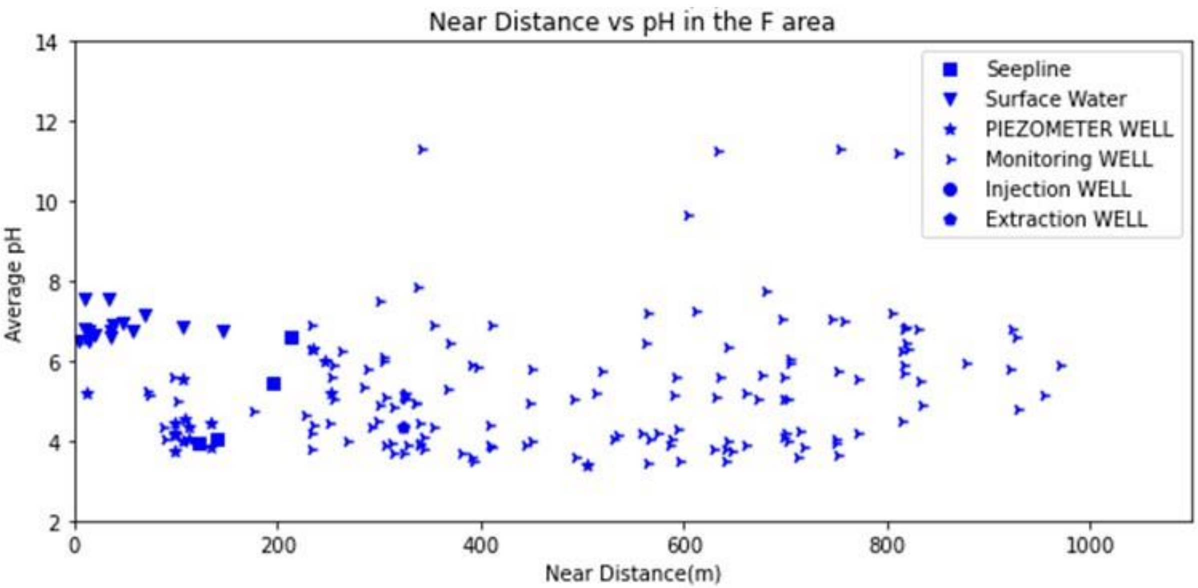

Figure 100. Near Distance vs pH based on the station type.

Last, a script was created that would calculate the average and variance of the pH and temperature variables at different locations within Fourmile Branch to examine their trends at the stations near the seepage lines as well as at stations that are further from the seepage lines that extend to the lower and upper aquifers and the Gordon Aquifer Unit (GAU). The locations included wells at varying aquifer depths (Lower Aquifer Zone (LAZ), Upper Aquifer Zone (UAZ), and GAU), and wells within the seeplines and just outside of the seeplines. Also included were 2 surface gauges (one upstream and one downstream) to see if and how these parameters change as the water flows downstream. From these various locations, a time series was generated using the available data from each of the monitoring stations so that further analyses could carried out. The DOE Fellow then worked on providing an improved summary of the variance and average pH and temperature. Time series graphs are also being prepared for the various wells.

In addition to the results presented above, more detailed analyses of the surface water observations at three stream gauges (FM-2BD, FAS-091, FMC-002F) were performed, focusing on long-term variations of pH, water temperature and specific conductance between the sites within the Fourmile Branch river network as well as throughout the year at a given location.

Both a boxplot and a time series graph were created for each station. The boxplot graphs were separated by quarter (see figure below). Outliers are also shown indicating points that are above Q3+1.5IQR and below Q1-1.5IQR. These outliers can correspond to both actual situations as well as errors within the observations. These outliers that appeared to be spikes were then removed to analyze how these outliers affected the overall average and variances of each of these parameters at the different stream gauges.

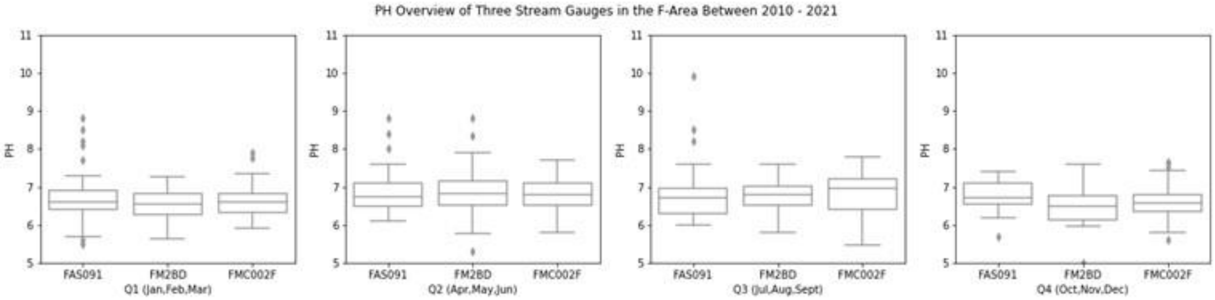

Figure 101. Distribution of the pH at different stream gauges and during different quarters.

The average pH and its range at FM-2BD and FMC-002F are very similar. Only in Q4 some variations between the three gauges can be observed though differences are small. However, FAS091 does show considerably more outliers compared to the other two locations. These outliers can potentially result from the addition of base solution added to the groundwater within F-Area as a remedial strategy, that has reached the surface water.

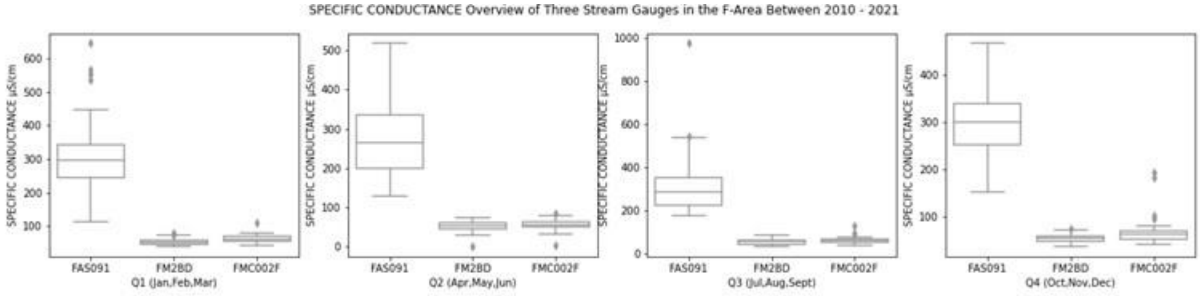

Figure 102. Distribution of the specific conductance at different stream gauges and during different quarters.

The impact of adding base solution can also observed at gauge FAS-091 when focusing on specific conductance. The boxplots in the figure above show the difference in specific conductance between stream gauge FAS-091 and the other gauges, FM-2BD and FMC-002F. The specific conductance at FM-2BD and FMC-002F also appear to have a smaller range of recorded data compared to FAS-091. From the boxplots, a hypothesis can be made that the specific conductance does not change much over time at these two gauges.

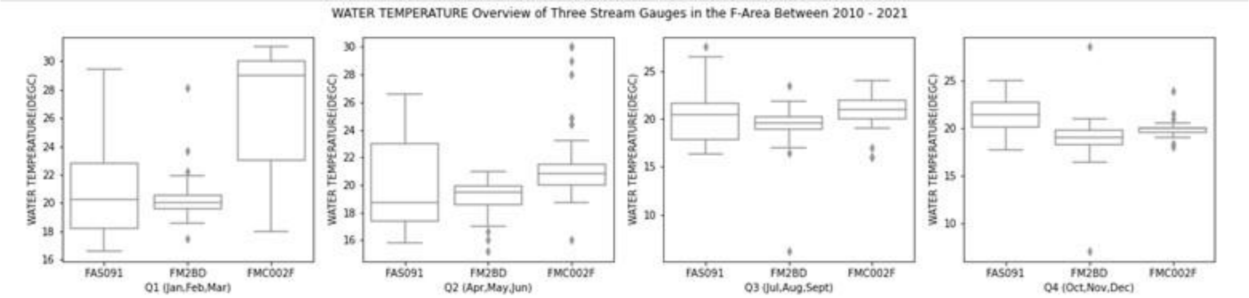

Figure 103. Distribution of the water temperatures at different stream gauges and during different quarters.

Lastly, boxplots of water temperature were generated for the various quarters. It can be observed that for Q1 and Q2, stream gauges FAS-091 and FMC-002F appear to have the largest variability in temperature. The median for FMC-002F is also noticeably higher when compared to the other gauges. This high median could be due to the amount of data recorded at FMC002F but can also be an impact due to the occurrence of erroneous outliers. To identify their occurrence, the figure below was created to show the long-term time series of pH, specific conductance and water temperature.

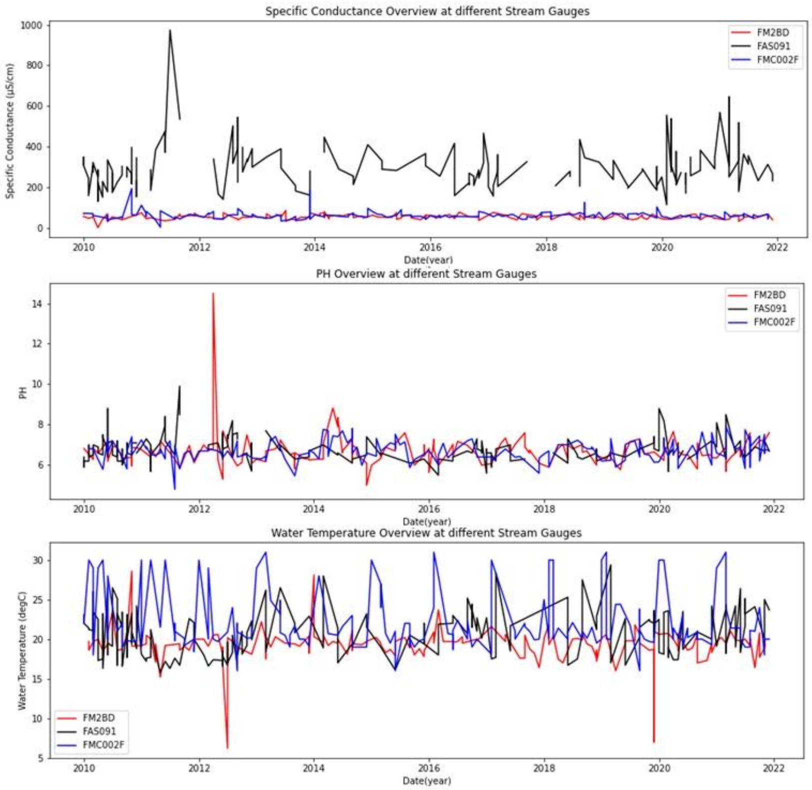

Figure 104. A time series summary of the different parameters at different stream gauges.

It can be observed from this figure that a number of large negative outliers in water temperature for stream gauge FM2BD are present, as well as large positive peaks in pH for stream gauge FM2BD. It is not believed that these outliers have a clear physical interpretation, so it was decided to remove these peaks from the data. Using the updated series, the mean and variances for each of these parameters were recalculated and the updated values were described in the Milestone 2021-P2-M6 report.

Since the abovementioned results show the occurrence of outliers within the observed data, it was decided to identify, for all sources of data, how often outliers exist within the datasets and how they impact estimates of mean and variance of pH, specific conductance and water temperature. Therefore, assuming observations are normally distributed, for each dataset the mean and standard deviation were estimated. An example can be seen below for monitoring station FBI 14D.

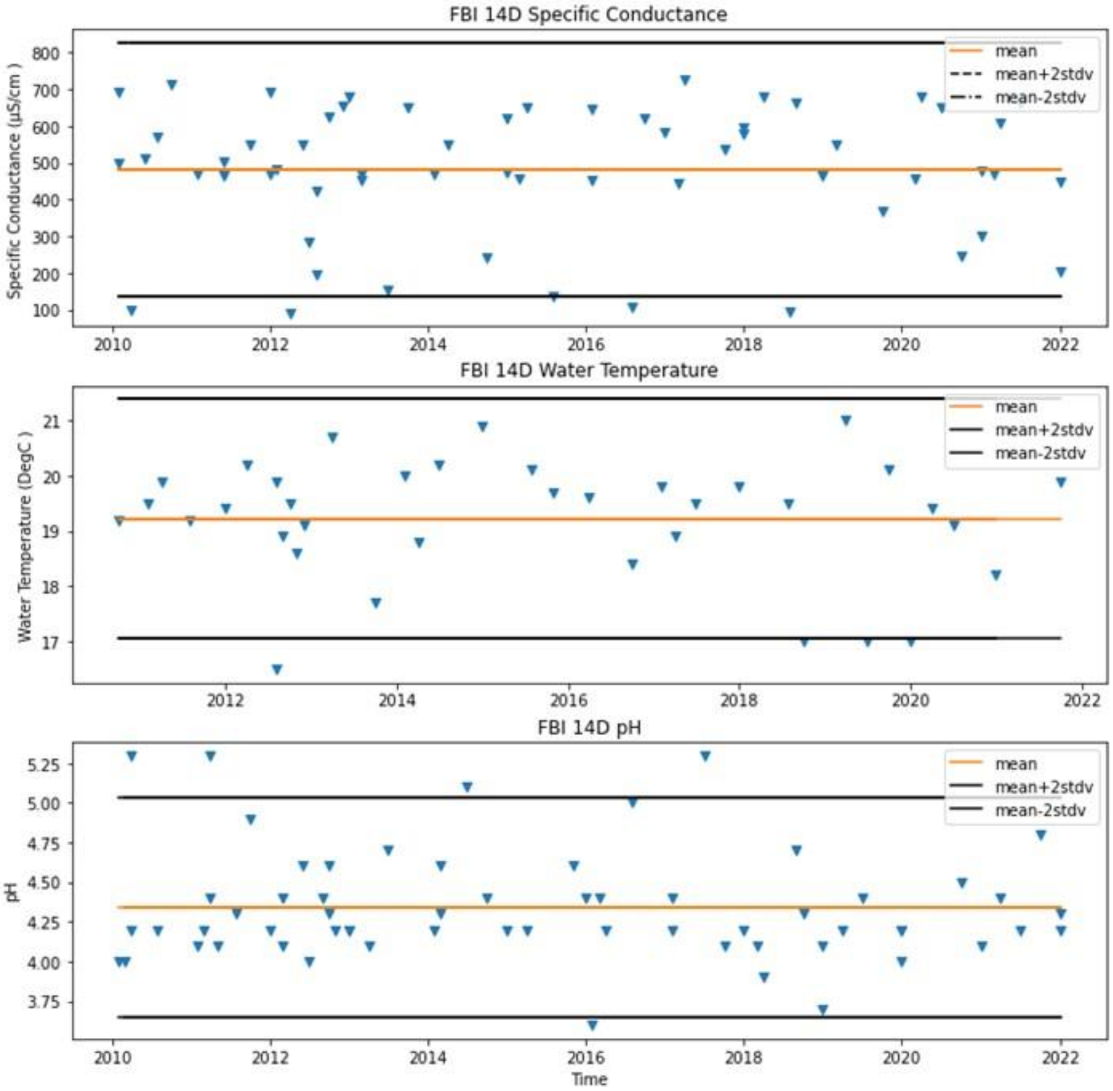

Figure 105. An example of the time series graphs of monitoring station FBI 14D.

For the specific conductance, water temperature and pH parameters, each subpanel in this figure shows an orange line that represents the average of a given parameter. Furthermore, the two black lines indicate the mean ± 2 standard deviation levels. In case data are normally distributed, beyond ± 2 standard deviations is considered to lie outside the 95% confidence level. Observations outside of these boundaries are marked and correspond either to an extreme observation related to a specific event or to erroneous observations. In terms of monitoring station FBI-14D, there does not appear to be any obvious outliers that might have to be removed from the data. FIU therefore continued focusing on the impact of not including the observations outside of these levels on the observed mean and variability and determining whether this impacts the conceptual understanding on the interactions between the various sources of water within the seepage face below F-Area. It was decided to remove those observations that were above or below two standard deviations from the mean. Removing these outliers leads to a reduction of the average of each monitoring station. Table 30 and Table 31 present the average and variability of the pH, temperature and specific conductance for all monitoring wells belonging to a given groundwater layer or the seepage face, as well as those situated within the river network.

Table 30. The Average and Variance of Temperature, pH and Specific Conductance for the Various Aquifer Layers and the seepline within the F-Area Domain

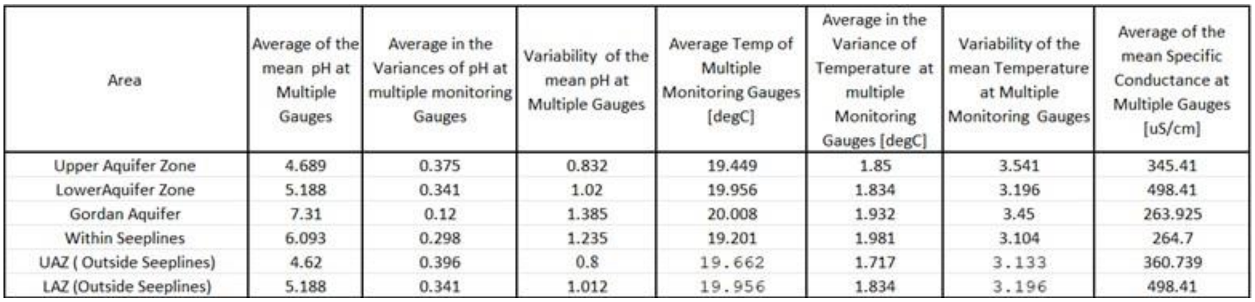

Area	Average of the mean pH at Multiple Gauges	Average in the Variances of pH at multiple monitoring Gauges	Variability of the mean pH at Multiple Gauges	Average Temp of Multiple Monitoring Gauges [degC]	Average in the Variance of Temperature at multiple Monitoring Gauges [degC]	Variability of the mean Temperature at Multiple Monitoring Gauges	Average of the mean Specific Conductance at Multiple Gauges [uS/cm]
Upper Aquifer Zone	4.689	0.375	0.832	19.449	1.85	3.541	345.41
LowerAquifer Zone	5.188	0.341	1.02	19.956	1.834	3.196	498.41
Gordan Aquifer	7.31	0.12	1.385	20.008	1.932	3.45	263.925
Within Seeplines	6.093	0.298	1.235	19.201	1.981	3.104	264.7
UAZ (Outside Seeplines)	4.62	0.396	0.8	19.662	1.717	3.133	360.739
LAZ (Outside Seeplines)	5.188	0.341	1.012	19.956	1.834	3.196	498.41

Table 31. The Average and Variance of Temperature, pH and Specific Conductance for Three Different Surface Water Gauges within the F-Area Domain

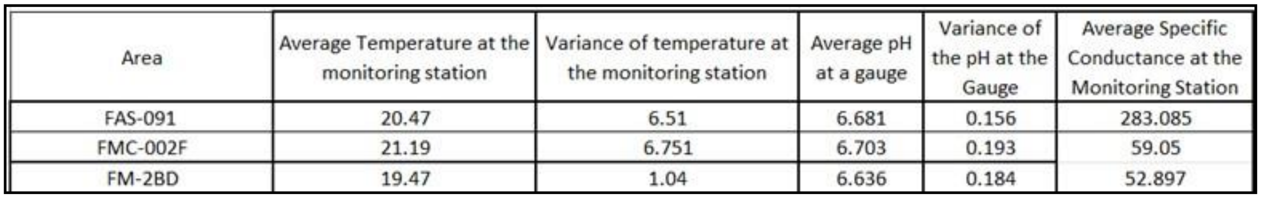

Area	Average Temperature at the monitoring station	Variance of temperature at the monitoring station	Average pH at a gauge	Variance of the pH at the Gauge	Average Specific Conductance at the Monitoring Station
FAS-091	20.47	6.51	6.681	0.156	283.085
FMC-002F	21.19	6.751	6.703	0.193	59.05
FM-2BD	19.47	1.04	6.636	0.184	52.897

Using the corrected data, during the month of May for Subtask 3.2, the spatial variability in temperature, pH and specific conductance was evaluated for the river network wells and seepage face wells in the F-Area seepline domain for the four different quarters of the year. Specifically, the various wells were lined up according to their locations along the river network

Finally, for each river network or seapage face gage, the average parameter values and its variability were converted into a spatial image. Results for the pH are shown in Figure 106 and Figure 107. The differences between the seepline groundwater well and those from the river network are currently being evaluated. These results will be presented in subsequent months.

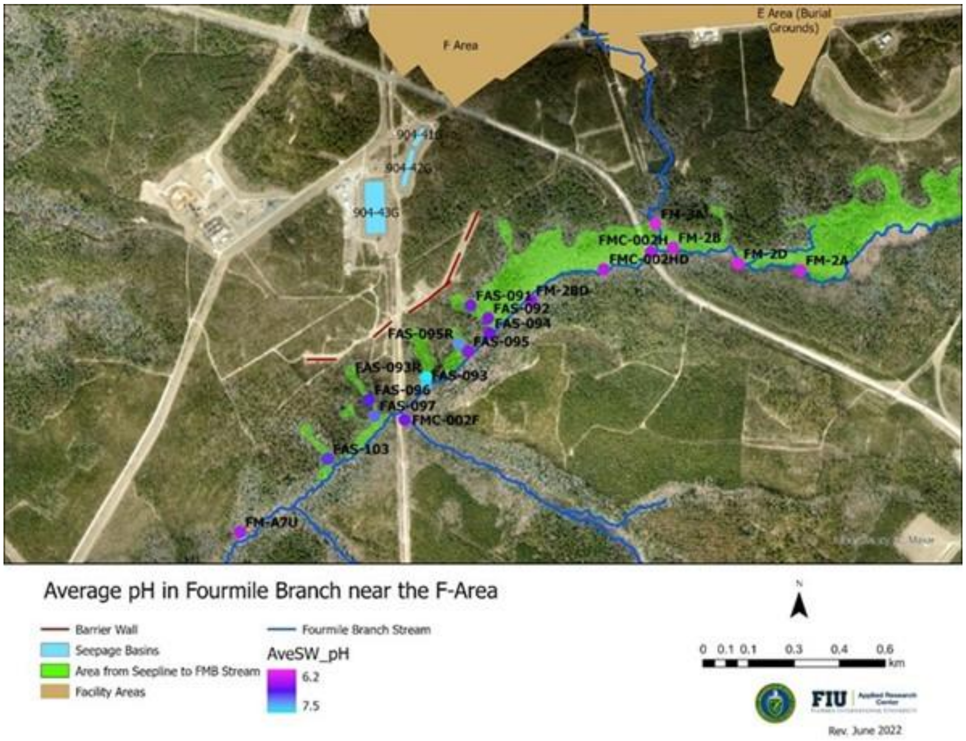

Figure 106. Average pH observed at a given groundwater well in the seepage face or for river network wells within the F-Area domain.

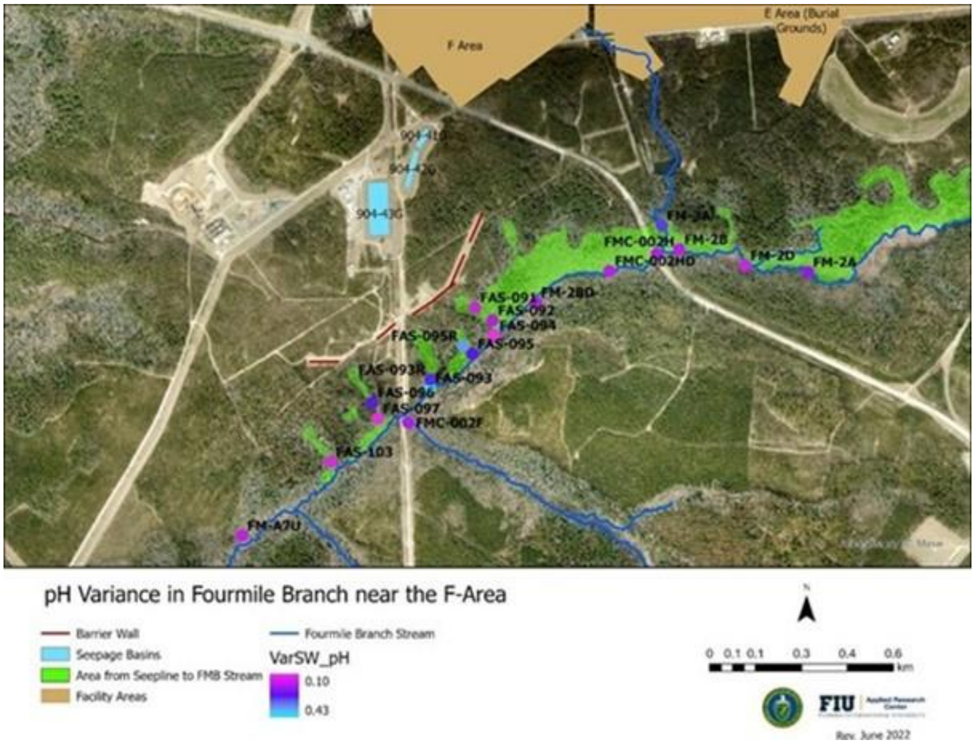

Figure 107. Variance of pH observed at a given groundwater well in the seepage face or for river network wells within the F-Area domain.

Hydrological modeling of Fourmile Branch using MIKE SHE/MIKE 11

The MIKE SHE/MIKE 11 model generation setup, as described in Subtask 3.1 was also applied to Fourmile Branch. As such, GIS was used in combination with Python to 1) generate the DEM and delineate the basin, 2) obtain land cover information, 3) generate forcing data, 4) obtain soil information, and 5) obtain the river network and cross-section information. FIU is now currently in the process of finalizing the initial version of a MIKE SHE/MIKE 11 model for Fourmile Branch by including subsurface information about groundwater flow characteristics. These results, as well as this model, will be presented in subsequent months.

In addition, FIU started applying the Python scripts developed in Subtask 3.1 to enable automatic generation of a MIKE model for Fourmile Branch. Our initial results predominantly focused on the river network. The MIKE 11 river network file is shown in Figure 108. Also, for Fourmile Branch, it was chosen to make use of a 250-meter resolution. An image of the MIKE SHE/MIKE 11 model for Fourmile Branch created in this manner is shown in Figure 109.

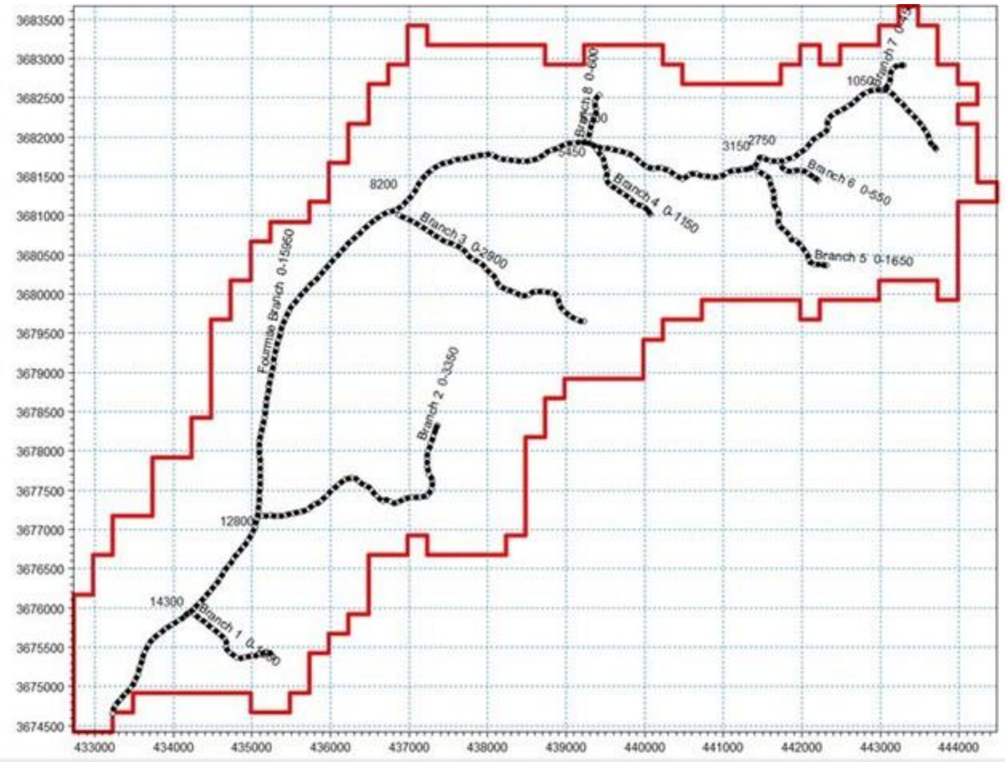

Figure 108. Fourmile Branch basin boundary at 250-meter resolution (red) and river network as derived from QGIS and Python script to be directly used by MIKE SHE/MIKE 11, with each lateral river network point being 50-meters apart.

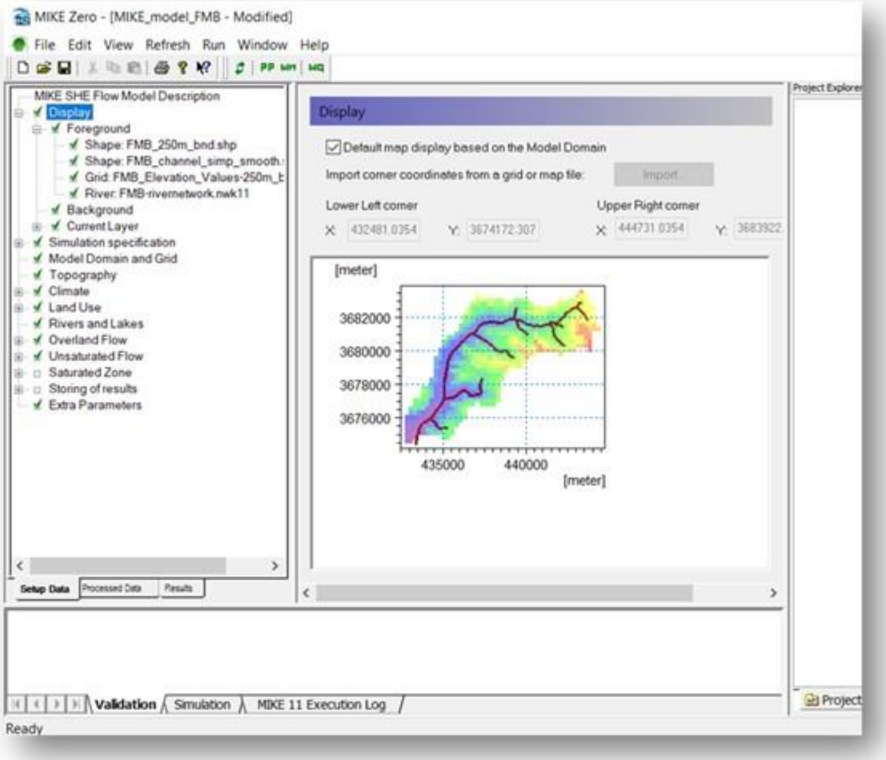

☑ Default map display based on the Model Domain

Import corner coordinates from a grid or map file:

Lower Left corner		Upper Right corner	
X: 432481.0354	Y: 3674172.307	X: 444731.0354	Y: 3683922

Figure 109. Example of the MIKE SHE/MIKE 11 model generated for Fourmile Branch Watershed.

Subtask 3.2: Conclusions

The work conducted over the past year under this subtask has included:

- A literature review to obtain information on the site background, history of contamination, and applied remediation technologies.
- Collection of climate, geospatial, hydrological and water quality data records from federal and state databases (USGS/USDA/SCDNR), or from SRNS and SRNL scientists and the SRNL Atmospheric Technologies Group.
- Development of a geodatabase to store and manage all the GIS data, and application of ArcGIS tools to process the data for model input and to visualize and map the study area.
- Preliminary analysis of timeseries data records (rainfall & discharge) to identify any significant storm events (500 yr/ 100 yr/ 50 yr, etc.).
- Training of an FIU undergraduate student (DOE Fellow) on geospatial mapping and analysis tools, as well as GIS and timeseries data retrieval, processing and analysis.

Subtask 3.2: References

Saksena, S. (2017, January 05). Plotting the flood frequency curve using Gumbel Distribution. Retrieved March 3, 2021, from

https://serc.carleton.edu/hydromodules/steps/166250.html

TASK 5: REMEDIATION RESEARCH AND TECHNICAL SUPPORT FOR WIPP

Subtask 5.2: Fate of Actinides in the Presence of Ligands in High Ionic Strength Systems

Subtask 5.2: Introduction

Radionuclide solubility is the key factor driving the fate and transport of radionuclides in the subsurface environment, especially in the far field of a nuclear waste disposal repository. An effective strategy for controlling radionuclide transport is the reduction of radionuclide solubility via sorption onto mineral phase(s) in aqueous media of the subsurface environment. Typically, sorption retards migration of actinide to the environment by allowing longer transport time, resulting in decay of larger portions of actinide inventory. It is normally expressed in terms of partition coefficient (K_{dc}), which is a measure of distribution of actinide between the immobile solid phase(s) and mobile aqueous phase(s). To demonstrate the long-term performance of a nuclear waste disposal facility such as the WIPP, analyses of thermodynamic data for actinide interactions with the subsurface environment is critical to providing a robust scientific basis for safe disposition of nuclear wastes. Simplified coefficient models have been routinely applied to obtain empirical formulas for deriving K_{dc}. Moreover, probability distribution and uncertainty of K_{dc} parameters and equilibrium constants can be employed in geochemical transport models to simulate the long-term safety performance of nuclear waste disposal sites. Actinides such as plutonium 239 (^{239}Pu) and neptunium 237 (^{237}Np) are important in performance assessment calculations for long-term performance of a nuclear waste repository because of their relative long half-life ($t_{1/2}$ for ^{239}Pu = 2.4 x 10^4 and ^{237}Np = 2.14 x 10^6 years), radiotoxicity and redox chemistry [Reed and Altmaier, 2013]. Moreover, under the reducing conditions expected in a deep geologic repository of the WIPP, Pu(IV) and Np(III) are considered the predominant valent states expected for plutonium and neptunium. Because the migration of actinides in the subsurface environment is largely controlled by interaction at the solid-water interface with environmental media (soil, sediment, water) a better understanding of key processes driving sorption processes can lead to realistic prediction of actinide mobility and development of a robust transport models. Specifically, the WIPP located near Carlsbad in New Mexico is a deep underground geologic repository used for disposal of legacy transuranic (TRU) radioactive wastes. Characterized by high ionic strength pore-waters (~ 7.4 M) the WIPP resides deep (~655 m) in the bedded salts of the Permian Salado Formation that consists predominantly of interbedded halite and anhydrite layers overlying the Castile Formation [Brown et al., 1999; Brush and storz, 1996; Stein, 1985](Figure 110). To comply with regulatory containment requirements of the U.S. Environmental Protection Agency the U.S. Department of Energy (DOE) was required to conduct a performance assessment (PA) for 10,000-year post-closure period. A potential release scenario envisioned in the WIPP performance assessment (PA) is groundwater intrusion through the highly transmissive Culebra Member overlying the WIPP that releases actinide species of concern to the environment. In this low-probability TRU release scenario americium (Am), neptunium (Np) and plutonium (Pu) are considered the most important actinides species to be mobilized from the WIPP environment.

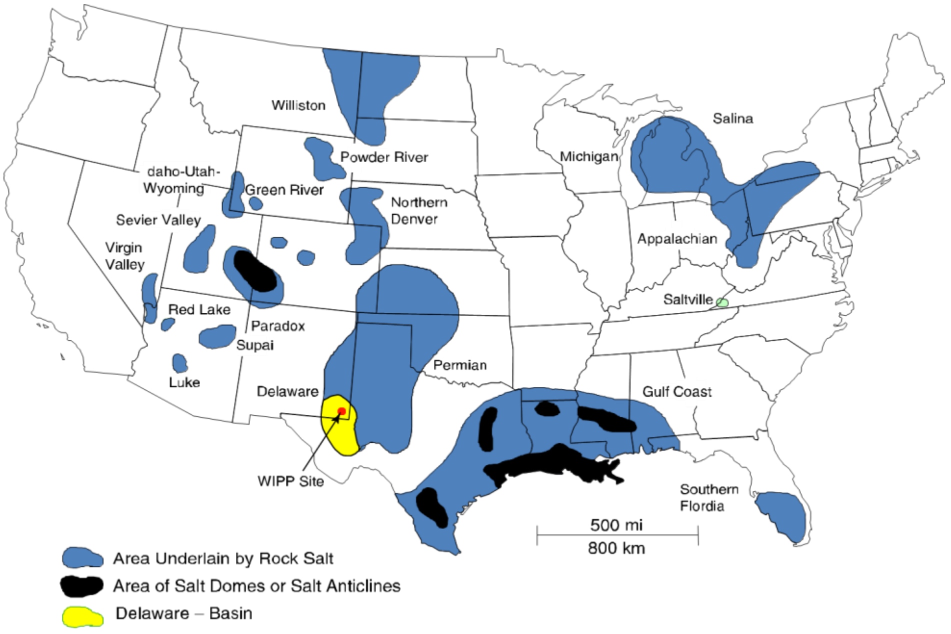

Figure 110. United States map depicting locations of various salt deposits and the Salado salt Formation of the Delaware Basin in the Permian salts of Texas and New Mexico that hosts the Waste Isolation Pilot Plant (WIPP), courtesy of DOE CBFO.

Waste streams reprocessing and degradation of repository components (e.g. cellulose degradation by calcium hydroxide present in cement, steel containers) resulted in formation of significant concentrations of ligands such as citrate, EDTA, oxalate, gluconate etc. in the WIPP that can form strong complexes with metals. The iron found in the steel waste containers and lead (Pb) in the shielded containers are expected to strongly react with sulfide and compete with actinides for complexation with the organic ligands found in the WIPP brines. Along with low-probability groundwater intrusion the presence of metal-chelating organic ligands, iron oxide minerals (magnetite), and intrinsic actinide colloids may provide a potential release pathway for migration of the actinides. The complexation effects of strong chelators such as EDTA and oxalate found in the WIPP have been accounted for in current performance assessment (PA) models. However, current PA models do not include iron oxide minerals and other organic ligands structurally similar to gluconate that are expected to be stable within WIPP-relevant conditions [Brady et al., 1999; Brown et al., 1999; Brush and storz, 1996]. Gluconate is an organic additive used for achieving fluidity necessary for cement pouring. It is structurally similar to isosaccharinate, an important byproduct of alkaline degradation of cellulose that is considered a major concern in many PA of nuclear waste repositories. Gluconate can form stable complexes with actinide with potential enhancement of its mobility.

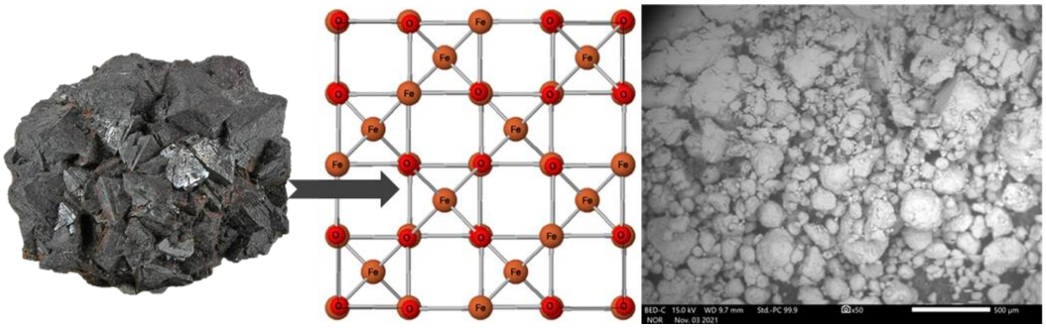

Figure 111. A 5cm-wide magnetite mineral (left) and its crystal structure (middle), and SEM micrograph at 50x magnification (right)

Thorium (Th) sorption onto natural clays, sandstone, and volcanic rocks has been shown to decrease in the presence of organic compounds [Baston et al., 1992]. Previous studies have demonstrated the ability of actinides to form complexes with gluconate in a wide range of pH [Baston et al., 1992; Sawyer, 1964; Tits et al., 2005]. In alkaline conditions, Th solubility increased in cement pore-waters (pH = 12) in the presence of gluconate [E. Colàs et al., 2011; Elisenda Colàs et al., 2013]. In the alkaline pH range and absence of Ca the An(IV)(OH)x(L)y species is expected to dominate the systems containing Th(IV), U(IV), Np(IV), and Pu(IV), where L is gluconate or ISA [Gaona et al., 2008]. However, sorption of actinides onto WIPP-relevant iron minerals (corrosion product, e.g. magnetite, Figure 111.) and in WIPP-relevant conditions has not been well studied. Thus, additional experiments that support the safety underpinnings employed in the PA models will provide an improved understanding of potential impacts of degradation or corrosion products on actinide mobility in the subsurface.

Subtask 5.2: Objectives

The main objective of this study is to assess the impact of gluconate and iron oxide minerals (magnetite) on actinide sorption behavior under anaerobic conditions and high ionic strength environment expected within the WIPP repository. To accomplish this objective: 1) batch sorption studies were conducted to examine the impact of ionic strengths and gluconic acid on the sorption of actinides onto magnetite; 2) experiments conducted in different brine types were used to assess the impact of solution chemistry and the nature of brine solutions on actinide migration; and 3) key variables controlling the sorption of actinides onto magnetite in the presence and absence of gluconic acid were determined. The findings of this study will provide updated K_{dc} parameters to support strong scientific basis for safety assessments of nuclear waste repositories and development of best management strategies for sites impacted by near-surface contamination.

Subtask 5.2: Methodology

Materials

Magnetite nanoparticles of magnetite (97%, Iron[II,III]oxide, Fe_3O_4) were procured from Alfa Aesar (Ward Hill, MA) (Figure 111.). The magnetite (Alfa Aesar) used in these studies had a reported particle size of 44 µm and iron contents of 20% ±0.6% for Fe^{2+} and 46% ±4% for Fe^{3+}, respectively [Lagos et al., 2018]. The measured BET surface area and pore size for the magnetite are ~8.13 m^2/g and ~11.5 nm, respectively. All chemicals were ACS reagent grade or better in purity and used as received. Sodium gluconate (TCI America, Portland, OR), sodium chloride, sodium bromide, sodium sulfate, potassium chloride, magnesium chloride, lithium chloride (Fisher Scientific, Pittsburg, PA), calcium chloride, sodium bromide (Acros Organics, Geel, Belgium), sodium tetraborate (MPI Biomedicals, Santa Ana, CA) and ultrapure deionized water (>18 MΩ) were used to prepare the brines and stock standard solutions. Additionally, along with UO_2^{2+}, Nd^{3+} and Th^{4+} were used as stable analogues for Am(III) and Pu(IV), respectively, to represent the dominant oxidation states of tri- and tetravalent actinides in the WIPP environment. All contaminant spikes were from stock standard solutions made in 2% nitric acid (HNO_3) from High-Purity Standards (Charleston, SC). The stock solution was stored at 4ºC and diluted to the desired final concentration for each experiment using deionized water, which was degassed with high-purity nitrogen.

The evaluated brines were spiked with a known actinide concentration and the pH was adjusted with either HCl/NaOH (0.1 or 1.0 *M*) to a pH value of 8 ±0.5. During the duration of the batch study the pHs of the spiked samples were not adjusted. All experiments were conducted in 50 mL polypropylene centrifuge tubes (Corning CentriStar). Contaminant concentrations in experimental samples were analyzed using a Thermo Fisher Scientific iCAP RQ inductively coupled plasma mass spectrometer (ICP-MS) with detection limits of 6.0 ng/L, 5.0 ng/L, and 37 ng/L for Nd, Th and U, respectively.

Adsorption Experiments

Batch sorption experiments were used to investigate the impact of ionic strength (0.1 – 5.0 *M*) and gluconate on the sorption of Nd(III), Th(IV), and U(VI) onto magnetite in brine solutions of NaCl, $MgCl_2$, $CaCl_2$, Generic Weep Brine (GWB) and The Energy Research and Development Administration Well 6 (ERDA-6). The GWB and ERDA-6 brines are synthetic brine used to simulate the intergranular Salado and Castile brines. Both brines have been widely used to evaluate the impact of various WIPP brine conditions on actinide mobility. The GWB brine is a simulant used to mimic a magnesium-rich WIPP environment, whereas ERDA-6 a low-magnesium environment. The composition of GWB and ERDA-6 brine is displayed in Table 32. Experiments were conducted under a nitrogen-rich atmosphere to simulate anoxic conditions (i.e. 98% N_2: 2% H_2) expected in the WIPP environment and to prevent interaction with atmospheric CO_2. Experiments were performed in triplicates with sampling time intervals of 15 min, 60 min, 180 min, 24 h, 48 h and 168 h in the presence and absence of gluconate. Additionally, contaminants concentration ($[C_M]_0 = 1000$ μg/L, where C_M = Nd, Th and U) representative of supersaturation limit were used to spike the brines. Batch samples were not filtered because previous studies reported losses of contaminants (especially Nd) to various filter materials (e.g. paper, cellulose ester, and PTFE filters). Samples were centrifuged at 8000 rpm for 20 min. The expected particle sizes remaining in solution after centrifugation is estimated as ≤80 nm.

Table 32. Composition of simulated WIPP brines, GWB and ERDA

Component	GWB (M)	ERDA-6 (M)
NaCl	2.874	4.254
$MgCl_2$	0.953	0.018
Na_2SO_4	0.166	0.159
NaBr	0.025	0.010
$Na_2B_4O_7$	0.037	0.015
KCl	0.437	0.092
$CaCl_2$	0.013	0.011
LiCl	0.004	-------
Density (g/m/L)	1.188	1.176
Ionic strength (M)	6.848	4.965

Subtask 5.2: Results and Discussion

To assess the impact of gluconate on adsorption behavior of U, Th and Nd onto magnetite a conditional solid-water partitioning coefficient (K_{dc}; mL/g) was calculated according to the equation below (Eq. 1 – 2) as the ratio of solid phase concentration to dissolved concentration:

$$\boldsymbol{K_{dc}(L\,kg^{-1}) = \frac{[M]_{sld}}{[M]_{aq}}} \qquad \textbf{Eq. 1}$$

$$[\boldsymbol{M}]_{\boldsymbol{sld}} = \frac{\boldsymbol{V_L}\left([\boldsymbol{M}]_{\boldsymbol{aq(0)}} - [\boldsymbol{M}]_{\boldsymbol{aq(t)}}\right)}{[\boldsymbol{W}]_{\boldsymbol{sld}}} \qquad \textbf{Eq. 2}$$

Where$[\boldsymbol{M}]_{\boldsymbol{sld}}$ is the amount of contaminants adsorbed onto solid phase(s) (µg/kg); $[\boldsymbol{M}]_{\boldsymbol{aq(o)}}$ and $[\boldsymbol{M}]_{\boldsymbol{aq(t)}}$ (µg/L) are the initial and final aqueous Nd, Th, U concentration after time (t); $\boldsymbol{V_L}$ is the volume of aqueous solution (L) and $[\boldsymbol{W}]_{\boldsymbol{sld}}$ is the added mass of solid phase (kg).

Sorption in NaCl Brine

Presented in Figure 112. are the results of batch sorption studies investigating the impact of gluconate on sorption of Nd, Th, and U onto magnetite in NaCl brine (0.1 to 5.0 *M*).

The K_{dc} values increased over time, approaching equilibrium at 1440 min, after which it progressed toward a steady state over the remaining time interval. This comports well with previous studies that reported 1440 min as adequate for achieving equilibrium of sorption processes to avoid formation of significant precipitation or colloids [14]. The batch sorption data showed a steady to increasing trends for removal of U, Th and Nd from the NaCl brine over the 168 h time period. As ionic strength increases, no discernable trend was observed for the sorption of actinide onto batch samples likely due to formation of precipitation or colloids (Figure 112.). Overall, the sorption of U, Th and Nd onto batch samples were higher in 1.0 *M* and 5.0 *M* NaCl brines compared to the 0.1 *M* NaCl. Typically, the amount of Th and Nd removed from the 0.1 – 5.0 *M* NaCl brine was one to two orders of magnitude higher than that for U and is likely due to contribution of precipitation or colloids to sorption of Nd and Th. The sorption trends observed for the gluconate-amended NaCl solutions were similar to that for the gluconate-free NaCl brine. The addition of gluconate had little impact on the solubility of U, Th, and Nd as no significant differences were observed in aqueous concentration of U, Th and Nd in gluconate-free and gluconate-amended batch samples (Figure 112.).

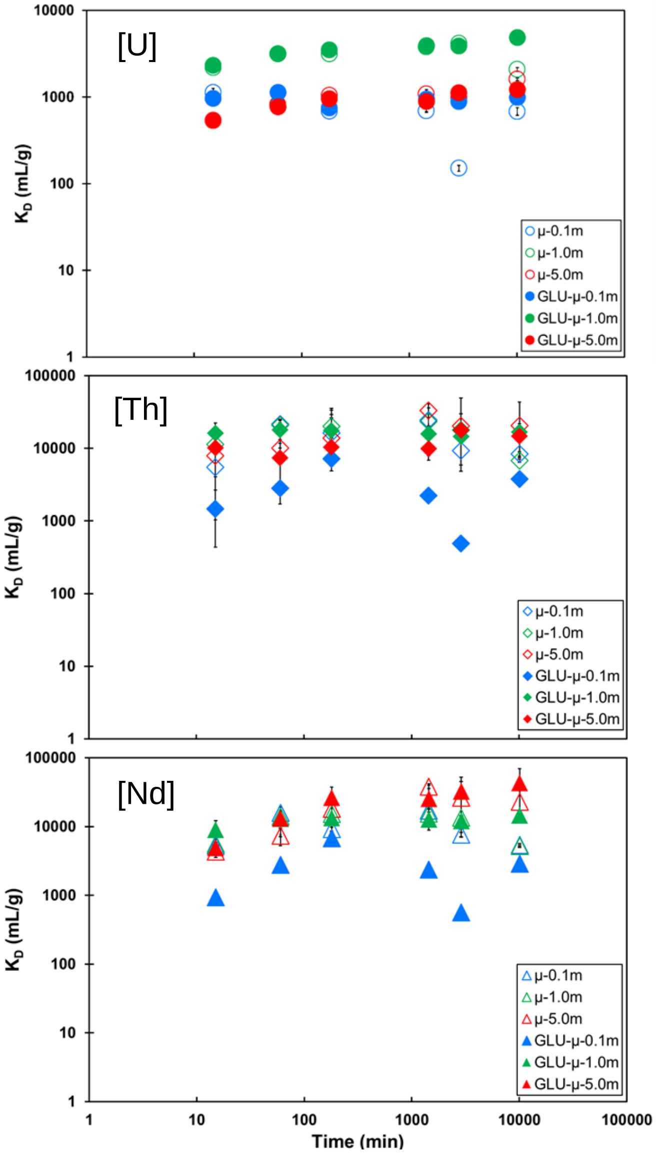

Figure 112. The K_{dc} values over time for sorption of U, Th, Nd (1000 μg/L) onto magnetite suspensions (1 g/L) in 0.1 - 5.0 M NaCl solutions. Filled symbols are gluconate-amended and unfilled symbols are gluconate-free samples. Error bars are based on sample triplicate; *x* and *y* axes are displayed in log scale for clarity.

Sorption in $MgCl_2$ Brine

Figure 113. presents the results of batch sorption studies in magnetite-amended $MgCl_2$ solutions (μ = 0.3 – 15 *m*) as a function of gluconate. The K_{dc} values for the $MgCl_2$ brines trended upward over time, approaching a steady state after 1440 min time interval. This is in good agreement with observed decreasing trends in aqueous concentration of U, Th and Nd in the studied brine (data not shown). The batch sorption data showed that the removal of U and Nd from $MgCl_2$ brine

increased over time, while that for Th varied over the same period (Figure 113.). Observed K_{dc} values for Th and Nd were one order of magnitude higher than those for U and could be due to formation of colloids or precipitation. With increase in ionic strength of brine, sorption of actinide onto batch samples decreased likely due to increased occupancy of sorption sites on magnetite by copious competing ions (Figure 113.). The sorption of U, Th and Nd onto batch samples was ranked as follows: 0.1 M $MgCl_2$ > 1.0 M $MgCl_2$ > 5.0 M $MgCl_2$. The higher K_{dc} values for Th sorption onto magnetite in the 0.1 – 5.0 *M* $MgCl_2$ brine may be indicative of significant precipitation or colloid formation. Overall, addition of gluconate does not promote actinide solubility because there was no discernable difference in aqueous U, Th, or Nd concentration between the gluconate-amended and gluconate-free samples. Furthermore, sorption trends observed for the gluconate-free brine was similar to that for the gluconate-amended brine (Figure 113.).

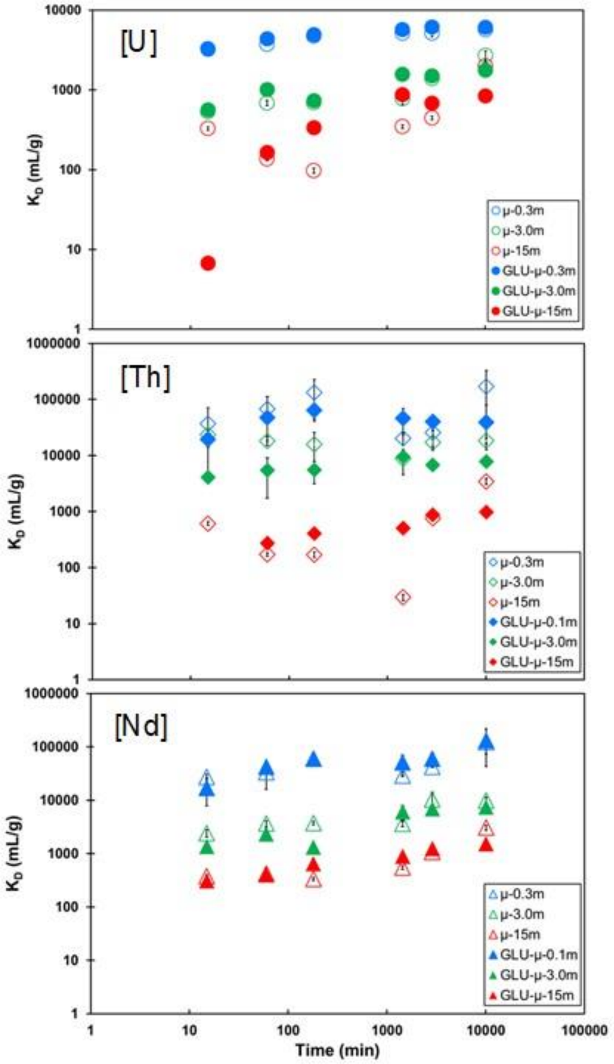

Figure 113. The K_{dc} values for sorption of U, Th, Nd (1000 µg/L) onto magnetite suspensions (1 g/L) in filtered 0.1 - 5.0 M $MgCl_2$ solutions. Filled symbols are gluconate-amended and unfilled symbols are gluconate-free samples. Error bars are based on sample triplicates; *x* and *y* axes are displayed in log scale for

clarity.

Sorption in $CaCl_2$ Brine

The impact of gluconate on sorption of actinide onto magnetite-amended $CaCl_2$ solutions (μ = 0.3 – 15 *m*) are displayed in Figure 114.. The K_{dc} values for the $CaCl_2$ brine increased over time and approached equilibrium at 24 h time interval. The sorption of U and Nd onto magnetite in the $CaCl_2$ brine exhibited a steady to increasing trend over the 168 h time period, while that of Th varied significantly over time likely due to solubility limitation or formation of precipitate. Actinide sorption onto batch samples generally decreased with increasing ionic strength presumably due to competition by copious ions for sorption sites on magnetite (Figure 114.). The sorption of actinide onto batch samples exhibited the decreasing trends: 0.1 *M* $CaCl_2$ > 1.0 *M* $CaCl_2$ > 5.0 *M* $CaCl_2$ (Figure 114.). Overall, amendment with gluconate does not enhance actinide solubility as there was no significant difference in aqueous U, Th and Nd concentration between gluconate-amended samples and gluconate-free samples. Sorption trends observed for the gluconate-free brines were similar to that for the gluconate-amended brines (Figure 114.).

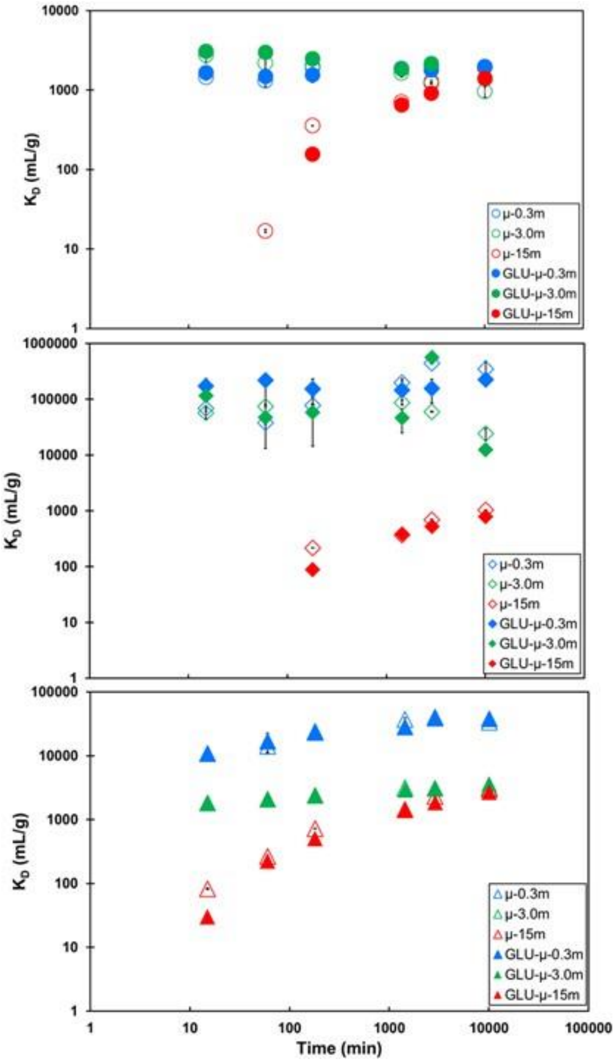

Figure 114. Progression of K_{dc} values over time for sorption of U, Th, Nd (1000 µg/L) onto magnetite suspensions (1 g/L) in 0.1 - 5.0 M $CaCl_2$ solutions. Filled symbols are gluconate-amended samples, unfilled

symbols are gluconate-free samples. Error bars are based on sample triplicate; *x* and *y* axes are displayed in log scale for clarity.

Sorption in GWB Brine

Figure 115 displays the results of actinide sorption onto magnetite-amended Generic Weep Brine (μ = 6.85 M) as a function of gluconate. The K_{dc} for sorption of Th and Nd in the GWB brine generally increased with time, approaching a steady state at about 1440 min interval, whereas it remained relatively unchanged for U. The averaged Kdc for U, Th and Nd were 495.3 ±18.7 mL/g, 704.8 ±42.3 mL/g and 1156.5 ±85.9 mL/g, respectively. The aqueous fractions (i.e. concentration measured in stock solution prior to the beginning of experiments) of U and Th decreased slightly (~20%) with time, while that of Nd declined significantly (20-60%), presumably due to formation of colloids/precipitates or loss to vessel walls. The gluconate-amended and gluconate-free brine exhibited similar steady-state K_{dc} trend for all studied contaminants (U, Th and Nd). There was no significant difference in actinide sorption between the gluconate-amended and gluconate-free brine samples, suggesting the little to no impact of gluconate addition on actinide solubility. To assess the impact of $MgCl_2$ on actinide sorption in GWB brine (GWB comprised of 0.95 M of $MgCl_2$), removal of actinides was compared in 1.0 M $MgCl_2$ and GWB brines. The removal of Th and Nd from GWB brine was one order of magnitude lower than that for 1.0 M $MgCl_2$ brine likely due to the relatively small aqueous fractions of Th and Nd that varied over time due to colloids/precipitate formation (Figure 117A).

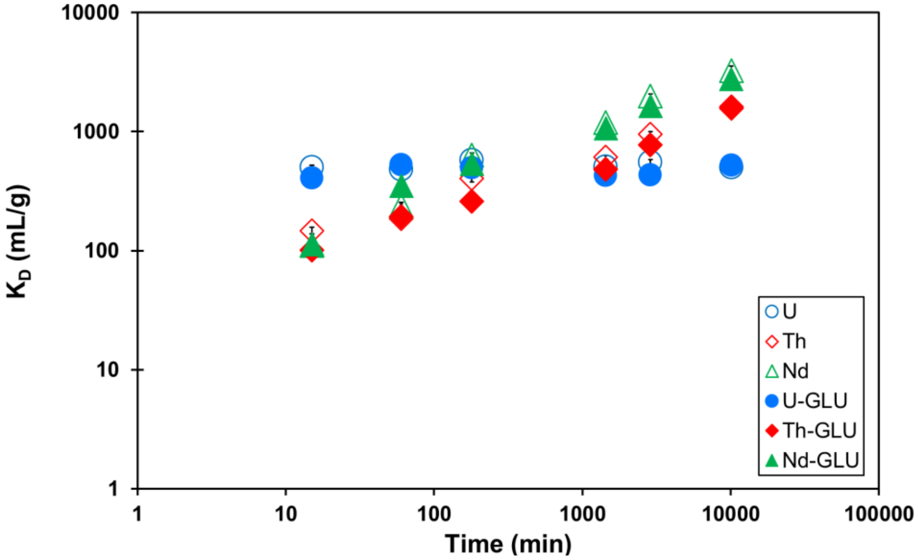

Figure 115. Change of K_{dc} values over time for sorption of U, Th, Nd (1000 μg/L) onto magnetite suspensions (~1 g/L) in Generic Weep Brine (6.85 M). Filled symbols are gluconate-amended and unfilled symbols are gluconate-free samples. Error bars are based on sample triplicates; *x* and *y* axes are shown in log scale for clarity.

Sorption in ERDA-6 Brine

Illustrated in Figure 116 are the results of the batch sorption study in ERDA-6 brine. The partition coefficient (K_{dc}) for sorption of Nd in the ERDA-6 brine increased with time, approaching a steady state at about 1440 min interval, whereas sorption was relatively unchanged for U and Th. The steady-state K_{dc} trend for all contaminants (U, Th, and Nd) was similar for the gluconate-amended and gluconate-free brine. The K_{dc} for U, Th and Nd averaged 137.52 ±4.57 mL/g, 11490 ±3769 mg/L and 5886 ±973 mL/g, respectively. The aqueous fractions of U decreased slightly (~20%) with time, while that of Th and Nd exhibited significant decline (20-80%), presumably due to formation of colloids/precipitates or losses to vessel walls. No discernable difference was observed in actinide sorption between the gluconate-amended and gluconate-free brine samples, implying that gluconate addition did not promote actinide solubility. Because ERDA-6 brine is predominantly NaCl (4.25 M), the impact of 5 M NaCl on actinide sorption was compared with that of ERDA-6 brine. Study result showed that removal of U and Nd was approximately an order of magnitude higher in the 5.0 M NaCl compared to that in the ERDA-6 brine, while that for Th was similar for both brines Figure 117B. The higher K_{dc} values in 5 M NaCl brine could be due to the smaller buffering capacity of the NaCl brine compared to the ERDA-6 brine that likely led to the formation of colloids/precipitate.

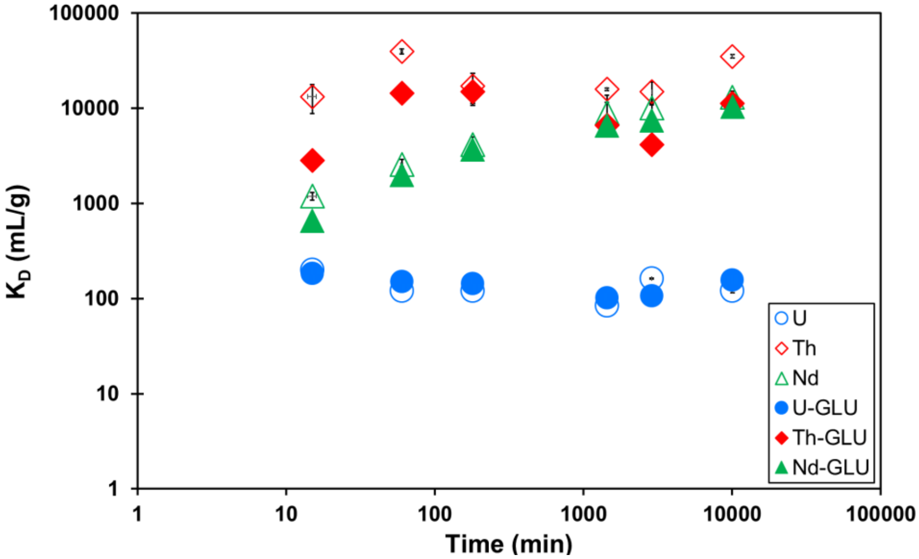

Figure 116. Change of K_{dc} values over time for sorption of U, Th, Nd (1000 μg/L) onto magnetite suspension (~1 g/L) in ERDA-6 brine. Filled symbols are gluconate-amended and unfilled symbols are gluconate-free samples. Error bars are based on sample triplicates; *x* and *y* axes are shown in log scale for clarity.

Subtask 5.2: Conclusions

In this work the impact of gluconate and iron oxide minerals (magnetite) on actinide sorption behavior under anaerobic conditions and high ionic strength environment representative of the WIPP repository were studied. Observed sorption trends in the gluconate-free brines were similar to those in gluconate-amended brines. Moreover, the addition of gluconate did not appear to enhance the solubility of U, Th and Nd, as there were no discernable differences in aqueous concentration of U, Th and Nd among evaluated batch samples. This could be indicative of little to no formation of tertiary gluconate complex with the studied actinides under the predicted pH range of this study. Higher ionic-strength brines tended to increase overall solubility of the studied contaminants likely due to strong competition from copious ions for sorption sites. The K_{dc} for sorption of U, Th and Nd in GWB brine averaged 495.3 ±18.7 mL/g, 704.8 ±42.3 mL/g and 1,156.5 ±85.9 mL/g, respectively. While the K_{dc} values in ERDA-6 brines were 137.52 ±4.57 mL/g, 11,490 ±3,769 mg/L and 5,886 ±973 mL/g for U, Th and Nd, respectively. The lower K_{dc} values for the GWB brine compared to ERDA-6 brine are likely due to the higher buffering capacity of the magnesium-rich GWB brine. Under the experimental conditions utilized in this study addition of gluconate to two WIPP-relevant brines, GWB and ERDA-6, resulted in little to no impact on sorption of actinides onto magnetite solid phase(s). This unexpected results contradict several studies that reported decrease in actinide sorption due to formation of soluble metal complexes with gluconate. The observed discrepancy could be explained by the insufficient concentration of gluconate (~1 mg/L) that was employed in these studies. To corroborate this assertion, a simple calculation of magnetite adsorption sites was undertaken as follows: utilizing a surface site density of 2.4 site/nm^2 [Mayant et al., 2008] and measured BET surface area of 8.13 m^2/g, the 1 g/L of magnetite used in this study contained approximately 32.4 µM of adsorption sites. The concentrations of actinide and gluconate used in this study were 4.3 µM and 4.6 µM, respectively, which were 0.13 and 0.14 times the number of adsorption sites on the magnetite surface. Therefore, a 1:1:2 molar ratio of magnetite, actinide and gluconate would be ideal for formation of copious complexes.

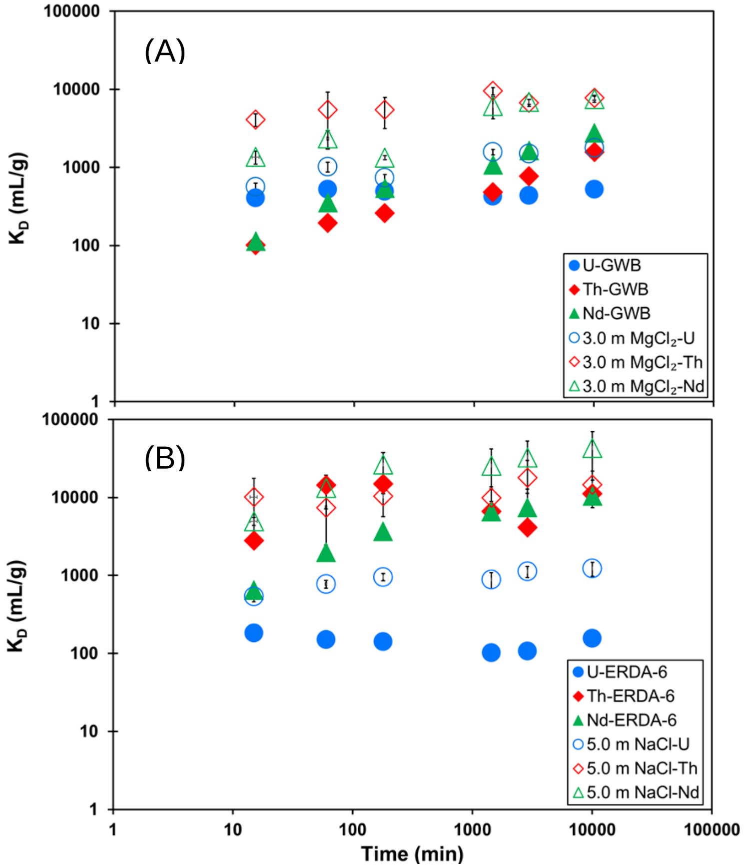

Figure 117. Change of K_{dc} values over time for sorption of U, Th, Nd (1000 µg/L) onto magnetite suspensions (~1 g/L) in WIPP-relevant brines. Filled symbols are GWB (top) and ERDA-6 (bottom), and unfilled symbols are 1.0 M $MgCl_2$ (top) and 5.0 M NaCl (bottom) brines. Error bars are based on sample triplicates; *x* and *y* axes are shown in log scale for clarity.

Subtask 5.2: References

Baston, G. M. N., J. A. Berry, K. A. Bond, M. Brownsword, and C. M. Linklater (1992), Effects of Organic Degradation Products on the Sorption of Actinides, Radiochim Acta, 58-9(2), 349-356, doi: https://doi.org/10.1524/ract.1992.5859.2.349.

Brady, P. V., H. W. Papenguth, and J. W. Kelly (1999), Metal sorption to dolomite surfaces, Appl Geochem, 14(5), 569-579, doi: Doi 10.1016/S0883-2927(98)00085-7.

Brown, G. O., D. A. Lucero, and W. G. Perkins (1999), Column Experiments for Radionuclide Adsorption Studies of the Culebra Dolomite: Retardation Parameter Estimation for Non-Eluted Actinide Species*Rep. SAND98-1005; Other: ON: DE00002672 United States 10.2172/2672 Other: ON: DE00002672 SNL English,* Sandia National Laboratories, Albuquerque, NM, and Livermore, CA.

Brush, L. H., and L. J. storz (1996), Revised Ranges and Probability Distributions of Kds for Dissolved Pu, Am, U, Th, and Np in the Culebra for the PA Calculations to Support the WIPP CCA*Rep.*, Albuquerque, New Mexico.

Colàs, E., M. Grivé, I. Rojo, and L. Duro (2011), Solubility of ThO2·xH2O(am) in the presence of gluconate, Radiochim Acta, 99(5), 269-273, doi: 10.1524/ract.2011.1837.

Colàs, E., M. Grivé, I. Rojo, and L. Duro (2013), The Effect of Gluconate and EDTA on Thorium Solubility Under Simulated Cement Porewater Conditions, Journal of Solution Chemistry, 42(8), 1680-1690, doi: 10.1007/s10953-013-0054-2.

Gaona, X., V. Montoya, E. Colas, M. Grive, and L. Duro (2008), Review of the complexation of tetravalent actinides by ISA and gluconate under alkaline to hyperalkaline conditions, J Contam Hydrol, 102(3-4), 217-227, doi: 10.1016/j.jconhyd.2008.09.017.

Lagos, L. E., Y. Katsenovich, R. Gudavalli, A. Lawrence, and M. Mahmoudi (2018), Environmental remediation science and technology - Year-end technical report*Rep.*, Applied Research Center, Florida International University, Miami, Florida.

Mayant, C., B. Grambow, A. Abdelouas, S. Ribet, and S. Leclercq (2008), Surface site density, silicic acid retention and transport properties of compacted magnetite powder, Physics and Chemistry of the Earth, Parts A/B/C, 33(14-16), 991-999, doi: 10.1016/j.pce.2008.05.011.

Reed, D. T., and M. Altmaier (2013), Proceedings of the Third International Workshop on Actinide and Brine Chemistry in a Salt-Based Repository (ABC-Salt III), Los Alamo National Laboratory, Santa Fe, New Mexico.

Sawyer, D. T. (1964), Metal-Gluconate Complexes, Chemical Reviews, 64(6), 633-643, doi: 10.1021/cr60232a003.

Stein, C. L. (1985), Mineralogy in the Waste Isolation Pilot Plant (WIPP) facility stratigraphic horizon*Rep. SAND-85-0321; Other: ON: DE86000571 United States 10.2172/5203761 Other: ON: DE86000571 NTIS, PC A03/MF A01. SNL English*, Medium: ED pp, Sandia National Labs., Albuquerque, NM (USA).

Tits, J., E. Wieland, and M. H. Bradbury (2005), The effect of isosaccharinic acid and gluconic acid on the retention of Eu(III), Am(III) and Th(IV) by calcite, Appl Geochem, 20(11), 2082-2096, doi: 10.1016/j.apgeochem.2005.07.004.

TASK 6: HYDROLOGY MODELING OF BASIN 6 OF THE NASH DRAW NEAR THE WIPP

The Waste Isolation Pilot Plant (WIPP) is the nation's only deep geologic waste repository in operation which isolates transuranic waste 2,150 feet underground within the Salado Salt Formation. This karst region formed from the dissolution of soluble rocks such as limestone, dolomite, and gypsum. Scientists and researchers are concerned about the long-term vulnerability of this karst topography and thus the eventual integrity and performance of the WIPP due to the influence of characteristic surface features, such as sinkholes, swallets, and karst valleys on groundwater recharge over time. The Rustler Formation which lies above the Salado Formation contains three fluid-bearing zones, the Rustler-Salado contact residuum, the Culebra dolomite and the Magenta dolomite, of which the Magenta and Culebra are of primary concern as they extend over the WIPP site. Just west of WIPP is the Nash Draw, which is an enclosed basin made up of thirty internally drained sub-basins identified from topography and field surveys. Nash Draw developed through solution and erosion of upper Permian rocks creating an array of surface features, including sinkholes, swallets, and karst valleys, and thus serves as an ideal area for this study with similar topography and representative surface hydrological features as that which overlies the WIPP.

This task therefore involves the development of a high-resolution digital elevation model (DEM) of Basin 6 of the Nash Draw to more accurately delineate surface hydrological features, as well as the development of hydrological models using the DOE-developed Advanced Simulation Capability for Environmental Remediation (ASCEM) modeling toolset to improve the current understanding of the regional water balance, particularly the relation between the Culebra recharge and the intense, episodic precipitation events typical of the North American monsoon. This relationship is essential for understanding the rate of propagation of the shallow dissolution front, and the impact of land-use changes around the WIPP facility and Nash Draw on water levels and chemistry in compliance-monitoring wells.

Subtask 6.1: Basin 6 DEM Development and Delineation of Surface Hydrological Features (Completed)

Subtask 6.1: Introduction

To study the impact of characteristic surface hydrological features on the groundwater recharge in Basin 6, in conjunction with soil properties and vegetation types, requires a revision of the current site conceptual model to couple surface water and groundwater processes, which both require a high-resolution digital elevation model (DEM), including channels and sink holes, to account for surface water routing and return flow. This subtask therefore involves the development of a high-resolution digital elevation model (DEM) and characterization of the physical characteristics of soils in Basin 6 of the Nash Draw, which is essential for more accurate delineation of these surface hydrological features that can influence regional groundwater recharge. A high-resolution DEM will improve the ability of the coupled surface/subsurface flow models to simulate the hydrologic response to a range of storm events, compute the surface water balance and provide more accurate estimates of regional-scale infiltration rates/groundwater recharge.

Subtask 6.1: Objectives

The objective of this subtask is to develop a high-resolution DEM of Basin 6 of the Nash Draw near the WIPP using UAV-based photogrammetry to support the development of regional surface and groundwater models by providing a more accurate ground surface representation for mesh generation, as well as a more detailed delineation of significant topographical and hydrological surface features that impact groundwater recharge. The aim is to develop the data layers for the terrestrial overland flow, channel routing, and subsurface flow processes of the regional flow models. Due to the karstic topography, local hydrologic features, such as sinkholes and brine lakes, play an essential role in the surface/subsurface water exchange in the WIPP and Nash Draw regions. As these geomorphological features are present at a very small scale (meters), a need for a high-resolution hydrological model is anticipated to accurately represent hydrological flow variability across small-scales.

Subtask 6.1: Methodology

In FIU Year 1, the development of a high-resolution (1-m) DEM was initiated by means of a photogrammetric approach using unmanned aerial vehicles (UAVs), where ~22 km^2 of the ~24 km^2 surface area of Basin 6 of the Nash Draw west of the WIPP was collected. The images were processed using photogrammetric techniques to build a high-resolution point cloud, which was then post-processed for vegetation removal, revealing the true ground surface. FIU graduate and undergraduate students (DOE Fellows) were trained on the use of photogrammetric software and techniques and drone operation. For FIU Year 2 the FIU team revisited the site and finalize the UAV observations and generate a high-resolution DEM for Basin 6. To evaluate the quality of the developed DEM, a subdomain of Basin 6 was chozen for wich a total of 87 ground control elevation points were obtained during February 2020. Furthermore, within this domain, in December 2021 additionally 21 points were sample at locations with vegetation and also vegetation height was recorded (see figure below).

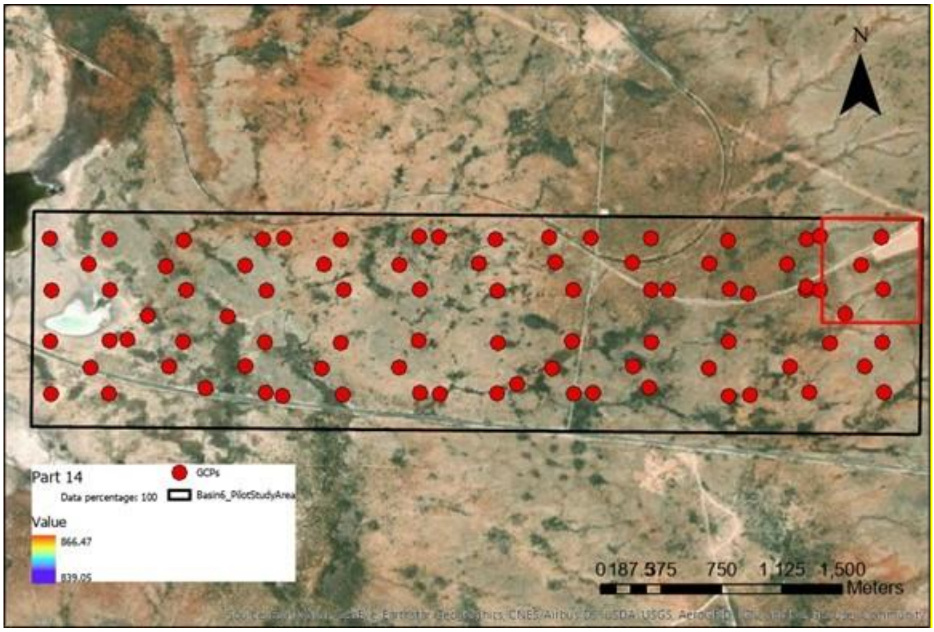

Figure 118. GCPs collected during February 2020 UAV survey of Basin 6 pilot study area.

In FIU Year 2 FIU traveled to Carlsbad, NM to complete the UAV-based survey of the remaining 5 km^2 of Basin 6, located within the Nash Draw west of the WIPP. Figure 119 shows a map of Basin 6 with the remaining area that was surveyed highlighted in blue (approx. 5 km^2).

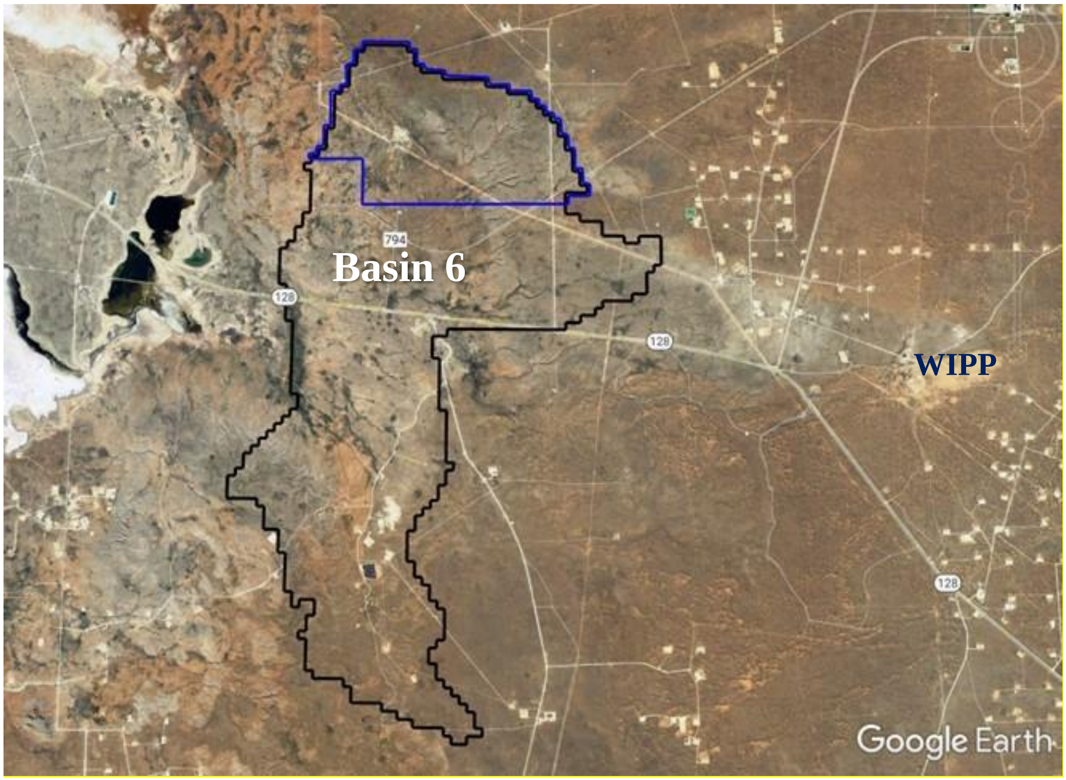

Figure 119. Completed survey area (blue outline) in Basin 6, Carlsbad, NM during December 2021 trip.

The resulting high-resolution DEM in FIU Year 2 will be evaluated for the presence of sinkholes to be compared to a previously performed in-situ based inventory. Also, we will evaluate the physical characteristics of the soils at different depth (e.g. texture, porosity, etc.) from available observations and databases and collect additional data while visiting the site for additional validation. The generated DEM and surface information of Basin 6 will be used to delineate and extract topographical features such as drainage basins, brine lakes, channels, sink holes, discharge points and other relevant hydrological features using ArcGIS geoprocessing tools, which will be essential for hydrological model development. FIU will continue to train undergraduate and graduate students (DOE Fellows) on UAV photogrammetry methods and provide mentorship and field experience through student summer internships in collaboration with Los Alamos National Laboratory (LANL), Carlsbad Field Office (CBFO) and Pacific Northwest National Laboratory (PNNL) scientists.

Subtask 6.1: Results and Discussion

There are several algorithms that have been tested and explored to highlight and extract vegetation to develop a bare ground DEM. Four different filtering algorithms, from commercial-ready software to user-supervised machine learning algorithms, were selected and tested to determine the effectiveness of filtering point clouds. These five different algorithms were chosen based on existing literature and available tools and include:

1. Ground point classification based on RGB-based VIs using Python package.
2. ArcGIS Pro point cloud classification.
3. LAStools
4. Pix4D point cloud classification.
5. CloudCompare classification using CANUPO plugin.

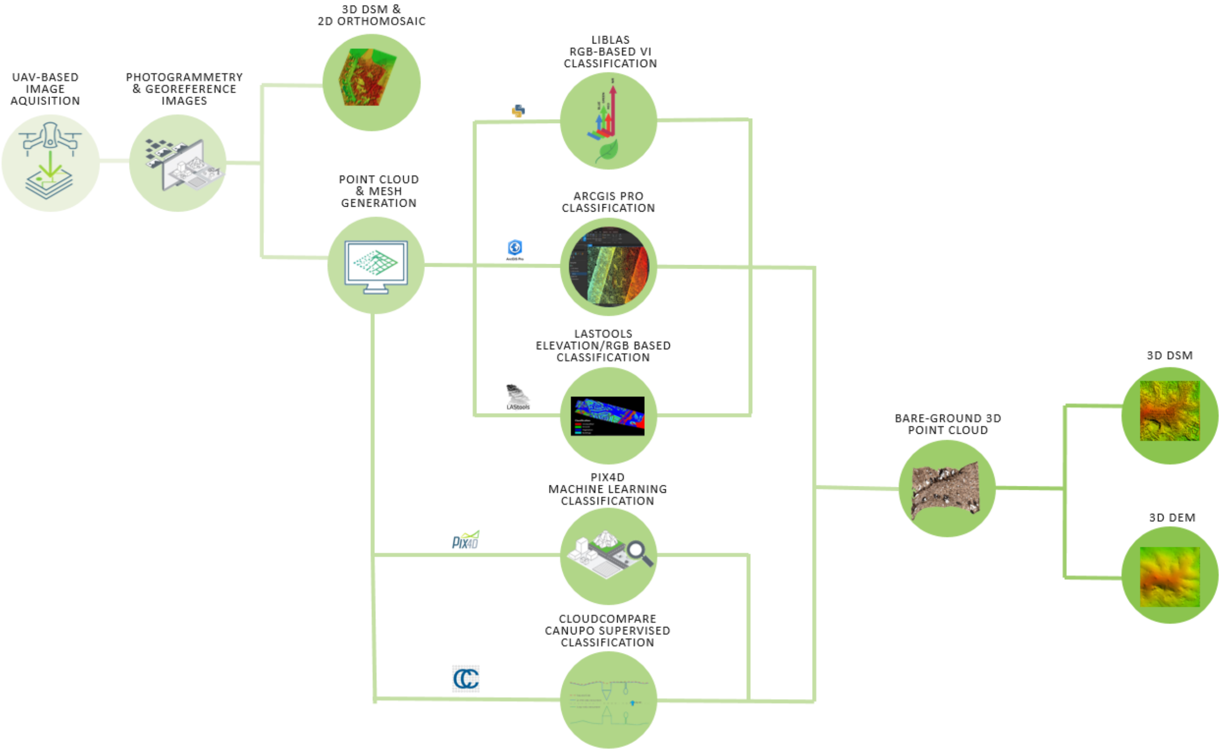

Figure 120. Methodology for developing a bare ground DEM.

Vegetation indexes (VI) have been widely used by scientists for a variety of purposes such as estimating crop yield, measuring water content, and determining health of vegetation. Recently, with the increased popularity of UAV-generated DSMs. As the Phantom IV drone only samples visible light, here five different VIs were applied to identify vegetation in observations:

Table 33. Vegetation Indices with references and purpose.

Vegetation Index	Formula (unitless)	Purpose
Red-Green Index (RGI)	$RGI = \frac{R}{G}$	Monitoring pigment changes during leaf development
Red-Green-Blue Vegetation Index (RGBVI)	$\frac{(G \times G) - (R \times B)}{(G \times G) + (R \times B)}$	Captures reflectance differences due to chlorophyll-a absorption and chlorophyll-b absorption
Green Leaf Index (GLI)	$\frac{2 \times G - R - B}{2 \times G + R + B}$	Estimates leaf chlorophyll content for various types of plants

Visible Atmospherically Resistant (VARI)	$\frac{G-R}{G+R-B}$	Mitigates illumination differences and atmospheric effects
Normalized Green Red Difference Index (NGRDI)	$\frac{G-R}{G+R}$	Determines biomass and nutrient status for the weed management of an area

Each VI was applied to the unclassified point cloud of a sub-region of Basin 6 to create an index map divided into twelve classes in order to determine an appropriate threshold to classify the ground and vegetation. A drawback of making use if RGB information for a point alone, is that it does not include the elevation information, which is also sampled, as well as information on the small-scale variability around the point. Therefore, to include this information more advanced algorithms were also applied. The standard point cloud classification method in ArcGIS Pro includes a slope tolerance for slope variation, which can capture gradual undulations in the ground's topography that VI approaches don't include. Lastools triangulaizes the point cloud to detect small-scale variability caused by vegetation and correct for it. Similary, Pix4D has an internal algorithm to classify point clouds into ground, road surface, high vegetation, building, and human-made object. These three algorithms all are based on unsupervised classification. To also include a supervised classification approach, CloudCompare was used. Using CloudCompare's CANUPO method a sample dataset was created with known "ground" and a "vegetation" points (see Figure 121). This dataset was used to train the CANUPO algorithm, which is subsequently used to identify vegetation within the point cloud dataset.

Figure 121. Bare ground (displayed in green) training samples and vegetation (displayed in blue) training samples created using a subregion of the Basin 6 pilot study area point cloud.

Each method resulted in two separate point clouds: ground only and vegetation only. The ground only point cloud was converted from a LAS dataset to raster with a 1 m DEM using the LAS to Raster tool in ArcGIS Pro in order to conduct a comparative analysis. To analyze the accuracy of each DEM generated, various Python scripts were developed to use the point clouds, orthomosaics, and DEMs generated from each methods were used to estimate the accuracy of each method. In addition to the DEMs, the GCPs and the vegetation heights collected were used to compare the heights that were successfully removed from the point cloud to calculate the accuracy of the vegetation removal from each dataset.

For the VI-based methodology, a visual analysis was first conducted to determine how much each index could distinguish bare ground from vegetation. First, orthomosaic images containing the marked GCPs were extracted from the Pilot Study Area and compared to side by side. Overall, from the visual comparative analysis, the VIs did not properly identify vegetation where there were plant heights associated at the GCPs (see Figure 122).

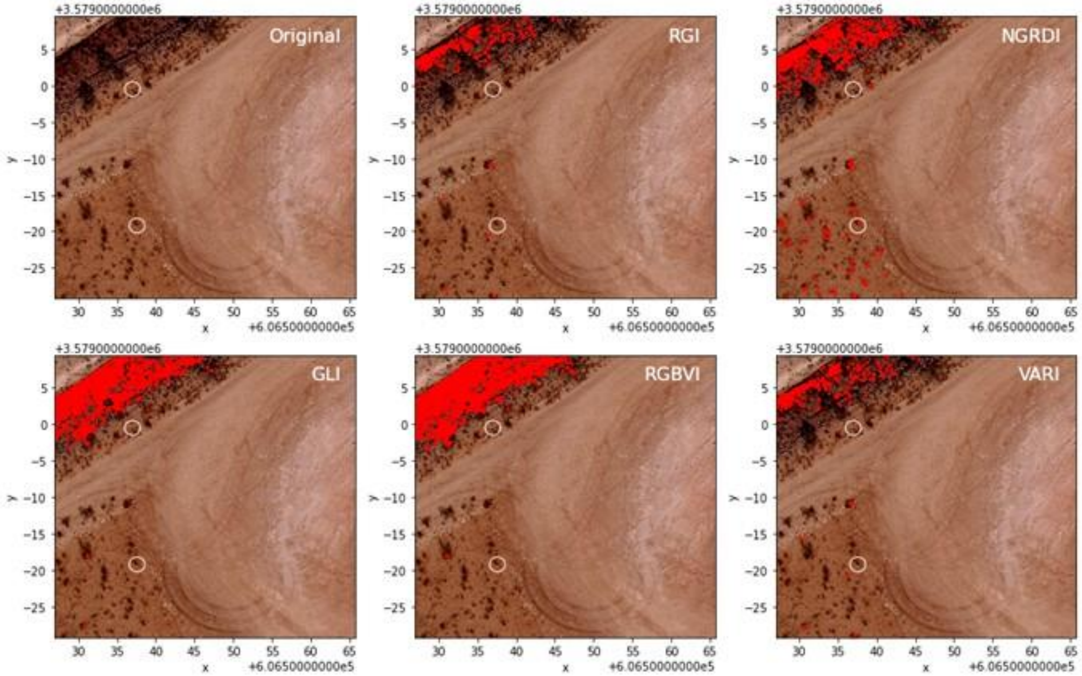

Figure 122. Top left panel shows the orthophoto for a small subdomain within Basin 6. The other panels show for each of the applied RGB methods the identified non-ground point cloud location as shown in red. The white circles indicate locations where vegetation was observed while performing the field work.

In addition to the visual comparative analysis, a quantitative analysis was done using the marked GCPs and the classified point cloud that was created using the determined threshold values for each VI. To do so, a script was created to quantify how many points within a 30 cm radius from 22 GCPs were identified and displayed through a boxplot. In Figure 123, all VIs, except VARI, were able to identify some pixels as vegetation at five out of the 22 locations, whereas VARI was the only method to identify vegetation pixels at nine locations. This further confirms the conclusion that the VIs did not perform effectively in identifying vegetation at GCPs were there were recorded plant heights.

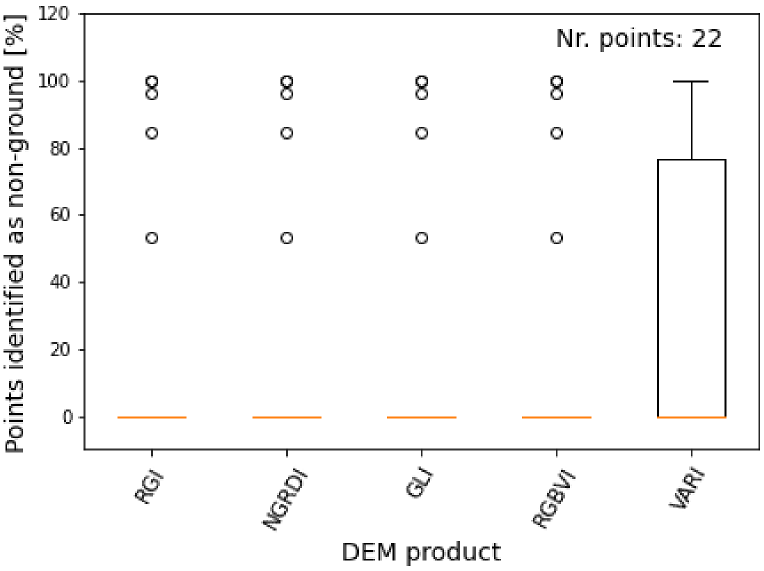

Figure 123. Boxplot displaying the number of points identified as non-ground by each VI.

After evaluating the VI performance, the resulting classified point clouds from the machine learning methods were assessed in order to determine which type of methodology performed best to create a high-resolution DEM. To determine the accuracy of the elevations, the USGS LiDAR point cloud (of 1-meter resolution) was used as well as the 10-meter USGS DEM.

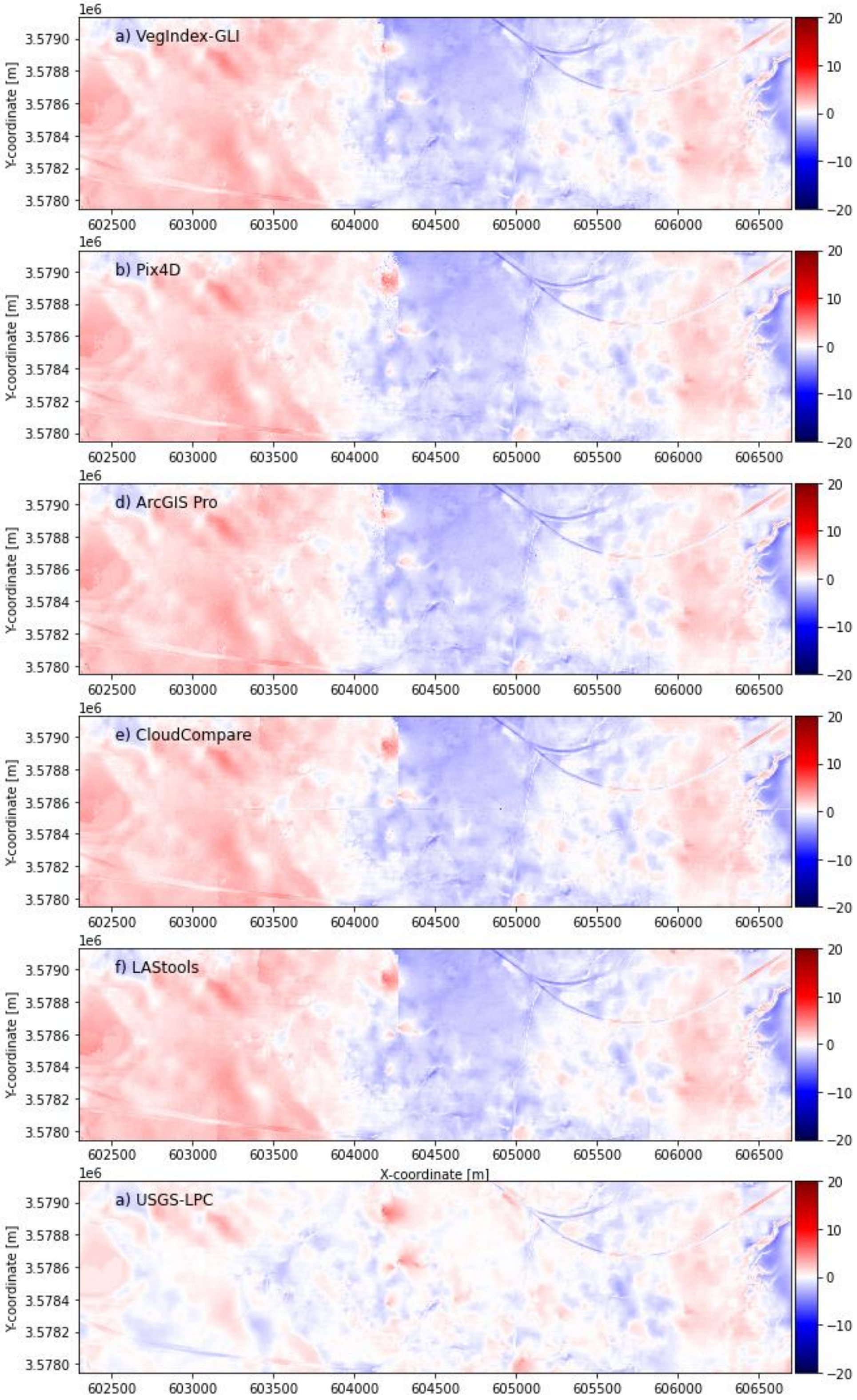

Figure 124. Elevation differences of UAV-generated DEM compared to USGS 10-meter DEM.

From the above figure, there were varying elevation differences for all methods in respect to the USGS 10 m DEM. For the UAV-generated DEMs, there is a defining line on the left-hand side of the domain (red shaded) area from the region in the middle of the domain. When displayed on ArcGIS Pro, the elevation had differences greater than 30 meters. A possible explanation for this distinction can be because the drone was flown over the course of four days. When the images were plotted, it can be seen that the flight path changes orientation during Flight 2. When the DSM created by Pix4D was plotted, it was also discovered that cells within the rasters in the overlapping regions between flights contained different elevation values.

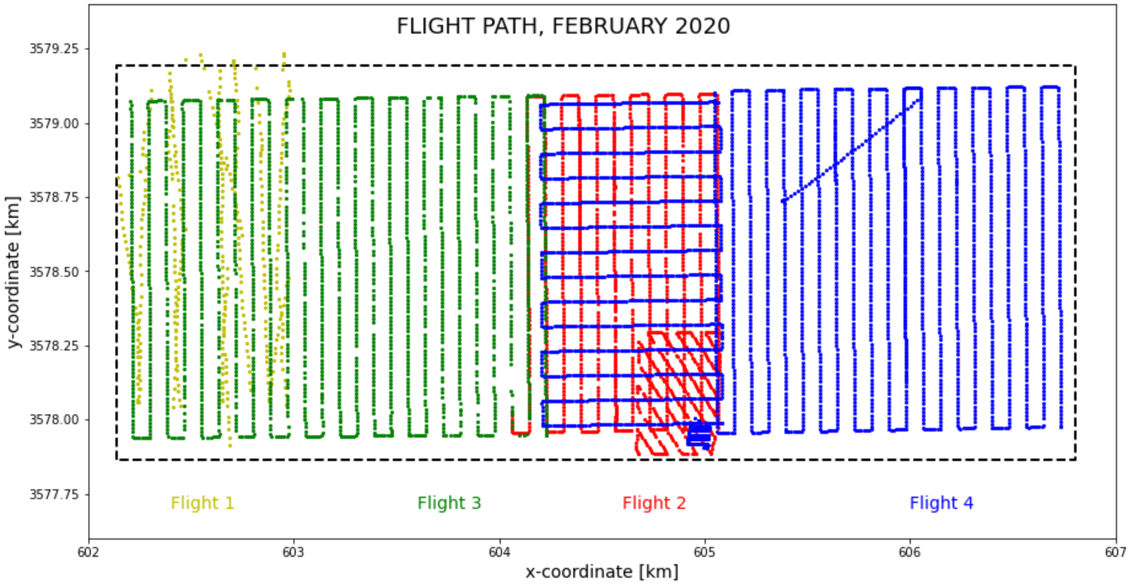

Figure 125. Drone flight paths observed during February 2020.

Additionally, the GCPs collected during the February 2020 visit as well as the vegetation heights recorded in August 2021 were used to compare the elevation differences once the vegetation was removed from the point cloud and processed to a DEM. From the boxplot figure (Figure 126), it is observed that the overall distribution widths for the tested removal methods and the USGS LPC is smaller compared to the 10-m USGS DEM. This signifies the advantage of using higher resolution DEMs which represent heights more accurately compared to a coarser resolution which might not capture features of interest. In the case of this research objective, it is important to capture features such as sinkholes, gulleys, and other features that are characteristic of this region for the purpose of developing a hydrologic model.

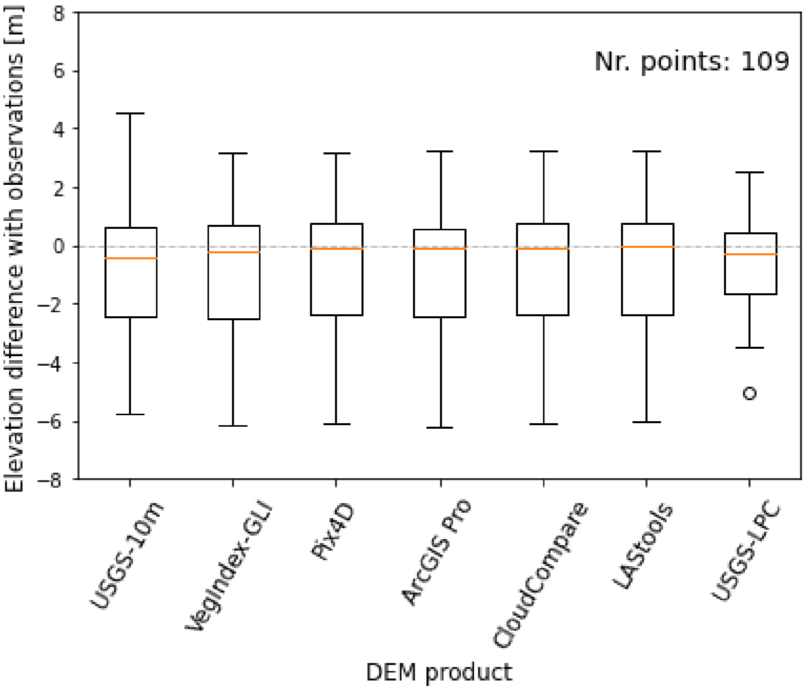

Figure 126. Boxplot displaying elevation differences with respect to observations measured (GCPs and vegetation heights).

In Figure 127, the GCPs with recorded plant heights were used to measure how many points were identified as non-ground. There is variability among all the machine learning methods but the ArcGIS Pro and CloudCompare method were able to identify vegetation at more GCPs.

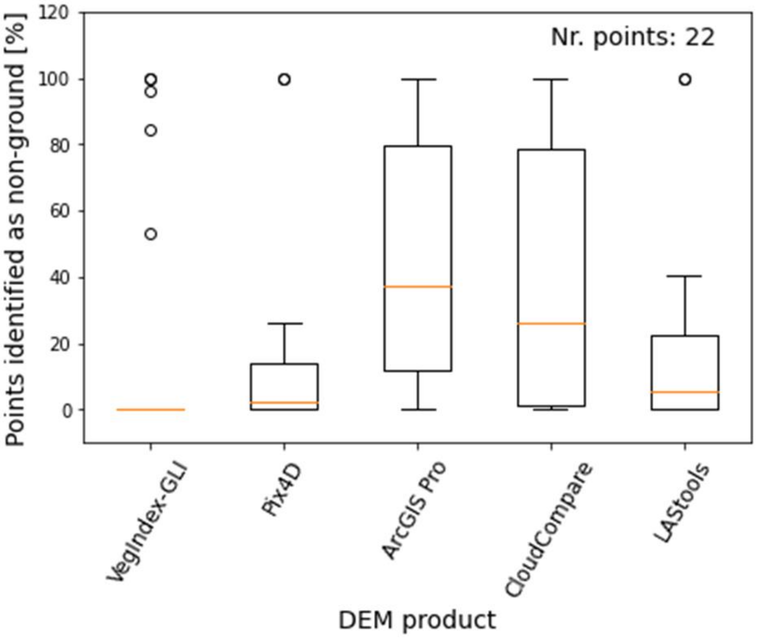

Figure 127. Points identified as non-ground for the tested vegetation removal methods.

Table 34. Tested vegetation removal methods and level of accuracy.

Method	Level of accuracy
VI	Low
ArcGIS Pro	High
Pix4Dmapper	Moderate
CloudCompare	High
LAStools	Moderate

To generate the 1-m DEM, the initial plan was to make use of point cloud data obtained from FIU field observations using the drone. However, the above results show that the recently released USGS lidar point cloud dataset performs very well in capturing the surface elevation at a 1m spatial resulotion. This dataset was not available at the start of this research, but it was decided to use this product in generating a high-resolution DEM. The figure below shows the final DEM. It should be noted that the boundaries of Basin 6 do not correspond with the topographic water divide. Therefore, the domain was extended beyond the Basin 6 boundary up to the water divide. The image below presents an overview of the 1-m DEM. This DEM was shared with our collaborators and is currently being processed to enable simulations within the Advanced Terrestrial Simulator (ATS).

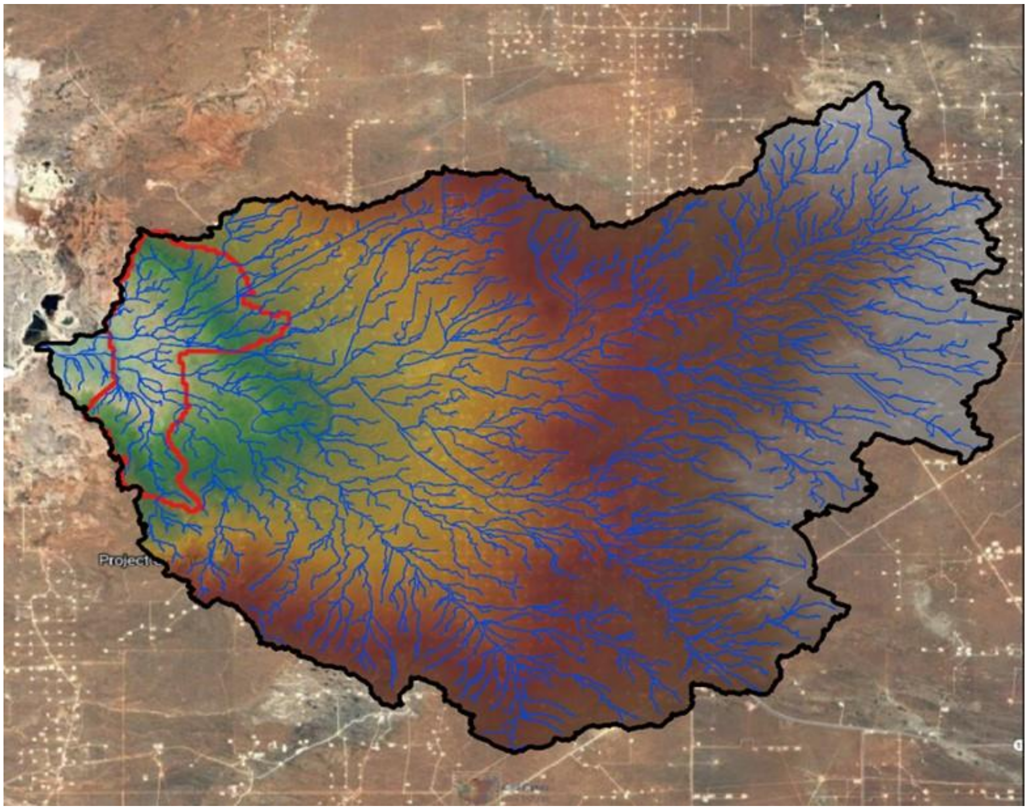

Figure 128. High-resolution DEM as generated from the USGS point cloud dataset. Basin 6 is shown in red, while the river network is shown in blue.

The USGS LPC was then used as input for the Sinkhole Mapper toolbox and the results were compared to the sinkhole inventory provided in Goodbar et al. (2020). Over 100 potential sinkholes were identified from the toolbox that were not captured in the inventory. Smaller sinkholes (with areas less than 20 m^2) were located throughout the study area with a majority of them located along gulleys and karst valleys. Bigger sinkholes were in lower topographic regions and alongside the Jai Highway, which bisects Basin 6. This number although, can alter depending on what is classified as a sinkhole. Sinkholes can be classified depending on size, depth, geology, etc. The goal of this post-processing step is to provide an example of how the high-resolution DEM can be used for further analysis which will aid in the analysis of how surface features can potentially impact the integrity and performance of the WIPP.

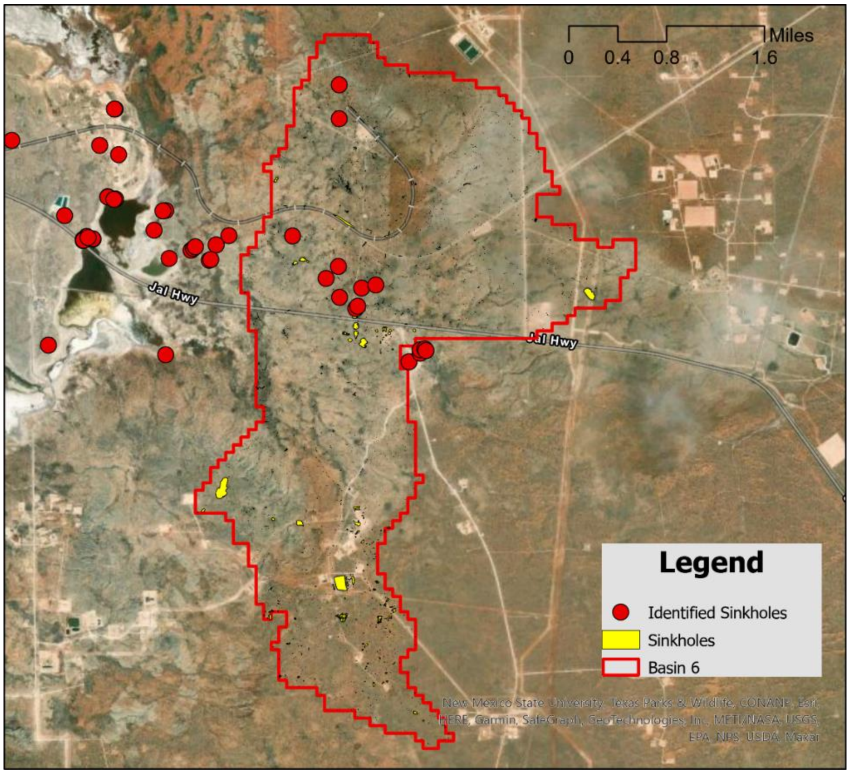

Figure 129. Identified sinkholes from field surveys (Goodbar et al., 2020) (red circle) and sinkholes identified with ArcGIS Pro toolbox (yellow areas) (Zhang et al., 2019).

Subtask 6.1: Conclusions

This subtask has been completed and the derived high resolution DEM provided to DOE collaborators at LANL. Several methods were applied to correct for the impact of vegetation contamination in the photogrammetry DEM product. The VI based methods do a poor job in identifying vegetation within Basin 6. In comparison, the more advanced algorithms that include both RGB, elevation and surrounding information do a much better job in identify points that are contaminated by vegetation, with the machine learning approach as available within CloudCompare showing the best results. The derived DEMs are of comparible quality to those obtained from the USGS lidar point cloud product. Given the fact that this product is available for a larger domain, it was decided to use the USGS LPC product to develop a 1-m DEM.

Using the 1-m DEM it was possible to extract Basin 6 and its upstream domain. This will be used to simulate the hydrological response of this region in Subtask 6.2. Furthermore, a sinkhole detecktion algorithm was run, which was able to detect a considerable amount of sinkholes within

Basin 6. There hydrological response during extreme events will be the focus of interest for the modeling study.

Subtask 6.1: References

Agarwal, A., Kumar, S., & Singh, D. (2020). An Adaptive Technique to Detect and Remove Shadow from Drone Data. *Journal of the Indian Society of Remote Sensing*, 1-8.a

Anders, N., Valente, J., Masselink, R., & Keesstra, S. (2019). Comparing Filtering Techniques for Removing Vegetation from UAV-Based Photogrammetric Point Clouds. Drones, 3(3), 61.

Deb, K., & Suny, A. H. (2014). Shadow detection and removal based on YCbCr color space. *SmartCR*, *4*(1), 23-33.

Goodbar, A. K., Powers, D. W., Goodbar, J. R., & Holt, R. M. (2020). Karst and sinkholes at Nash Draw, southeastern New Mexico (USA).

Sadeghi-Tehran, P., Virlet, N., Sabermanesh, K., & Hawkesford, M. J. (2017). Multi-feature machine learning model for automatic segmentation of green fractional vegetation cover for high-throughput field phenotyping. Plant methods, 13(1), 103.

Sandino, J., Gonzalez, F., Mengersen, K., & Gaston, K. J. (2018). UAVs and machine learning revolutionising invasive grass and vegetation surveys in remote arid lands. Sensors, 18(2), 605.

Serifoglu Yilmaz, C., & Gungor, O. (2018). Comparison of the performances of ground filtering algorithms and DTM generation from a UAV-based point cloud. Geocarto international, 33(5), 522-537.

Skarlatos, D., & Vlachos, M. (2018). Vegetation removal from UAV derived DSMS, using combination of RGB and NIR imagery.

Yilmaz, V., Konakoglu, B., Serifoglu, C., Gungor, O., & Gökalp, E. (2018). Image classification-based ground filtering of point clouds extracted from UAV-based aerial photos. Geocarto international, 33(3), 310-320.

Zhang, C., & Xie, Z. (2013). Object-based vegetation mapping in the Kissimmee River watershed using HyMap data and machine learning techniques. Wetlands, 33(2), 233-244.

Subtask 6.2: Model Development

Subtask 6.2: Introduction

The proposed work to develop a groundwater model (GWM) for Basin 6 of the Nash Draw near the WIPP. After evaluating various open-source surface hydrological models (among others: Community Land Model (CLM), WRF-Hydro) it was decided to make use of the Advanced Terrestrial Simulator (ATS) to simulate the near-surface hydrological response (i.e. infiltration and evapotranspiration) and how this impacts groundwater recharge.

ATS is an ecosystem-based, integrated, distributed hydrology simulator that is built on the underlying multi-physics framework provided by Amanzi, the high performance computing simulator developed in the ASCEM program used for environmental applications to provide flexible and extensible flow and reactive transport simulation capability. The output of the ATS model includes predictions of infiltration rates over selected regions of interest, such as sinkholes, and groundwater recharge, and hence ensembles of ATS simulations facilitate sensitivity and uncertainty analysis of groundwater and surface water flows.

The first phase of this task is to develop a detailed understanding of the ATS-Amanzi model as well as identification of available relevant hydrological data (as obtained from Subtask 6.1), followed by the development of a coupled ATS-Amanzi model to enable simulation of regional scale groundwater recharge and assess the role of small-scale hydrological features (e.g. sink holes, brine lakes and gullies).

Subtask 6.2: Objectives

The objective of the proposed task is to develop a groundwater model for Basin 6 of the Nash Draw near the WIPP site using the ASCEM toolset coupled with the Advanced Terrestrial Simulator (ATS) to account for the surface and near-surface processes. These models will be used to compute the water balance across multiple scales and to reduce uncertainties in recharge estimates and propagation of the shallow dissolution front.

Subtask 6.2: Methodology

During FIU Year 2, FIU initiate the development of an ATS model of the Basin 6 study domain using the data derived from Subtask 6.1. Hydrological, climate and topography datasets were collected from various national database platforms. Given the uncertainty of the impact of small-scale hydrological features on infiltration and groundwater recharge, these analyses focus on using both a high-resolution DEM developed in Subtask 6.1 as well as other available coarser-scale DEMs (e.g. at 10, 30 or 90 m resolution). For FIU Year 2, the modeling workflow was established during a student summer internship at Los Alamos Laboratory will be employed for the Basin 6 study area to perform a series of ATS simulations, including the generation of meshes from the DEM data, setting up of meteorological forcing data, development of input files for the ATS, executing simulations on local or remote systems, and analyzing the output. Jupyter notebooks will be utilized to detail each of the steps in this workflow.

Subtask 6.2: Results and Discussion

During FIU Year 2 a python script was developed to delineate the ATS Basin 6 mesh using the python package TINerator. Three (3) different DEMs were obtained to test the script being used to generate the Basin 6 mesh that will be used for ATS model development. In Figure 130, the 10-meter DEM is shown.

Figure 130. Sample 10-meter DEM of Basin 6.

In Figure 131, sinkhole data (red dots) can be seen layered on top of the 10-meter DEM of Basin 6. In the previous reports, sinkhole data was omitted. Including the sinkhole data will result in a more accurate mesh to be exported for visualization.

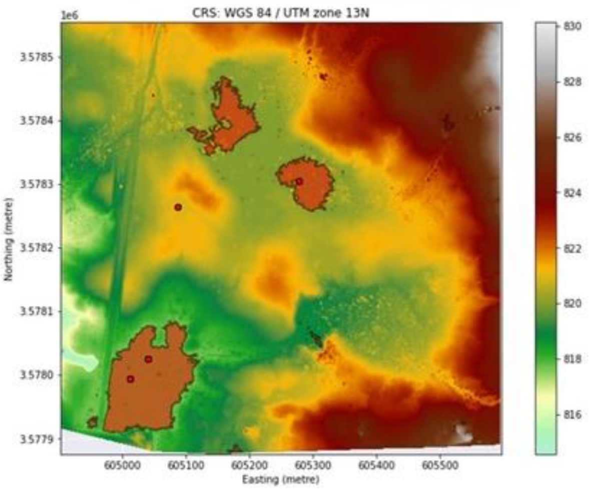

Figure 131. Sinkhole layer added to DEM in TINerator.

Watershed delineation values were then adjusted with upstream area values in order for the river network to be generated. The parameters of the side, top, and bottom mesh were also changed, as the size of the DEM greatly varied. The changes allowed for the DEM to fit in the mesh creation. To evaluate the workings of the mesh generation script using TINerator, three different DEMs (10-meter, 30-meter, and 90-meter) were used. In Figure 132, the watershed delineation results can be seen for each DEM. The threshold value is the “cut-off” value above which it is assumed that the river network starts to be observed. All cells below this value are assumed not to be part of the river network. The watershed delineation is determined through the D8 method. As the DEM resolution lowers, the threshold value must be decreased to sustain a similar upstream area.

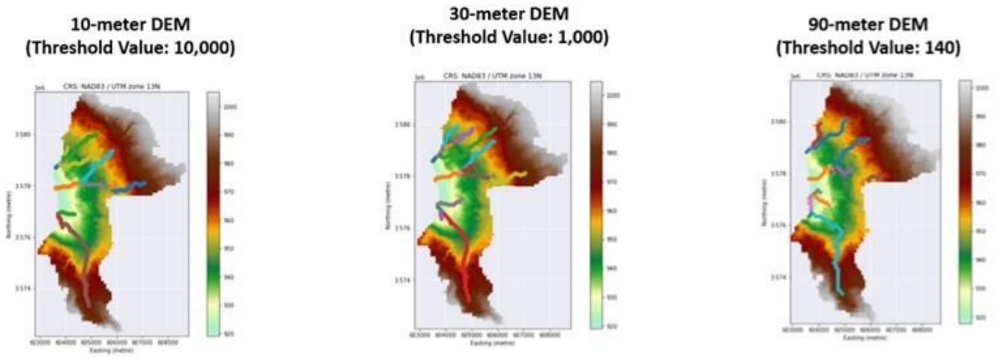

Figure 132. Watershed delineation of 3 DEMs of Basin 6 of varying spatial resolution (10m, 30m and 90m).

As stated above, the three DEMs were tested in the TINerator script. A surface mesh was generated for the 10-, 30-, and 90-meter DEMs. A surface mesh is developed through a combination of triangles. The triangles are controlled by a minimum and maximum edge length. The “min_edge_length” is what is seen near the watershed delineation lines and the “max_edge_length” is what is seen away from the watershed delineation lines and near the boundary of the domain. Increasing “min” will decrease total cells. Increasing “max” decreases total cells. Having fewer triangles means the simulation of the model will run faster. Although this is convenient, it will be less accurate. However, if many triangles are added to locations with limited hydrological variability (hillslope vs groundwater, seepage, elevation gradients, etc.), computational time is potentially wasted. Therefore, the goal is to increase the refinement around the streams, adding more triangles there and fewer triangles upstream with limited elevation gradients.

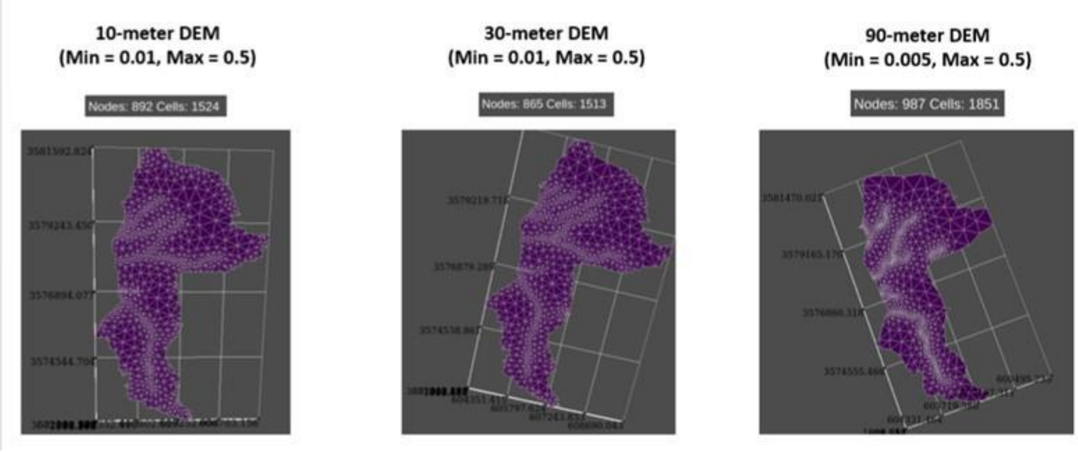

Figure 133. New mesh for 10-meter DEM of Basin 6.

Once the meshes were developed at the coarser grid resolution, it was decided to focus on the 1-meter DEM developed in Subtask 6.1. Because of the large data requirements at this high resolution it was decided to first delineate two sub-basins within Basin 6, one in the northern part of Basin 6 (Sub-Basin 2, ~3.7 km^2) and the other in the southern part (Sub-Basin 1, ~0.8 km^2).

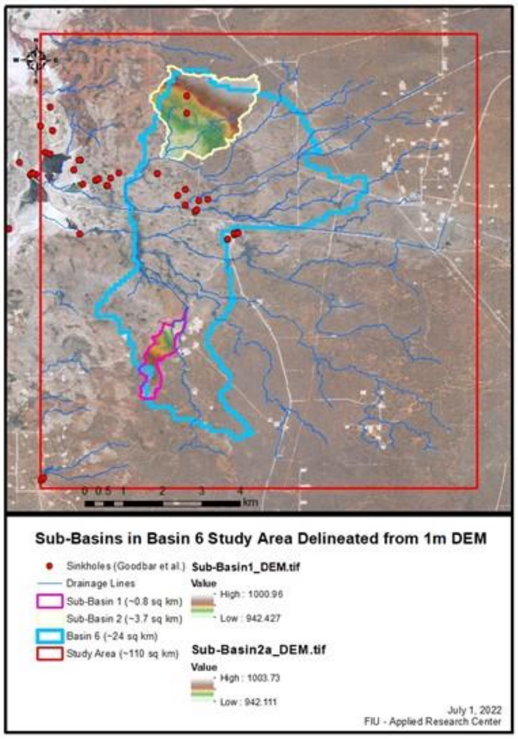

Figure 134. Sub-basins delineated from 1 m DEM of Basin 6.

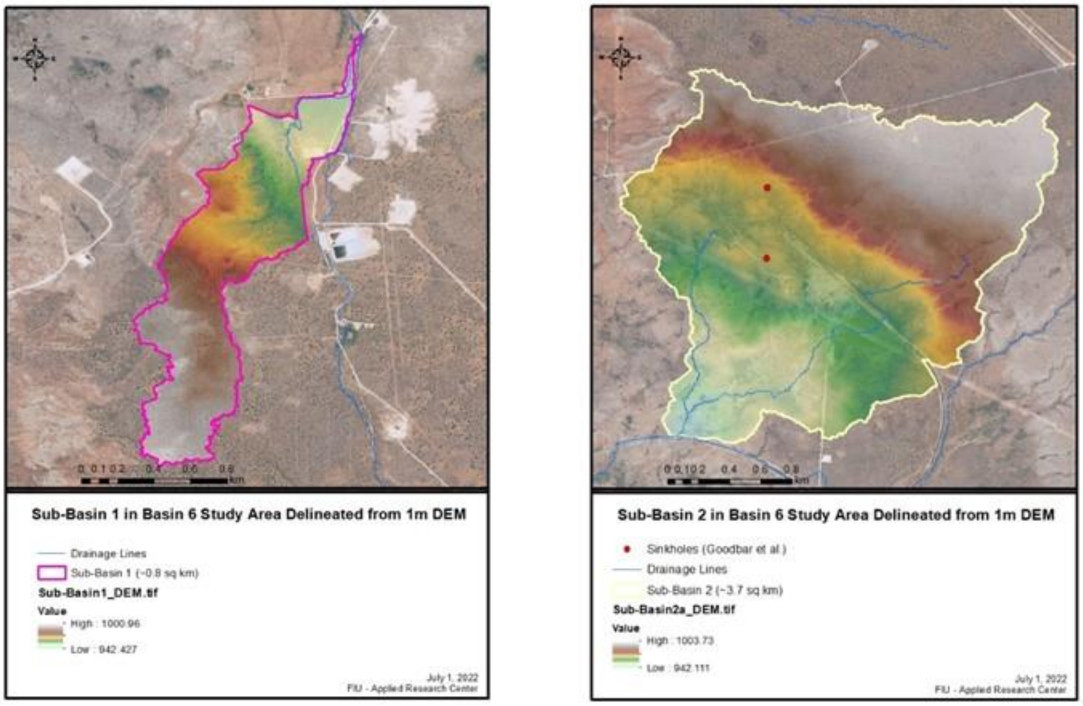

Figure 135. Sub-Basin 1 (left) and Sub-Basin 2 (right) used for training on ATS model development.

For each of these subbasins a mesh was generated using Tinerator. Below is a screenshot of a 12-hr simulation with rainfall for the first 4 hrs across the entire surface of Sub-Basin 2, with an outlet at the bottom of the basin to analyze the surface ponded depth.

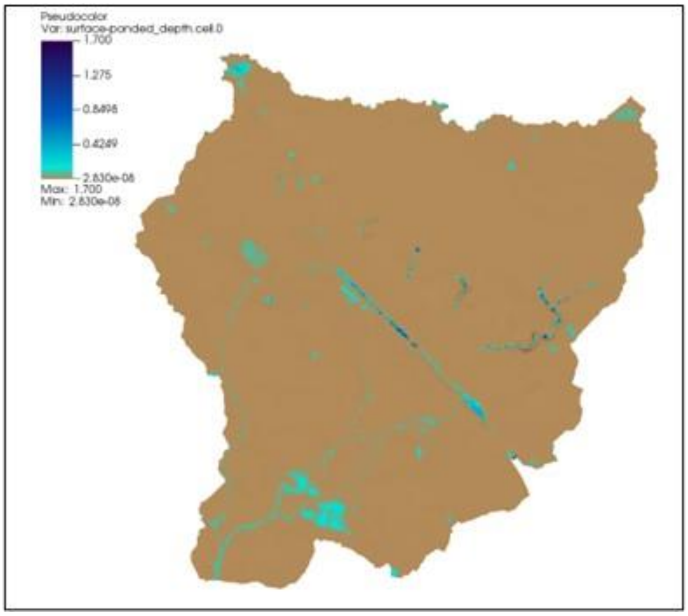

Figure 136. Visualization of rainfall on Sub-Basin 2 of Basin 6.

A plot of the associated runoff was also generated in ATS, as seen in the figure below, where water accumulates towards the outlet after 6 hours and decreases once the rain stops as there is less ponded water on the surface to drain.

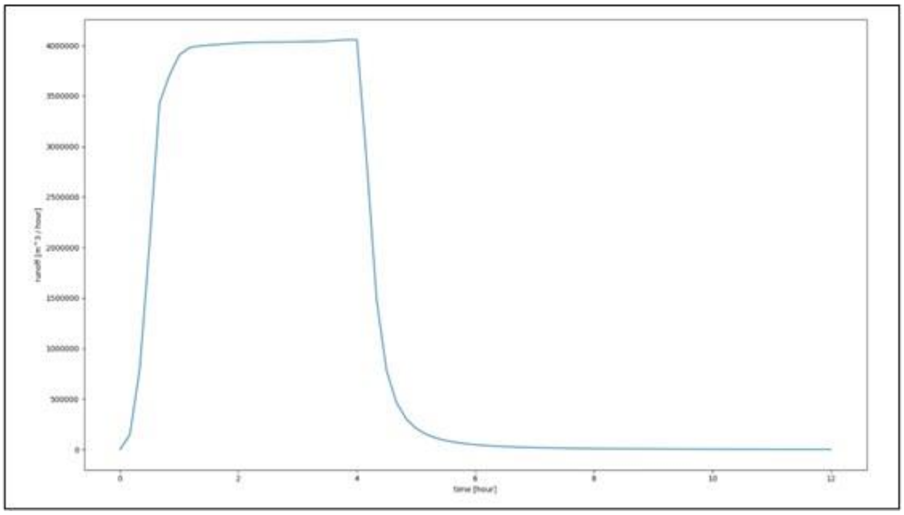

Figure 137. Runoff of Sub-Basin 2 of Basin 6.

After completing the ATS training over the summer, FIU initiated the development of a preliminary model of the entire Basin 6 study area using a coarser 10-m resolution DEM to minimize run time. The following table provides the input parameters used in this first draft of the Basin 6 ATS model.

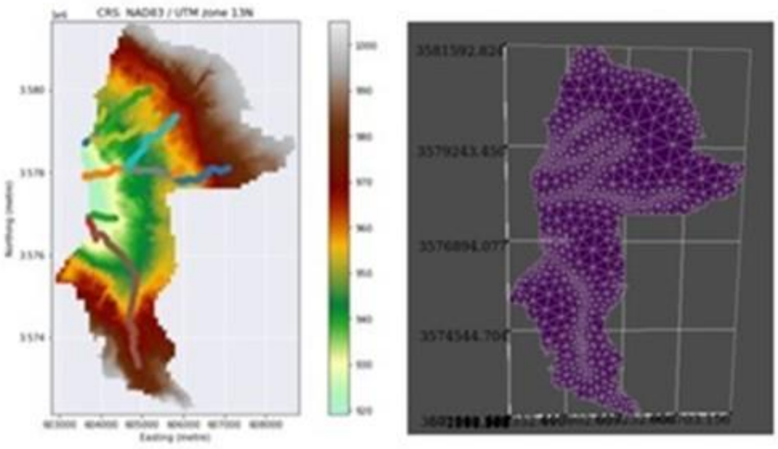

Figure 138. 10-m DEM of Basin 6 (left) and volume mesh generated in TINerator (right).

Using the volume mesh created from a 10-meter DEM of Basin 6 (Figure 138), a simulation was run to show the effect of rainfall on Basin 6. A 12-hour simulation was performed with rain homogeneously falling during the first 4 hours. Using TINerator, two outlets were added to the mesh. Figure 139 (right) shows a screenshot from the video simulation where the location of the outlets can be seen circled in red. The parameter analyzed in the visualization is the surface ponded depth. Accumulation of water toward the two outlets was observed after 6 hours. In the simulation, sinkholes were defined as a region with a different surface Manning's coefficient than the rest of the basin. This is more representative of the basin than having the entire surface with one Manning's coefficient. The image in Figure 139 (left) shows the locations where these sinkholes were located.

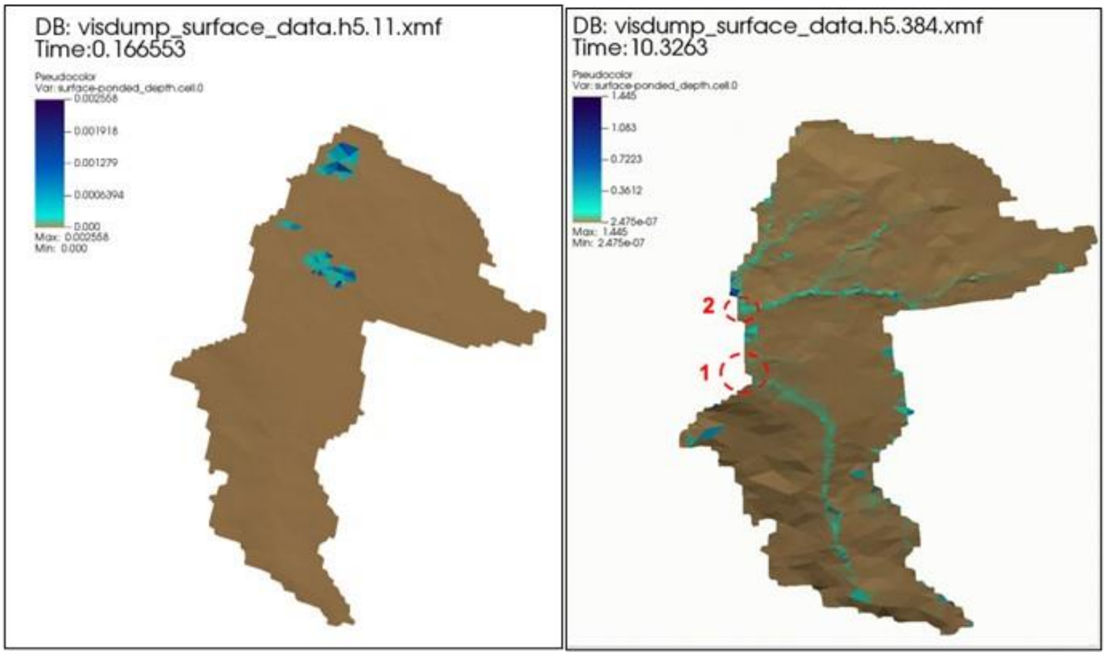

Figure 139. Visualization of Basin 6 infiltration regions (left) and simulation of surface runoff after 4 hours of rainfall in Basin 6 (right).

For these simulations, Outlet 1 had a maximum runoff of 1,000,000 m3/hr while Outlet 2 had a maximum runoff of 15,000,000 m^3/hr (Figure 140). This is important to determine where the majority of runoff is heading in the basin. These plots can also be generated for other elements of the basin, such as infiltration into the surface and subsurface.

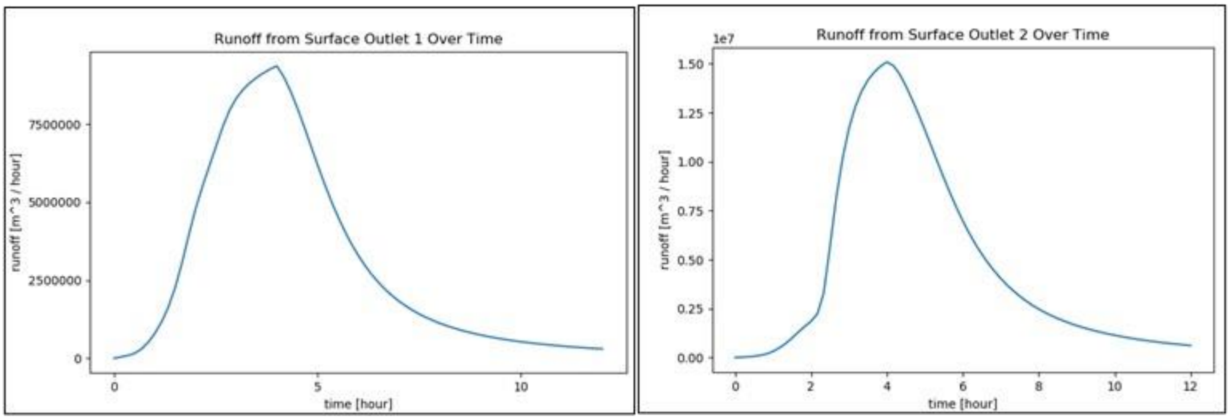

Figure 140. Runoff plot of Outlets 1 (left) and Outlet 2 (right) from Basin 6.

The simulation described above was performed to simulate overland flow only, however a second simulation was also performed incorporating a subsurface layer to test the fully integrated surface/subsurface model. A visualization of the model output can be seen in Figure 141.

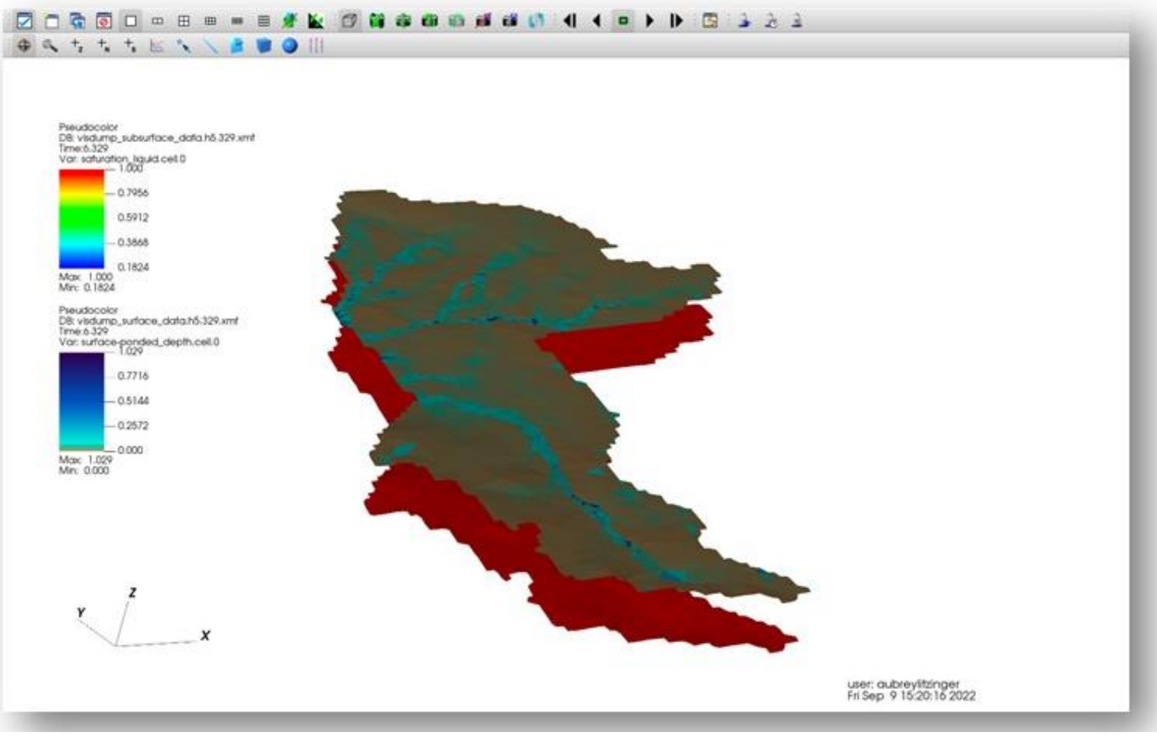

Figure 141. Visualization of the integrated surface/subsurface ATS model of Basin 6.

The next step will be to update the current version of the model with the high-resolution (1-m) DEM of Basin 6 and follow the established workflow for development of an integrated surface/subsurface model of Basin 6, incorporating significant surface features such as sinkholes, swallets and brine lakes that increase infiltration and can have an impact on the regional groundwater recharge. The model will then be calibrated, and simulations performed to evaluate the impact of climate change on the regional hydrology so DOE-EM scientists can better predict the rate of halite dissolution and propagation of the shallow dissolution front in order to quantify the potential impact on the WIPP repository performance.

Subtask 6.2: Conclusions

During FIU Year 2, FIU was successfully able to generate the ATS model mesh using TINerator. This was performed for various resolution DEMs of Basin 6. Furthermore, we were successfully able to setup and run an ATS model for both Basin 6 and some of its subdomain, with the latter using the 1-meter DEM generated in Subtask 3.1 as input. For FIU Year 3 we will apply this high-resolution dataset for the full domain of Basin 6.

Subtask 6.2: References

Beauheim, R. L. (2009). Collection and integration of geoscience information to revise the WIPP hydrology conceptual model. In *Approaches and challenges for the use of geological information in the safety case for deep disposal of radioactive waste*.

Coon, E. T., Moulton, J. D., & Painter, S. L. (2016). Managing complexity in simulations of land surface and near-surface processes. Environmental modelling & software, 78, 134-149.

Corbet, T. F., & Knupp, P. M. (1996). *The role of regional groundwater flow in the hydrogeology of the Culebra Member of the Rustler Formation at the Waste Isolation Pilot Plant (WIPP), southeastern New Mexico* (No. SAND-96-2133). Sandia National Lab, Albuquerque, NM (United States).

Freedman, V. L., Agarwal, D., Bensema, K., Finsterle, S., Gable, C. W., Keating, E. H., Krishnan, H.. Lansing, C., Moeglein, W., Pau, G. S. H., Porter, E., Scheibe, T. D. *Akuna: An Open Source User Environment for Managing Subsurface Simulation Workflows.* American Geophysical Union, Fall Meeting 2014.

Hart, D. B., McKenna, S. A., & Beauheim, R. L. (2009). *Calibration of the WIPP culebra transmissivity fields* (No. SAND2009-7334C). Sandia National Lab.(SNL-NM), Albuquerque, NM (United States); Sandia National Laboratories,, Carlsbad, NM.

Hayes, A. (2019). *Culebra Hydrologic Model in WIPP Performance Assessment* (No. SAND2019-4432PE). Sandia National Lab.(SNL-NM), Albuquerque, NM (United States).

Sampson, K., & Gochis, D. (2018). *WRF Hydro GIS Pre-Processing Tools, Version 5.0 Documentation.* Boulder, CO: National Center for Atmospheric Research, Research Applications Laboratory.

Wehbe, Y., Temimi, M., Weston, M., Chaouch, N., Branch, O., Schwitalla, T., Wulfmeyer, V., Zhan, X., Liu, J. and Al Mandous, A. (2019). *Analysis of an extreme weather event in a hyper-arid region using WRF-Hydro coupling, station, and satellite data.* Natural Hazards & Earth System Sciences, 19(6).

Yucel, I., Onen, A., Yilmaz, K. K., & Gochis, D. J. (2015). *Calibration and evaluation of a flood forecasting system: Utility of numerical weather prediction model, data assimilation and satellite-based rainfall.* Journal of Hydrology, 523, 49-66.

Zeitler, T. R. (2016). *WIPP Performance Assessment* (No. SAND2016-8142PE). Sandia National Lab.(SNL-NM), Albuquerque, NM (United States).

TASK 7: ENGINEERED MULTI-LAYER AMENDMENT TECHNOLOGY FOR MERCURY REMEDIATION ON THE OAK RIDGE RESERVATION

Task 7: Introduction

Over 3,000 mercury-contaminated sites have been identified worldwide as a result of legacy wastes from past weapons production and industrial uses ranging from coal-fired power plants to artisanal gold mining [Kocman et al., 2013]. As increased economic activity and the disposal of mercury-added products continue to outpace efforts to curtail mercury releases to the environment, there are growing needs for long-term, low-cost remedial technologies to combat mercury contamination [Futsaeter and Wilson, 2013]. Because of its persistent geochemistry, bioaccumulative effect and continuous cycling through the environment, mercury remediation poses health and economic challenges. Furthermore, the presence of diffuse mercury sources complicate efforts to develop effective technology for mercury remediation in freshwater stream ecosystems, such as the East Fork Poplar Creek (EFPC) in Oak Ridge, Tennessee [Southworth et al., 2010].

As a case study, EFPC, a 26-kilometer low-gradient stream in Oak Ridge, Tennessee, received approximately 128,000 ±35,000 kg of mercury (Hg) from the headwaters at Y-12 (National Security Complex) from 1950 to 1963, resulting in contamination of the EFPC floodplain soils, surface water, and streambed sediment [Brooks and Southworth, 2011]. Despite targeted remedial actions in the early 1980s that significantly reduced Hg inputs at the Y-12 source zone, EFPC is still classified as an impaired waterbody due to elevated Hg concentrations in soil, water, and biota. Annual mercury and methyl mercury fluxes from streambank soil to EFPC are estimated at 38.6 kg and 5.6 g, respectively [Watson et al., 2016]. The vast majority of mercury export from the EFPC watershed is attributed to streambank soils and Y-12 discharge. Although floodplain runoff and infiltration exert some impact on Hg flux to the EFPC stream system, they are considered minor in comparison to Hg flux from Y-12 and streambank soils. The spatial distribution, speciation and extent of Hg contamination have been well documented in several studies conducted within EFPC in recent years [Peterson et al., 2018; Riscassi et al., 2016; Southworth et al., 2010]. About 60% of mercury exiting Y-12 is in the dissolved inorganic phase (Hg^{2+}), which becomes increasingly complexed with natural dissolved organic matter (DOM) with distance downstream. Total DOM concentration in EFPC water typically ranges from 2.5 to 3.5 mg/L [Dong et al., 2010].

Mercury remediation technology typically involves either reducing its bioavailability for methylation or reducing its flux to the environment. While sorbent amendments are effective at removing mercury from the environment, they are less effective at reducing mercury bioavailability for methylation [Katherine A. Muller and Brooks, 2019; K. A. Muller et al., 2019]. Furthermore, sorbent fouling issues can result in constituents and particulates leaching into waterbodies, severely limiting their applications for Hg sequestration [Johs et al., 2019]. Mercury fate and transport in EFPC are governed by its strong interaction with DOM, rendering Hg^{2+} binding to sorbents and removal from the water column by strong reductants like stannous chloride ($SnCl_2$) problematic [Dong et al., 2010; Liang et al., 2010]. Dissolved organic matter are recalcitrant transformation products of plants and microbial remains that are known to form strong complexes with Hg^{2+} ions by either limiting adsorption onto solid phase(s) or enhancing the solubility of Hg precipitates. The molecular weight of DOM ranges from 300 – 3000 Daltons with an average of ~800 Daltons (g/mol) [Averett et al., 1995]. Functional groups found on DOM are as follows: reduced sulfur (S_{red}) or thiols (R–SH or S_{red}), O- and N-containing groups such as carboxylic (R–COOH), phenolic (R–OH), amino (R–NH–R, $R–NH_2$), quinone, and hydroquinone (R–C=O). Dissolved organic matters are characterized by the following sorption sites: (1) Site 1 (weak sites, FA1), these sites are involved in territorial binding of counter-ions in the vicinity of humic diffuse layer (electrostatic interaction) and (2) Site 2 (strong sites, FA2), less abundant (thiol, phenolic) sites on which site-specific metal binding occur involving electron transfer interactions. Generally, weak sites are more common than strong sites due to abundant carboxylic functional groups [Averett et al., 1995]. At a low Hg:DOM ratio, strong Hg^{2+} binding by thiol groups is favored, whereas at a high Hg:DOM ratio weak binding of Hg^{2+} to carboxylic, phenolic, amino, quinone and other functional groups is preferred. Moreover, at $Hg^{2+}:S_{red}$ molar ratios of < 0.10–0.15, 0.15–0.40 and >0.40, Hg^{2+} forms 1:2 complexes with two RS^-, mixed complexes with one RS^- and O–Hg–S or N–Hg–S, and complexes with RO^- or RN^- functional groups [Dong et al., 2010]. It has been shown that DOM can compete with mercury for sorption sites on amendment materials such as activated carbon (AC) and biochar, reducing their overall effectiveness for mercury capture [K. A. Muller et al., 2019]. The reduction in overall effectiveness is attributed to the interaction of AC with DOM rather than the direct interaction of AC with Hg [Eckley et al., 2020].

Despite the widespread use of amendments for in-situ organic contaminant sequestration, large-scale application of sorbent media for Hg remediation is uncommon [Gomez-Eyles et al., 2013; Schwartz et al., 2019; Wang et al., 2020; Wang et al., 2019]. Mercury sorbents may be effective in reducing Hg transport to the environment; however, their widespread use may be ineffective and cost-prohibitive in the presence of DOM.

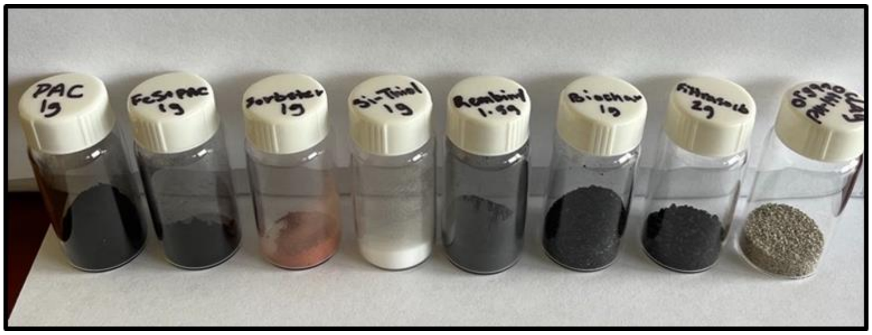

Figure 142. Image of eight evaluated sorbent media

Task 7: Objectives

The overarching objective of this study is to evaluate a suite of reactive sorbent media for cost-effective removal of mercury in the presence of abundant DOM. The specific scope of this study was to determine the kinetics, maximum sorption capacity and adsorption mechanism to inform robust designs of effective remedial technologies for mercury retention.

Table 35. A list of Evaluated Sorbent Media for Mercury Sorption.

Media Acronym	Description	Manufacturer
nsPAC	Finely milled activated carbon particles produced from lignite coal	Cabot Corporation, Boston, MA
fsPAC	An equal blend of abiotically synthesized mackinawite and finely ground carbon produced from lignite coal	Redox Solutions, Carmel, IN
PBC	Charcoal, anaerobically produced via high-temperature, slow pyrolysis of plant biomass (mostly wood chips)	Biochar Now, LLC, Loveland, CO
F300	Granular activated carbon produced from bituminous coal via reagglomeration process	Calgon Carbon Corporation, Moon Township, PA
Si-SH	A silica gel (backbone) modified with sulfur-containing organic compound (1-propanethiol)	Biotage LLC, Charlotte, NC
eBind	Powdered carbon-mineral blend of aluminum oxyhydroxide, activated carbon, clays and other proprietary additives	RemBind Pty Ltd, Thebarton, Australia
eSorb	An activated alumina blended with iron oxide and sulfur	Sorbster, Inc., Euclid, OH
Q-Clay	Sodium bentonite clay modified with quaternary ammonium	CET COMineral Technologies, Hoffman Estates, IL

Task 7: Methodology

A suite of sorbent media was tested for removal of aqueous mercury (Hg^{2+}) phase(s) from DOM-laden creek water (Figure 142 and Table 35). The investigated sorbent materials included the following: (1) *PBC* (Biochar Now), (2) *eSorb* (Sorbster, Inc.), (3) *Si-SH* (Biotage LLC), (4) *fsPAC* (Redox Solutions, LLC), (5) *nsPAC* (Cabot Corporation), 6) *Q-Clay* (CETCO Minerals Technologies), 7) *F300* (Calgon Carbon Corporation) and (8) *eBind* (RemBind Pty Ltd). The sorbents were evaluated due to their sustainability, low-cost (except Si-thiol) and anticipated high adsorptive capacity for removal of aqueous Hg in the presence of DOM. A majority of these sorbent media were either carbon-based materials or functionalized silica/clays (Table 35).

Mercury Standards

A mercury stock standard traceable to NIST SRM 3133 was purchased from Alfa Aesar (Ward Hill, MA). The as-received stock solution (Specpure®) containing 1,000 ± 5 µg/mL Hg^{2+} in 5% HNO_3 was stored at 4ºC and was diluted to the desired working concentration for the batch sorption studies using 5% HNO_3.

Artificial Creek Water (ACW)

An artificial creek water (solution) was employed in these batch sorption studies. The ACW solution is a simulant whose chemical composition closely mimics natural, uncontaminated creek water chemistry found in EFPC. The composition of the ACW is as follows: 41.5 mg/L Ca^{2+}, 27.38

mg/L Na^+, 1.89 mg/L K^+, 12.05 mg/L Mg^{2+}, 14.83 mg/L Cl^-, 197.06 mg/L NO_3^-, and 33.86 SO_4^{2-} [Goñez-Rodríguez et al., 2021]. All chemicals were ACS reagent grade or better in purity and used as received. Sodium chloride, sodium nitrate, sodium sulfate, potassium nitrate, magnesium nitrate (Fisher Scientific, Pittsburg, PA), calcium nitrate (Acros Organics, Geel, Belgium), and ultrapure deionized water (>18 MΩ) were used to prepare the ACW. The pH of the ACW was adjusted with either HNO_3 or NaOH (0.1 or 1.0 M) to a pH value of 8 ±0.5.

Dissolved Organic Matter (DOM)

The DOM used in these studies is an aquatic organic matter isolate from the Suwannee River (SRNOM) that was procured from the International Humic Substances Society (IHSS). The chemical composition reported by IHSS for SRNOM (2R101N) in % (w/w) is as follows: H_2O (5.69), Ash (4.01), C (50.7), H (3.97), O (41.48), N (1.27), S (1.78) [Driver and Perdue, 2014]. The carboxylic functional groups of the SRNOM is 4.5 times higher than its phenolic groups. The SRNOM comprised predominantly of fulvic acid (~80%) and humic acid and humin substances (20%) [Averett et al., 1995]. To prepare a DOM stock solution, SRNOM (600 mg/L) was mixed into a liter of ACW that was placed on shaker at 100 rpm for 48 h and subsequently filtered through a 0.2-µm polyethersulfone (PES) filter. The pH of the DOM solution was not pH adjusted. The stock solution was covered with aluminum foil to limit exposure to light and stored in amber glass bottles at 4 ºC until used. The estimated total concentration of dissolved organic carbon (DOC) in the DOM stock solution (C_{OM}) was ~300 mg/L.

Batch Sorption Studies

Batch sorption studies were performed to determine mercury adsorption onto eight sorbent media as a function of time (kinetic) and varying concentration (isotherms) in ACW simulant spiked with DOM (DOM solution). Aliquots of Hg^{2+} ranging from 100 ± 15 µg/L (kinetic studies) to 500 ± 15 µg/L (isotherm studies) were added to DOM solutions that were allowed to pre-equilibrate for 120 h for strong complexation of Hg^{2+} with DOM. The molar ratio of Hg:C_{OM} in the final solution (Hg-DOM) was 2×10^{-4} and 10^{-4} for kinetic and isotherm studies, respectively. For the kinetic studies, 0.35 to 5.0 g/L of sorbent media were added to each batch reactor containing Hg-DOM solutions, whereas for isotherm studies batch reactors were amended with sorbent dosages ranging from 0.2 to 20 g/L. Without pH adjustment of the suspensions, the slurry mixtures were stirred on a slow shaker at 100 rpm for up to 5760 min at 25°C (room temperature). At each time interval, the suspensions were either centrifuged with a Sorvall Legend Micro 17 centrifuge (Thermo Scientific, Inc.) at 9,000 rpm for 10 min or filtered through a 0.2-µm Supor® membrane filter (Acrodisc®). Approximately 0.1-0.2 g of the filtrates were transferred to nickel boats for Hg^{2+} analysis on a DMA-80 *evo* (Milestone, Inc.). Distribution coefficient (K_d), kinetic and sorption capacity values were subsequently calculated from the filtrate concentrations using rate equations and adsorption isotherms.

The rate equations (Eq.1 – Eq. 8) given below were used to assess the kinetics of Hg^{2+} sorption as Hg-DOM complexes onto the studied sorbent material(s).

The percent adsorption or removal efficiency (R_E) and adsorbed amount (Q_t) of Hg^{2+} were computed as follows:

$$R_E\ (\%) = \frac{C_0 - C_t}{C_0} \times 100 \qquad \text{Eq. 1}$$

$$\mathrm{Q_t = \frac{V(C_0 - C_t)}{m}} \qquad \text{Eq. 2}$$

$$\mathrm{K_d = \frac{(C_0 - C_t)}{C_t} \times \frac{V}{m}} \qquad \text{Eq. 3}$$

where C_0 is the initial aqueous Hg^{2+} concentration in the sorbent-free solution (Hg^{2+} concentration at the beginning of the experiment); and C_t (mg/L) is the effluent final Hg^{2+} concentrations after equilibration with the sorbents; K_d (mL/g) is the distribution coefficient; V is the volume of suspension (L) and m is the mass of added sorbent phase(s) (g).

The pseudo-first order, PFO (Lagergren's equation) is expressed below as follows [Lagergren, 1898]:

$$\mathrm{\ln(Q_e - Q_t) = \ln Q_e - k_1 t} \quad \text{(Linear form)} \qquad \text{Eq. 4}$$

$$\mathrm{Q_t = Q_e\left(1 - e^{-k_1 t}\right)} \quad \text{(Nonlinear Form)} \qquad \text{Eq. 5}$$

The expressions of the pseudo-second order (PSO) are given below [Blanchard et al., 1984]:

$$\mathrm{\frac{t}{Q_t} = \frac{1}{k_2 Q_e^2} + \left(\frac{1}{Q_e}\right) t} \quad \text{(Linear form)} \qquad \text{Eq. 6}$$

$$\mathrm{Q_t = \frac{Q_e^2 k_2 t}{1 + k_2 Q_e t}} \quad \text{(Nonlinear form)} \qquad \text{Eq. 7}$$

The initial adsorption rate h is derived from the expression: $h = k_2 Q_t^2$

The intraparticle diffusion model is useful for distinguishing rate-controlling steps and predicting reaction pathways and adsorption mechanism. This kinetic model is dependent on the porosity, size of particles, solution concentration and agitation velocity. Its linearized expression is as follows [Weber Jr and Morris, 1963]:

$$\mathrm{Q_t = k_p \sqrt{t} + C} \quad \text{(Linear Form)} \qquad \text{Eq. 8}$$

where Q_t (mg/g) and Q_e (mg/g) are the amount of Hg^{2+} adsorbed at time t (min) and at equilibrium, respectively; k_1 (1/min) is the pseudo-first-order rate constant; k_2 (g/mg × min) is the pseudo-second-order rate constant; kp is the intraparticle diffusion constant (mg/g × $min^{1/2}$) and C (mg/g) is the liquid film or boundary layer thickness.

The Langmuir adsorption isotherm describes monolayer adsorption onto homogeneous finite sites of sorbent surfaces without interaction between adsorbed molecules (i.e., the adsorbate species). When the observed experimental data are well described by the Langmuir model, the R_L (a dimensionless separation factor; Eq. 11) is especially useful for predicting the favorability of the adsorption process based on the initial concentration of the adsorbate (Hg^{2+}). When $R_L > 1$, the adsorption is considered unfavorable; $R_L = 1$, the adsorption is linear; $0 < R_L < 1$, the adsorption is favorable, and when $R_L = 0$, the adsorption is irreversible.

The Freundlich isotherm describes multilayer adsorption onto heterogeneous surfaces that are characterized by interaction among adsorbates.

The Langmuir equations are expressed below [24]:

$$\frac{1}{\mathrm{Q_t}} = \left(\frac{1}{\mathrm{Q_m K_L}}\right)\frac{1}{\mathrm{C_t}} + \frac{1}{\mathrm{Q_m}} \quad \text{(Linear model)} \qquad \text{Eq. 9}$$

$$\mathrm{Q_t} = \frac{\mathrm{Q_m K_L C_t}}{1 + \mathrm{K_L C_t}} \quad \text{(Nonlinear model)} \qquad \text{Eq. 10}$$

$$\mathrm{R_L} = \frac{1}{1 + \mathrm{K_L Q_m C_0}} \qquad \text{Eq. 11}$$

The expressions for the Freundlich equations are as follows [Langmuir, 1918]:

$$\log \mathrm{Q_t} = \mathrm{n} \log \mathrm{C_t} + \log \mathrm{K_F} \quad \text{(Linear model)} \qquad \text{Eq. 12}$$

$$\mathrm{Q_e} = \mathrm{K_F C_t^n} \quad \text{(Nonlinear model)} \qquad \text{Eq. 13}$$

Where K_L (L/mg) is the Langmuir constant related to the affinity between the adsorbate (Hg^{2+}) and sorbent, and it is essentially the reciprocal of the concentration at which the sorbent is 50% saturated; Q_m (mg/g) is the maximum monolayer adsorption capacity of the sorbent; K_F [(mg/g)/(mg/$L)^n$] is the Freundlich constant characterizing the adsorption strength; n is the dimensionless Freundlich intensity parameter related to adsorption intensity and/or surface heterogeneity.

Studies have shown that errors associated with experimental data are typically transformed during the linearization of adsorption data. Thus, non-linearized regression analyses were conducted on the original form of adsorption equations. Nonlinear regression typically involves the minimization of error distribution between the experimental data and predicted values. The estimation of the pertinent sorption parameters in the nonlinear models were performed using experimental data. The estimated values were subsequently used for validation by comparing the predicted values with the observed values over the duration of the batch sorption experiments.

The modeling errors for the nonlinear models were evaluated with the sum of squared errors (SSE), which is the difference between the predicted and measured adsorption values as follows:

$$\mathrm{SSE} = \sum_{\mathrm{i}}^{\mathrm{n}} (\mathrm{O_i} - \mathrm{P_i})^2 \qquad \text{Eq. 14}$$

Where is O_i and P_i are experimental and model-predicted values, respectively.

The minimization of SSE was performed in a Microsoft Excel spreadsheet using the add-in Solver coupled with the generalized reduced gradient nonlinear algorithms. A small SSE value is indicative of the quality and predictive performance of the model to accurately fit the observed experimental data. Moreover, the determination coefficient (R^2), an indicator of the model precision, and therefore the quality of the fit, was calculated as follows [Lima et al., 2015; Schwarz, 1978]:

$$\mathrm{R^2} = 1 - \left(\frac{\sum_{\mathrm{i}}^{\mathrm{n}} (\mathrm{O_i} - \mathrm{P_i})^2}{\sum_{\mathrm{i}}^{\mathrm{n}} (\mathrm{O_i} - \overline{\mathrm{O}}_{\mathrm{i}})^2}\right) \qquad \text{Eq. 15}$$

Where $\overline{O}_i$ is the average value of observed experimental data. To evaluate the robustness of models, the differences in Bayesian Information Criteria (ΔBIC) were employed. The expression is given in the equation below [Lima et al., 2015]:

$$\mathrm{BIC} = \mathrm{nLn}\left(\frac{\mathrm{SSE}}{\mathrm{n}}\right) + \mathrm{pLn(n)} \qquad \mathrm{Eq.\,16}$$

Where n is the number of data points, p is the number of parameters in the fitting model

The ΔBIC is defined as the difference between a BIC value from one model (e.g. Langmuir model) and BIC value from another model (e.g. Freundlich model). When the $\Delta\mathrm{BIC} \leq 2$, there is no significant difference between the applied models; $2 < \Delta\mathrm{BIC} < 6$, there is a high probability that the model with the lower BIC value is the most appropriate; $6 < \Delta\mathrm{BIC} < 10$, there is high probability that the model with the lower BIC is the better fitting model, and $\Delta\mathrm{BIC} > 10$, it can be predicted with a high degree of confidence that the model with the lower BIC is the better fitting model [Schwarz, 1978].

Mercury Speciation Modeling

Selected Hg^{2+} thermodynamic reaction constants and ACW composition were used in the aqueous speciation modeling (Visual MINTEQ v. 3.1) to assess the degree of complexation of Hg^{2+} with aqueous inorganic species and DOM [Gustafsson and Berggren Kleja, 2005]. The speciation modeling employed the NICA-Donna approach, in which humic substances (HS) molecules are thought to form spherical gel (Donna) phase(s) separated from the bulk water phase, and all the charges on the molecules inside the gel are neutralized by counter ions inside the gel. A detailed description of the NICA-Donna model has been extensively published in literature [Benedetti et al., 1996; Kinniburgh et al., 1996].

Using known DOM concentrations and the equations given below, the concentrations of thiol, carboxylic and phenolic ligands were estimated in the DOM:

$$\mathrm{DOM_{SH}} = [\mathrm{DOM}]\mathrm{F_1F_2}\frac{\mathrm{F_3}}{\mathrm{MW_S}} \text{ (Thiol)} \qquad \mathrm{Eq.\,17}$$

$$\mathrm{DOM_{COOH}} = \mathrm{C_1}\frac{[\mathrm{DOC}]}{1000} \text{ (Carboxylic)} \qquad \mathrm{Eq.\,18}$$

$$\mathrm{DOM_{OH}} = \mathrm{C_2}\frac{[\mathrm{DOC}]}{1000} \text{ (Phenolic)} \qquad \mathrm{Eq.\,19}$$

Where DOM_{SH}, DOM_{COOH} and DOM_{OH} are concentrations of thiol, carboxylic and phenolic groups in mmol/L; [DOM] and [DOC] are concentrations of DOM and DOC in mg/L; F_1, F_2, F_3 are total sulfur content in DOM, percent reduced sulfur and percent reduced sulfur as reactive thiol for binding Hg^{2+}, respectively. MW_S is the molecular mass of sulfur (g/mole), C_1 and C_2 are carboxylic and phenolic ligands charge density in DOM (meq/g C). DOM concentration is assumed twice that of DOC [Dong et al., 2010; Liu et al., 2019]. The F_1, F_2 and F_3 values taken from literature were 1.78% (IHSS), 50% and 2%, respectively. C_1 and C_2 values of 11.2 and 2.47 mmol/g were from literature [Driver and Perdue, 2014].

Task 7: Results and Discussion

The result of the geochemical modeling presented in Table 36 showed that >99% of Hg^{2+} is strongly bound to thiol or phenolic groups of the DOM, forming stable Hg-DOM complexes. This predominance of Hg-DOM complexes is likely due to relatively low Hg concentrations and the abundance of available thiol or phenolic sorption sites on the DOM. Calculated S_{red}, carboxylic and phenolic groups in DOM-amended ACW is ~3.34 µM, 3.36 µM and 0.74 µM, respectively. Moreover, the Hg^{2+}/S_{red} ratio of ≤0.15 indicates abundance of available DOM for formation of either bidentate or monodentate Hg-DOM complexes, corroborating the result of the geochemical modeling.

Table 36. Visual MINTEQ speciation result of major constituents of batch sorption experiments.

Component	Dissolved Inorganic (M)	Bound to DOM (M)	Total Dissolved (M)	Dissolved (%)
Ca^{2+}	9.59 x 10^{-4}	7.64 x 10^{-5}	1.04 x 10^{-3}	100
CO_3^{2-}	1.32 x 10^{-5}	1.84 x 10^{-11}	1.32 x 10^{-5}	100
H^+	5.08 x 10^{-5}	-2.44 x 10^{-5}	2.64 x 10^{-5}	100
$Hg(OH)_2$	1.22 x 10^{-15}	5.00 x 10^{-7}	5.00 x 10^{-7}	100
K^+	4.79 x 10^{-5}	2.68 x 10^{-7}	4.82 x 10^{-5}	100
Mg^{2+}	4.57 x 10^{-4}	3.89 x 10^{-5}	4.96 x 10^{-4}	100
Na^+	1.18 x 10^{-3}	6.64 x 10^{-6}	1.19 x 10^{-3}	100
NO_3^-	3.13 x 10^{-3}	8.60 x 10^{-8}	3.13 x 10^{-3}	100
SO_4^{2-}	3.53 x 10^{-4}	5.86 x 10^{-10}	3.53 x 10^{-4}	100

The rate of sorption of Hg^{2+} as Hg-DOM complexes onto sorbent media is presented in Figure 143. The kinetic data showed that sorption of Hg-DOM complexes onto tested sorbent media reached a steady state within 60-1440 min time interval, with the exception of Q-Clay media wich did not achieve steady-state adsorption over the entire duration of this study (10,880 min) as only ~36% of Hg-DOM was adsorbed on Q-Clay sorbent media. Typically, the rate for Hg-DOM sorption was rapid to moderately rapid (*nsPAC, eBind and F300),* moderately rapid (*fsPAC* and *eSorb)*, moderate (*S-SH and PBC)* and very slow (*Q-Clay)*. Increasing the sorbent dosages resulted in faster rate of Hg-DOM sorption onto the evaluated sorbents. Extension of the adsorption duration up to 10,880 min (data not shown) did not appreciably alter the established equilibrium adsorption of Hg-DOM onto sorbent media. Based on the kinetic rates, the evaluated sorbents were ranked as follows: nsPAC < F300 < eBind ≤ fsPAC ≤ eSorb < PBC < Si-SH << Q-Clay.

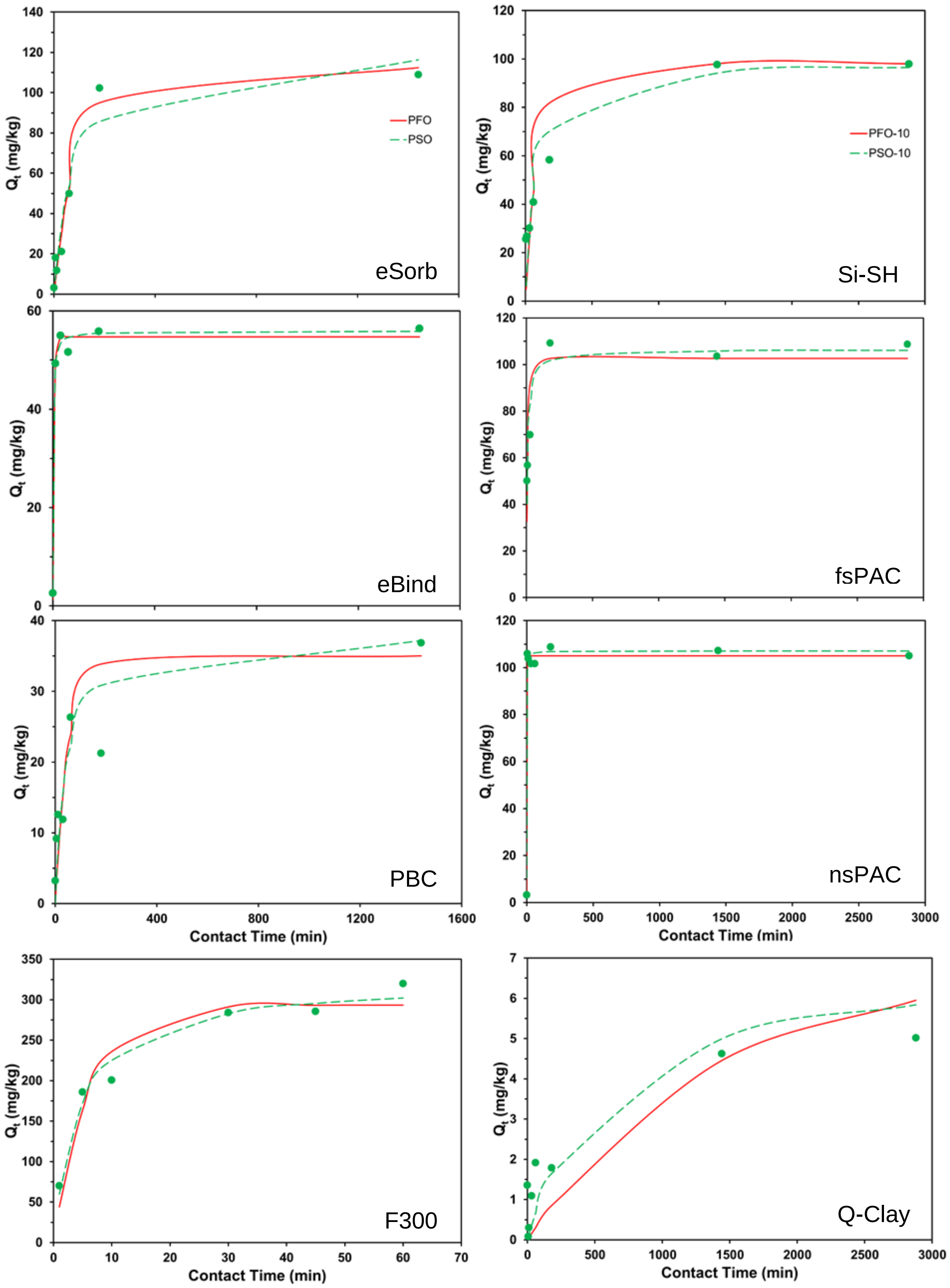

Figure 143. The nonlinear pseudo first and pseudo second order plot for Hg^{2+} adsorption onto a suite of sorbents media in Hg^{2+}-pre-equilibrated DOM solution. Experimental conditions included a Hg^{2+} concentration of 100 ±75 µg/L µg/L, solid:liquid ratio of 0.35-5 g/L, contact time of 1 – 2880 min, and four replicates.

Calculated model parameters for all evaluated kinetic models further demonstrated the applicability of the nonlinear pseudo-second-order as a better fitting model compared to the pseudo-first-second model to describe the observed experimental data ($\Delta BIC \geq 2$). The adsorption kinetic is primarily controlled by intra-particle (pore) diffusion when a plot of Q_t against $\sqrt{t}$ is linear and passes through the origin, whereas a plot yielding multiple linear regions is considered an adsorption process governed by a multistep mechanisms. The results of the intraparticle diffusion model (IDM) for a select set of tested sorbents are displayed in Figure 144. The intraparticle diffusion plot is non-linear, giving multiple linear regions that can be grouped into different linear stages over the studied time interval. The initial steep stage accounts for the external mass transfer of the Hg-DOM from the bulk solution onto the external surface of the sorbent media through the hydrodynamic boundary film or layer (film or external diffusion). The later stage of the model is attributed to the pore diffusion (transport of Hg-DOM from the adsorbent exterior into the pores of the adsorbent, along pore-wall surfaces, or both) and gradual equilibration of the adsorption process. Thus, the adsorption of Hg-DOM onto the evaluated sorbent media is primarily controlled by film diffusion. This observed adsorption mechanism is similar for all sorbent media evaluated in this study. Furthermore, the values of the observed intercept (C) were positive, confirming the influence of boundary layer (film diffusion) restriction on the adsorption process.

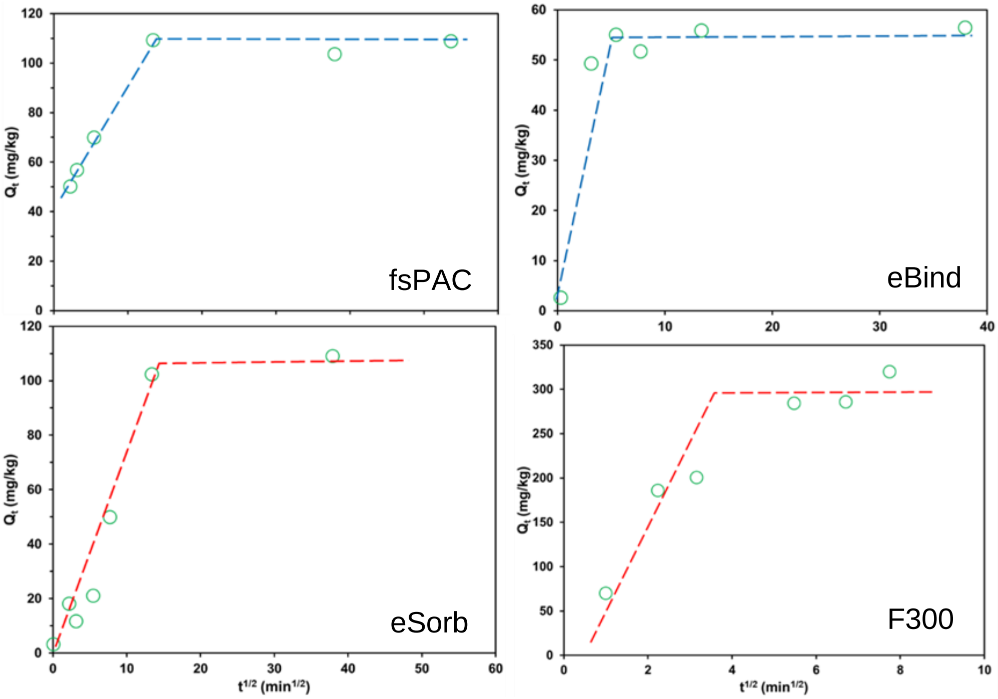

Figure 144. The intraparticle diffusion plot for adsorption of Hg-DOM onto select sorbent media in mercury-preequilibrated DOM solution. Experimental conditions included a Hg^{2+} concentration of 100 ±15 µg/L; Molar Hg:DOC ratio of 2×10^{-4}; Solid:liquid ratio of 1 g/L; four replicates.

Presented in Figure 145 are isotherm data for sorption of Hg-DOM complexes onto eight evaluated sorbent media. Partition coefficient (K_D) are useful for assessing the adsorption behavior of a contaminant under prevailing geochemical site conditions. It is expressed as the distribution of contaminants between the solid (immobile) phase(s) and aqueous (mobile phase) phase(s). The inverse proportionality between the sorbent use rate and K_D allows for ranking of sorbent effectiveness in removing Hg-DOM complex from contaminated aqueous media. Calculated K_D and sorbent use rate for an effective treatment of a liter of DOM-amended ACW containing 500

±15 µg Hg^{2+}/L are presented in Figure 146. The K_D values for the evaluated sorbents ranged from 69.7 mL/g (Q-Clay) to 41,510 mL/g (Si-SH) with a use rate varying from 0.024 g/L (Si-SH) to 14.34 g/L (Q-Clay), respectively. Typically, the most effective sorbents are characterized by relative low use rate values. Overall, the effectiveness of the evaluated sorbent media for sorption of Hg-DOM complexes was ranked as follows: Si-SH > eSorb > nsPAC > fsPAC > eBind> F300 > PBC >> Q-Clay. Study results indicated that a majority of the evaluated sorbents are promising candidates for efficient removal of Hg-DOM complexes from DOM-laden freshwater ecosystems such as EFPC.

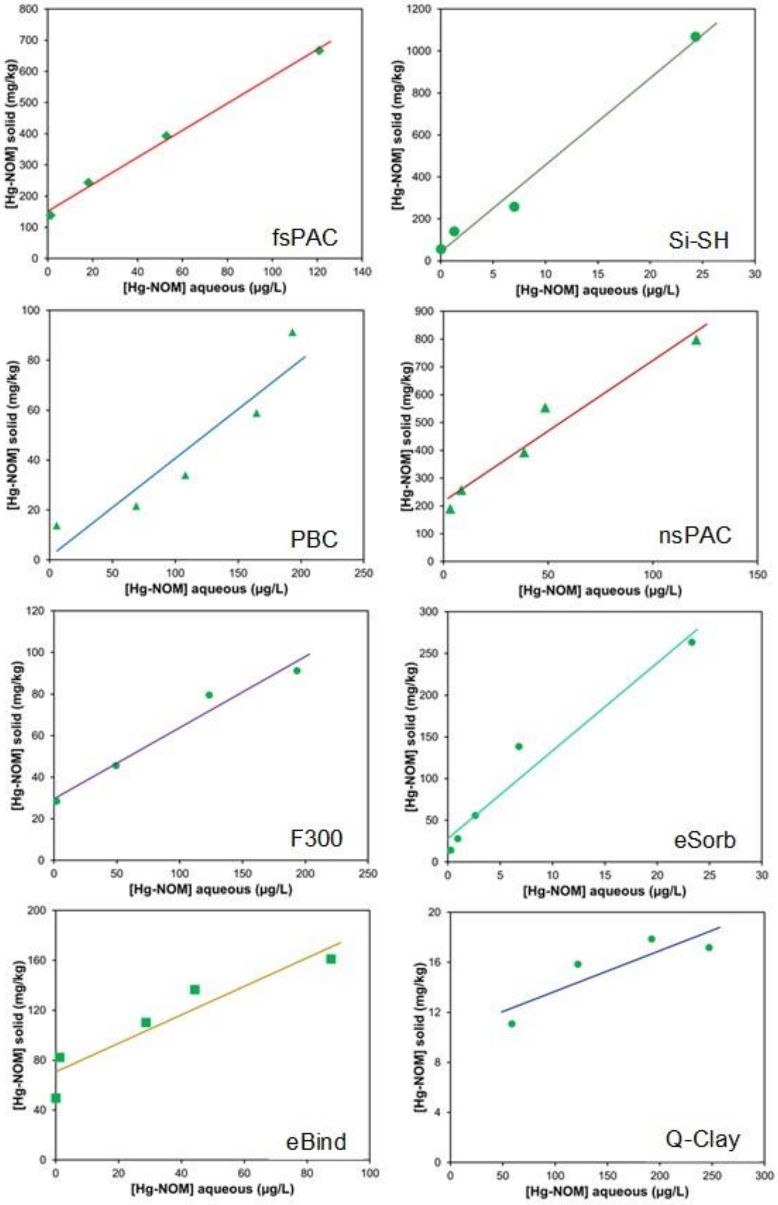

Figure 145. The linear isotherm plot for adsorption of Hg-DOM complex onto a suite of sorbent media in mercury-preequilibrated dissolved organic matter solution. Experimental conditions included a Hg^{2+} concentration of 500 ±15 µg/L; molar Hg:DOC ratio of 10^{-4}; solid:liquid ratio of 0.2-20 g/L; equilibration time: 48 h; four replicates.

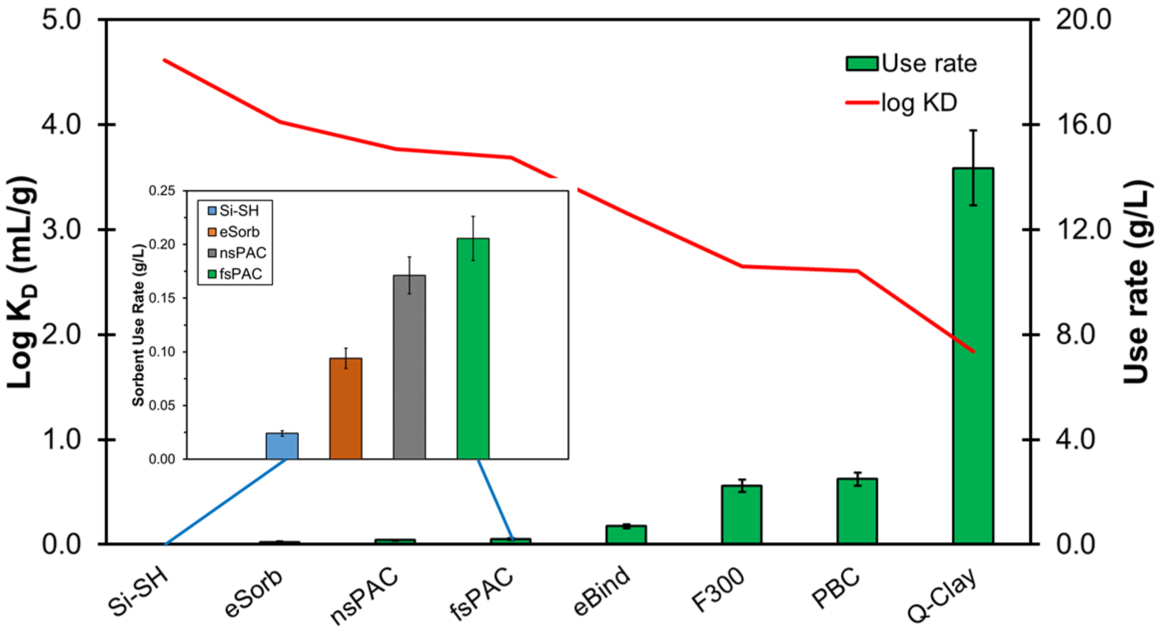

Figure 146. Comparison of distribution coefficient (K_D) and sorbent use rate among sorbent media in mercury-preequilibrated dissolved organic matter solutions. The inset shows a close up for sorption onto four of the tested sorbent media. Experimental conditions included a Hg^{2+} concentration of 500 ±15 µg/L; molar Hg:DOC ratio of 10^{-4}; solid:liquid ratio ranges from 0.2-20 g/L; equilibration time: 48 h; four replicates.Task 7: Conclusions

Eight low-cost sorbent media were evaluated for mercury removal as Hg-DOM complexes from a contaminated freshwater stream whose composition is representative of the EFPC ecosystem. Kinetic parameters computed with kinetic models demonstrated that the nonlinear pseudo-second-order model is a better fitting model compared to the nonlinear pseudo-first-order model to describe observed experimental data ($\Delta BIC > 2$). Furthermore, kinetic data suggest liquid film diffusion was the rate-limiting step that controls sorption of Hg-DOM complexes on the tested sorbents. The K_D values for the evaluated sorbents generally ranged from 69.7 mL/g (Q-Clay) to 41,510 mL/g (Si-SH) with a use sorbent rate varying from 0.024 g/L (Si-SH) to 14.34 g/L (Q-Clay), respectively. Overall, the evaluated sorbent media were ranked in terms of decreasing sorptive capacity for Hg-DOM complexes as follows: Si-SH > eSorb > nsPAC > fsPAC > eBind> F300 > PBC >> Q-Clay. Study results indicated that a majority of the evaluated sorbents are effective reactive media removal of Hg-DOM complexes from the highly Hg-contaminated system such EFPC freshwater ecosystem.

Task 7: References

Averett, R. C., J. A. Leenheer, D. M. McKnight, and K. A. Thorn (1995), Humic Substances in the Suwannee River, Georgia: Interactions, Properties, and Proposed Structures*Rep.*, 217 pp, U.S. Geological Survey, U.S. Geological Survey, Denver, Colorado 80225.

Benedetti, M. F., W. H. Van Riemsdijk, L. K. Koopal, D. G. Kinniburgh, D. C. Gooddy, and C. J. Milne (1996), Metal ion binding by natural organic matter: from the model to the field, Geochimica et Cosmochimica Acta, 60(14), 2503-2513.

Blanchard, G., M. Maunaye, and G. Martin (1984), Removal of heavy metals from waters by means of natural zeolites, Water research, 18(12), 1501-1507.

Brooks, S. C., and G. R. Southworth (2011), History of mercury use and environmental contamination at the Oak Ridge Y-12 Plant, Environ Pollut, 159(1), 219-228, doi: 10.1016/j.envpol.2010.09.009.

Dong, W., L. Liang, S. Brooks, G. Southworth, and B. Gu (2010), Roles of dissolved organic matter in the speciation of mercury and methylmercury in a contaminated ecosystem in Oak Ridge, Tennessee, Environmental Chemistry - ENVIRON CHEM, 7, doi: 10.1071/EN09091.

Driver, S. J., and E. M. Perdue (2014), Acidic functional groups of Suwannee River natural organic matter, humic acids, and fulvic acids, in Advances in the Physicochemical Characterization of Dissolved Organic Matter: Impact on Natural and Engineered Systems, edited, pp. 75-86, ACS Publications.

Eckley, C. S., C. C. Gilmour, S. E. Janssen, T. P. Luxton, P. M. Randall, L. Whalin, and A. Carrie (2020), The assessment and remediation of mercury contaminated sites: A review of current approaches, Science of the Total Environment, 707, doi: 10.1016/j.scitotenv.2019.136031.

Futsaeter, G., and S. Wilson (2013), The UNEP Global Mercury Assessment: Sources, Emissions and Transport, E3S Web of Conferences, 1, 36001, doi: 10.1051/e3sconf/20130136001.

Gomez-Eyles, J. L., C. Yupanqui, B. Beckingham, G. Riedel, C. Gilmour, and U. Ghosh (2013), Evaluation of Biochars and Activated Carbons for In Situ Remediation Of Sediments Impacted With Organics, Mercury, And Methylmercury, Environmental Science & Technology, 47(23), 13721-13729, doi: 10.1021/es403712q.

Goñez-Rodríguez, L., A. Johs, K. A. Lowe, K. E. Carter, F. E. Löffler, and M. A. Mayes (2021), Evaluation of engineered sorbents for the sorption of mercury from contaminated bank soils: a column study, Environmental Science and Pollution Research, 28(18), 22651-22663, doi: 10.1007/s11356-020-12073-4.

Gustafsson, J. P., and D. Berggren Kleja (2005), Modeling salt-dependent proton binding by organic soils with the NICA-Donnan and Stockholm Humic models, Environmental science & technology, 39(14), 5372-5377.

Johs, A., V. A. Eller, T. L. Mehlhorn, S. C. Brooks, D. P. Harper, M. A. Mayes, E. M. Pierce, and M. J. Peterson (2019), Dissolved organic matter reduces the effectiveness of sorbents for mercury removal, Sci Total Environ, 690, 410-416, doi: 10.1016/j.scitotenv.2019.07.001.

Kinniburgh, D. G., C. J. Milne, M. F. Benedetti, J. P. Pinheiro, J. Filius, L. K. Koopal, and W. H. Van Riemsdijk (1996), Metal ion binding by humic acid: application of the NICA-Donnan model, Environmental Science & Technology, 30(5), 1687-1698.

Kocman, D., M. Horvat, N. Pirrone, and S. Cinnirella (2013), Contribution of contaminated sites to the global mercury budget, Environmental Research, 125, 160-170, doi: https://doi.org/10.1016/j.envres.2012.12.011.

Lagergren, S. (1898), About the theory of so-called adsorption of soluble substances Kungliga Svenska Vetenskaps Akademiens., 24(4), 1-39.

Langmuir, I. (1918), The adsorption of gases on plane surfaces of glass, mica and platinum, Journal of the American Chemical society, 40(9), 1361-1403.

Liang, L., B. Gu, S. C. Brooks, C. L. Miller, F. He, D. Elias, D. B. Watson, and M. J. Peterson (2010), Challenges and opportunities of mercury remediation in East Fork Poplar Creek, Oak Ridge, Tennessee (Invited), in *AGU Fall Meeting Abstracts*, edited.

Lima, É. C., M. A. Adebayo, and F. M. Machado (2015), Kinetic and equilibrium models of adsorption, in Carbon nanomaterials as adsorbents for environmental and biological applications, edited, pp. 33-69, Springer.

Liu, P., C. J. Ptacek, and D. W. Blowes (2019), Mercury complexation with dissolved organic matter released from thirty-six types of biochar, Bulletin of environmental contamination and toxicology, 103(1), 175-180.

Muller, K. A., and S. C. Brooks (2019), Effectiveness of Sorbents to Reduce Mercury Methylation, Environmental Engineering Science, 36(3), 361-371, doi: 10.1089/ees.2018.0375.

Muller, K. A., C. C. Brandt, T. J. Mathews, and S. C. Brooks (2019), Methylmercury sorption onto engineered materials, J Environ Manage, 245, 481-488, doi: 10.1016/j.jenvman.2019.05.100.

Peterson, M. J., S. C. Brooks, T. J. Mathews, M. A. Mayes, A. Johs, D. B. Watson, K. A. Muller, L. Gonez Rodriguez, C. R. Derolph, and S. Surendrannair (2018), Mercury Remediation Technology Development for Lower East Fort Poplar Creek - FY2018 Update*Rep. ORNL/SPR-2018/912 United States 10.2172/1490603 ORNL English*, Medium: ED; Size: 59 p. pp, ; Oak Ridge National Lab. (ORNL), Oak Ridge, TN (United States).

Riscassi, A., C. Miller, and S. Brooks (2016), Seasonal and flow-driven dynamics of particulate and dissolved mercury and methylmercury in a stream impacted by an industrial mercury source, Environ Toxicol Chem, 35(6), 1386-1400, doi: 10.1002/etc.3310.

Schwartz, G. E., T. A. Olsen, K. A. Muller, and S. C. Brooks (2019), Ecosystem Controls on Methylmercury Production by Periphyton Biofilms in a Contaminated Stream: Implications for Predictive Modeling, Environ Toxicol Chem, 38(11), 2426-2435, doi: 10.1002/etc.4551.

Schwarz, G. (1978), Estimating the dimension of a model, The annals of statistics, 461-464.

Southworth, G. R., M. S. Greeley Jr, M. J. Peterson, K. A. Lowe, R. H. Ketelle, and S. B. Floyd (2010), Sources of Mercury to East Fork Poplar Creek Downstream from the Y-12 National Security Complex: Inventories and Export Rates*Rep. ORNL/TM-2009/231*, Medium: ED pp, Oak Ridge National Lab. (ORNL), Oak Ridge, TN (United States); Oak Ridge Electron Linear Accelerator.

Wang, A. O., C. J. Ptacek, D. W. Blowes, Y. Z. Finfrock, D. Paktunc, and E. E. Mack (2020), Use of hardwood and sulfurized-hardwood biochars as amendments to floodplain soil from South River, VA, USA: Impacts of drying-rewetting on Hg removal, Science of The Total Environment, 712, 136018, doi: https://doi.org/10.1016/j.scitotenv.2019.136018.

Wang, A. O., C. J. Ptacek, D. W. Blowes, B. D. Gibson, R. C. Landis, J. A. Dyer, and J. Ma (2019), Application of hardwood biochar as a reactive capping mat to stabilize mercury derived from contaminated floodplain soil and riverbank sediments, Science of The Total Environment, 652, 549-561, doi: https://doi.org/10.1016/j.scitotenv.2018.10.213.

Watson, D. B., S. C. Brooks, T. J. Mathews, M. S. Bevelhimer, C. DeRolph, C. C. Brandt, M. J. Peterson, and R. Ketelle (2016), Evaluation of Lower East Fork Poplar Creek Mercury Sources, Medium: ED; Size: 128 p.

Weber Jr, W. J., and J. C. Morris (1963), Kinetics of adsorption on carbon from solution, Journal of the sanitary engineering division, 89(2), 31-59.

CONFERENCE PARTICIPATION, PUBLICATIONS, AWARDS & ACADEMIC MILESTONES

Peer-reviewed Publications

Brooks, S. C., C. L Miller, A. L Riscassi, K. A Lowe, J. O Dickson, G. E Schwartz, (August 2021). Increasing temperature and flow management alter mercury dynamics in East Fork Poplar Creek, Hydrological Processes, 35, e14344 (https://doi.org/10.1002/hyp.14344).

Di Pietro, SA., Emerson., HP., Katsenovich, Y., Johnson, TJ., Francis RM., Mason HE, Marple, M., Sawvel, A., Szecsody, JE. Solid phase characterization and transformation of illite mineral with gas-phase ammonia treatment. Journal of Hazardous Materials, v. 424, Part C. February 2022, p.127657.

Kandel, S., Katsenovich, Y., Boglaienko, D., Emerson, HP., Levitskaia, T. Time Dependent Zero Valent Iron Oxidation and the Reductive Removal of Pertechnetate at Variable pH. Journal of Hazardous Materials, v.424, Part B, 15 February 2022, 127400.

Drozd, V., Katsenovich, Y., Asmussen, R. M., Kandel, S., Maratos, A., Gudavalli, R. and L. Lagos, Effect of Grout-Contacted Solution on the Glass Dissolution Behavior. Proceedings of the Waste Management Symposia 2022, March 6-10, 2022, Phoenix, AZ.

Dickson, J., Estrada, C., Katsenovich,Y., Lagos, L., Johs, A. and E. Pierce, Sustainable Sorbent Technology for Mercury Remediation in a Freshwater Aquatic System. Proceedings of the Waste Management Symposia 2022, March 6-10, 2022, Phoenix, AZ.

Conference Presentations

Oral Presentations (presenter is underlined)

Dickson, J., Caridad Estrada, Yelena Katsenovich, Leonel Lagos, Alexander Johs, Eric Pierce. "Sustainable Sorbent Technology for Mercury Remediation in a Freshwater Aquatic System Waste Management" Virtual Conference, Phoenix, AZ, March 2022.

Doughman M., Katsenovich K., Lagos L., O'Shea K., Emerson H., Freedman V., Szecsody J., Qafoku N., Oral Presentation: Impact of Major Groundwater Components on the Adsorption of Uranium (VI) to Hanford Formation Sediment; at the RemPlex 2021 Global Summit on Environmental Remediation. November 8-12, 2021, Virtual.

Drozd, V., Yelena Katsenovich, R. Matthew Asmussen, Shambhu Kandel, Alicia Maratos, Ravi Gudavalli, Leonel Lagos. "Effect of Grout-Contacted Solution on the Glass Dissolution Behavior". Waste Management Conference, Phoenix, AZ, March 2022.

Pham P., Gonzalez-Raymat H., Gudavalli R. (Oral) *Sorption of Iodide and Iodate on Wetland Soils (22609),* at the Waste Management Symposia 2022. March 6-10, 2022, Phoenix, AZ.

DOE Fellows, Mariah Doughman and Juan Morales, participated virtually in the RemPlex 2021 Global Summit on Environmental Remediation held on November 7 - 12, 2021.

Morales, J., (oral) Modeling Episodic Heavy Metal Transport and Toxicity for the Assessment of Remediated Surface Waters" presented at the Emerging Contaminants session of the RemPlex 2021 Global Summit on Environmental Remediation held on November 7 - 12, 2021.

Poster Presentations (presenter is underlined)

Doughman M., Katsenovich K., Lagos L., O'Shea K., Emerson H., Freedman V., Szecsody J., Qafoku N., Poster: *Impact of Major Groundwater Components on the Adsorption of Uranium (VI) to Hanford Formation Sediment*; at the Waste Management Symposia 2022. March 6-10, 2022, Phoenix, AZ.

Doughman M., Katsenovich K., Lagos L., O'Shea K., Poster: *Competing Attenuation Processes for Mobile Contaminants in Hanford Sediments*; at the American Chemical Society National Meeting & Exposition Fall 2021. August 21-26, Atlanta, GA.

Gutierrez-Zuniga, G., Moulton, D. and D. Livingston. *Utilization of Amanzi-ATS to Develop an Integrated Hydrology Model of the Nash Draw Basin West of the Waste Isolation Pilot Plant (WIPP).* (Poster) Waste Management Conference, Phoenix, AZ, March 2022.

Pham, P., Ravi Gudavalli, Hansell Gonzalez-Raymat. *Removal of Iodine-129 by Organoclays MRM and PM-199.* (Poster) Waste Management Conference, Phoenix, AZ, March 2022.

Pham P., Gonzalez-Raymat H., Poster: *Sorption of Iodide and Iodate on Wetland Soils*, at the Waste Management Symposia 2022. March 6-10, 2022, Phoenix, AZ.

Pham P., Gonzalez-Raymat H., Gudavalli R., Poster: *Effective removal of Iodine species by organoclays MRM and PM-199*; at the American Chemical Society National Meeting & Exposition Fall 2021. August 21-26, 2021, Atlanta, GA.

Almaguer, A., Yelena Katsenovich, Hilary Emerson, James Szecsody, Vicky Freedman, Nikolla Qafoku. *Re-oxidation of Technetium (^{99}Tc) Comingled with Uranium (^{238}U) and Nitrate (NO_3^-) Immobilized by Strong Reductants*. (Poster) Waste Management Conference, Phoenix, AZ, March 2022.

Charles, S., Wainwright, H., Gonzalez-Raymat, H. and A. Lawrence. *Surface Water Dynamics within the F-Area of Savannah River Site and its Linkages with Groundwater and I-129 Geochemistry*. (Poster). Waste Management 2022 Conference, Phoenix, AZ, March 2022.

Dickson, J., Caridad Estrada, Yelena Katsenovich, Leonel Lagos, Alexander Johs, Eric Pierce. *Sorbent-Based Technology for Mercury Remediation in a Freshwater Aquatic System*. American Geophysical Union (AGU) Fall Meeting 2021, New Orleans, LA, December 13 -17, 2021.**A**

Awards

Six DOE Fellows working on Project 2 presented their posters at the annual DOE Fellows poster competition. Caridad Estrada won first place for the undergraduate section, Mariah Doughman won second place for the graduate students' section, and Phuong Pham won third place for the graduate students' section.

DOE Fellows Mariah Doughman and Caridad Estrada were selected as 2022 Roy G. Post Foundation scholarship recipients at the graduate and undergraduate levels, respectfully. This scholarship supported their travel to attend the Waste Management Symposia 2022 to present their research conducted for Project 2.

DOE Fellow Caridad Estrada, who is supporting Project 2 - Task 7, won 1st place among undergraduate research presentations at the annual Maximizing Access to Research Careers - Undergraduate Student Training for Academic Research (FIU MARC-U*STAR) symposium held on December 1, 2021. The title of her oral presentation was "*Sustainable Sorbent Technology for Mercury Remediation in Freshwater Aquatic Systems*".

Juan Morales received the "best presentation" award for his outstanding presentation titled *"Modeling Episodic Heavy Metal Transport and Toxicity for the Assessment of Remediated Surface Waters"* during the Emerging Contaminants session of the RemPlex 2021 Global Summit on Environmental Remediation held on November 7 - 12, 2021. His discussion was based on research conducted at Savannah River Site (SRS) in the Tims Branch watershed in an attempt to comprehend the regulatory and toxicological variables associated with surface water treatment.

Academic Milestones

DOE Fellow Aubrey Litzinger graduated with a bachelor's degree in environmental engineering at FIU in fall 2022. Additionally, Ms. Litzinger received the *"Outstanding Graduate in Environmental Engineering"* award at the commencement ceremony.

DOE Fellow Juan Morales who is scheduled to complete his PhD in Environmental Health Sciences at FIU by the end of 2022, accepted a position at the Savannah River National Laboratory (SRNL) as a MSIPP Postdoctoral Fellow beginning mid-June 2022. Fellow Morales has supported and provided major contributions to the Project 2 Tims Branch hydrological and contaminant transport modeling work at Savannah River Site.

DOE Fellow Gisselle Gutierrez accepted a position as a Civil Analyst in the Surface Water Dept. at Kimley-Horn and Associates, Inc. in August 2022. She will defend her thesis and graduate with a master's degree in Environmental Engineering in Fall 2022.

ACKNOWLEDGEMENTS

Funding for this research was provided by U.S. DOE Cooperative Agreement #DE-EM0005213. FIU's Applied Research Center would like to acknowledge the commitment of DOE-EM to this specific Environmental Remediation Science and Technology project and to all the collaborators at DOE-EM HQ and the National Labs for support of the research being conducted as part of the Cooperative Agreement. The partnership between DOE EM and FIU has also resulted in the development and training of outstanding minority STEM students that will benefit this country as a whole.

FIU also gratefully acknowledges Thomas Beasley from FIU FCAEM facilities for his assistance with the SEM/EDS analyses.

APPENDIX A

The following documents are available at the DOE Research website for the Cooperative Agreement between the U.S. Department of Energy Office of Environmental Management and the Applied Research Center at Florida International University:
https://doeresearch.fiu.edu/SitePages/Welcome.aspx

FIU Year 2 Annual Research Review Presentations:

1. FIU Research Review - Project 1
2. FIU Research Review - Project 2
3. FIU Research Review - Project 3 – D&D
4. FIU Research Review - Project 3 – IT ML
5. FIU Research Review - Project 4 & 5
6. FIU Research Review - Project 4 - DOE Fellow Aubrey Litzinger
7. FIU Research Review - Project 4 - DOE Fellow Aurelien Meray
8. FIU Research Review - Project 4 - DOE Fellow Joel Adams
9. FIU Research Review - Project 4 - DOE Fellow Mariah Doughman
10. FIU Research Review - Project 4 - DOE Fellow Nicholas Espinal
11. FIU Research Review - Project 4 - DOE Fellow Philip Moore
12. FIU Research Review - Project 5 - DOE Fellow Olivia Bustillo
13. FIU Research Review - Project 5 - DOE Fellow Shawn Cameron
14. FIU Research Review - Wrap Up - Project 1
15. FIU Research Review - Wrap Up - Project 2
16. FIU Research Review - Wrap Up - Project 3 – D&D
17. FIU Research Review - Wrap Up - Project 3 – IT ML
18. FIU Research Review - Wrap Up - Project 4
19. FIU Research Review - Wrap Up - Project 5

APPENDIX B

Draft manuscript in preparation by DOE Fellow Mariah Doughman titled *"Impact of Chromium (VI) as a Co-mingled Contaminant on the Attenuation Mechanisms of Uranium (VI) in Quartz, Plagioclase Feldspar, and Carbonate Dominated Sediment Under Oxic Mildly Alkaline Conditions"*.